A STUDY OF ARC WELDABILITY OF γ′-STRENGTHENED COBALT-BASED SUPERALLOY

BY

HAMID ABEDI

A Thesis Submitted to the Faculty of Graduate Studies of the University of Manitoba in Partial Fulfillment of the Requirement for the Degree of

DOCTOR OF PHILOSOPHY

Department of Mechanical Engineering, University of Manitoba
Winnipeg, Canada

ABSTRACT

CoWAlloy1 is a new gamma prime (γ′) precipitation-strengthened cobalt (Co)-based superalloy that is developed to replace conventional nickel (Ni)-based superalloys for high-temperature applications in land-based and aero turbine engines. Welding superalloys is an essential part of the manufacture and repair of complex-shaped components of turbine engines. Unfortunately, joining precipitation-hardened superalloys such as CoWAlloy1 is severely limited due to their high susceptibility to cracking during welding. Therefore, this research conducts a comprehensive study on the cracking susceptibility and corresponding properties of CoWAlloy1 that is subjected to gas tungsten arc welding (GTAW) and develops an effective approach to eliminate/minimize cracking during welding.

The numerical model developed to simulate GTAW shows an adequate level of accuracy for predicting the solidification behavior of the fusion zone (FZ) and selecting the window of welding parameters that prevent FZ cracking during the welding of CoWAlloy1. Although optimum GTAW parameters prevent cracking in the FZ, welding produces heat-affected zone (HAZ) cracking in the alloy. A careful examination of the microstructure shows that a primary cause of HAZ cracking in this alloy is intergranular liquation due to the subsolidus liquation reaction of the MC-type carbides and γ′ precipitates, which are identified by electron microscopy and spectroscopy to be present in the material before welding.

Detailed weldability studies reveal that the grain boundary elemental segregation of boron (B) controls the cracking susceptibility of the HAZ during welding. In addition, it is observed that a reduction in grain size contributes to the resistance of CoWAlloy1 to HAZ cracking. Accordingly, a new pre-weld heat treatment that couples reduction in grain boundary segregation of B with a

small grain size is found to effectively inhibit HAZ cracking not only during welding but also after the post-weld heat treatment (PWHT). Furthermore, the new pre-weld heat treatment produces tensile properties and hot corrosion resistance after PWHT that are comparable to those of the alloy that has not been subjected to welding, which demonstrates that the new pre-weld heat treatment prevents the deleterious effects of welding on tensile properties and does not produce a substantial reduction in the hot corrosion resistance of this new superalloy.

ACKNOWLEDGMENT

I would like to express my deepest appreciation to my advisor Dr. O.A. Ojo for providing me with the opportunity to work under his mentorship. I am also extremely grateful for his timely advice, financial support, substantial contribution to the research work, and the provision of all materials and equipment required for the successful completion of my doctoral program. I would also like to thank my late co-advisor, Dr. Xinjin Cao, for his valuable suggestions and contribution to this research. I also want to express my gratitude to my advisory committee members, Dr. Rodrigo França and Dr. Matt Khoshdarregi, for their valuable advice and contribution to the success of this research work.

I wish to express my gratitude to the University of Manitoba and the Faculty of Graduate Studies for the financial support through the International Graduate Student Entrance Scholarship and the Research Completion Award, respectively. Financial support from the Natural Sciences and Engineering Research Council of Canada (NSERC) towards this research is gratefully acknowledged.

I wish to thank Mike Boskwick and his wonderful colleagues for their technical assistance and Dr. Lina Zhang for her support with laboratory supplies throughout this research study. I extend my sincere thanks to Dr. Abdul Khan for his support during this research work. I also thank my friends Dr. Mallikarjuna Thammaiah, Oguntuase Oluwasanmi, Lulu Guo, Dr. Ehsan Zarrinabadi, Dr. Osamudiamen Olaye, Dr. Oluwadara Afolabi, Dr. Gbenga Asala, James Adu, Chidinma Anyanwu, and Hassan Sada for their immense support.

I would like to express my greatest appreciation to my parents, my siblings Hamed, Hojar, and Amir hossein, and all other member of the Abedi and Noorbakhsh family for their love, support, and guidance toward my upbringing.

DEDICATION

I dedicate this doctoral dissertation to

My Father, Mr. Majid Abedi

My Mother, Mrs. Tahereh Noorbakhsh

And

My Late Grandmother, Mrs. Nosrat Farazan

TABLE OF CONTENTS

LIST OF TABLES

LIST OF FIGURES

LIST OF ABBREVIATIONS

AC	Air-Cooled
APB	Anti-Phase Boundary
APDL	Ansys Program Designed Language
ATCL	Average Total Crack Length
BCC	Body-Centered Cubic
BM	Base Metal
BOP	Bead-On-Plate
CET	Columnar to Equiaxed Transition
CRSS	Critically Resolved Shear Stress
DS	Directionally Solidified
DSC	Differential Scanning Calorimetry
DTA	Differential Thermal Analysis
EBW	Electron Beam Welding
EDM	Electrical Discharge Machine
EDS	Energy Dispersive Spectrometer
EPMA	Electron Probe Microanalysis
ESW	Electro Slag Welding
FCAW	Flux-Cored Arc Welding

FCC	Face-Centered Cubic
FEA	Finite Element Analysis
FZ	Fusion Zone
GMAW	Gas–Metal Arc Welding
GTAW	Gas-Tungsten Arc Welding
HAZ	Heat-Affected Zone
HIP	Hot Isostatic Pressing
HTHC	High-Temperature Hot Corrosion
LBW	Laser Beam Welding
LSW	Lifshitz, Slyozov, and Wagner model
LTHC	Low-Temperature Hot Corrosion
NSERC	Natural Sciences and Engineering Research Council of Canada
OAW	Oxyacetylene Welding
OQ	Oil-Quenched
PAW	Plasma Arc Welding
PDAS	Primary Dendrite Arm Spacing
PSD	Particle Size Distribution
PWHT	Post-Weld Heat Treatment
SEM	Scanning Electron Microscopy

SHT	Standard Heat Treatment
SIMS	Secondary Ion Mass Spectrometry
SMAW	Shielded Metal Arc Welding
TCL	Total Crack Length
TCP	Topologically Close-Packed
TEM	Transmission Electron Microscopy
TIG	Tungsten Inert Gas
ToF-SIMS	Time-of-Flight Secondary Ion Mass Spectrometry
UTS	Ultimate Tensile Strength
WQ	Water-Quenched
XRD	X-Ray Diffraction

CHAPTER 1

Introduction

1.1 Background Information

Superalloys are used as the primary material for gas turbine components such as turbine blades and vanes. They are the material of choice due to their excellent ability to reliably operate at high stress and in elevated temperatures (750–1100°C [1]) and corrosive environments. Superalloys are classified into three main categories of nickel (Ni), iron, and cobalt (Co)-based superalloys. Ni-based and Co-based superalloys are extensively used in the hottest environments that require engine components (combustion section) to be operated at temperatures higher than 800°C. For a long time, Ni-based superalloys have been primarily used for hot-section components that require excellent high-temperature mechanical properties and hot corrosion resistance. The high-temperature strength of Ni-based superalloys is mainly attributed to their precipitation strengthening by the gamma prime (γ') Ni_3(Al, Ti) precipitates. For the past 50 years [2], conventional carbide-strengthened Co-based superalloys have been employed in hot section components that require a higher degree of hot-corrosion resistance but relatively lower stress levels compared to Ni-based superalloys [1][3]. One of the most remarkable properties of Co-based superalloys compared to Ni-based superalloys is their outstanding resistance against the attack of hot corrosive gases, which increases the operating life and reduces the maintenance of engine parts. However, the application of Co-based superalloys has been limited due to the lack of a comparable precipitation hardening mechanism which results in lower high-temperature strength compared to Ni-based superalloys.

The discovery of γ′ (Co_3(Al, W)) precipitation-strengthened Co-based superalloys [3] has resulted in the development of novel γ′-strengthened Co-based superalloys. These superalloys have exceptional elevated-temperature mechanical properties compared to Ni-based superalloys that justify higher alloy cost [4][5][6][7][8][9]. Therefore, they can replace conventional Ni-based superalloys for high-temperature applications to enhance the efficiency of aero-engines and land-based power generation gas turbines and reduce greenhouse gas emissions. Among these advanced superalloys, CoWAlloy1 is a new γ′ (Co_3(Al, W)) precipitation-hardened Co-based superalloy, developed for high-temperature applications over 750ºC [10]. This alloy shows the remarkable characteristics of a large processing temperature window (235°C), a high volume fraction of γ′ precipitates (51%) [11], high oxidation resistance, and low creep rate [10], and therefore exceeds the capability of several other conventional Ni-based superalloys including IN718, Udimet 720Li, and Waspaloy.

Due to the geometric complexities of gas turbines, the components of large sections are manufactured from smaller parts that are joined together with the most appropriate fusion welding process [12]. In addition, the repair of damaged or service-degraded parts is often preferred to total replacement owing to the high manufacturing cost of new components. Therefore, welding is a necessary process in the manufacturing and repair of gas turbine engine parts. Among the many fusion welding methods, gas tungsten arc welding (GTAW) is widely applied in the gas turbine engine manufacturing and repair industry [13]. However, welding precipitation-strengthened superalloys is often accompanied by cracking in both the fusion zone (FZ) and the heat-affected zone (HAZ) which significantly degrades the mechanical properties in both the HAZ and FZ [12]. To avoid cracking, the welding process needs to be precisely controlled and the microstructure needs to be changed before and after welding.

The final microstructure of the FZ has a considerable impact on the mechanical properties and the susceptibility of the FZ to hot cracking [14]. The FZ microstructure is significantly controlled by the solidification microstructure, which is affected by the thermal history of the FZ during welding [15]. The microstructure of the FZ can be predicted by evaluating the thermal history during the welding process. An exclusive experimental study is challenging because of the transient and spatial variations during solidification. However, numerical modeling, such as a finite element analysis (FEA), can help to predict the solidification behavior with high accuracy [16], which would be less costly and more time-efficient compared to random experimental trials. In addition, the weldability and welding process parameters for the newly developed Co-based superalloy, CoWAlloy1, have not been studied. Therefore, reliable numerical modeling of GTAW is required to evaluate the influence of GTAW variables on the FZ microstructure of CoWAlloy1. This numerical modeling would help to acquire the appropriate range of process parameters for welding CoWAlloy1 which could eliminate the formation of FZ cracks.

In addition to FZ cracking, as with γ′-strengthened Ni-based superalloys [17][18][19][20], γ′-strengthened Co-based superalloys are also susceptible to HAZ cracking during welding [21]. Since HAZ cracking can deteriorate the elevated-temperature mechanical properties of weldments [17], enhancing resistance to cracking during the welding of CoWAlloy1 is vitally important in industrial applications of this new alloy. Although there have been several research works on the weldability of various Ni-based superalloys, there are few studies on the cracking susceptibility of the HAZ of γ′-strengthened Co-based superalloys [21]. Therefore, a systematic study on the primary factors that produce HAZ cracking in CoWAlloy1 needs to be conducted which could help to develop an effective approach to eliminate/minimize HAZ cracking during welding and post-weld heat treatment (PWHT).

Although altering the microstructure of the CoWAlloy1 during pre-weld and post-weld processes can eliminate/minimize the susceptibility to cracking during welding and PWHT, doing so may also deteriorate the mechanical properties and corrosion resistance of this alloy [22][23]. Considering the harsh conditions during service, it is crucial to investigate and understand the effect of microstructural modification on the mechanical properties and hot corrosion characteristics of CoWAlloy1 when subjected to GTAW.

Due to the ever-increasing demand for increased turbine engine efficiency and reductions in greenhouse emissions, advanced heat-resistant materials such as CoWAlloy1 are in development for high-temperature applications to replace conventional Ni-based superalloys. Therefore, to successfully replace conventional Ni-based superalloys with CoWAlloy1, it is essential to significantly mitigate or eliminate the cracking problem in this alloy, with minimal deterioration of the mechanical properties and hot corrosion resistance.

1.2 Research Objectives

This research study conducts a systematic and comprehensive study on the hot cracking susceptibility of a newly developed Co-based superalloy, CoWAlloy1, which is subjected to GTAW, and ways to minimize/eliminate cracking during welding and PWHT. The following are the objectives to realize the work:

1. To develop a numerical model of GTAW to obtain a window of optimum welding parameters that prevent cracking in the FZ.

2. To conduct a systematic study on the primary factors that produce HAZ cracking in CoWAlloy1, which could contribute to the development of an effective approach to eliminate/minimize HAZ cracking during welding and after PWHT.

3. To evaluate the effect of pre-weld microstructural modifications on the mechanical properties and hot corrosion resistance of CoWAlloy1 after PWHT.

1.3 Research Methodology

The following research methods are adopted to achieve the stated objectives:

1. The development of a three-dimensional (3D) transient thermal model based on an FEA to evaluate the effect of GTAW parameters on the FZ microstructure of CoWAlloy1.

2**.** The characterization of the pre-weld microstructure of CoWAlloy1 in the as-received and standard heat-treated (SHTed) conditions by using various advanced microstructural characterization techniques, including scanning electron microscopy (SEM), transmission electron microscopy (TEM), and differential scanning calorimetry (DSC).

3. The optimum process parameters acquired from the developed numerical model are used to determine the GTAW performance.

4. An analysis of the microstructure of the FZ is conducted by using various advanced characterization techniques, including SEM, TEM, and electron probe microanalysis (EPMA).

5. The primary causes of HAZ cracking in CoWAlloy1 are investigated by using microstructural analysis techniques, including SEM and TEM.

6. The alloy microstructure is changed prior to welding through systematic exposure to various pre-weld heat treatments.

7. The weldability is extensively examined and the effect of the factors that contribute to the cracking susceptibility of the HAZ is examined after applying pre-weld and post-weld heat treatments by using advanced microstructural characterization techniques including SEM and secondary ion mass spectrometry (SIMS).

8. The γ′ re-precipitation behavior is examined through DSC and SEM.

9. The mechanical properties and hot corrosion resistance of the PWHTed CoWAlloy1 are evaluated.

1.4 Summary of Major Findings

The numerical model developed to simulate the GTAW of CoWAlloy1 shows an adequate level of accuracy for predicting the solidification behavior of the FZ and selecting the window of welding parameters that prevent FZ cracking.

The TEM analysis of the FZ confirms the formation of secondary solidification products that consist of MC-type carbides and γ-γ′ eutectics within the interdendritic regions. Furthermore, the TEM study confirms the inhomogeneous distribution of γ′ precipitates within the FZ.

Although the optimum parameters of the GTAW inhibit cracking in the FZ, welding produces HAZ cracking in the alloy. A microstructural study shows that a primary cause of the HAZ cracking is intergranular liquation due to the subsolidus liquation reaction of MC-type carbide particles and γ′ precipitates, which are found to be present in the pre-weld condition.

A detailed weldability investigation and microstructural characterization of the HAZ reveal that the grain boundary elemental segregation of boron (B) controls cracking susceptibility during the welding of CoWAlloy1. In addition, a significant reduction in HAZ cracking during welding and PWHT is achieved by using the developed pre-weld thermal processing procedure based on minimizing the grain boundary segregation of B and grain size refinement.

Significant degradation in the tensile properties due to the occurrence of HAZ cracking of the weld can be avoided in CoWAlloy1 if the material is subjected to the pre-weld heat treatment identified in this work. In addition, hot corrosion studies reveal that by using the new pre-weld heat treatment, welding does not produce a substantial reduction in hot corrosion resistance of the alloy. The slight reduction in hot corrosion resistance can be due to the preferential corrosion in the welded specimen as a result of elemental segregation.

The newly developed pre-weld heat treatment procedure coupled with the selection of appropriate GTAW parameters is very effective in minimizing cracking both during GTAW and PWHT. In addition, the new pre-weld heat treatment has minimal deteriorating effects on the mechanical properties and hot corrosion resistance of CoWAlloy1. Therefore, the findings of this study provide practical insight into the fabrication and repair of gas turbine components made of CoWAlloy1 which could allow wider industrial applications of the new material developed for higher gas turbine efficiency. The results have already been published in four journals and presented at one conference at the time of writing of this thesis.

1.5 Thesis Organisation

This thesis consists of six chapters as follows.

Chapter 1 presents the background information, research objectives, research methodology, and a summary of the major findings of this research work.

Chapter 2 is a literature review on the physical metallurgy of CoWAlloy1, welding metallurgy of superalloys, welding defects that occur during fusion welding, weldability testing techniques, and hot corrosion resistance of superalloys. Furthermore, the scope of this research is presented at the end of this chapter.

Chapter 3 presents a detailed description of the developed numerical model, and experimental methods and equipment used in this research.

Chapter 4 provides the results of the developed numerical model of the GTAW. Subsequently, the results of the microstructural characterization of CoWAlloy1 before welding are presented. This is followed by a detailed study of the FZ and HAZ microstructures and the investigation of the primary causes of HAZ cracking. Furthermore, detailed weldability studies and the development of an effective thermal treatment procedure for the alloy to minimize HAZ cracking during welding and PWHT are presented in this section. At the end, the effect of the developed pre-weld heat treatment on both the mechanical properties and hot corrosion resistance of CoWAlloy1 is discussed.

Chapter 5 presents a detailed summary of the major findings of this research.

Chapter 6 provides the recommendations for future work.

Lastly, the research contributions and references are provided at the end of the thesis.

CHAPTER 2

Literature Review

2.1 Introduction

This chapter provides a literature review on Co-based superalloys (Section 2.2) and the physical metallurgy of the newly developed Co-based superalloy - CoWAlloy1 (Sections 2.3 and 2.4). This is followed by a general review of the welding techniques for joining superalloys and GTAW process (Section 2.5). Details of the weld microstructure including the FZ and HAZ are discussed in Section 2.6. Subsequently, weld defects including residual stress, weld cracking, and the associated theories are reviewed in Section 2.7. In Section 2.8, various weldability testing techniques are discussed. This is followed by a review of the hot corrosion resistance of superalloys (Section 2.9) and ends with the objectives and scope of the thesis (Section 2.10).

2.2 Co-Based Superalloys

Co has a face-centered cubic (FCC) structure at high temperatures with a melting point of 1495ºC which is 40ºC higher than the melting point of Ni [24]. Co-based superalloys have been used in the wrought or cast form to manufacture gas turbine components since 1936 due to their excellent high-temperature creep, fatigue strength, resistance to hot corrosion, and wear resistance [25]. However, the development of γ'-strengthened Ni-based superalloys during 1950-1970 with higher strength at elevated temperatures has significantly surpassed the capabilities of Co-based superalloys. Consequently, conventional Co-based superalloys have now been relegated to a secondary position in the gas turbine industry as they are not able to compete with Ni-based superalloys for highly stressed parts, such as turbine blades. Therefore, conventional Co-based

superalloys are used for low-stress static components that are used for long periods of time, such as stator blades, nozzle guide vanes, and combustion chambers in gas turbines.

The main reason that conventional Co-based superalloys are not widely used as Ni-based superalloys in the gas turbine manufacturing industry is due to the lack of a comparable precipitation hardening mechanism which results in a comparatively lower high-temperature strength. The high-temperature strengthening of conventional Co-based superalloys is accomplished mainly through the two mechanisms of solid solution and carbide precipitation hardening. Solid-solution alloying elements such as molybdenum (Mo), tungsten (W), tantalum (Ta), and niobium (Nb) tend to reduce the stacking fault energy, thereby inhibiting dislocation cross-slip and climb in the glide plane. Furthermore, carbide precipitation strengthening is quite effective in pinning glide dislocations and strengthening conventional Co-based superalloys.

2.3 Newly Developed γ′-Strengthened Co-Based Superalloys

The discovery of γ′ (Co_3(Al, W)) precipitation-strengthened Co-Al-W ternary superalloys that was first reported by Sato et al. [3], has resulted in the development of novel γ′-strengthened Co-based superalloys. These superalloys have exceptional elevated-temperature mechanical properties compared to conventional Ni-based and Co-based superalloys including similar creep properties to first-generation Ni-based superalloys [4][5][6], higher liquidus and solidus temperatures, better hot corrosion and oxidation resistance [7], lower solidification segregation [8], and comparable or even higher flow stress above 900°C [9]. Therefore, they can replace conventional Ni-based and Co-based superalloys for high-temperature applications to enhance the efficiency of jet engines and reduce greenhouse gas emissions.

Since the discovery of Co-Al-W ternary alloys, several alloying elements such as Ni [26], chromium (Cr) [3], Ta [27], titanium (Ti) [28], hafnium (Hf) [29], B [30], silicon (Si) [7], Mo [31], zirconium (Zr) and carbon (C) [10] have been added to improve the high-temperature capabilities of these alloys. Among these advanced superalloys, CoWAlloy1 is a new γ′ (Co_3(Al, W)) precipitation-hardened Co-based superalloy, developed for high-temperature applications over 750ºC [10]. This alloy shows the exceptional characteristics of a large processing temperature window (235°C), a high volume fraction of γ′ precipitates (51%) [11], high oxidation resistance, and low creep rate [10], and therefore exceeds the capability of several other conventional Ni-based superalloys including IN738, Udimet 720Li, and Waspaloy.

2.4 Physical Metallurgy of CoWAlloy1 Superalloy

CoWAlloy1 consists of an FCC γ, Co solid solution matrix hardened by a stable γ′ phase (up to 950°C) with an $L1_2$ structure [3]. The nominal chemical composition of CoWAlloy1 is provided in Table 2.1. Adding Ni to Co-Al-W ternary alloys helps to stabilize the Co_3(Al, W) intermetallic phase and widen the narrow γ/γ′ two-phase region in the phase diagram [26]. Ti, Ta, and Hf also partition to the γ′ phase aside from Ni, and improve the stability of the γ′ precipitates. Furthermore, Ti, Ta, and Hf slightly increase the γ′ solvus temperature which enhances the high-temperature properties of CoWAlloy1 [32]. Cr partitions preferentially to the γ matrix and acts as a solid solution hardener. In addition, a Cr content above a certain limit increases the oxidation and corrosion resistance [3]. The presence of B can improve the grain boundary strength, ductility, and oxidation resistance. The addition of Si reduces the oxide scale growth rate and enhances the

formation of chromia oxide scales. Zr and C strengthen the grain boundaries and form the carbides [10].

There have been limited studies on the mechanical and physical properties of CoWAlloy1. The available mechanical and physical properties of CoWAlloy1 subjected to a standard heat treatment (SHT) are summarised in Table 2.2 [10][11][33]. This table clearly shows that CoWAlloy1 maintains a high strength even above 750°C, while the conventional Ni-base superalloys exhibit a drastic decrease in strength at temperatures above 750°C [11].

Table 2.1. Composition of CoWAlloy1 (at. %)

Alloy	Co	Ni	Al	W	Ti	Ta	Cr	Si	Hf	Zr	B	C
CoWAlloy1	42.3	32	6	3	2.5	1.5	12	0.4	0.1	0.01	0.08	0.08

Table 2.2 Mechanical and physical properties of CoWAlloy1* [10][11][33]

Temperature (ºC)	Tensile Yield Strength (MPa)	Ultimate Tensile Strength (MPa)	Elongation (%)
500	971	-	-
600	941	-	-
750	969	1294	4.87
800	862	-	-
850	717	848	4.5
1000	411	385	4.61
Solidus (ºC)		1305	
Density (gr/cm³)		8.83	

*Standard heat treatment (SHT): 1050°C, 4 hrs, oil-quenched (OQ) + 900°C, 4 hrs, air-cooled (AC) + 750°C, 16 hrs, AC [10]

2.4.1 Microstructure of Cast CoWAlloy1

The SHTed CoWAlloy1 has a recrystallized microstructure, including coarse grains of 1600 μm in size and carbides within the grains and at the grain boundaries. The presence of two major phases of the γ matrix and γ′ intermetallic phase has been confirmed in CoWAlloy1 [10]. However, the formation of carbides and their chemical composition have not been confirmed in this alloy, until now. The main phases that can be found in CoWAlloy1 are the gamma (γ), gamma prime (γ′), carbide, boride, and topologically close-packed (TCP) phases.

2.4.1.1 Gamma Phase

The γ phase is a continuous matrix of close-packed FCC Co-based austenite and consists of a high percentage of solid solution elements, such as Cr, Ni, W, Al, Ti, and Ta, which their atomic diameters differ from Co by 1–18%. These elements are substitutional atoms in the Co crystal structure and produce a distorted lattice with a symmetrical stress field. The stress field can interact with the dislocation stress field, thus producing elastic interaction between the solute atoms and dislocations which results in solid solution strengthening [34]. In other words, the stress field formed around the solute atoms interacts with that of the dislocation and increases the stress required to move the dislocation. In addition, the solid-solution alloying elements tend to lower the stacking fault energy, which leads to an increase in the high-temperature stability of the alloy [25]. It is worth mentioning that as the diffusion of substitutional alloying elements tends to be slower in Co compared to Ni, Co-based superalloys show a lower creep rate compared to Ni-based superalloys [25].

2.4.1.2 Gamma Prime Phase

The γ′ phase as the main strengthening phase in CoWAlloy1 is an FCC ($L1_2$) ordered intermetallic component with the basic composition of Co_3(Al, W) [3][10]. The schematic diagram of the γ′ phase with an $L1_2$ crystal structure is presented in Figure 2.1. Although the γ′ precipitates have a similar crystal structure as that of the γ matrix and are coherent with the matrix, the lattice parameters of γ′ and the matrix are different. The degree of lattice mismatch (misfit) is known to impact the strengthening effect and morphology of γ′ precipitates [35]. The small lattice mismatch between the γ matrix and γ′ precipitates leads to the formation of coherent precipitates, thereby, elastic coherency strains in the matrix, which significantly contributes to alloy strengthening. The coherency or misfit hardening mechanism is attributed to the interaction of the glide dislocations with the elastic coherency stress field around the coherent γ′ precipitates. In addition, the γ/γ′ lattice misfit significantly affects the morphology of the γ′ precipitates. A lattice misfit between 0-0.2% leads to the formation of γ′ with a spherical morphology, between 0.5-1.0% cuboidal, and the γ′ precipitate morphology becomes a plate shape at mismatches above 1.25% [36]. A moderate misfit between the γ and γ′ [10] in CoWAlloy1 leads to the formation of a coherent two-phase microstructure where submicron cuboidal γ′ precipitates form [9][37].

The exceptional high-temperature strength of superalloys is significantly controlled by the distribution, morphology, and size of the γ′ precipitates [35]. Once the critically resolved shear stress (CRSS) of a crystal is exceeded under the effect of a load, the slip plane is activated and dislocations can glide through the crystal. In γ′-strengthened superalloys, precipitation hardening is attributed to the interactions between the moving dislocations and γ′ precipitates. Generally, when the γ′ particle is small in size, the moving dislocations tend to shear the particle but bypass the γ′ particle when the particle size is large [38].

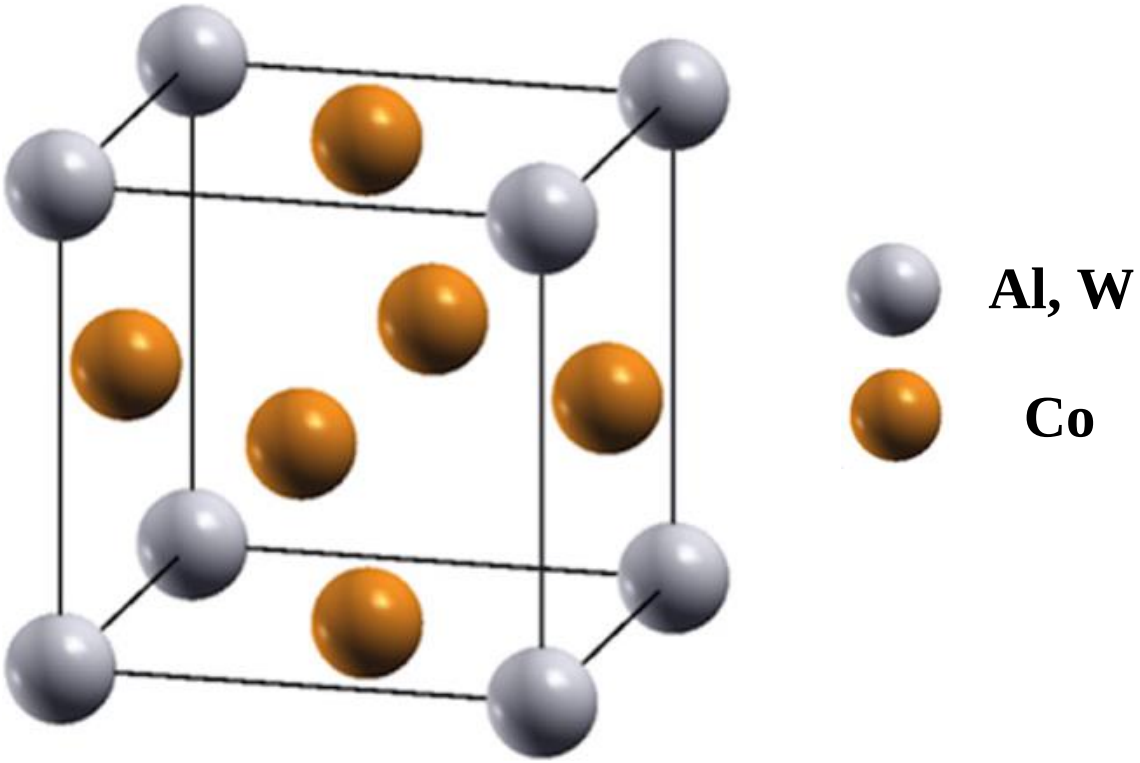

Figure 2.1 Unit cell that shows $L1_2$ ordered FCC lattice of γ' phase

Several theories have been reported to explain for the dislocation-particle interaction in alloys. Among these theories, the precipitate cutting or shearing (order hardening) and the Orowan looping or by-passing mechanisms are the two main mechanisms that have been used to describe precipitation strengthening in many superalloys [38].

According to the order hardening mechanism, precipitation strengthening occurs when the ordered γ′ precipitates are sheared by a moving dislocation that glides through the matrix which creates an anti-phase boundary (APB) on the slip plane of the precipitate. The energy per unit area on the slip plane, γ_{apb} (APB energy) characterizes the force per unit length that resists the dislocation glide as it penetrates the particles. During shearing, the dislocations that cause plastic deformation travel in pairs. Therefore, the shearing of the ordered particles occurs by coupled pairs of dislocations. The passage of the trailing dislocation through the particles restores perfect order on the {111} slip plane in which an APB is created by the leading dislocation. This increases the amount of energy required to pass dislocations through the precipitates. The CRSS for the case of a single dislocation interacting with small particles is described as [38]:

$$\tau_c = \frac{\gamma_{apb}}{b}\left(\frac{3\pi^2\gamma_{apb}fr}{32\Gamma}\right)^{1/2} \tag{2-1}$$

where b represents the Burgers vector, f denotes the precipitate volume fraction, r is the average particle radius and Γ is a parameter used to define the characteristics of the dislocation. A more accurate expression for CRSS, which considers the effect of the trailing dislocation, is:

$$\tau_c = \frac{\gamma_{apb}}{2b}\left[\left(\frac{3\pi^2\gamma_{apb}fr}{32\Gamma}\right)^{1/2} - f\right] \tag{2-2}$$

For a dislocation pair, a simple and common assumption is that the second dislocation remains straight while the first dislocation bows out between the obstacles. Equation 2-2 proposes that, for an alloy hardened by the distribution of small spherical particles, the CRSS should increase with an increase in f and r within the particle size range for which the equation is valid. According to the literature, the order hardening mechanism appears to be the most dominant dislocation-particle interaction when the particle size is only a few nanometers [38].

As the γ′ particle size increases, the moving dislocation tends to bypass the particles either through looping or climbing. The critical particle size for the change in mechanism from shearing to by-passing depends on the alloy and varies from 300 Å to 2500 Å. According to the Orowan mechanism, particles are strong enough to withstand applied local stress from moving dislocations without shearing or fracturing. The dislocation bypasses the particles, leaving dislocation loops around them. The stress necessary for the dislocation to by-pass the γ′ particles is termed Orowan stress; the simplest form of which is [39]:

$$\tau_O = \frac{Gb}{\lambda} \qquad (2\text{-}3)$$

where G is the shear modulus, b is the Burgers vector, and λ the mean spacing of the particles.

2.4.1.3 Carbides

The addition of C in the range of 0.02–0.2 wt. % in superalloys leads to the formation of carbides. Carbides form as a result of the reaction between reactive elements, such as Ti, Ta, Hf, and Nb with C [34] and precipitate at both the granular and intergranular regions [36]. Although carbides can be beneficial in grain boundary strengthening of γ′-strengthened Co-based superalloys, they can significantly deteriorate the weldability of these novel superalloys. It is worth mentioning that the presence of carbide phases in CoWAlloy1 has not been confirmed in previous studies. Common types of carbides in Co-based superalloys are the primary carbides of MC and M_7C_3 types and secondary carbides of $M_{23}C_6$ [1][2].

MC carbides are primary carbides and form from supersaturated solid solutions (melt) at high temperatures during freezing [36]. The preferred order of formation (decreasing stability) for these carbides is HfC, TaC, NbC, and TiC [36]. MC carbides have a discrete blocky morphology with regular geometric features, such as diamonds or cubes, and are found in random positions such as interdendritic, intergranular, or granular sites [2]. The basic formation reaction of MC carbides is as follows [2]:

$$M + C \rightarrow MC$$

$$(Ti, Hf, Nb, W, Ta, Mo) + C \rightarrow (Ti, Hf, Nb, W, Ta, Mo)C$$

M_7C_3 carbides are primary, Cr-rich carbides that typically form in Co-based superalloys with a low Cr/C alloying ratio [1][36][40]. Generally, M_7C_3 forms at the grain boundaries and has a blocky shape morphology [36]. The basic formation reaction of M_7C_3 carbides is [41]:

$$M + C \rightarrow M_7C_3$$

$$(Cr, CO, W) + C \rightarrow (Cr, CO, W)_7C_3$$

The primary carbides of MC and M_7C_3 which form during solidification can be degraded to secondary carbides ($M_{23}C_6$) during long-service exposure or heat treatment [2].

The $M_{23}C_6$ carbides that form in Co-based superalloys have a high Cr/C alloying ratio [40]. These carbides precipitate primarily at the grain boundaries and have an irregular, a discontinuous, rounded, or blocky morphology [36]. The formation of $M_{23}C_6$ carbides in Co-based superalloys increases the stress and creep rupture resistance by impeding grain sliding. $M_{23}C_6$ contains Co and W, in substitution for Cr, and forms during heat treatment and service from the degeneration of MC and M_7C_3 carbides [2][36][41]:

$$MC + \gamma \rightarrow M_{23}C_6$$

$$(Ti, Hf, Nb, W, Ta, Mo)C + (Co, Cr, Al, Ti) \rightarrow (Cr, CO, W)_{23}C_6$$

$$M_7C_3 \rightarrow M_{23}C_6$$

$$(Cr, CO, W)_7C_3 \rightarrow (Cr, CO, W)_{23}C_6$$

2.4.1.4 Borides

The addition of B in superalloys can lead to the formation of borides as a result of the reaction between B and the reactive elements. Typically borides precipitate at the grain boundaries and increase resistance to grain boundary sliding and enhance creep-rupture properties [34]. In Co-Al-W ternary Co-based superalloys, a higher content of B above 0.04 at. % promotes the formation of W and Hf-rich borides with a blocky or half-moon morphology [36][42]. Similar to carbides, the presence of borides at the grain boundaries in superalloys can negatively affect the weldability of the superalloy.

2.4.1.5 Topologically Close-Packed Phases

A high percentage of refractory elements such as Cr, Mo, and W in Co-based superalloys can result in the formation of TCP phases. These phases form during heat treatment or service with a plate or needle-like morphology. TCP phases are generally undesirable and detrimental to the mechanical properties of superalloys at high temperatures. Co-based superalloys are more susceptible than Ni-based superalloys in the formation of these unwanted phases [2]. TCP phases that have been observed in Co-based superalloys are the sigma (σ), mu (μ), and Laves phases. The σ phase is based upon stoichiometry A_2B and has a tetragonal crystallography; for example $Cr_{61}Co_{39}$. The μ phase is based on the ideal stoichiometry A_6B_7 and has a rhombohedral crystallography including W_6Co_7 and Mo_6Co_7 [34]. The Laves phase precipitates in both the acicular and/or blocky morphologies with AB_2 structures such as Co_2W, Co_2Ta, and Co_2Ti [1].

2.4.2 Precipitation Behaviour of γ′ in Cast CoWAlloy1

As stated earlier, CoWAlloy1 is a potential replacement for several other types of Ni-based superalloys, so it is critical to study the precipitation behavior of the γ′ phase during service and material processing such as additive manufacturing, welding, and work hardening. It has been reported that continuous and rapid cooling during these processes can change the γ′ characteristics, which directly influences the strength and weldability of the material. For example, Bennett et al. [43] investigated the effect of the cooling rate on the mechanical properties of IN718 produced by laser deposition additive manufacturing. The authors concluded that as the cooling rate is reduced, the ultimate tensile strength (UTS) decreases due to the formation of a coarse microstructure [43]. Similarly, Sajjadi et al. [44] concluded that increasing the cooling rate of Udimet 500 results in

microstructural inhomogeneity, an increase in strength and a decrease in ductility [44]. Mallikarjuna et al. [45] studied the characteristics of the γ′ precipitates in IN738LC during different cooling rates and concluded that as the cooling rate increases, the corrosion resistance deteriorates due to the formation of smaller and spherical precipitates [45]. Mei et al. [46] investigated the effect of cold rolling on the precipitation kinetics and morphological changes in IN718 alloy using DSC experiments. The authors observed that an increase in the percentage of cold rolling results in shifting the DSC peaks to lower temperatures, which is attributed to an increase in the precipitation rate [46].

Masoumi et al. [47] used a differential thermal analysis (DTA) to study the effect of the cooling rate on precipitate behavior in AD730^{TM}. They reported butterfly-shaped and spherical-shaped γ′ precipitate morphologies at low and high cooling rates, respectively. Similarly, Yang et al. [48] investigated the morphologies of different γ′ precipitates obtained at various cooling rates in a K5 Ni-based superalloy. They found that increasing the cooling rate results in the formation of small spherical precipitates [48]. In contrast, Behrouzghaemi and Mitchell [49] observed that γ′ precipitates exhibit a cloverleaf-shaped morphology with increases in the cooling rate of IN738LC. They attributed this behavior to morphological instability [49]. The stability of the γ/γ′ microstructure at high temperatures is controlled by the solute diffusivity in the matrix [50]. Several authors [51][52][53][54][55] have extensively studied the γ′ precipitation kinetics in Ni-based superalloys and agreed that the kinetics follow the theory proposed by Lifshitz, Slyozov, and Wagner (LSW). According to this theory, the solute diffusion through the matrix is a rate-limiting step, which tends to control the precipitation behavior of the γ′ phase [56]. Similar studies have been carried out in Co-Al-W ternary alloys, which show good agreement with the classical LSW theory [56][57].

2.5 Welding

The welding process involves joining two similar or different materials with or without a filler by applying pressure or/and heat to obtain continuity between the two materials. Owing to the structural complexity of the gas turbine engine, the components of large sections are manufactured from smaller parts that are joined together using a welding process to form an integrated part. Furthermore, due to the cost of replacing the damaged parts of the gas turbine engine, repair is preferred by using welding. Therefore, welding has become an essential part of the manufacturing and repair processes in the gas turbine industry. Three main welding processes of solid-state, brazing, and fusion welding can be applied to all types of superalloys [34].

Solid-state welding is capable of producing the same result as fusion welding by applying pressure at a temperature below the melting temperature of the material to be joined. This joining method usually uses a bonding aid, such as an interface foil or coating, to facilitate bonding and prevent the formation of low-temperature eutectics or brittle phases. Therefore, in this welding method, the defects accompanying the FZ and HAZ such as elemental segregation, and cracking do not occur. However, due to low solubility for interstitial elements in Ni-based and Co-based superalloys, these alloys are not easy to join through solid-state welding (diffusion bonding) [58].

The brazing method relies on the melting and subsequent solidification of an interlayer (braze metal) without any melting of the base metals (BMs). The brazing process is very similar to soldering but with higher bond strength and application temperature (above 450°C). Although this process avoids melting BMs, the service temperature of the joined parts is restricted to the braze metal melting point as at elevated temperatures, braze metal loses its stability. Considering that novel Co-based superalloys are developed for elevated-temperature applications which are

significantly above the melting point of conventional braze metals, applying this method requires careful development of brazing material and brazing cycle.

Fusion welding methods involve the melting and solidification of the components to be joined with or without a filler material. These welding methods are the most promising and practical ways to manufacture and repair gas turbine components [59]. The three major types of fusion welding processes are [36]:

1. Gas welding such as oxyacetylene welding (OAW).

2. Arc welding such as GTAW, shielded metal arc welding (SMAW), plasma arc welding (PAW), gas–metal arc welding (GMAW), flux-cored arc welding (FCAW), submerged arc welding (SAW), and electro slag welding (ESW).

3. High-energy beam welding such as electron beam welding (EBW) and laser beam welding (LBW).

Among all the fusion welding processes, GTAW which is also called tungsten inert gas (TIG) welding is the most widely applied method to join superalloys. Figure 2.2 shows the schematic of GTAW. In this method, an arc is created between the non-consumable tungsten electrode and the workpiece [60]. The BM is melted and filler metal is fed in this arc manually or automatically. Some applications such as welding thin plates and bead-on-plate (BOP) welding do not require a filler metal. In GTAW, a protective gas such as argon is supplied by a welding torch and covers the weld area to protect the weld bead and HAZ from the oxygen (O), nitrogen, and hydrogen contained in the air atmosphere [2]. This versatile method produces high-quality welds with little distortion as a result of precise control over the welding process. In addition, this process does not create any spatters that must be later cleaned up.

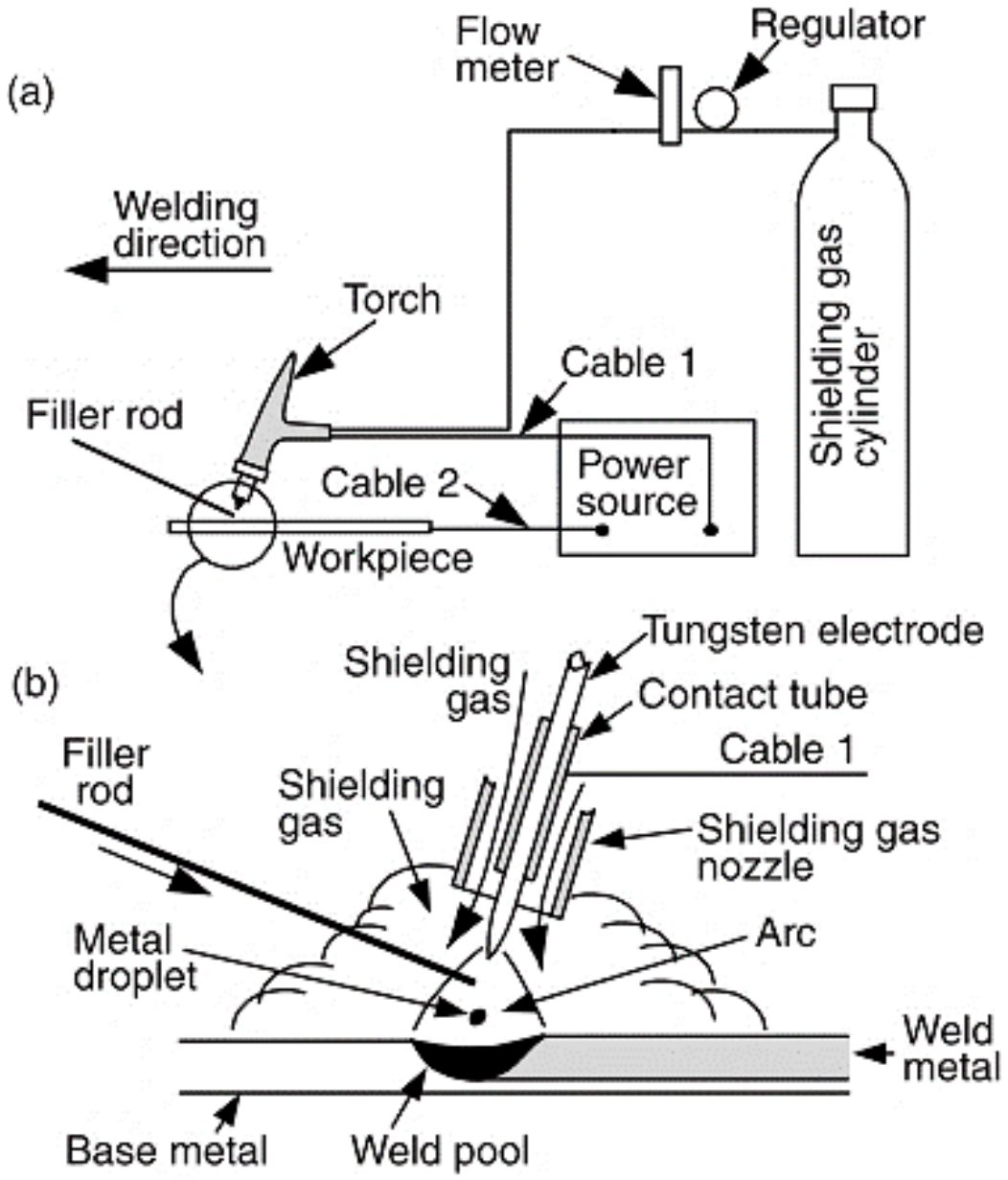

Figure 2.2 GTAW process: a. Overall process, and b. Welding area (magnified) [60].

(Reproduced with permission from John Wiley and Sons)

Rapid heating and cooling during GTAW can result in the formation of several defects in the weld zone such as hot cracking which is considered as one of the major defects in the welding of superalloys. Furthermore, the lack of fusion, surface oxidation, and discontinuity in bead formation are the other possible weld defects that can be minimized by properly controlling the welding process and adjusting the input parameters, including the welding speed and arc power. The welding process and formation of defects can significantly affect the mechanical and physical properties of the superalloy and cause failure in gas turbine engines [12]. Therefore, a detailed analysis of the metallurgical phenomena during welding superalloys is essential.

2.6 Weld Microstructure

Typically, weldments consist of three separate regions: the FZ, HAZ, and unaffected BM [62]. The FZ is the region in which the complete melting and resolidifying occur during fusion welding. This zone is often metallographically distinct from the HAZ and BM. Based on the usage of filler and the filler material in the welding process, there are three main types of FZ: autogenous FZ in which no filler is used and FZ essentially has the same composition as the BM, homogeneous FZ in which filler with a similar composition as the BM is used, and heterogeneous FZ in which a dissimilar filler material is used [61][62]. The HAZ is the region between the FZ and the unaffected BM. As the temperature in this zone is below the alloy solidus temperature, often all the phase transformations occur in the solid state. The different weld zone regions in GTAW are illustrated in Figure 2.3.

The mechanical properties of fusion welds significantly depend on the solidification behavior of the weld pool, which is primarily controlled by the cooling rate that deviates from equilibrium. Cooling rates in welds vary from 10 to 10^3 Ks^{-1} for conventional oxyfuel and arc welding processes, including SMAW, FCAW, SAW, ESW, GTAW, and GMAW [61]. Due to rapid heating and cooling, the welding process always occurs under non-equilibrium conditions in which diffusion is often limited. Thus, weld solidification is accompanied by the nucleation and growth of dendrites, segregation, and diffusion processes, causing local compositional variations which can lead to welding problems and influence performance in service. Many metallurgical processes in weldments occur in the solid state, including phase transformations, diffusion, precipitation reactions, recrystallization, and grain growth. However, liquation reactions may also occur in the weldments and affect their properties. For example, liquation reactions in which liquid films may form outside of the FZ can result in cracking problems [62].

Figure 2.4 shows a schematic of the interaction between a moving heat source and the metal part in an autogenous welding process [63]. During the welding process, the welding speed and heat input alter the solidification rate (R) and temperature gradient (G) around the molten pool which significantly affects the weld pool geometry as well as the FZ microstructure. Typically, a molten pool formation in an elliptical or circular shape can be seen in the process, including during the use of high-energy beam welding and arc welding at low speeds. These molten pool structures result in the formation of a finer FZ grain structure. However, at high welding speeds and heat inputs, a teardrop-shaped molten pool appears and leads to large columnar grain growth [14]. It can be observed in Figure 2.5 that for all weld pool shapes, the degree and direction of the G, and the R vary in the molten pool [64]. The parameters of G and R can be used to predict the FZ dendritic and grain structure developed during solidification.

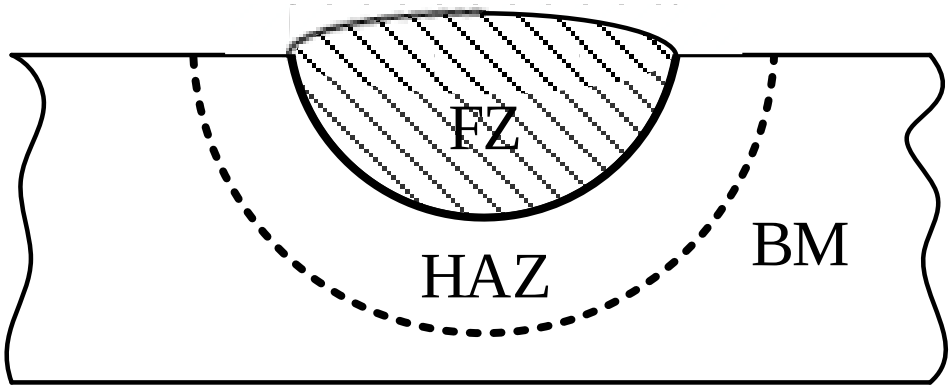

Figure 2.3 Typical weld zone regions in GTAW

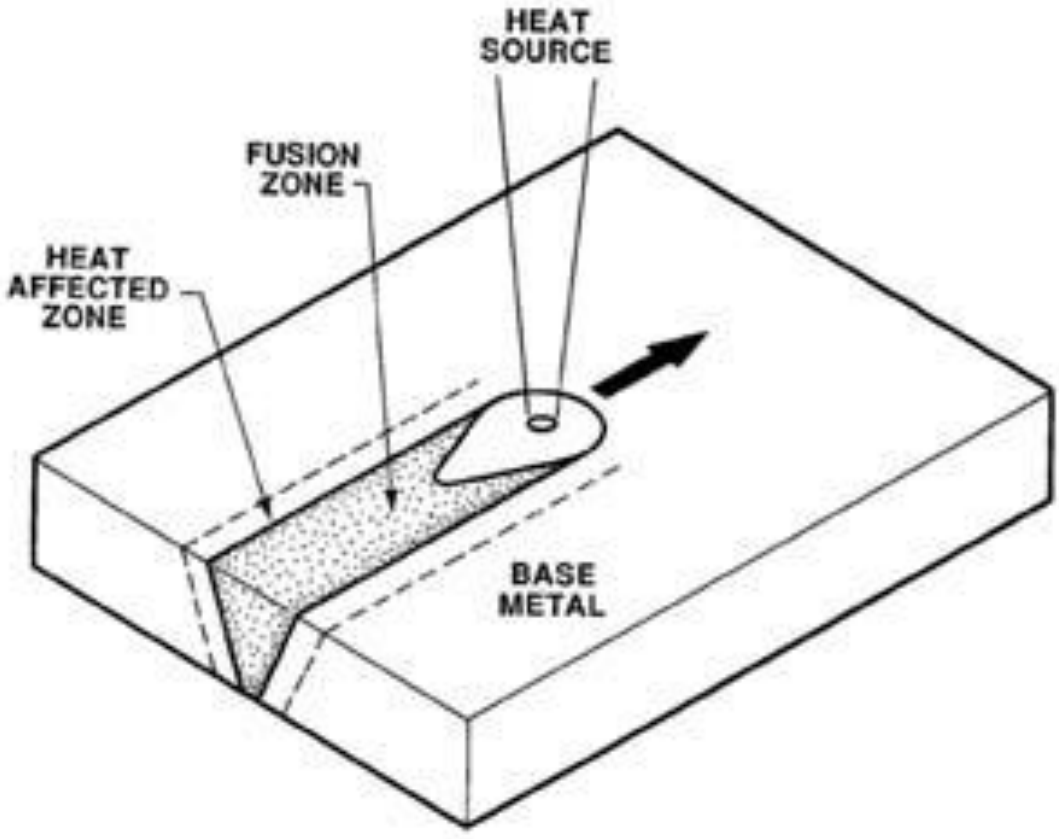

Figure 2.4 Schematic diagram of interaction between the heat source and the BM [63].

(Reproduced with permission from Springer Nature)

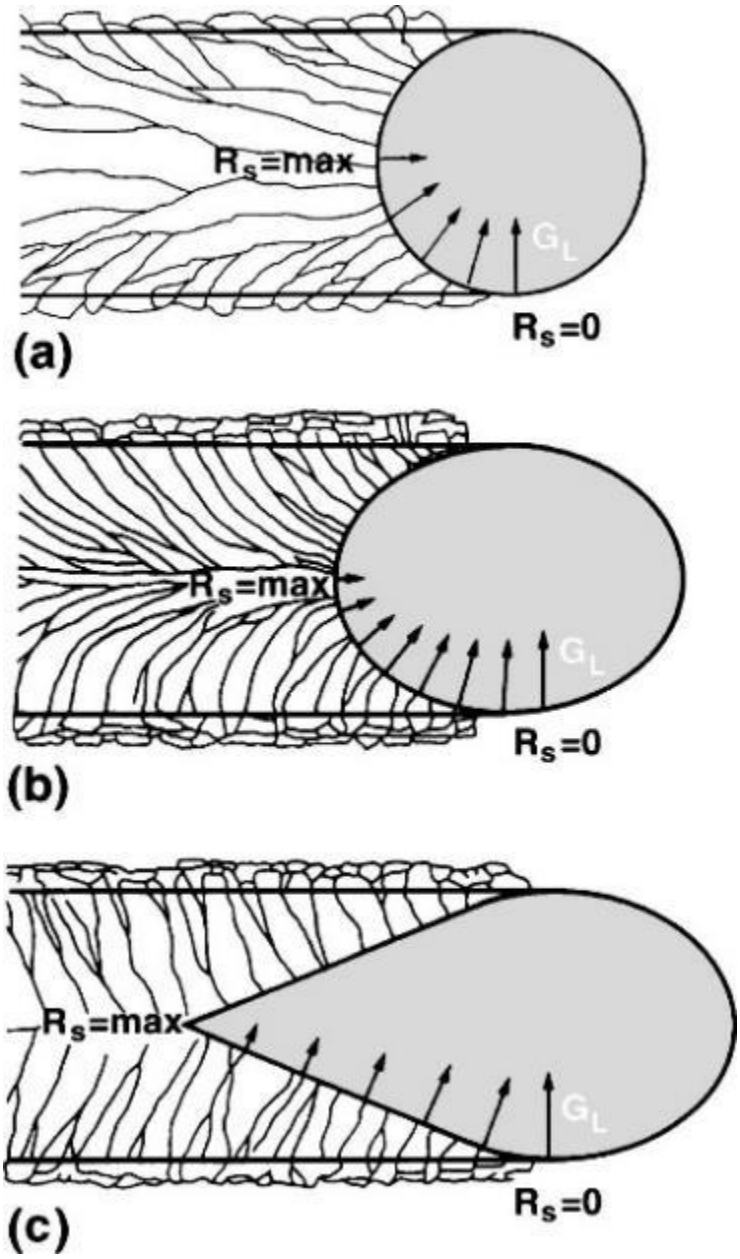

Figure 2.5 Variations in the G and R, and grain structure development for various pool shapes: a. Circular, b. Elliptical, and c. Tear-drop [64].

(Reproduced with permission from AIP Publishing)

2.6.1 Fusion Zone

Due to the complete melting and re-solidifying of the material during GTAW, the solidified microstructure of the FZ is considerably complex and depends on the alloy composition and solidification conditions [62]. During the fusion welding process, the weld zone can be considered as a small casting process. Therefore, the existing BM grains at the fusion line act as a mold and the substrate for the nucleation of crystals from the liquid. In autogenous or BOP welding, epitaxial nucleation and growth take place in which nucleation occurs near the fusion line without altering the existing crystallographic orientations of the BM. However, further from the fusion line, the grain structure is controlled by a competitive growth mechanism. During FZ solidification that takes place further from the fusion line, the grains tend to grow in the direction perpendicular to the molten pool boundaries as this direction provides the maximum G and hence maximum heat extraction. However, columnar or cell dendrites within each grain tend to grow along the easy-growth direction. Therefore, during solidification, grains with their easy-growth direction essentially perpendicular to the molten pool boundaries will grow more easily and crowd out the less favorably oriented grains, as shown schematically in Figure 2.6. The competitive growth mechanism dominates the grain structure of the bulk weld metal [60].

During FZ solidification, the shape of the solid-liquid (S/L) interface affects the development of the microstructural features. The stability of the S/L interface is mostly controlled by the thermal and constitutional conditions (constitutional supercooling) that are found near the S/L interface. Depending on these conditions and due to the composition and cooling rate variations in FZ, solidification can occur through different modes including planar, cellular, columnar dendritic, and equiaxed dendritic. The solidification mode is controlled by the material system as well as the welding condition. Typical microstructures of the FZ are shown in Figure 2.7 [60].

The planar solidification mode is mainly affected by heat flow and characterized by preventing the formation of the substructure (Figure 2.7a). In this solidification mode, the direction of growth is perpendicular to the solidification front which is along the direction of the maximum thermal gradient. Lancaster [65] reported that a high G and low R facilitate the planar solidification mode in an S/L interface. The cellular solidification mode is characterized by the formation of several cells that grow relatively and uniformly parallel to one another. Similar to planar growth, the direction of the cell growth is also controlled by heat flow conditions (Figure 2.7b).

Contrary to the planar and cellular growth modes, dendritic growth is controlled mainly by the crystal orientation. Thus, grains with a preferred crystallographic axis that closely aligns with the heat flow directions survive while others that are not so well aligned are eliminated. In alloys with a body-centered cubic (BCC) and FCC crystallography, the <100> directions are the preferred directions [60]. Dendritic growth consists of two main types of growth: columnar and equiaxed dendritic growth. The former is defined as the growth of a packet of dendrites along the same direction which combines to form one grain with a well-developed substructure. On the contrary, the latter is defined as the growth of dendrites with different orientations in a liquid-cooled sufficiently below the liquidus temperature, so that spontaneous nucleation is possible. Neighboring dendrites are not necessarily parallel to each other and therefore each dendrite consists of a separate grain in the final solidified structure.

As mentioned earlier, the cooling rate within the molten pool directly affects the solidification mode of the FZ microstructure [66]. As the cooling rate varies within the molten pool, any combination of columnar and equiaxed grains may form in the FZ. Lampman [14] reported that a coarse columnar grain size increases the susceptibility of a microstructure to hot cracking, while an equiaxed microstructure with a finer grain size is highly resistant to hot cracking. In addition,

the mechanical properties of a weld greatly depend on the (polycrystalline or single crystal) grain structure of the FZ. For example, to enhance the creep resistance of a gas turbine blade, a columnar grain structure along the length of the blade is necessary [67]. Kurz et al. [67] reported that accurate control of the heat input is important for obtaining a desirable microstructure of the FZ. Several researchers have reported that the R and G are altered through heat input, which directly controls the columnar to equiaxed transition (CET) [68][69][70][71][72][73]. An enhancement in CET has been reported with an increase in the R and a decrease in the G. Therefore, a smaller G/R ratio means a more equiaxed grain structure [69]. Schempp and Rethmeier [70] showed that a low welding speed (large G/R ratio) throughout the GTAW of aluminum alloys leads to a columnar grain structure. In contrast, a high welding speed (small G/R ratio) leads to the formation of an equiaxed grain structure. Park et al. [71] concluded that reducing the laser power and welding speed can reduce the G/R ratio below the critical value and prevent the formation of new grains (stray grains) in welds.

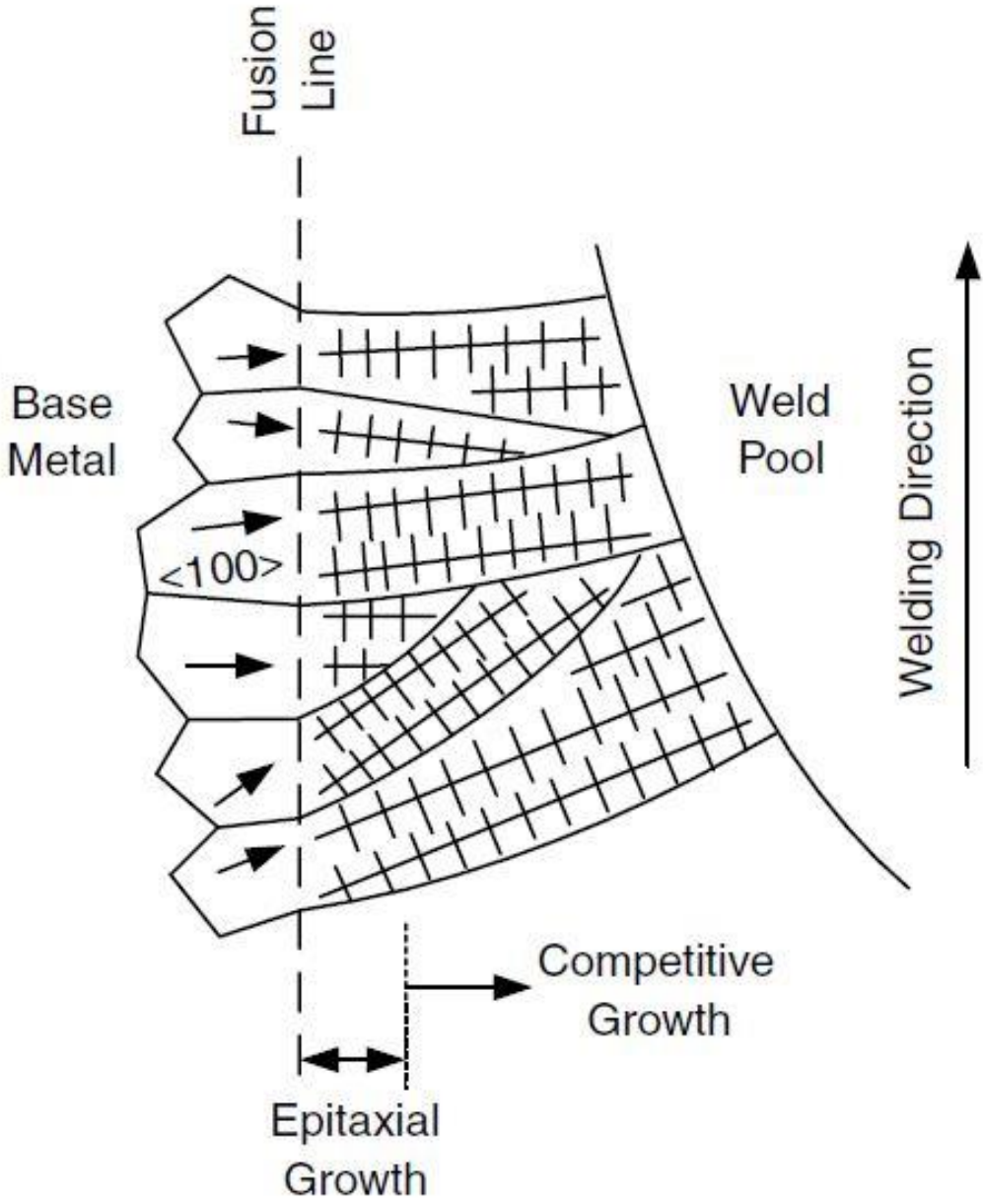

Figure 2.6 Epitaxial growth of weld metal near fusion line and competitive growth in bulk FZ [60]

(Reproduced with permission from John Wiley and Sons)

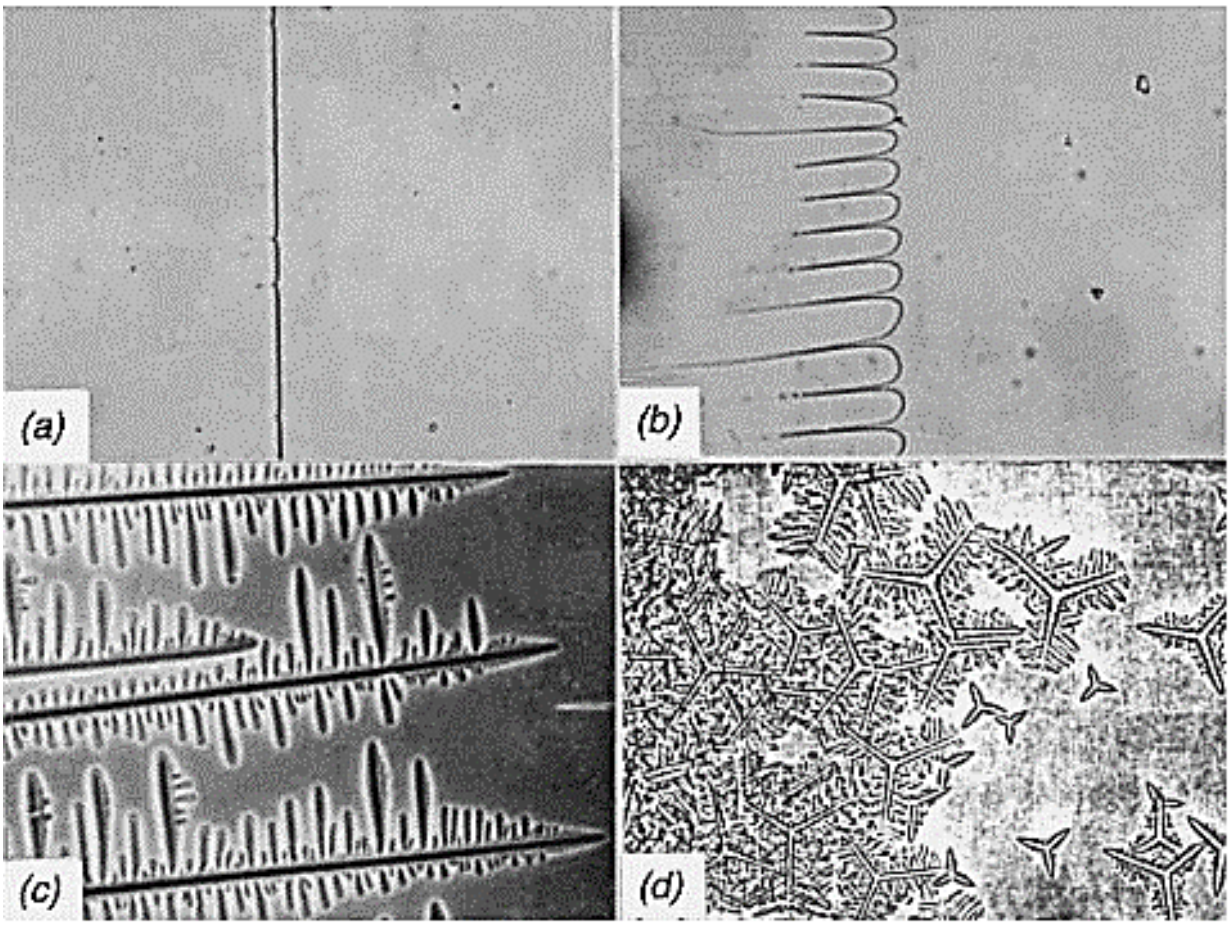

Figure 2.7 Various solidification modes in the FZ [60]: a. Planar, b. Cellular, c. Columnar dendritic, and d. Equiaxed dendritic solidification

(Reproduced with permission from John Wiley and Sons)

2.6.1.1 Dendrite Arm Spacing

Non-equilibrium solidification during GTAW leads to the formation of a dendritic microstructure in the FZ, which considerably affects its mechanical properties [14]. The solidification substructure can be quantified through primary and secondary dendrite arm spacings which can be used to measure the effect of the solidification conditions on the microstructure. Secondary dendrite arm spacing (SDAS) is the most common microstructural feature used to evaluate cast alloys and FZ mechanical properties and susceptibility to hot cracking [72]. Xue and Xu [73] concluded that refining the SDAS enhances the hardness of the alloy. Franke et al. [74] reported an inverse relationship between the cooling rate and dendrite arm spacing. Mei et al. [75] stated that a finer dendritic structure can be observed with the use of EBW as opposed to conventional fusion welding techniques. They attributed the microstructure changes to a higher cooling rate, resultant of the high heat input density of the focused beam with EBW [75]. Li et al. [66] showed that different cooling rates change the solidification mode of the microstructure, which transitions from cellular to columnar dendrite with distance from the fusion boundary. They also stated that an increase in heat input results in a reduction in the cooling rate, consequently increasing the primary dendrite arm spacing (PDAS) [66]. Similarly, Bal et al. [76] investigated the effect of voltage used during EBW and concluded that an increase in voltage results in a reduction in the cooling rate and enhancement of the SDAS. It has been well established that the SDAS can be evaluated by studying the cooling rate in the different areas of the FZ [77]. The following expression is used to calculate the SDAS [77]:

$$\lambda_2 = a(G \times R)^b \qquad (2\text{-}4)$$

where λ_2 is the SDAS, a and b are constants with values that depend on the alloy, and $G \times R$ is the cooling rate.

2.6.1.2 Solute Partitioning

High cooling rates during the welding process lead to inhibiting diffusion and solidification under non-equilibrium conditions which result in unavoidable redistribution or partitioning of the solutes between the liquid and solid [61][77]. Solute distribution or partitioning of alloying elements across the dendritic structure which is also referred to as microsegregation, is a critical phenomenon during alloy solidification that can considerably affect the weld microstructure and weldability [17]. Lampman [14] reported that non-equilibrium solidification during GTAW leads to dendritic microsegregation in the FZ. Dendritic microsegregation typically causes the formation of solidification constituents within the interdendritic region and the inhomogeneous distribution of secondary phase precipitates. These microstructural changes are known to considerably affect the properties of the FZ [14]. Ding et al. [78] reported that the formation of non-equilibrium eutectic-type microconstituents can reduce the resistance of the FZ to hot cracking. Brooks and Krenzer [79] showed that FZ cracking in the A-286 superalloy is attributed to the presence of a low melting Laves phase, which is a TCP phase, in the FZ. Similarly, Ding et al. [78] who investigated a Ni_3Al-based alloy, IC6, showed that the formation of the NiMo (Y) phase leads to severe FZ cracking. Ojo et al. [80] concluded that the formation of low melting solidification constituents such as M_3B_2 and Ni_7Zr_2 in the FZ of IN738LC increases susceptibility to cracking in the PWHT.

Furthermore, in some instances, the elements that form the main strengthening phase could combine with the subsequent non-equilibrium intermetallic precipitates, which leads to the inhomogeneous distribution of the γ' strengthening phase particles. This can have detrimental effects on the mechanical properties at elevated temperatures [80][81]. Ojo et al. [80] also confirmed the formation of non-homogeneously distributed γ' particles in the FZ of IN738LC.

They showed that the FZ microstructure consists of coarse γ′ precipitates in the interdendritic regions and fine γ′ precipitates in the dendrite core. Similarly, Chen et al. [82] observed the non-uniform distribution of the γ′ precipitates in Fe-Ni-based alloy following post-weld aging. They concluded that this inhomogeneity results in reduced microhardness of the FZ compared to the BM with a uniform distribution of γ′ particles [82].

The detrimental microstructural changes in the FZ summarized above can be remedied through a PWHT to modify the as-welded microstructure and release the residual stresses. Strum et al. [81] reported that as-weld microstructures are the primary factor that determines how superalloy welds respond to the PWHT.

2.6.2 Heat-Affected Zone

Microstructural changes in the HAZ are generally governed by the composition of the superalloy, previous processing history, and thermal factors associated with the welding process [14]. During the welding process, peak temperatures, as well as heating and cooling rates significantly affect the nature of the reactions in this region. The peak temperature found in the HAZ varies with distance from the fusion line. The maximum peak temperature is the liquidus temperature of the alloy at the fusion boundary [60]. Several metallurgical reactions including phase transformations and elemental segregation occur throughout the thermal cycle of the weld, which may affect the properties of the HAZ. Among these reactions, liquation is prominent and it is known to be a critical cause of grain boundary embrittlement both during welding and the PWHT. Liquation reaction and cracking in the HAZ are further discussed in Section 2.7.3.

2.7 Welding Defects

During the welding of superalloys, several defects and discontinuities (flaws) may occur, either due to inappropriate welding techniques or metallurgical-related issues, which can significantly affect the high-temperature performance of the weldment [83]. Figure 2.8 shows some of the weld defects that occur during fusion welding. Typical weld defects include porosity, slag inclusion, lack of penetration, undercutting, and lack of fusion, which can be minimized/eliminated by optimizing the welding procedure and parameters. Porosity is defined as small cavities that form as a result of gas trapped in the weld metal (Figure 2.8a). The formation of porosity during welding is typically caused by improper amperage, inaccurate shielding, moisture, and excessive arc length. Slag inclusions (Figure 2.8b) happen when slag or other non-metallic matter is trapped in the weld metal and causes discontinuity which eventually leads to failure. Lack of penetration (Figure 2.8c) occurs when the weld metal has not penetrated the bottom of the weld joint. It is usually caused by improper welding techniques or incorrect root gaps. Undercutting (Figure 2.8d) refers to an unfilled groove left at the toe of the weld following the melting of the BM. This defect often occurs due to excessive amps/volts, excessive travel speed, incorrect electrode angle, or incorrect welding technique. The occurrence of this defect can lead to a reduction in the material thickness. Hence, concentrated stress emerges from which failure such as fatigue fractures can occur. Lack of fusion (Figure 2.8e) includes discontinuities as a result of the incomplete coalescence of some portion of the filler metal with the BM or between weld beads in the case of multi-pass welds. This defect usually forms in the direction of the welding with either sharp or rounded edges due to insufficient heat absorbed by the underlying metal from the weld which leads to incomplete melting.

Cracking and micro-fissuring (Figures 2.8f and 2.8g) are metallurgical-related defects and refer to discontinuities that are produced by local ruptures. Cracks can occur in both the FZ and HAZ due

to high stress/strain generation during the welding process or PWHT in combination with inherent material properties. Contrary to the previously mentioned welding defects that can be eliminated by properly controlling the welding process, inhibiting or eliminating weld cracking requires extensive knowledge of metallurgical-related factors. A detailed review of the various types of cracking and associated mechanisms are discussed in Sections 2.7.2 to 2.7.4.

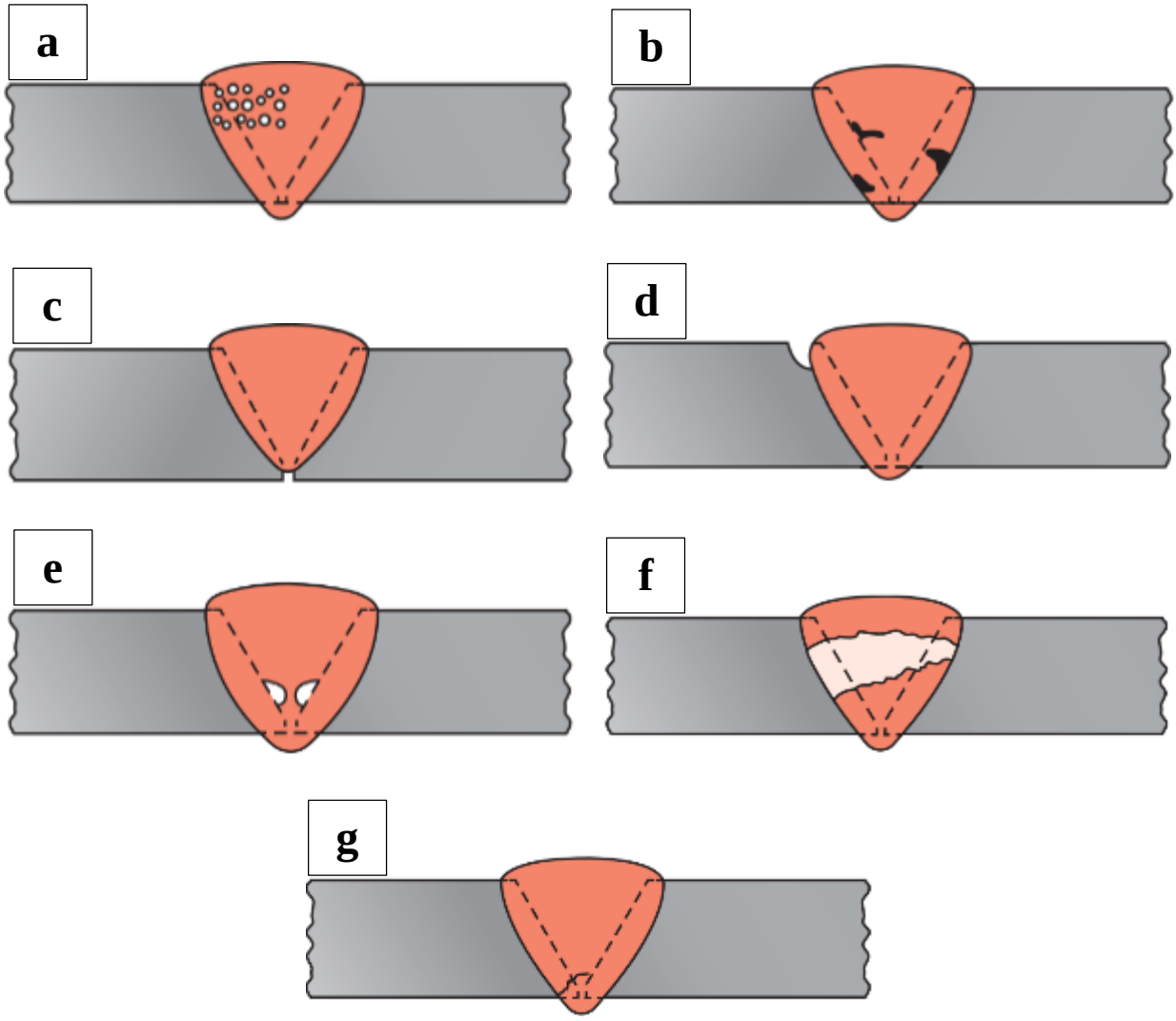

Figure 2.8 Typical fusion welding defects: a. Porosity, b. Slag inclusion, c. Lack of penetration, d. Undercut, e. Lack of fusion, f. Traverse cracking, and g. Longitudinal root cracking [83]

(Reproduced with permission from Cengage Learning)

2.7.1 Welding Stress Distribution

During the welding process, weldments are subjected to localized heating which results in the non-uniform distribution of temperature in the weldments. Typically, the FZ and HAZ are subjected to temperatures considerably higher than those of the unaffected BM. As the cooling stage of the welding process begins, the FZ solidifies and shrinks, which induces stress to the HAZ and BM. When the FZ first solidifies, it is still hot and relatively weak; thus, it creates little stress. However, once the weld cools to room temperature, the stress in the weldment increases and eventually reaches the yield point of the BM and HAZ. As the welding process continues, the parts that have already solidified resist the shrinkage of the later portions of the weld bead. Therefore, the portions welded first are strained in tension in a direction longitudinal to the weld, that is, down the length of the weld bead, as shown in Figure 2.9. Furthermore, it can be observed in Figure 2.9 that, due to the shrinkage in the weld, transverse stress is also present. In addition, distortion may appear in the butt joints as both longitudinal and transverse shrinkage or contraction. It may also appear as an angular change (rotation) when the face of the weld shrinks more than the root (Figure 2.10). Angular change produces transverse bending in the plates along the weld length. Residual stress in weldments is defined as the stress that exists after all of the external loads are removed. It is worth mentioning that the residual stress that occurs due to non-uniform temperature distribution during the welding process is usually termed thermal stress [62][84].

Figure 2.11 schematically shows the variations in temperature and stress that occur during the welding process. Here, BOP welding is performed along line X-X. As shown in Figure 2.11a, the welding arc, which is moving at velocity v, is located at Point O. Figure 2.11b depicts the temperature distributions transverse to line X–X at locations A, B, C, and D. Across Section A–A, which is in front of the welding arc, the temperature variation (ΔT) is zero. However, the

temperature distribution is extremely steep across Section B-B, which crosses the welding arc. Along Section C–C, which is behind the welding arc, the temperature distribution is considerably less steep. Farther away from the welding arc, the temperature across Section D–D has returned to a uniform distribution.

The normal stress distribution in the x-direction (σ_x) of Sections A–A, B–B, C–C, and D–D is shown in Figure 2.11c. The normal stress in the y-direction (σ_y) and the shear stress (τ_{xy}) also exist in a two-dimensional stress field, although these are not shown in Figure 2.11. In Section A–A, the thermal stress is nearly zero. There is almost no stress in the regions below the weld pool at Section B–B as the hot metal cannot support a load. Stress in the HAZ on both sides of the weld pool is compressive as the expansion of these areas is restrained by the surrounding metal that is at lower temperatures. As the temperature close to the arc is considerably high, and the resulting yield strength is low, the compressive stress will reach the yield level at the temperature of the metal. The level of the compressive stress peaks with increasing distance from the weld (decreasing temperature). Due to equilibrium conditions, at a certain distance away from the weld pool, the tensile and compressive stresses must balance in the HAZ. The stress distribution along Section B–B is presented in Figure 2.11c.

In Section C–C, the weld metal and HAZ have cooled down. As they start to shrink, tensile stress is induced in the weld metal. This tensile stress is balanced by the compressive stress in the BM which has a lower temperature. The stress distribution is illustrated in Figure 2.11c. The final condition of the residual stress in the weld is shown in Section D–D. Along this section, high tensile stress is found in the weld and HAZ, while compressive stress is found in the BM away from the weld.

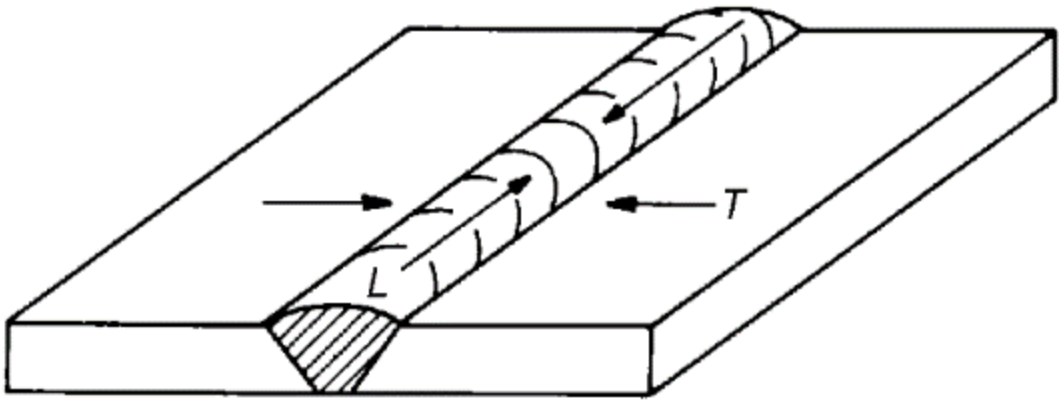

Figure 2.9 Longitudinal (L) and transverse (T) shrinkage stress in butt joint weld [84]

(Reproduced with permission from American Welding Society)

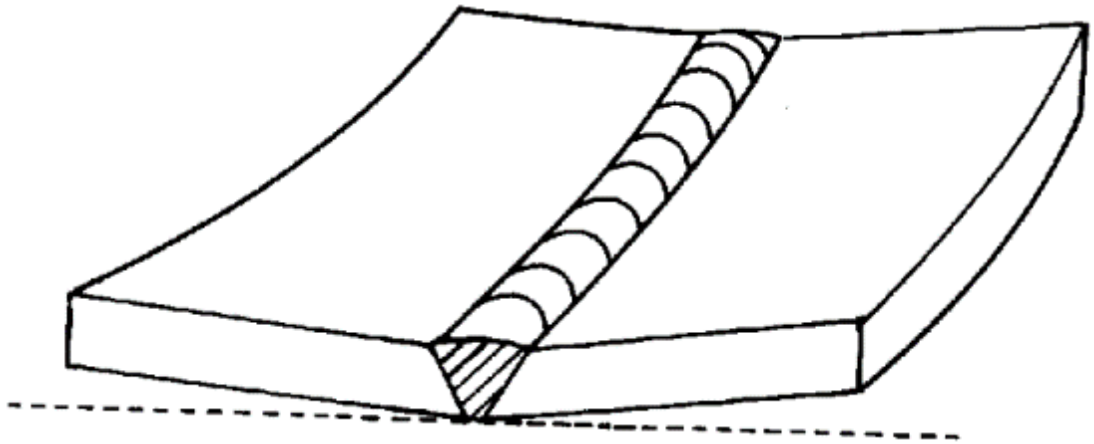

Figure 2.10 Schematic representation of distortion in a butt joint [84]

(Reproduced with permission from American Welding Society)

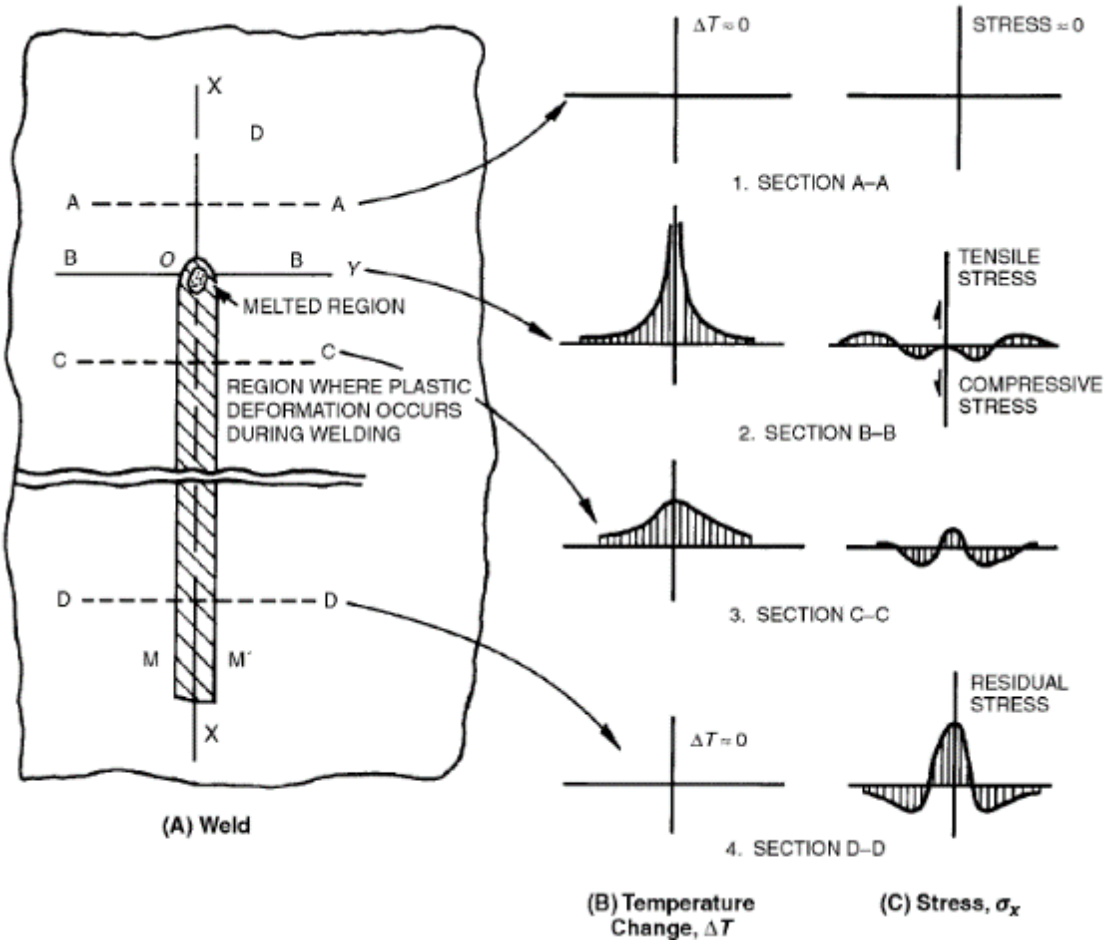

Figure 2.11 Distribution of temperature, ΔT, and stress, σ_x, during BOP welding [84]

(Reproduced with permission from American Welding Society)

The formation of tensile stress in the FZ and HAZ during the welding process plays a vital role in the occurrence of weld cracking in superalloys. This tensile stress is known as the main mechanical factor that extensively contributes to cracking during the fusion welding of superalloys. In addition to the tensile stresses that occur during the cooling stage of the welding process, other metallurgical factors are also contributors to the formation of weld cracks. Generally, cracking that occurs in the HAZ and FZ during welding and PWHT is termed hot cracking. Typical types of hot cracking in superalloys are:

1. Solidification cracking or FZ cracking
2. Liquation cracking or HAZ cracking
3. PWHT cracking which can occur in both the FZ and HAZ

2.7.2 Solidification cracking

Solidification or FZ cracks that form along the grain boundaries have an intergranular nature and mostly occur along the centreline of the FZ. Solidification cracks form during the terminal stage of the FZ solidification in which the tensile stresses developed across the adjacent grains exceed the strength of the almost completely solidified weld metal. Figure 2.12 illustrates the solidification cracking mechanism. During solidification, the alloying elements with a low partitioning coefficient tend to segregate into the solidifying liquids and form low melting phases and eutectics with the metal which results in grain boundary wetting by the liquid film. The prevalence of liquid films at the grain boundaries when the weld is partially solidified reduces the ductility of the solidifying weld metal. Therefore, the grain boundaries are weakened and cracks form under the effect of the tensile stresses that are produced during the cooling stage of the welding process [60][85].

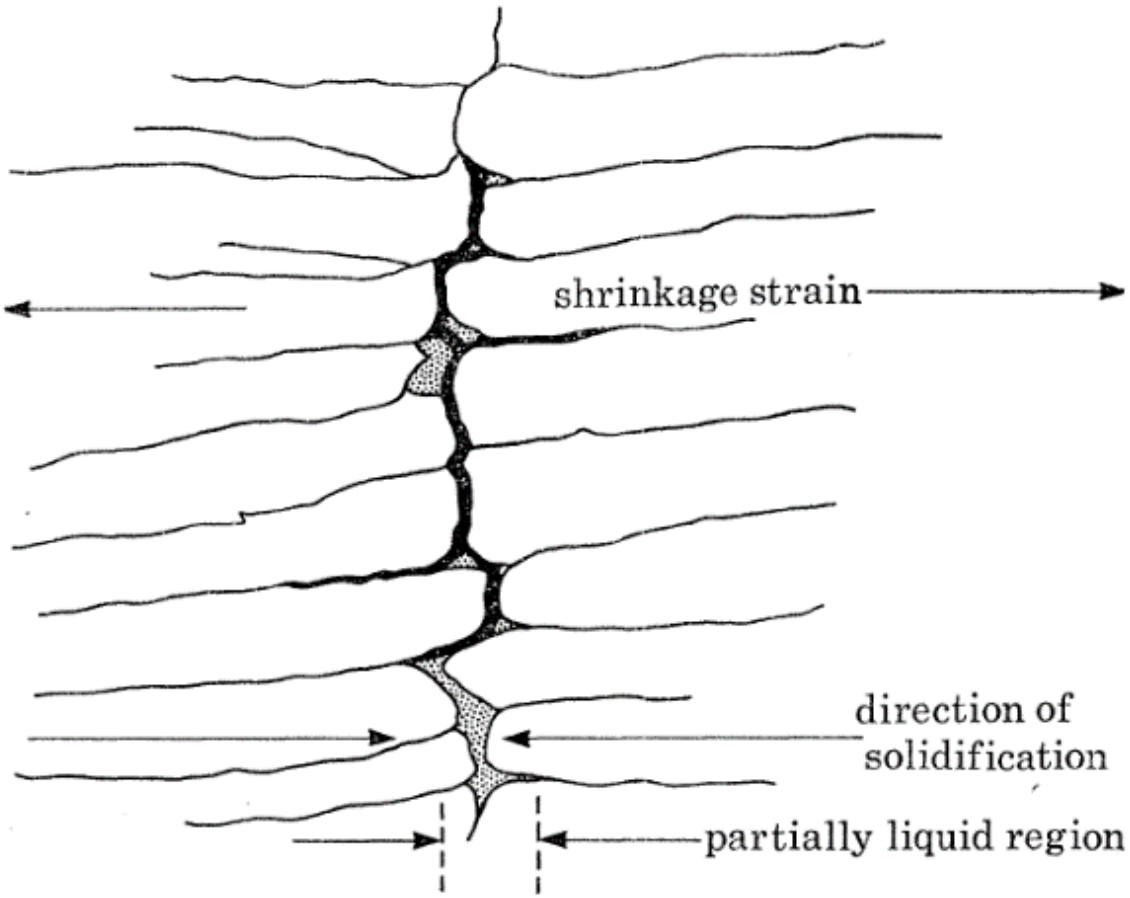

Figure 2.12 Schematic diagram of the mechanism of solidification cracking [85]

(Reproduced with permission from the Royal Society (U.K.))

Susceptibility to solidification cracking is affected by several metallurgical and mechanical factors. Metallurgical factors that have been reported to affect the susceptibility of a weldment to solidification cracking are [85]:

1. Solidification Temperature Range: Typically, as the solidification (freezing) temperature range increases, susceptibility to solidification cracking is also enhanced due to a larger and weak mushy zone. The presence of undesirable impurities such as sulphur (S) and phosphorus (P) or intentionally added alloying elements can enhance the solidification range and solidification cracking susceptibility. In addition, phase transformations, especially eutectic reactions, can often occur during the terminal stage of solidification and extend the solidification temperature range.

2. Amount of Liquid during Terminal Solidification: There is a threshold amount of liquid between grains that can lead to maximum solidification cracking. Pure metals are known to be immune to solidification cracking due to the absence of low-melting-point eutectics at the grain boundaries that cause solidification cracking. On the other hand, in highly alloyed metal, the amount of eutectic liquid at the grain boundaries can be considerably large to induce crack healing. Therefore, the maximum cracking susceptibility occurs somewhere in between these two composition levels, where the amount of the liquid can be just adequate to form a thin, continuous grain boundary film to make the materials rather susceptible to solidification cracking but without extra liquid for healing cracks.

3. Grain Structure of Weld Metal: The grain structure can significantly affect the susceptibility of superalloys to solidification cracking. Fine equiaxed grain structures are less susceptible to solidification cracking compared to coarse columnar grain structures. This is because fine equiaxed grains deform more easily to accommodate contraction strains. In addition, as the surface area of

the grain boundaries is much larger in a fine equiaxed microstructure, segregates of the melting point depressant elements are less concentrated at the grain boundaries. Furthermore, liquid feeding and healing of incipient cracks can also be more effective in fine equiaxed grains [60].

4. Ductility of Solidifying Weld Metal: Reduction in the ductility of solidifying weld metal can lead to an increase in the susceptibility to solidification cracking.

Solidification cracking does not occur without the presence of stresses acting on adjacent grains during solidification which is considered as a mechanical factor that contributes to the formation of solidification cracking. Such stresses can be due to thermal contraction or solidification shrinkage or both. The degree of restraint of the workpiece is another mechanical factor that contributes to solidification cracking. For the same joint design and material, solidification cracking will more likely occur in a workpiece with a higher degree of restraint. Generally, thicker or stronger plates require a higher degree of restraint which leads to more residual stress and susceptibility to solidification cracking.

2.7.3 Liquation Cracking

HAZ liquation cracking is the most common defect in welding superalloys [61]. Contrary to FZ cracking which can be eliminated by properly controlling the welding process, HAZ liquation cracking is a considerably challenging defect with several metallurgical and mechanical factors that contribute to the cracking. Generally HAZ cracking occurs due to both the formation of a liquid film along the grain boundaries and the effect of tensile stress produced during weld cooling [86]. Figure 2.13 shows the occurrence of liquation cracking in the HAZ in which the formed liquid wets the grain boundaries and spreads along them to create a continuous film. Subsequent

to the complete formation of the continuous intergranular film, cracks can form along the grain boundaries and extend into the FZ due to sufficient tensile thermal stresses [85].

Generally, the liquid film in the HAZ can form through either non-equilibrium phase transformation below the alloy solidus temperature (subsolidus) or melting above the solidus temperature (supersolidus). The latter is anticipated to occur in all weldments due to heating above the equilibrium solidus temperature of an alloy [87]. The formation of subsolidus liquation is more damaging in terms of HAZ cracking because it increases the melting range of the alloy and affects the characteristics of the supersolidus melting by forming a non-equilibrium liquid film at lower temperatures [88].

Two main mechanisms have been reported to describe the occurrence of sub-solidus liquation in the HAZ; grain boundary penetration and grain boundary segregation [86]. The former involves the eutectic melting of constituents formed at the grain boundaries such as MC carbides, borides (M_5B_3 and M_2B), and γ-γ' eutectics [89], and constitutional liquation of second-phase particles in the HAZ during welding. Subsequently, the resulting liquid film penetrates the grain boundary regions. The latter includes the segregation of surface-active elements such as B to the grain boundaries which results in a localized composition with a lower melting point. In reality, both grain boundary penetration and segregation can be attributed to the occurrence of HAZ cracking.

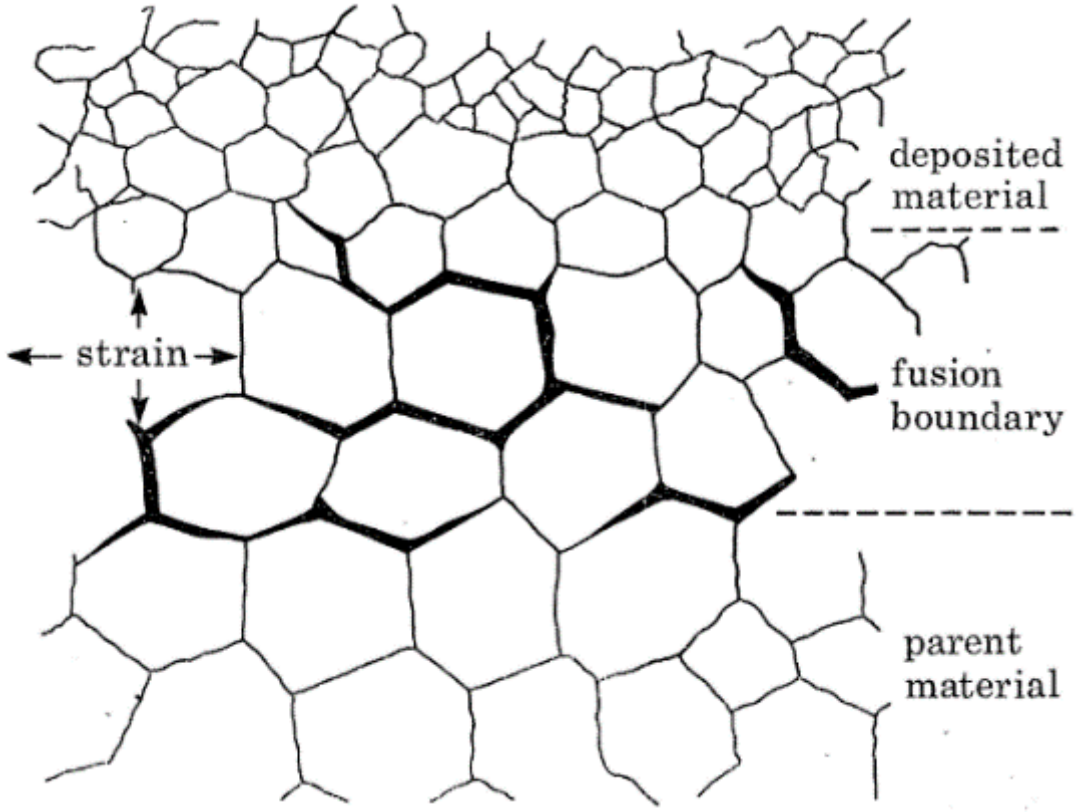

Figure 2.13 Schematic diagram of liquation cracking [85]

(Reproduced with permission from the Royal Society (U.K.))

2.7.3.1 Constitutional Liquation

The constitutional liquation mechanism, first proposed by Pepe and Savage in the 1960s [90], requires a eutectic reaction between the surrounding matrix and second-phase precipitates. Under the conditions of constitutional liquation, the second phase particles do not melt, however, local melting occurs at the constituent/matrix interface, hence the term constitutional liquation. Two conditions need to be satisfied for this mechanism to be viable [91].

1. The constituent particles must react with the surrounding matrix to create a composition gradient around the particles.

2. The reaction zone composition must undergo melting below the melting temperature of the surrounding matrix.

Figures 2.14 and 2.15 describe the constitutional liquation mechanism. Figure 2.14 shows a binary phase diagram for a eutectic reaction between a particle A_xB_y and the matrix α. From this figure, a reaction between the matrix and the particle occurs as an alloy with a composition of C_A is heated. Figure 2.15 schematically illustrates the nature of that reaction at temperatures T_1, T_2, T_e, and T_3. From Figure 2.15a, the spherical particle A_xB_y resides in a matrix of composition C_0 at an ambient temperature. During slow heating (equilibrium heating), the particle dissolves through a diffusional process as the temperature exceeds the solvus temperature at about T_2. Further increases in temperature at the same slow heating rate to around T_3 just below the solidus temperature of the alloy would not lead to any phase transformation, but rather, the occurrence of grain growth and equilibrium grain boundary segregation. However, during rapid heating (non-equilibrium heating conditions) which occurs in the HAZ during most welding processes, not only does the particle not dissolve entirely, but also starts to react with the surrounding matrix at T_2. As

equilibrium is normally maintained at the particle-matrix interface, the particle of composition A_xB_y is in contact with a matrix composition specified by Point b on the solvus line. A composition gradient that originated from the partial particle dissolution is now found in the matrix. This occurs in the reaction zone that surrounds the particle where B atoms are diffusing into the surrounding matrix (Figure 2.15b). The slope of the concentration gradient produced depends on:

1. The heating rate: Higher heating rate results in a steeper concentration gradient.

2. Solute diffusivity: Slower diffusivity of the solute B atoms leads to a shallower concentration gradient.

3. Accommodation factor: More easily accommodated solute atoms within the α-matrix result in a shallower concentration gradient.

As the alloy is heated from T_2 to T_e, the interface composition continues along the solvus line of the phase diagram. When this composition reaches Point c at the eutectic temperature as seen in Figure 2.15c, equilibrium dictates that a liquid of composition d must be in contact with the solid. Therefore, a liquid of eutectic composition is formed in the system within the reaction zone. This liquid completely surrounds the particles and characterizes the onset of constitutional liquation. Further heating to T_3 leads to the formation of additional liquid in the system. The composition of this liquid ranges from g at the particle interface to f at the matrix interface (Figures 2.14 and 2.15d). The composition of the matrix in contact with the liquid is now signified by Point e on the solidus line. Again, all of the interface compositions must have microscopic equilibrium as dictated by the phase diagram. Note that a solute hump is predicted in the solid matrix within the reaction zone. This occurs because the solid composition achieved at T_e (Point c) has now decreased to e since the solid composition must lie along the solidus line. Above T_3, additional constitutional

liquation will occur around the particles until the alloy exceeds the solidus temperature and bulk melting of the matrix begins.

Therefore, under rapid heating (non-equilibrium), constitutional liquation occurs and leads to the formation of solute-rich liquid pools at temperatures well below the equilibrium solidus of the alloy. During fusion welding, interactions between these liquated regions and the grain boundaries result in a microstructure that is susceptible to intergranular liquation cracking.

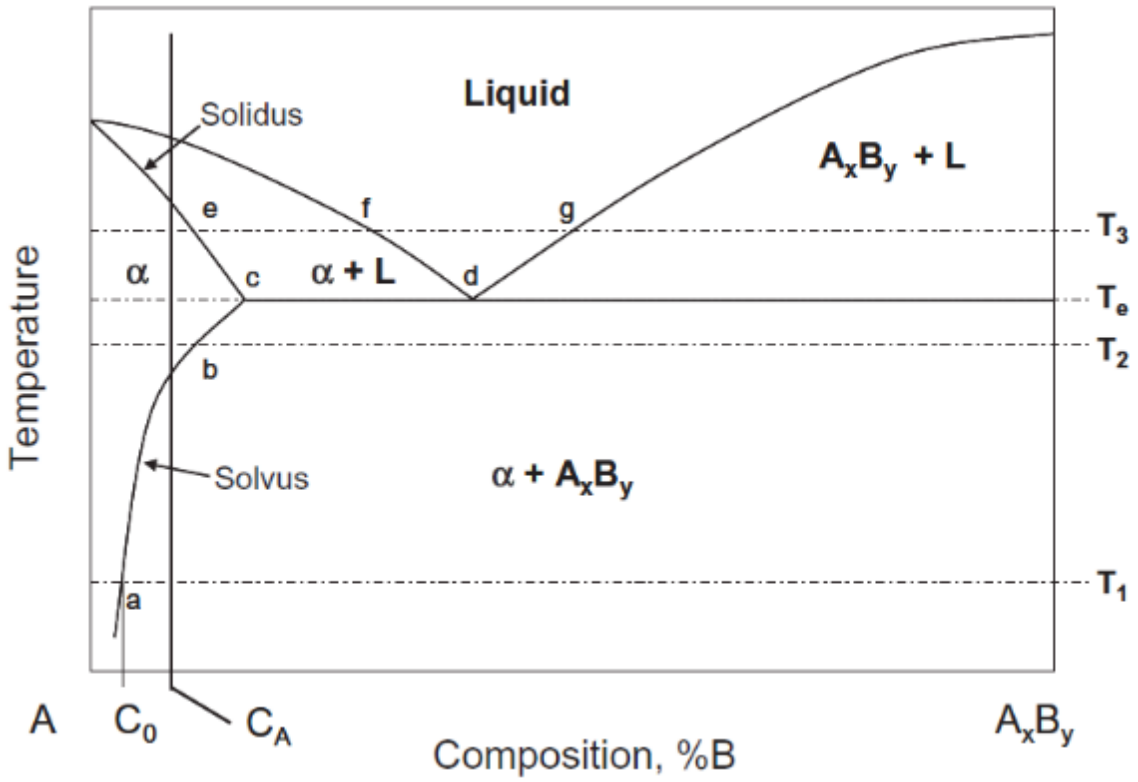

Figure 2.14 Binary phase diagram used to describe constitutional liquation [91]

(Reproduced with permission from John Wiley and Sons)

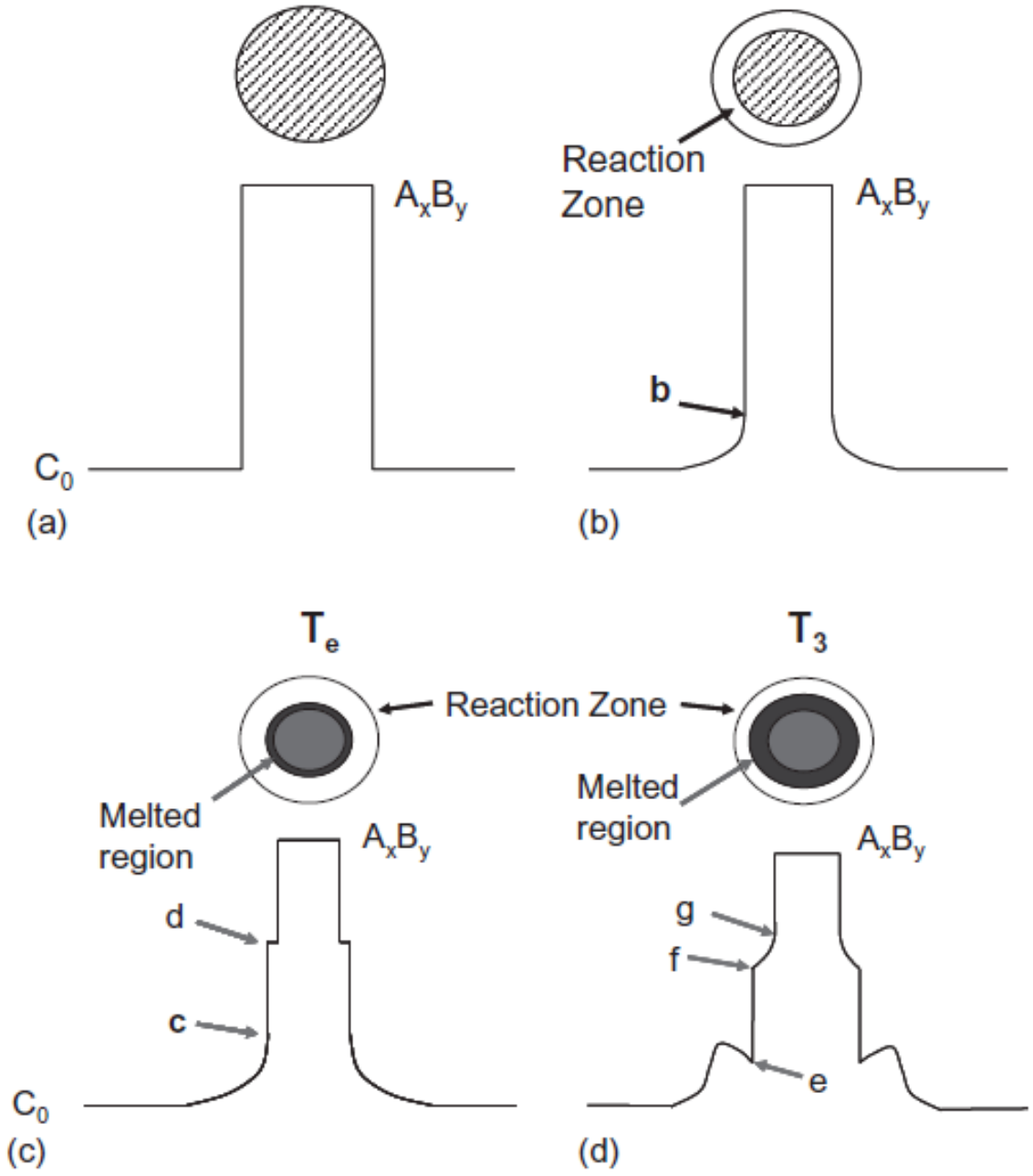

Figure 2.15 Schematic illustration of constitutional liquation mechanism [91]

(Reproduced with permission from John Wiley and Sons)

2.7.3.2 Grain Boundary Segregation

Another mechanism that can lead to the formation of liquid film at the grain boundaries is grain boundary segregation. This mechanism occurs due to the segregation of the melting point depressant elements to the grain boundaries, which decreases the melting point of the grain boundaries compared to the surrounding matrix and results in sub-solidus grain boundary melting in the HAZ during welding [12]. Grain boundary elemental segregation can occur both before and during the welding process. The grain boundary elemental segregation before welding is more critical and categorized as equilibrium and non-equilibrium segregation. Equilibrium segregation occurs during heat treatment when solute atoms diffuse from within the grain to the grain boundary to reduce the grain boundary free energy. The extent of this segregation increases with a decrease in the heat treatment temperature [88]. Non-equilibrium segregation takes place during cooling from high temperatures and relies on the formation of vacancy-solute complexes. The reduction of the concentration of vacancies at the grain boundary during cooling from high temperatures leads to a concentration gradient of the vacancy-solute complexes, which results in the diffusion of the complexes from within the grains to the grain boundaries. This diffusion induces a high concentration of solute atoms in the vicinity of the grain boundaries. The extent of the non-equilibrium grain boundary segregation is mainly governed by the initial temperature and cooling rate. Adequate time available during air cooling allows vacancy-solute complexes to diffuse to the grain boundaries, thus resulting in enhanced non-equilibrium segregation. Furthermore, at the same cooling rate, increasing the heat-treatment temperature leads to an increase in non-equilibrium segregation. However, this type of segregation is less affected by the cooling rates at lower temperatures [92].

Huang et al. [93] found that the heat treatment condition significantly influences the grain boundary elemental segregation of B in IN718. They reported that even though increasing the heat treatment temperature reduces the extent of equilibrium segregation, doing so leads to an increase in non-equilibrium segregation. In addition, every heat treatment consists of both equilibrium and non-equilibrium segregations which result in a certain amount of grain boundary segregation. Furthermore, Huang et al. [93] identified a transition temperature at which the least segregation of the grain boundaries occurs as shown in Figure 2.16. Therefore, equilibrium segregation is predominantly found below the transition temperature, while non-equilibrium segregation is found above the transition temperature which mainly controls the extent of the total segregation.

Several studies have reported a close relationship between the grain boundary segregation of minor elements and cracking susceptibility of the HAZ in superalloys [12][19] [93][94]. Huang et al. [93] studied the HAZ cracking susceptibility of IN718 and showed that increasing the pre-weld heat treatment temperature first leads to a reduction in the cracking susceptibility of the HAZ. However, a further increase in temperature above a critical temperature increases the cracking susceptibility. Huang et al. [93] reported that the trend similarity between B segregation variation with temperature and the total crack length (TCL) of the HAZ suggests that the grain boundary segregation of B controls the TCL of the HAZ. They confirmed this observation by using a SIMS analysis on welded samples which showed the strong segregation of B along the HAZ crack region. Therefore, it can be concluded that HAZ cracking is reduced as a result of the balance between equilibrium and non-equilibrium elemental grain boundary segregation.

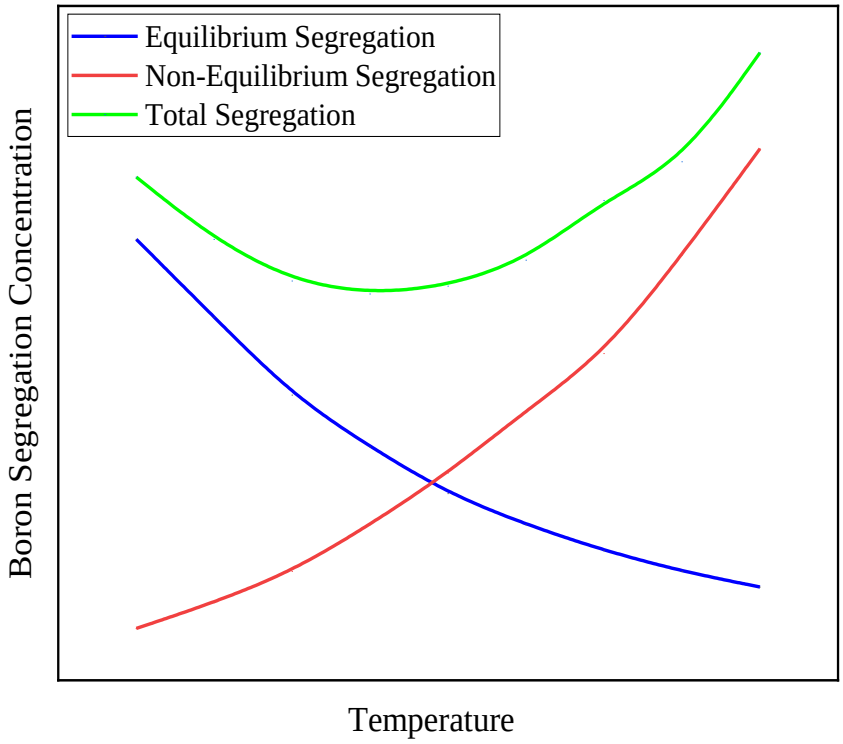

Figure 2.16. Effect of temperature on grain boundary elemental segregation of B in IN718 [93]

(Reproduced with permission from Elsevier)

2.7.4 Post-Weld Heat Treatment Cracking in Superalloys

PWHT is an essential process after welding superalloys as the process reduces the residual stresses that occur during welding, restores the weldment strength, and enhances other mechanical properties [95]. The PWHT of γ′-strengthened superalloys typically consists of two stages; solutionizing and aging to form the γ′ precipitates [96]. Sidhu et al. [97] reported that the precipitation of the γ′ phase occurs at temperatures where welding stress relief is normally expected, which can lead to the hardening of the material. The combination of welding residual stresses with hardening due to γ′ precipitation can lead to PWHT cracking in the HAZ which is also referred to as strain age cracking either through the extension of cracks that have already occurred during welding or by the formation of new intergranular cracks [96].

2.8 Weldability Testing Techniques

Joining superalloys is often accompanied by some defects (as discussed in Section 2.7) which can significantly affect the high-temperature properties of superalloys. To evaluate the properties that can be affected during welding and after PWHT, weldability testing techniques are used. These techniques are intended to assess actual service conditions through the responses of the alloy to various actual or simulated welding conditions. Weldability tests can be divided into two major types of tests [61]:

1. Direct tests, in which actual samples of the weld metal or entire weld zone, are evaluated, such as crack-susceptibility tests performed after the welding process.

2. Indirect tests in which examination is carried out based on metallurgical and mechanical principles and performed by simulating the weld thermal cycle and in some cases strain conditions to create a simulated weld zone. The best-known example of an apparatus to accomplish this is the Gleeble system.

2.8.1 Self-Restraint Tests

Self-restraint tests use the restraint within the specimen without external loading to form cracking in weld metal or BM. The specimen is designed to induce varying restraint intensities on the weld joint, thus causing cracking. Figure 2.17 shows an example of a self-restraint test called Lehigh restraint test to qualitatively evaluate the extent of restraint at which cracking occurs in weldments during cooling. As can be observed in Figure 2.17, a plate with slots machined onto the sides and ends is used in the Lehigh test. A single pass weld is made along a groove that has been previously machined along the centerline of the plate. The restraint from the plate and slots forms different levels of cracking in the weld. The level of restraint is modified by changing the length of the slots. The restraint is measured as 2x, where x is the distance from the centerline of the weld groove to the bottom of the slots (Figure 2.17). A variety of samples with different lengths of slots are usually welded. The threshold level of restraint is determined as a width that is just sufficient to cause cracking [98].

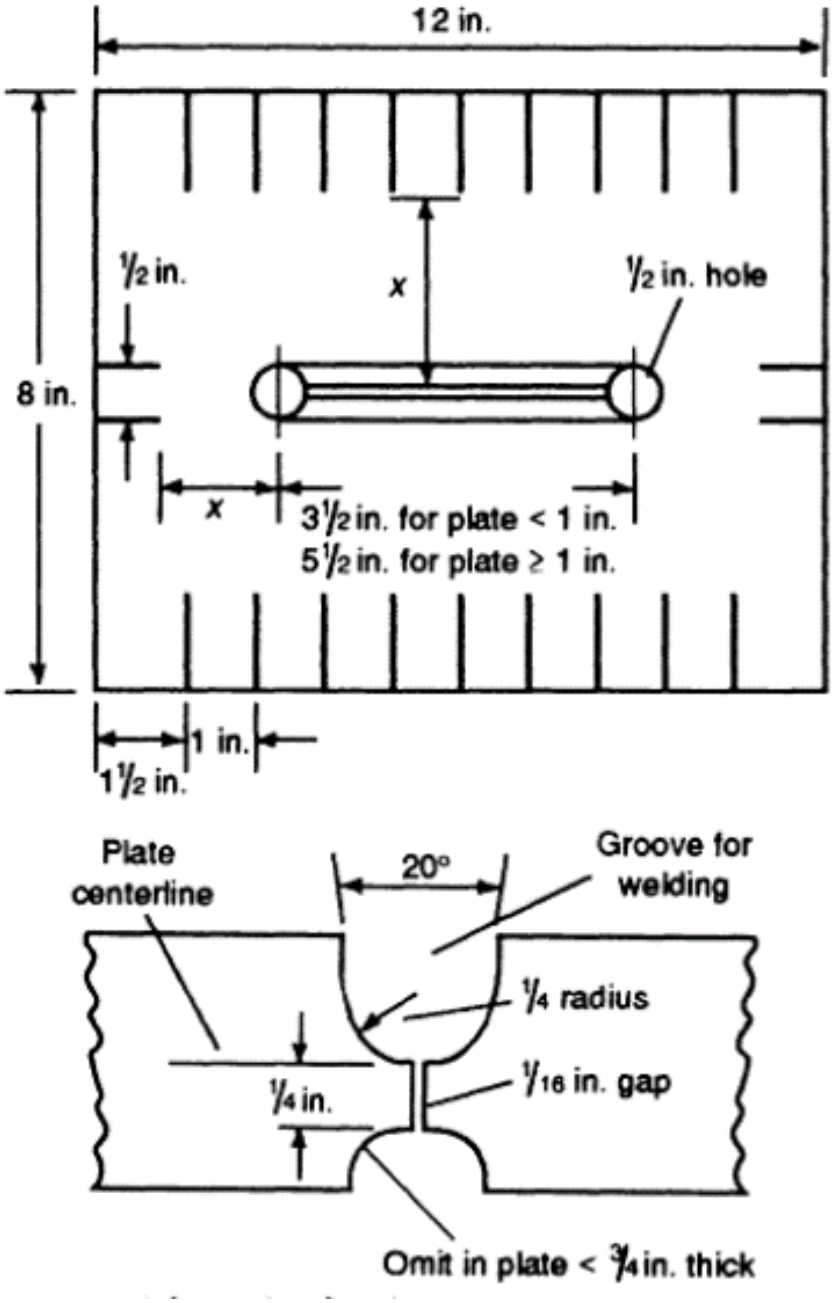

Figure 2.17 Schematic of slotted plate specification for Lehigh restraint test [98]

2.8.2 Externally Loaded Tests

As opposed to self-restraint tests, externally loaded tests involve an external load to evaluate the sample weldability during welding. To modify the stress state and consequently the severity of the cracking, the externally applied load is often varied. Figure 2.18 shows an example of this type of weldability test called the Varestraint test (hot cracking test). As can be observed in Figure 2.18, one side of a rectangular bar (usually 205×50×6.4 mm) is fixed while the opposite side is attached to a pneumatically operated ram. In this method, GTAW is usually used to produce a weld at the top of the plate along its longitudinal centerline from the free end to the fixed end. Once the arc reaches a pre-determined location over the die block, the plate is bent to conform to the radius of the die block. This bending causes an augmented longitudinal strain on the welded surface of the specimen. To measure the strain level at which cracking begins, several die blocks with various radii can be employed. For material evaluation, however, a single die block of a known radius, which produces cracking in all of the samples, is used. Hot cracks usually form along the edge of the weld pool and in the HAZ. The mean values of the TCL, number of cracks, or maximum crack length in duplicate samples of each material are used as a quantitative means of evaluating BM weldability [98].

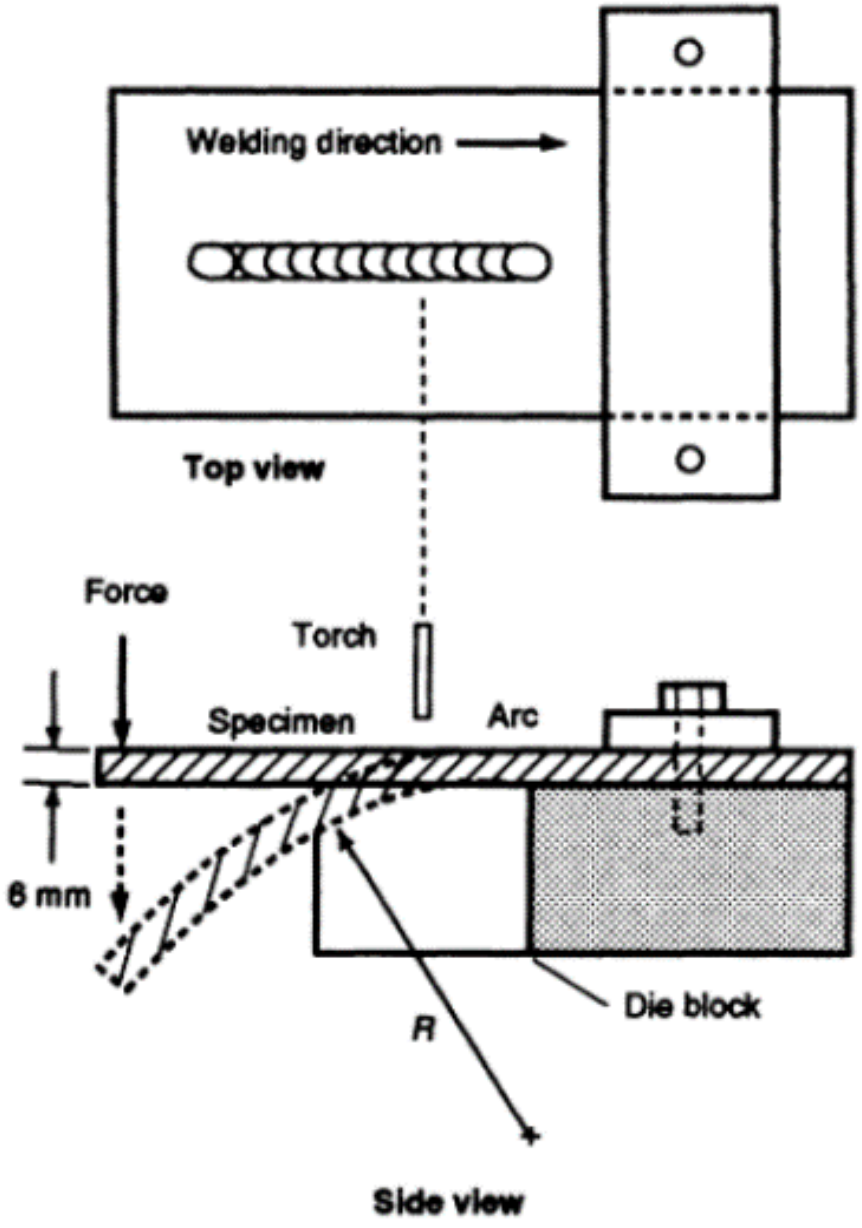

Figure 2.18 Setup and sample specifications for the Varestraint test [98]

2.8.3 Gleeble Testing

The Gleeble is a thermomechanical testing device that can replicate the thermal cycles and strain in a workpiece during welding [61]. Gleeble testing is used in a wide range of applications such as examining hot ductility [99], mechanical properties of the HAZ [19], continuous cooling transformation diagrams [100], stress relief cracking, precipitation kinetics [47], strain age cracking [101], constitutional liquation [102], and liquid metal embrittlement (LME) [103]. The Gleeble test method is shown schematically in Figure 2.19. A cylindrical specimen is held in a pair of water-cooled copper grips and tested under load and no-load conditions as shown in Figures 2.19a and 2.19b, respectively. In this method, the specimen is heated at rates up to 20,000°C/s by using a low-frequency alternating current introduced through the copper grips. By properly sequencing preprogrammed time cycles of temperature and displacement or force, the gauge region of the specimen develops the same microstructure as the actual weld [98]. The Gleeble is a fully computer-interfaced system, readily programmed to provide reference signals for closed-loop control of both thermal and mechanical operations. The feedback signal necessary for closed-loop control is typically acquired from a fine wire thermocouple percussion welded to the surface of the specimen at the gauge region. However, for temperatures above the operating limits of thermocouples, a radiation pyrometer can be used for some sacrifice in the overall response time of the system [14].

.

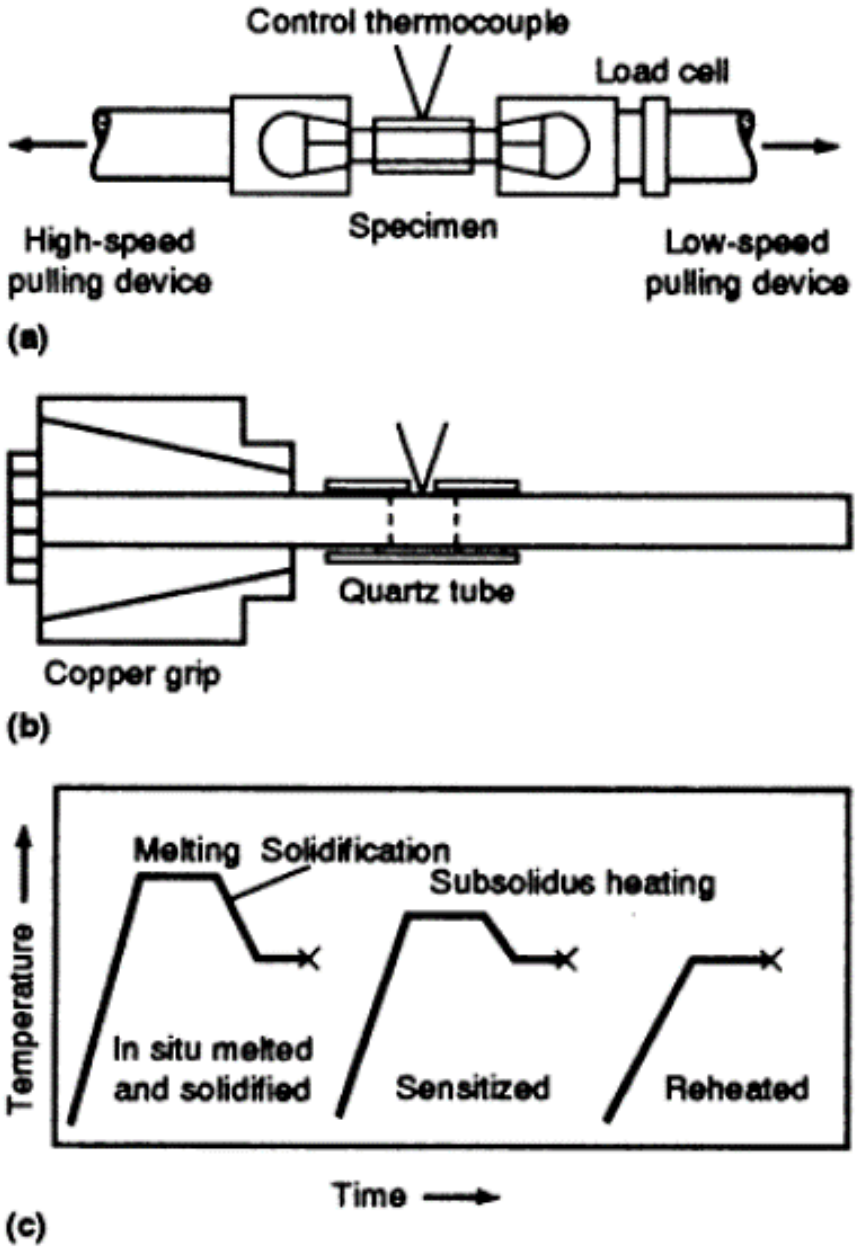

Figure. 2.19 Gleeble test method: a. Primary components, b. Close-up view of a resistance heater, and c. Programmed thermal cycle [14]

2.8.4 Measurement of Total Crack Length

The weldability of superalloys can also be evaluated by measuring the TCL in welded samples. In this method, the welded sample is sectioned transversely to the welding direction and the TCL in each section is evaluated by using microscopic techniques. The TCL can be used to study alloy cracking susceptibility in two different ways [104]. First, the TCL measured from various specimens can be compared to evaluate weldability. For this technique to be valid, the specimens must be welded by using the same set of welding parameters, which is anticipated to produce approximately the same HAZ size. The crack length in the transverse section of the specimen can be given as:

$$L = \sum_{n=1,2,\ldots}^{k} l_n \qquad (2\text{-}5)$$

where l is the length of an individual crack in a section and n stands for the number of cracks in a section. The welded specimens are usually sectioned into about 10 pieces or more and the sum of the L values from each section is calculated to determine the TCL which is given as:

$$TCL = \sum_{i=1}^{10} L_i \qquad (2\text{-}6)$$

Secondly, if the specimens are welded by using different sets of welding parameters or under different welding conditions, the calculation of the cracking index (CI) may be required. The CI is a measure of the TCL normalized with the total area of the HAZ and given by

$$CI = \sum_{i=1}^{10} L_i / A_T \qquad (2\text{-}7)$$

where A_T is the total area of the HAZ, measured from all the sections. The CI provides a quantitative evaluation of the weldability of a material in terms of the crack length per unit area. Other measurements that can be derived from the TCL measurement involve average total crack length (ATCL), the number of cracks, and maximum crack length (MCL).

2.9 Hot Corrosion

Superalloys, as the material of choice for the hot section of gas turbines, are continuously exposed to high temperatures and corrosive environments, especially in marine environments. The combination of elevated temperature and the presence of impurities in fuel such as S and vanadium (V) as well as atmospheric contaminants such as NaCl results in the formation of some low-temperature eutectic salts and deposition of these salts on the surfaces of gas turbine components [105]. Hence, the occurrence of hot corrosion which, unlike oxidation, can degrade the material at an unpredictably rapid rate and consequently leads to catastrophic failure due to the loss of the structural material [106]. According to the exposure temperature and mechanism, hot corrosion is divided into the two main categories of Type I or high-temperature hot corrosion (HTHC), and Type II or low-temperature hot corrosion (LTHC) [106].

Type I or HTHC mainly occurs over a temperature range of 800-950ºC. However, it has been reported that HTHC can also be observed at temperatures as low as 750ºC [107]. Initially, as superalloys are exposed to a corrosive environment, an oxide scale, including several oxide layers, is formed, followed by two stages of hot corrosion including the initiation and propagation stages. In the first stage (initiation), the alloy surface is exposed to the molten deposited salt due to the dissolution of the oxide scale by the molten salt or cracking of the oxide scale. Subsequently, the

propagation stage is initiated which is characterized by the severe attack of the Cr-depleted region through internal sulphidation/oxidation. As the propagation stage shows considerably higher corrosion rates than the initiation stage, it is reported that the turbine engine component must be removed from service at this stage [105]. Generally, the macroscopic appearance of HTHC is characterized by an internal sulphidation and a depletion region beneath the porous and nonprotective scales [106].

Several mechanisms have been reported to describe the process of HTHC. Salt fluxing is the most accepted mechanism for HTHC [107]. According to this mechanism, the protection capability of the oxide layer might be lost due to fluxing of this layer in molten salt. Fluxing in which the dissolution of the protective oxide layers occurs is divided into two types of basic and acidic fluxing. Basic fluxing involves the dissolution of the protective oxide layer by a highly basic melt (Na_2O rich) and the combination of oxides with O^{2-} to form anions. On the other hand, acidic fluxing consists of the dissolution of the protective oxide layer by a highly acidic melt (SO_3 rich) and the decomposition of oxides into the corresponding cations and O^{2-}. Acidic fluxing has been reported to have considerably severe oxidation compared to basic fluxing and occurs when the O^{2-} activity in the molten salt is significantly low. In general, the hot corrosion of superalloys with high contents of Al and Cr is often reported to occur according to the basic fluxing mechanism. On the contrary, hot corrosion of alloys with high contents of W, Mo, and V are often reported to follow the acidic fluxing mechanism [106].

The dominant salt in HTHC is sodium sulfate (Na_2SO_4) due to its high thermodynamic stability. The most significant source of Na is the marine atmosphere (sea salts contain NaCl), but can also be found in fuel. During the combustion process, Na_2SO_4 can form from the Na and S present in the fuel. Other impurities either in the fuel or air, such as V, P, lead (Pb), and chloride (Cl), can

combine with sodium sulfate to form a mixture of salts with a lower melting temperature. This results in broadening the temperature range of the attack and degradation of the structural components at lower temperatures. For example, the melting point of Na_2SO_4 (884ºC) can be lowered by the addition of NaCl. Na_2SO_4-NaCl eutectic is found to have a melting point of about 620ºC [106].

Type II or LTHC is observed mainly within the temperature range 600-750ºC which is substantially below the melting temperatures of alkali sulphate [106]. In LTHC, the nature of the attack is attributed to a localized failure of the scale due to a local chloride attack, thermal cycling, or erosion. For example, salt may be trapped locally in crevices produced by scale cracking. Such deposits could be retained and allow local changes in salt composition to occur. A common mechanism for the occurrence of LTHC is the formation of a low melting point eutectic Na_2SO_4-MSO_4 (where M is either Ni or Co) through the reaction between BM sulphates and alkali metal sulphates, followed by a molten eutectic formation which degrades the component. In LTHC, the propagation of attack occurs as a result of migration of SO_3 and Co or Ni inward and outward, respectively, through the liquid salt. Generally, the macroscopic appearance of LTHC is characterized by the formation of mixed oxide-sulphide scales and pitting attack with little or no internal sulphidation or alloy depletion [107].

As mentioned earlier in this thesis, Co-based superalloys are generally more resistant to hot corrosion compared to Ni-based superalloys mainly due to the following two reasons. First, it has been reported that the diffusivity of S in Co-based superalloys is approximately 100 times slower than that of Ni-based superalloys which results in much slower inward diffusion of S and internal sulphidation in Co-based superalloys compared to that of Ni-based superalloys. Second, during the hot corrosion of superalloys, low melting eutectic phases form that accelerate the hot corrosion

process. It has been reported that the melting temperature of Co-Co_4S_3 eutectic (877ºC) is considerably higher than that of Ni-Ni_3S_2 eutectic (645ºC) which leads to higher hot corrosion resistance in Co-based superalloys [108].

The hot corrosion resistance of superalloys is known to be affected by several factors including temperature, characteristics of the deposited salt, chemical composition of the superalloy, and primarily, the microstructure of the attacked material. Generally, the microstructure of the alloy is determined by the processing history such as casting, wrought, welding, and additive manufacturing. It has been reported that welding superalloys can reduce the resistance to hot corrosion due to chemical inhomogeneity [22][23]. Therefore, it is essential to study the effect of the welding process on the hot corrosion resistance of superalloys.

2.10 Scope and Objectives of the Present Study

As previously mentioned, due to the ever-increasing demand for improved gas turbine efficiency and reduction of greenhouse emissions, a new γ′ precipitation-hardened Co-based superalloy, CoWAlloy1, has been developed for high-temperature applications to replace conventional Ni-based superalloys. CoWAlloy1 has unique characteristics that surpass the performance of some of the conventional Ni-based superalloys. Welding superalloys is a necessary process in the manufacturing and repair of gas turbine parts. Similar to γ′-strengthened Ni-based superalloys [17][18][19][20] and γ′-strengthened Co-based superalloys [21], CoWAlloy1 is susceptible to weld cracking which mainly occurs in the HAZ. Although there have been several research works on the weldability of various Ni-based superalloys, weldability and the factors responsible for cracking in CoWAlloy1 during fusion welding have not been reported prior to the present study.

Therefore, improving the crack resistance during the welding and PWHT with minimal deterioration of the mechanical properties and hot corrosion resistance is vitally important in the industrial application of this new alloy. The present study is initiated with the three following major objectives.

1. To develop a numerical model of the GTAW to obtain a window of optimum welding parameters that prevent cracking in the FZ.

2. To conduct a systematic study on the primary factors that produce HAZ cracking in CoWAlloy1, which could contribute to the development of an effective approach to eliminate/minimize HAZ cracking during welding and after PWHT.

3. To evaluate the effect of pre-weld microstructural modifications on the mechanical properties and hot corrosion resistance of CoWAlloy1 after PWHT.

CHAPTER 3

Modeling and Experimental Methods

3.1 Introduction

In this chapter, the numerical modeling and experimental procedures performed to achieve the objectives are presented in two sections. The first section (Section 3.2) applies the developed numerical model to simulate the GTAW of CoWAlloy1 and to determine the optimum window of parameters that would eliminate typical weld defects and FZ cracking. The second section (Section 3.3) presents the materials and experimental procedures conducted in this research to achieve Objectives 2 and 3. In this section, the materials and experimental procedures performed to carry out GTAW, pre-weld heat treatment plan, and detailed microstructural characterization before and after welding, are presented. In addition, the experiments conducted to evaluate the effect of the pre-weld heat treatment and the welding process on the mechanical properties and the hot corrosion behavior of CoWAlloy1 are explained in this section.

3.2 Numerical Modeling Using ANSYS

3.2.1 Finite Element Model

A finite element (FE) software - ANSYS was used to model the GTAW of CoWAlloy1 and analyze the thermal cycle history in the FZ. A 3D FE transient thermal analysis was carried out through coding with an ANSYS program designed language (APDL). A non-linear transient temperature field in the thermal analysis due to the volumetric moving heat source was evaluated by solving a constitutive equation for heat conduction with applied boundary conditions. The welding input parameters used in the FE transient thermal model are provided in Table 3-1.

3.2.1.1 Model Meshing

During GTAW, the sample is exposed to a high heat input with a steep thermal gradient. To analyze the thermal behavior of the area that is affected, it is critical to maintain a finer mesh size. Sun et al. [109] reported that a reduced mesh size increases the accuracy of the calculations. However, this would also require a longer calculation time, which results in a large volume of processed data. In this work, the mesh size of the FZ is optimized to a value of 0.3 mm for greater accuracy and calculation efficiency. At the same time, the mesh size of the remaining parts is kept at 0.8 mm. Figure 3.1 shows the structural model for the simulation process. The FE model consists of 153,712 elements and 664,059 nodes and requires a simulation time of approximately 3 hrs. The model consists of quadratic brick elements with 20 nodes, a single degree of freedom, and the temperature of each node. A similar element has been used in previous works, which has shown a high level of accuracy for thermal analyses [110][111].

3.2.2 Model Description

3.2.2.1 Volumetric Moving Heat Source Model

The modeling of a moving heat source depends on the welding process, thermal field, and weld pool geometry [112]. For example, Bonifaz and Richards [68] used surface heat flux as a moving heat source to numerically model GTAW. However, Ghosh et al. [113] reported that using a volumetric moving heat source with a Gaussian distribution leads to enhanced model accuracy and, therefore, a more accurate prediction of the distribution of the transient temperature during GMAW.

Table 3-1 Welding parameters in FE modeling

Parameter	Weld 1	Weld 2	Weld 3
Voltage (V)	10	10	10
Current (A)	60	60	60
Velocity (mm/min)	50	70	100
Shielding gas flow rate (l/hr)	60	60	60

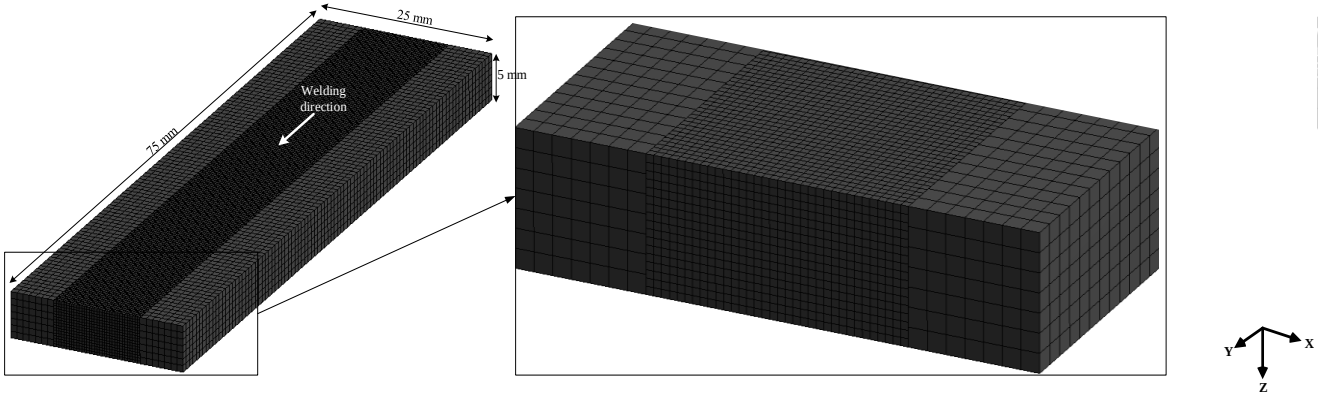

Figure 3.1 FE model of specimen geometry and meshing conditions

In this research, a conical-shaped volumetric moving heat source with a Gaussian heat density distribution radially and a linear distribution axially (Figure 3.2) is applied to characterize the shape and distribution of the heat density during GTAW. Figure 3.2 schematically illustrates the heat source model. The mathematical form of the volumetric moving heat flux (Q_v) is [111]:

$$Q_v(r,z,t) = Q_{\max}.\exp(-\frac{3r^2}{r_c^2}) \quad (3\text{-}1)$$

where Q_{max} represents the maximum volumetric heat density and r_c is the heat distribution parameter that shows the radius at height z, and *r* denotes the current radius, which is,

$$r = \left[(x - x_0)^2 + (y - y_0 - vt)^2\right]^{\frac{1}{2}} \quad (3\text{-}2)$$

where ν is the welding speed, (x, y) the Cartesian coordinate of each node at time t, and (x_0, y_0) is the origin of the Cartesian coordinate system. The heat distribution parameter, r_c, is calculated from Equation 3-3.

$$r_c = f(z) = r_i + (r_e - r_i)\frac{z - z_i}{z_e - z_i} \quad (3\text{-}3)$$

where r_i and r_e are the smaller and larger radius of the conical-shaped volumetric moving heat source, respectively. Similarly, z_i and z_e are the lower and upper z-coordinates of the conical-shaped, respectively. In Equations 3-4 and 3-5, the Q_{max} is obtained by integrating the conical-shaped volumetric heat flux, Q_v, over the conical-shaped region (Figure 3.2) and reordering it to the net heat input (Q_0).

$$Q_0 = \int_0^{Z_e - Z_i} \int_0^{2\pi} \int_0^{r_c} Q_{\max} . \exp(-\frac{3r^2}{r_c^2}) r dr d\theta dh \qquad (3\text{-}4)$$

$$Q_{\max} = \frac{9Q_0}{\pi(1-e^{-3})} \cdot \frac{1}{(z_e - z_i)(r_e^2 + r_e r_i + r_i^2)} \qquad (3\text{-}5)$$

where Q_0 is calculated by using $Q_0 = \eta VI$ in which I denotes the current, V represents the voltage, and η is the process efficiency which for this model, a heat transfer efficiency (η) of 80% is used.

3.2.2.2 Thermal Analysis

The thermal cycle history at each point of the (x,y,z) coordinates and time (t) was calculated numerically by solving the constitutive equation of heat conduction and law of conservation of energy [109]:

$$\left\{ \frac{\partial}{\partial_x}\left[k(T)\frac{\partial T}{\partial x}\right] + \frac{\partial}{\partial_y}\left[k(T)\frac{\partial T}{\partial y}\right] + \frac{\partial}{\partial_z}\left[k(T)\frac{\partial T}{\partial z}\right] \right\} + Q_v(r,z,t) = \rho(T) C_p(T) \frac{\partial T}{\partial t} \qquad (3\text{-}6)$$

where $K(T)$, $\rho(T)$, and $C_p(T)$ are the temperature-dependent thermal conductivity, density, and specific heat, respectively, simulated by using JMatPro.

The modeling of a volumetric moving heat source was performed by using APDL coding in the ANSYS workbench environment. APDL coding evaluates the temperature at each node for time and conical-shaped heat flux. The volumetric moving heat source model was calibrated by adjusting the heat source parameters (listed in Section 3.2.2.1) to match the weld pool geometry acquired from the GTAW experiment and the numerical modeling result.

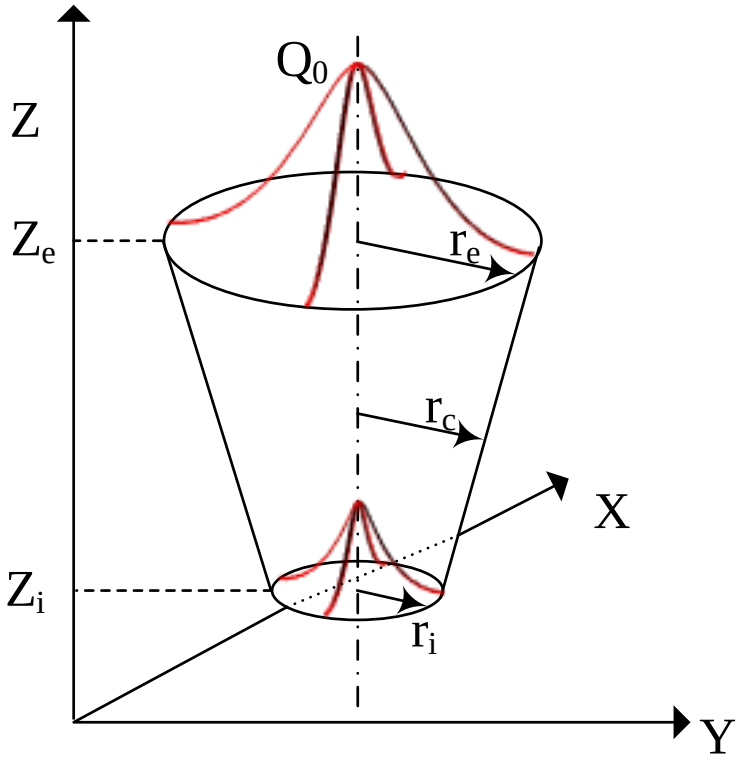

Figure 3.2 Schematic of conical-shaped model of volumetric moving heat source

3.2.2.3 Initial and Boundary Conditions

During GTAW, some of the energy is lost owing to convection and radiation heat loss. To accurately model this process in ANSYS, several initial and boundary conditions have been considered. Bonifaz and Richards [68] reported two types of convection heat loss of free and forced convections that occur during GTAW. The convection (q_{conv}) and radiation (q_{rad}) heat losses are calculated by using Equations 3-7 and 3-8, respectively, as the boundary conditions.

$$q_{conv} = h_c(T - T_\infty) \tag{3-7}$$

$$q_{rad} = \sigma\varepsilon\left[(T - T_{abs})^4 - (T_\infty - T_{abs})^4\right] \tag{3-8}$$

where h_c is the convection coefficient (free or forced), T_∞ is the ambient temperature set at 20ºC, T_{abs} is the absolute zero temperature, ε is the emissivity, which is assumed to be constant and similar to that of other superalloys (0.7) [68], and σ denotes the Stefan-Boltzmann constant (5.67×10^{-8} W.m^{-2}. K^{-4}). During GTAW, the area below the nozzle experiences forced convection owing to the shielding gas flow rate. The forced convection, according to the model in Bonifaz and Richards [68], is assumed to be constant with a value of 242 W.m^{-2}.K^{-1}. The convective coefficient for the other areas is considered to be a free convection value of 10 W m^{-2} K^{-1}.

3.2.2.4 Thermal Analysis Evaluation

The cooling rate, G, and R at various regions of the FZ can be evaluated by using a thermal numerical model. It has been well established that the SDAS, as well as the grain microstructure

of the FZ, can be evaluated by studying the cooling rate in the different areas of the FZ [74]. The following equation is used to calculate the SDAS [68]:

$$\lambda_2 = a(G \times R)^b \quad (3\text{-}9)$$

where λ_2 represents the SDAS, a and b are constants and controlled by the alloy structure, and $G \times R$ is the cooling rate. The values of a = 50 and b = 0.3 μm were adapted [68] to evaluate the SDAS from the calculated cooling rate.

The FZ microstructure can be predicted by evaluating the ratio of the G to the R (G/R). The R, which is related to the shape of the weld pool [114], can be determined by using the following equation:

$$R = v.cos\theta \quad (3\text{-}10)$$

where v is the welding speed, and θ represents the angle between the normal vector of the liquid-solid interface and the welding direction (Figure 3.3). θ at each node around the weld pool is evaluated based on the weld pool geometries acquired from the numerical modeling. Therefore, G can be calculated by using the predicted cooling rate (G×R) and Equation 3-10.

In this work, the CET criteria developed by Gäumann et al. [115] are used to predict the type of grain structure of the FZ. Bonifaz and Richards [68] reported that this method can be applied to study the CET quantitatively during GTAW. According to this model, a fully equiaxed structure can be achieved when the G^n/R ratio is smaller than the critical value of $K = 2.7 \times 10^{24}$ ($K^{3.4}/m^{4.4}s$). The constant n depends on the alloy [115] and is considered to be 3.4.

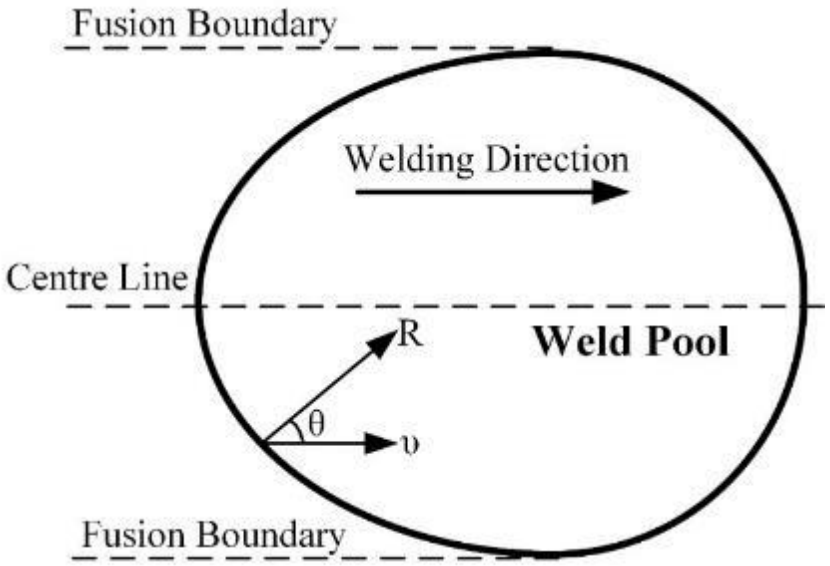

Figure 3.3 Schematic of the relationship between welding speed υ and R.

3.3 Materials and Experimental Procedures

3.3.1 Materials Preparation

Cast polycrystalline CoWAlloy1 was received in a form of a plate with dimensions of 304×75×25.4 mm from Sophisticated Alloys Inc. (Butler, USA). The alloy was manufactured through a vacuum induction melting process and subsequently subjected to hot isostatic pressing (HIP) at 1200ºC for 4 hrs at a pressure of 15 ksi. The chemical composition (wt. %) of the CoWAlloy1 is as follows: 30.6% Ni, 10.2% Cr, 9.0% W, 4.4% Ta, 2.6% Al, 2.0% Ti, 0.3% Hf, 0.2% Si, 0.02% C, 0.02% Zr, 0.01% B, and balance Co. The welding coupons with dimensions of 75×20×5 mm were machined by using an electrical discharge machine (EDM). Subsequently, the welding coupons were subjected to pre-weld heat treatments; see Table 3-2 for the details. For example, 870°C AC denotes that the sample was heat treated at 870°C for 4 hrs and then AC. These heat treatments were performed to help with the investigation of various aspects of microstructural variables known to characteristically affect the susceptibility of superalloys to weld cracking. Prior to GTAW, the heat-treated welding test coupons were surface grinded and polished to remove the surface oxide followed by solvent cleaning in an ultrasonic bath.

3.3.2 Gas Tungsten Arc Welding

The pre-weld heat-treated coupons were welded by using autogenous BOP GTAW along with a 6 DOF Panasonic VR-004 robot (Figure 3.3) with the welding parameters provided in Table 3-3. Subsequently, 10 weld cross-sections were cut from each welded coupon by using the EDM and the samples were grinded and polished with standard metallographic techniques.

Table 3-2 Pre-weld heat treatments

Code	Heat Treatment Condition
870°C AC	870°C, 4 hrs./ AC
870°C WQ	870°C, 4 hrs./ WQ
970°C AC	970°C, 4 hrs./ AC
970°C WQ	970°C, 4 hrs./ WQ
1010°C AC	1010°C, 4 hrs./ AC
1010°C WQ	1010°C, 4 hrs./ WQ
1070°C AC	1070°C, 4 hrs./ AC
1070°C WQ	1070°C, 4 hrs./ WQ
1170°C AC	1170°C, 4 hrs./ AC
1170°C WQ	1170°C, 4 hrs./ WQ

Note: AC = air-cooled, WQ = water-quenched

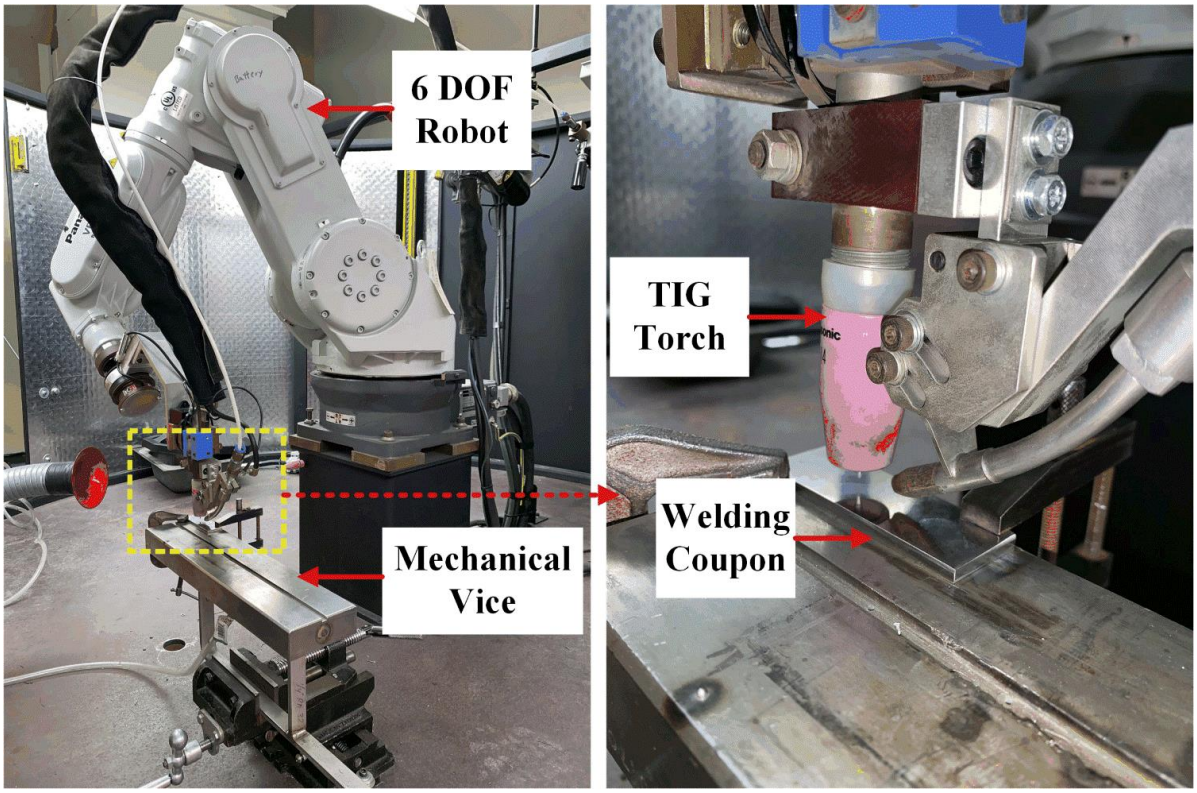

Figure 3.4 TIG welder fitted with 6 DOF PANASONIC VR-004 robot

Table 3-3 GTAW parameters

Parameter	
Current (A)	60
Voltage (V)	10
Speed (mm/min)	50
Shielding gas flow rate (l/hr)	60

3.3.3 Hardness Measurement

The hardness of the various samples in the as-received, pre-weld heat-treated, welded, and PWHTed conditions, and DSC samples were measured by using a Buehler Vickers microhardness tester with an indenter size of 36.5 μm and an applied load of 500 gf. Ten measurements were made on each specimen with 0.01 mm spacing to average the hardness values along with the standard deviation.

3.3.4 Metallographic Sample Preparation

To study the microstructure of the as-received, pre-weld heat-treated, welded, and PWHTed conditions and DSC samples, they were first hot-mounted by using Bakelite. Subsequently, the mounted specimens were grinded with 600 and 1200 SiC papers followed by polishing with 6 μm and 1 μm diamond suspension, respectively. To examine the optical microstructure, the polished samples were chemically etched with 10 g of copper sulfate + 50 ml of distilled water + 50 ml of hydrochloric acid solution. Furthermore, the polished samples were electrochemically etched in 80 ml of nitric acid + 96 ml of sulphuric acid + 24 ml of phosphoric acid solution at 5 V for 3 seconds to study the details of their microstructure through SEM and EPMA.

3.3.5 Optical and Scanning Electron Microscopies

The preliminary microstructural study was performed on the chemically etched specimens by using a Zeiss Axiovert 25 inverted phase contrast microscope, equipped with CLEMEX Vision 3.0 image analysis software. Furthermore, a detailed microstructural analysis and spectroscopy

were conducted by using a JEOL 5900 scanning electron microscope equipped with an Oxford (Oxford Instruments, Oxford, United Kingdom) ultra-thin window energy dispersive spectrometer (EDS). The cracking susceptibility of the HAZ was evaluated by measuring the average of the TCL in 10 cross-sections of each welded coupon with the optical and scanning electron microscopes. In addition, the average grain size of the alloy in the as-received and heat-treated conditions was measured by using optical micrographs and the linear intercept method.

3.3.6 Electron Microprobe Analysis

The composition of the dendrite core regions within the FZ was quantitatively determined by using a CAMECA SX100 electron microprobe analyzer (EPMA) equipped with ϕ (p,z) correction algorithm and operated at 15 keV with a beam current of ≤ 20 nA. The EPMA is capable of quantitatively determining the composition of particles as small as 1 μm in diameter with adequate accuracy.

3.3.7 Transmission Electron Microscopy

A TEM analysis was carried out on as-received, SHTed, and welded specimens by using an FEI Talos F200X transmission electron microscope with a field emission electron source (X-FEG) equipped with an Oxford energy dispersive spectrometer. The TEM samples were produced by electro-polishing foils that are 3 mm in diameter with a thickness of 120 μm with 100 ml perchloric acid + 900 ml methanol solution at -30ºC and 1 V. The electropolishing involves the preparation of very thin foil with perforation suitable for TEM examination and analysis. A selected area diffraction pattern (SADP) analysis was used to identify the crystal structure of the various phases

found in the areas of interest on the thin foil. The lattice parameters of the phases were accordingly determined from reflections obtained from the SADPs.

3.3.8 Secondary Ion Mass Spectroscopy

Elemental grain boundary segregation was evaluated using time-of-flight secondary ion mass spectrometry (ToF-SIMS). In this method, the surface of the sample is bombarded with a primary ion beam which leads to the emission of secondary ions from the surface. The mass of sputtering atomic species can be analyzed by using a mass spectrometer to determine the elemental, molecular, or isotopic composition of the surface. Due to a spatial resolution of 150 nm and an elemental resolution of a few ppm, SIMS is capable of detecting trace amounts of elements on a surface. The primary ion beam species used in SIMS include Cs^+, O_2^+, O^-, Ar^+, $Ga^{+,}$ and Xe+ [116].

The SIMS samples were cut by using the EDM into dimensions of 10×10×3 mm, followed by mounting in Bakelite. Subsequently, they were polished to 1 μm and marked with the nano-indenter to identify the grain boundary location. The specimens were then carefully removed from the Bakelite, followed by solvent cleaning in an ultrasonic bath. The specimens were sent to the Chemical Imaging Infrastructure of the Chalmers University of Technology, and the University of Gothenburg for conducting the ToF-SIMS analysis with ToF-SIMS (IONTOF V) and primary ion beam of Cs^+. SIMS line scans of B were performed by imaging positive secondary ions of B^+.

3.3.9 Differential Scanning Calorimetry

DSC was used to evaluate the main equilibrium phase transformation temperatures and study the γ′ precipitation behavior in CoWAlloy1. DSC is based on the principle of measuring heat flow variations with respect to phase transformation at specific heating or cooling rates. A DSC 404 C (Netzsch) equipped with a TASC 414/4 controller (Netzsch) with a maximum operating temperature of 1500ºC was used. The system can accommodate a maximum heating and cooling rate of 40ºC/min. The DSC setup was coupled with purging and vacuum systems. To avoid the oxidation of the specimens, N_2 gas was used as the purging gas at a flow rate of 50 ml/min. The specimens (1.5×1.5×1.5 mm) were sectioned by using EDM, followed by grinding with 600 grit SiC paper to remove the oxide layer on the surface, and further degreased with acetone. Since DSC is a measure of heat flow per unit mass, all of the specimens were weighed before testing by using a highly sensitive electronic balance with a resolution of ±0.0001 g. Prior to the testing, the DSC equipment was calibrated by scanning two symmetric empty crucibles to obtain the baseline. The crucibles were first heated to 1200ºC and then cooled to 25ºC at a given cooling rate. In addition, to determine the sensitivity of the equipment at each cooling rate of interest, the baseline and specimen measurements were carried out by using standard specimens, including pure Ni, gold (Au), Al, bismuth (Bi), and indium (In). DSC studies were performed at four different cooling rates: 2.5, 10, 15, and 40ºC/min. The specimens were first heated to 1200ºC and then cooled to 25ºC at the same rate. After calibration, thermographs for the material of interest were taken by using the same procedure as explained above for calibration purposes.

The temperature and time-dependent enthalpy were used to study the precipitation behavior with DSC. The fraction of the phase transformation *F(T)*, which is precipitated at a given temperature, is determined by using [47]:

$$F(T) = \frac{A(T)}{A(T_f)} \tag{3-11}$$

where *A(T)* is the area of the peak, which is the area between the onset temperature T_i (beginning of precipitation) and a temperature T (any temperature on the signal), and $A(T_f)$ is the area under the peak between T_i and the end temperature T_f (end of precipitation). In the DSC analysis, the precipitation rate, *dF/dt*, is correlated to the cooling rate, β, by [47]:

$$\frac{dF}{dt} = \frac{dF}{dT} \times \beta \tag{3-12}$$

To determine the activation energy (Q) required for the γ′ precipitation, the Kissinger equation is used [47]:

$$Q = -\frac{\ln\left(\frac{T_F{}^2}{\beta}\right)}{\left(\frac{1}{RT_F}\right)} \tag{3-13}$$

where T_F is the temperature at which the maximum precipitation rate (*dF/dt*) occurs and R is the gas constant, $J \cdot K^{-1} \cdot mol^{-1}$.

3.3.10 Tensile Test

The mechanical properties of the welded CoWAlloy1 subjected to the recommended SHT as the PWHT were evaluated by using a uniaxial tensile test. Sub-size tensile samples with the weld positioned in the middle of the gauge section were machined by using a water jet machine (Figure 3.5) in accordance with ASTM-E8 standard [117]. The samples were then polished to achieve smooth, notch-free surfaces and remove any surface oxide. The tensile properties were acquired by using an MTS Landmark servo-hydraulic universal test system that has a maximum load-bearing capacity of 100 KN at room temperature at a strain rate of 0.03 s^{-1}. To ensure repeatability and accuracy, three tests were conducted for each heat treatment condition and the average of the three tests was calculated and used for the analysis reported in this study.

3.3.11 Hot Corrosion Experiment

The specimens for the hot corrosion test were cut into dimensions of 10×5×2 mm with the EDM from the welded CoWAlloy1 subjected to the recommended SHT. Figure 3.6 shows the profile of the hot corrosion specimen in the welded condition, which includes a BM, HAZ, and FZ. The hot corrosion specimens were first polished with SiC paper to 600 grit and then ultrasonically cleaned with acetone for 15 min. Approximately 3.0 ± 0.1 mg of a salt mixture of 75 wt. % Na_2SO_4 + 25 wt. % NaCl was deposited on each of the test specimens. This salt mixture has been used in previous studies on the hot corrosion resistance of γ′-strengthened Co-based superalloys [118][119] [120]. A saturated solution was produced by dissolving Na_2SO_4 and NaCl in distilled water at a ratio of 75:25, respectively, to prepare a low melting eutectic of Na_2SO_4-NaCl with eutectic melting temperatures of 630°C [121]. The hot corrosion specimens were heated to 150°C

by using a hot plate while simultaneously spraying the salt mixture on the surface with a spray gun. During the salt deposition, the specimens were weighed frequently to ensure that the proper quantity of salt was deposited. The coated specimens were individually placed in alumina crucibles and subjected to 750°C for 100 hrs. The hot corrosion experiment was repeated three times to ensure the reliability of the results. To evaluate the weight change, the weight of the salt-coated specimen was measured before and after the hot corrosion experiment by using a Sartorius Entris 64-1S scale balance with an accuracy of 0.1 mg. To take the mass change into account precisely, all of the crucibles that contained specimens and spalled scales were weighed.

To evaluate the detailed characteristics of the corroded specimens, an SEM microstructural analysis was used. In addition, to study the type of oxide layers and corrosion products formed on the surface of the corroded specimens, an X-ray diffraction (XRD) analysis was conducted using a Bruker D8 advance XRD instrument collected from 18 to 80° 2θ at a 0.02° step size and step time of 5 s.

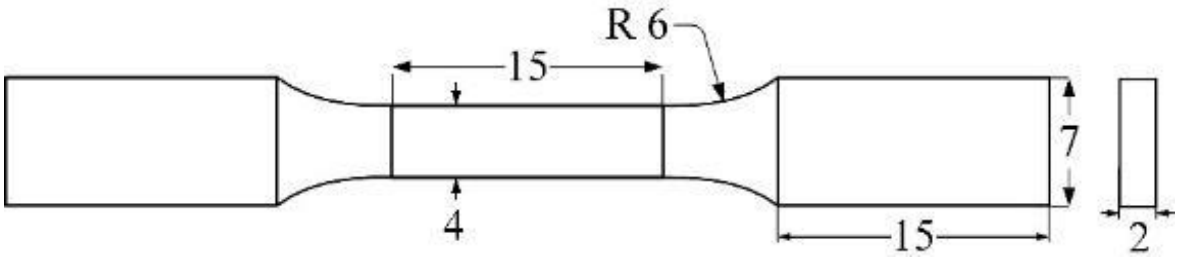

Figure 3.5 Sub-size tensile sample dimensions (mm)

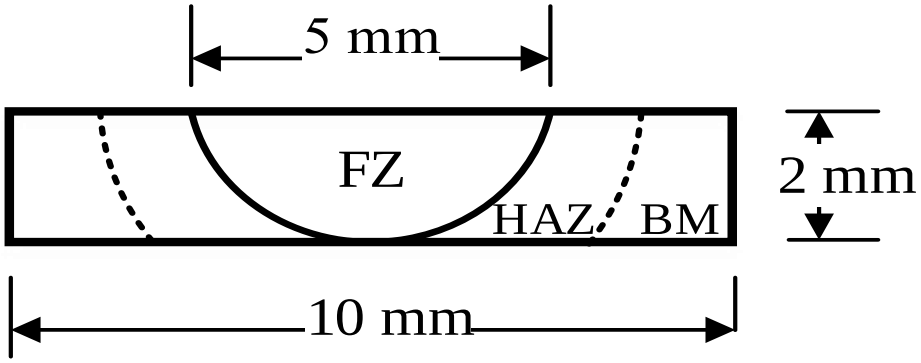

Figure 3.6 Specimen dimensions used for hot corrosion test

CHAPTER 4

Results and Discussion

4.1 Introduction

In this chapter, the details of the results and discussion of the study performed on the arc weldability of CoWAlloy1 are presented. First, the results of the developed numerical model for the GTAW which results in obtaining a window of optimum welding parameters are discussed; see Section 4.2. As the pre-weld microstructure significantly affects the superalloy behavior during the welding process, the results of the microstructural characterization of CoWAlloy1 before welding are subsequently provided in Sections 4.3 and 4.4. This is followed by a detailed study of the FZ and HAZ microstructures and an investigation of the primary causes of HAZ cracking in Section 4.5. The development of a solution to eliminate/minimize the HAZ cracking problem during welding and after PWHT is presented in Sections 4.6 and 4.7. The γ' re-precipitation behavior which significantly influences HAZ cracking in CoWAlloy1 is discussed in Sections 4.8 and 4.9. The effect of the pre-weld heat treatment procedure and welding process on the tensile properties and hot corrosion resistance of CoWAlloy1 is discussed in Section 4.10. Finally, the effect of overaging on the cracking susceptibility of HAZ during welding and PWHT is discussed in Section 4.11.

4.2 Numerical Modeling of GTAW

4.2.1 Physical Properties of CoWAlloy1

To model the GTAW of CoWAlloy1, some physical properties need to be initially evaluated. The temperature-dependent thermo-physical properties of CoWAlloy1, such as density (ρ), thermal

conductivity (k), and specific heat (C_p), were evaluated over a temperature range of 0°C to 1400°C by using a thermodynamics simulation software called JMatPro. The properties are shown in Figure 4.1 and subsequently used to develop the FE transient thermal model.

4.2.2 Differential Scanning Calorimetry Analysis

To obtain the main phase transformation temperatures and evaluate the solidification range in CoWAlloy1, a DSC analysis was performed in which the specimens were heated to 1400ºC at the rate of 2.5ºC/min. As presented in Figure 4.2, the following transformation temperatures are obtained: liquidus temperature, T_L=1384°C, solidus temperature, T_S=1306°C, and γ′ solvus temperature, $T_{\gamma'}$ =1072°C, which are in good agreement with previous studies on CoWAlloy1 [10][11]. The T_S and T_L temperatures in Figure 4.2 are used to calculate the solidification temperature of the alloy. Furthermore, the DSC results show an exothermic peak at a temperature of 1203°C (Figure 4.2) which could be related to the γ-γ′ eutectic temperature ($T_{(\gamma-\gamma')_e}$=1203°C).

4.2.3 Heat Source Verification

To validate the model, a comparison was carried out between the experimental and simulation results of the weld pool geometry. Here, the volumetric moving heat source parameters (listed in Section 3.2.2) were adjusted to obtain a similar geometry as that of an actual molten pool. The r_e, r_i, and z_e-z_i were calculated to be 2.41, 1.23, and 1.13 mm, respectively. Figure 4.3 shows that there is a good agreement between the experimental and modeled results of the weld pool geometry. Furthermore, the modeled mushy region and fusion boundary are similar to those of the actual experiment. The optical microscope image shows that a mushy region is formed at the solid-liquid interface (1306ºC-1384ºC) which has a coarse dendritic structure. Bonifaz and Richards [68] reported similar observations during the GTAW of IN738.

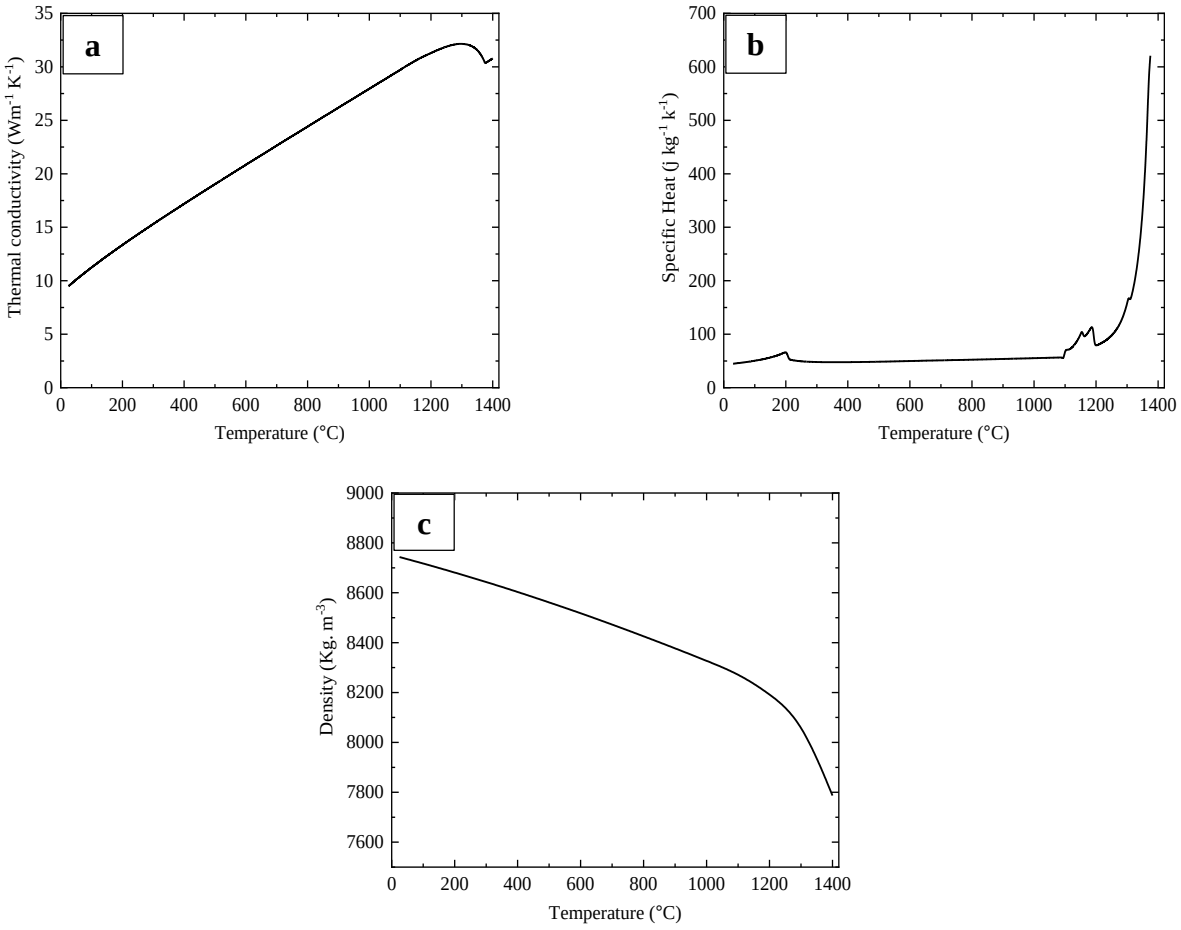

Figure 4.1. JMatPro predicted temperature dependence properties of CoWAlloy1: a. Thermal conductivity, b. Specific heat, and c. Density

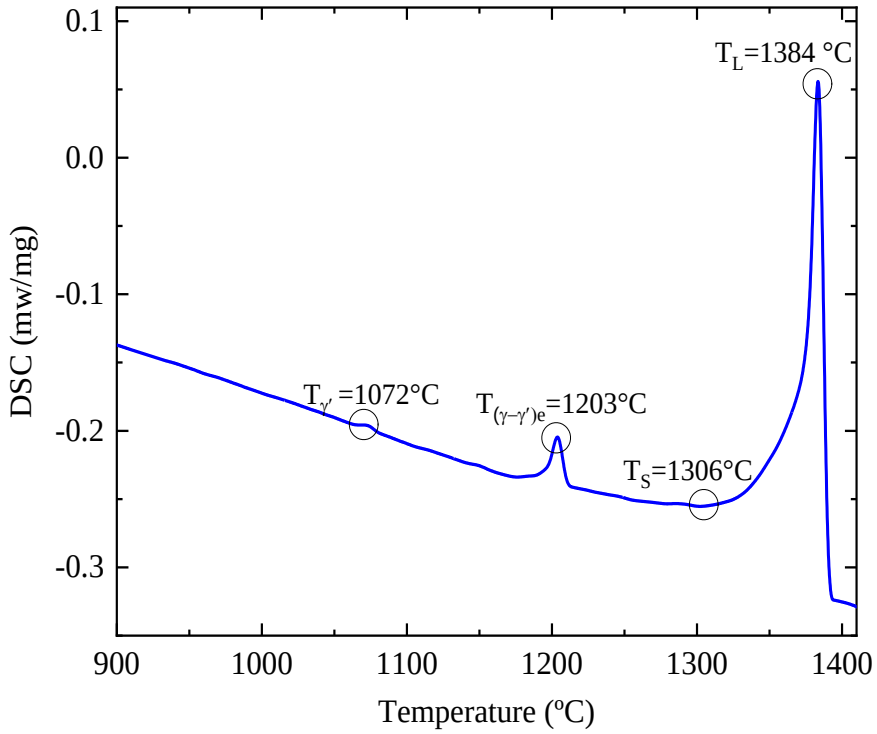

Figure 4.2 DSC curve for CoWAlloy1 at a heating rate of 2.5°C/min.

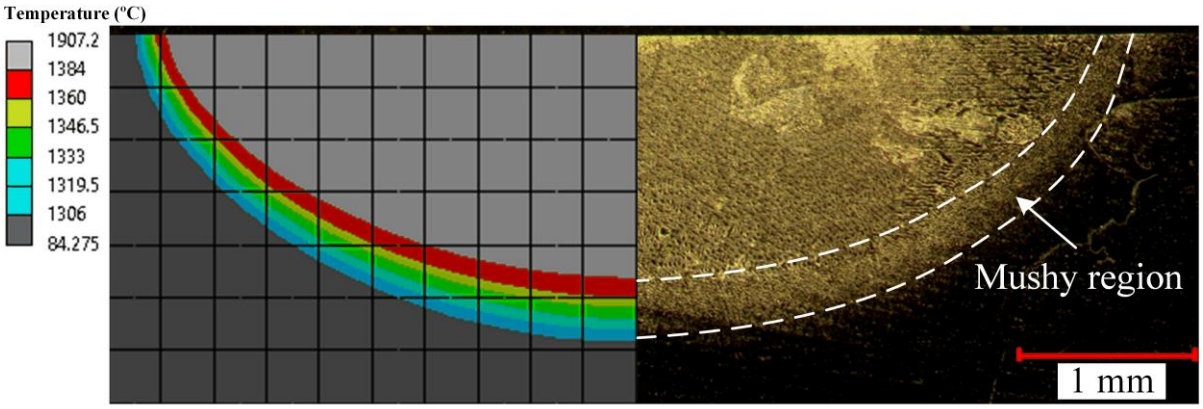

Figure 4.3 Comparison between experimental and modeled results of molten pool geometry

4.2.4 Thermal Model Output

Figure 4.4 shows the results of the numerical model simulation, including the weld pool geometry and G at the weld pool/fusion boundary interface. The thermal cycle history was evaluated at three different fusion boundary points (red/white color interface region), which are labeled as A, B, and C in Figure 4.4. The molten pool profile and thermal cycle at three different points, including along the centerline of the molten pool, depth of the penetration, and fusion boundary for three different welding speeds, are shown in Figure 4.5. It can be observed in the figure that at a constant arc power, the molten pool geometry increases in depth of penetration and width and becomes more elliptical in shape as the welding speed is reduced from 100 mm/min to 50 mm/min. Similarly, Liu and Zhang [122] reported that at a constant GTAW arc voltage, the molten pool width and length increase as the welding speed is reduced, which is attributed to an increase in total heat input. Furthermore, Sudhakaran et al. [123] showed that at a constant GTAW arc voltage, reducing the welding speed leads to an increase in depth of penetration, which is due to an increase in the total heat input. This phenomenon accounts for the change in heat input as a result of the various welding speeds. Furthermore, Figure 4.5 also shows that an increase in the welding speed leads to a reduction in the peak temperature at the centerline of the molten pool, which is also attributed to low heat input. Moosavy et al. [124] stated that the mushy area is one of the factors that can be examined to determine the susceptibility of a weld to hot cracking during GTAW. They also reported that there is a direct relationship between the mushy zone thickness and hot cracking, in which an increased thickness of the mushy zone results in increased hot cracking [124]. In this study, a decrease in the welding speed increases the mushy zone thickness, which then increases the susceptibility of the weld to cracking. Coniglio and Cross [125] reported that increasing the welding speed reduces the mushy zone thickness, which consequently inhibits the formation of hot cracks.

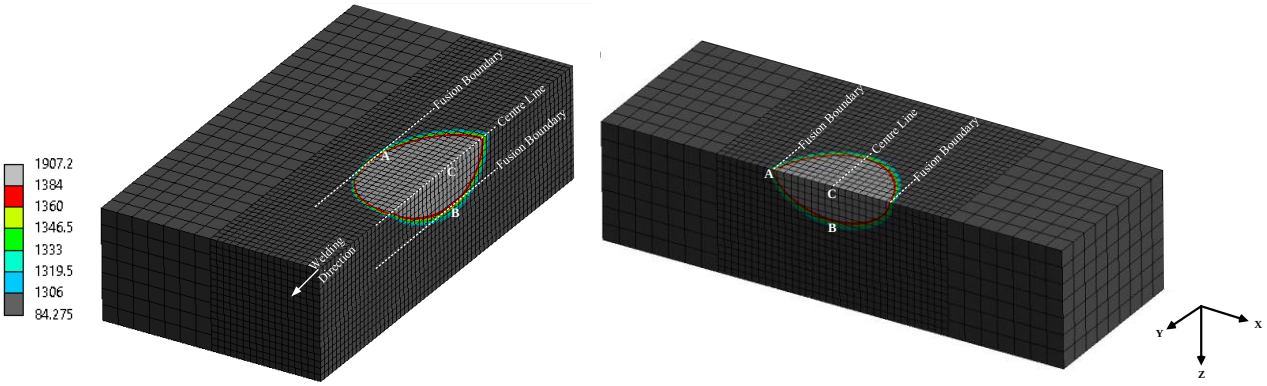

Figure 4.4 Molten pool boundaries and solidification temperature range for Weld 1

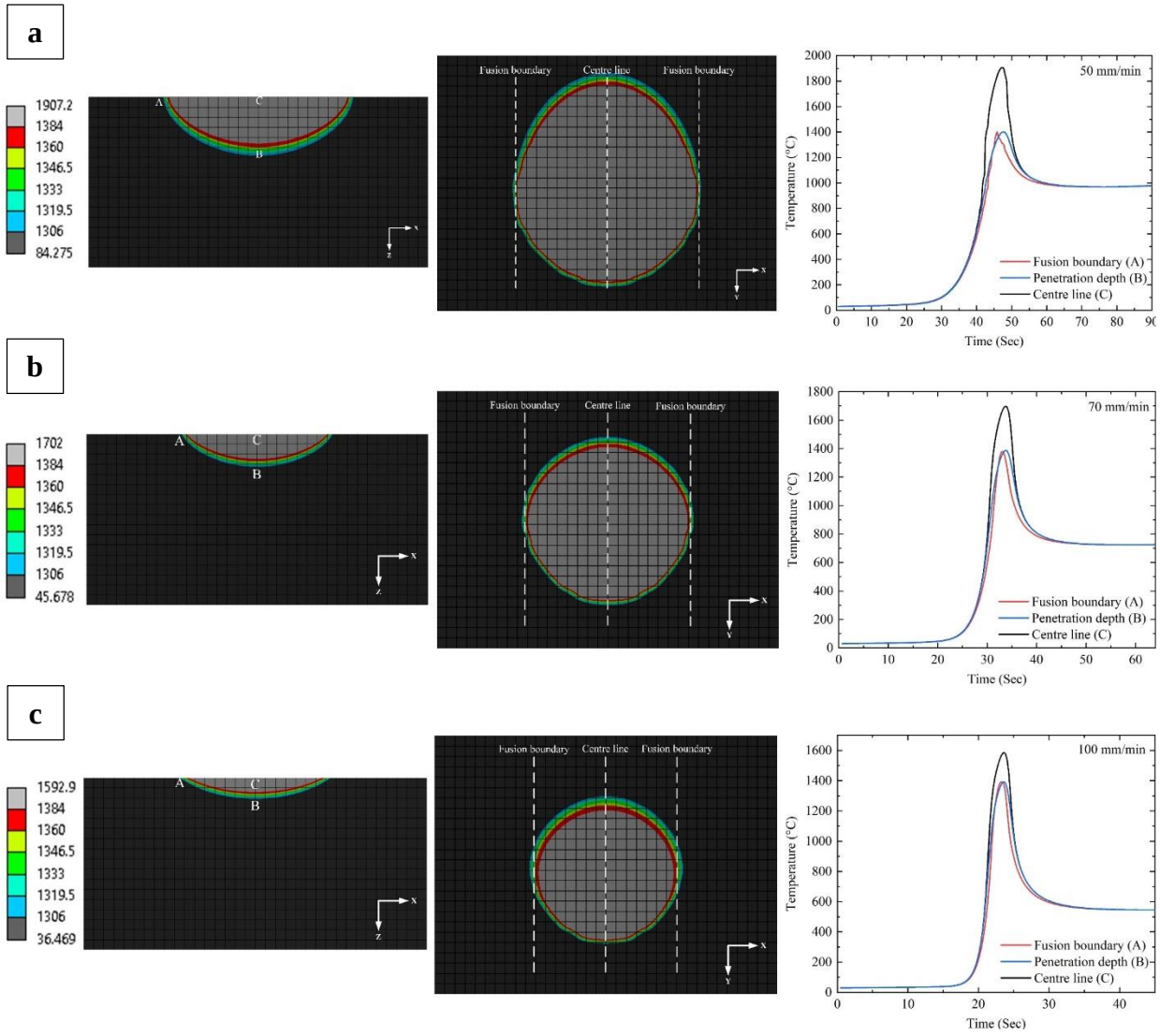

Figure 4.5 Thermal cycle and molten pool geometry at different welding speeds: a. 50 mm/min, b. 70 mm/min, and c. 100 mm/min

Figure. 4.6 shows the thermal history from the centerline to the fusion boundary at different points around the molten pool. The figure clearly shows that the peak temperature at the centerline of the molten pool is the highest and gradually reduces with distance to the fusion boundary. This trend is more obvious at lower welding speeds.

Figure. 4.7 shows the cooling rate variations in the molten pool for different welding speeds. The cooling rate is gradually reduced from the centerline to the fusion boundary. Furthermore, increasing the welding speed, which reduces the heat input, significantly accelerates the cooling rate in the molten pool. Li et al. [126] support these findings. The cooling rate variations at Points A, B, and C at various welding speeds are shown in Figure. 4.8. It can be seen that increasing the welding speed results in an increase in the cooling rate at Points A, B, and C. However, this increase is more significant at Point C.

Many studies [76][127] have reported a relationship between cooling rate and dendrite arm spacing. For example, Geng et al. [15] found that the SDAS decreases with an increase in the cooling rate in the FZ. In this study, the SDAS is determined by using Equation 3-9, and the result is shown in Figure 4.9. It can be observed in the figure that the SDAS is increased from the centerline to the fusion boundary, which is attributable to a reduction in the cooling rate. Furthermore, increasing the welding speed results in the formation of a finer dendritic structure. Figure 4.9 also suggests that the variation in SDAS is more significant at lower welding speeds than at higher welding speeds. Figure 4.10 shows the SDAS at Points A, B, and C. It can be observed that the SDAS at Point C is the smallest compared to Points A and B, which is attributed to the higher cooling rate at Point C.

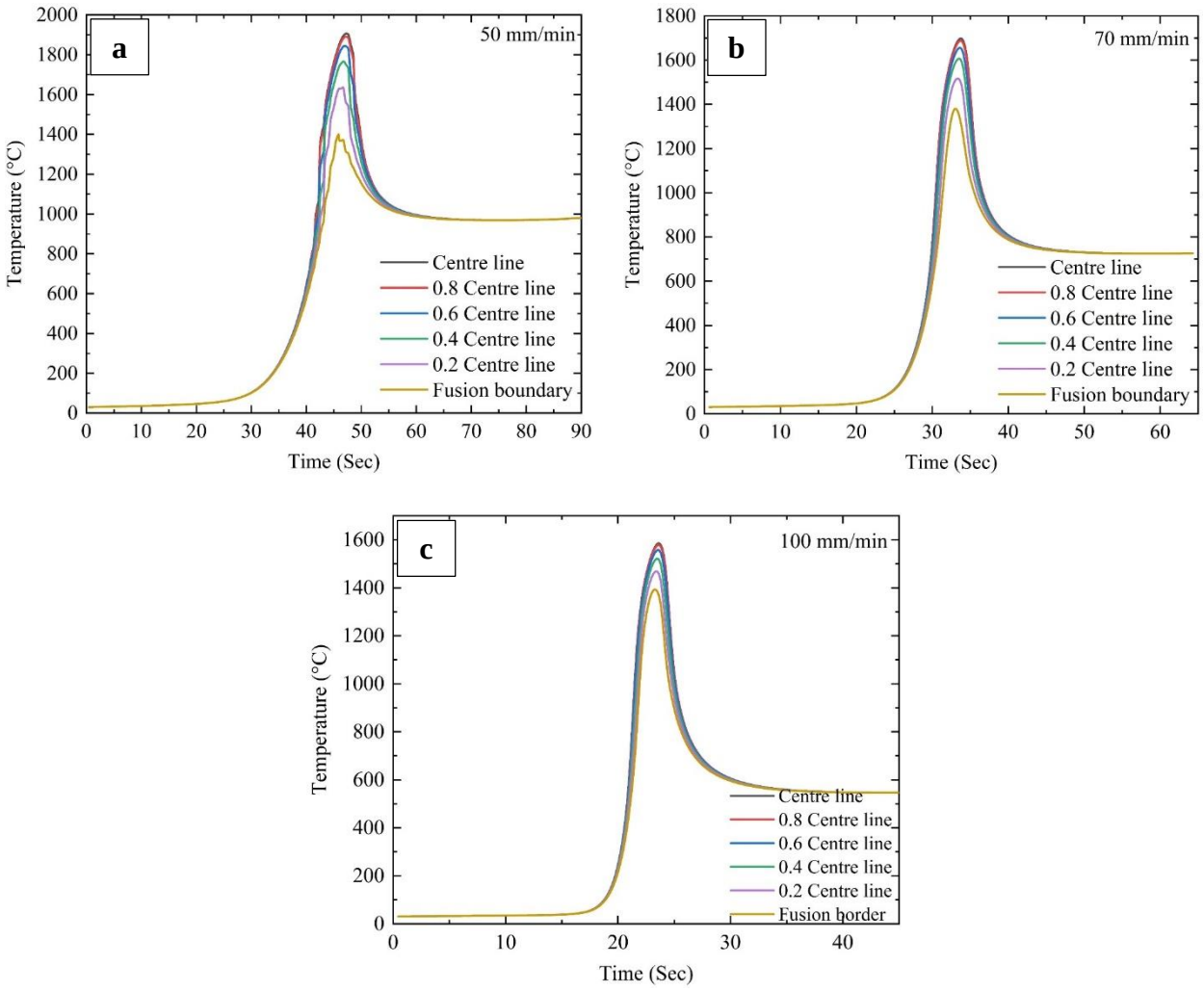

Figure 4.6 Thermal cycle history from centerline to fusion boundary at various welding speeds: a. 50 mm/min, b. 70 mm/min, and c. 100 mm/min

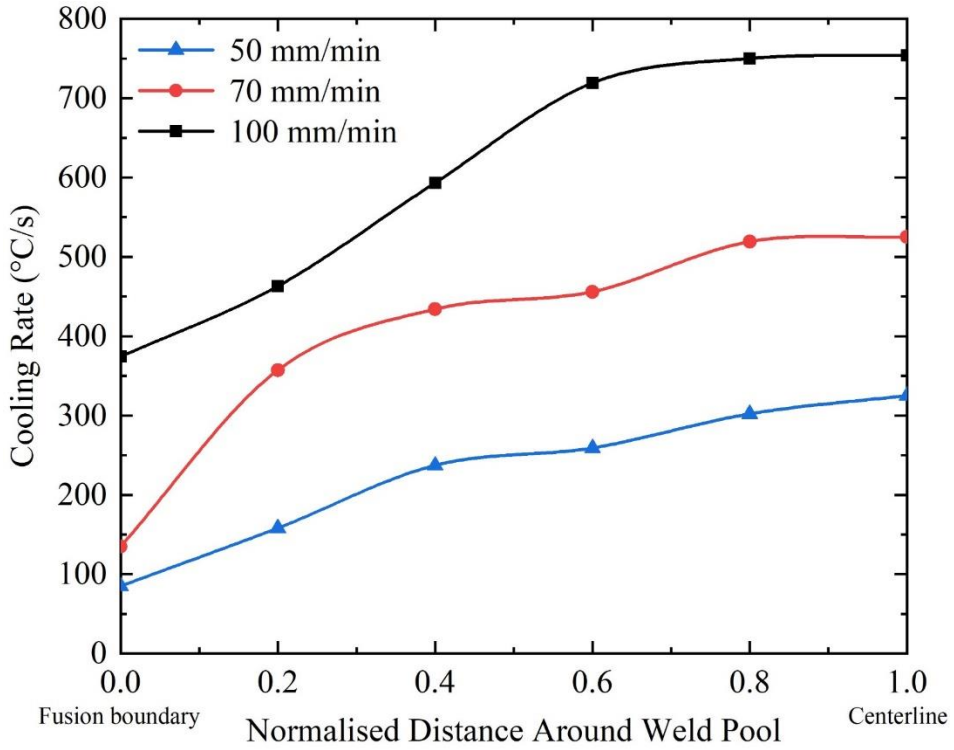

Figure 4.7 Predicted cooling rates as a function of normalized distance around the weld pool at various welding speeds

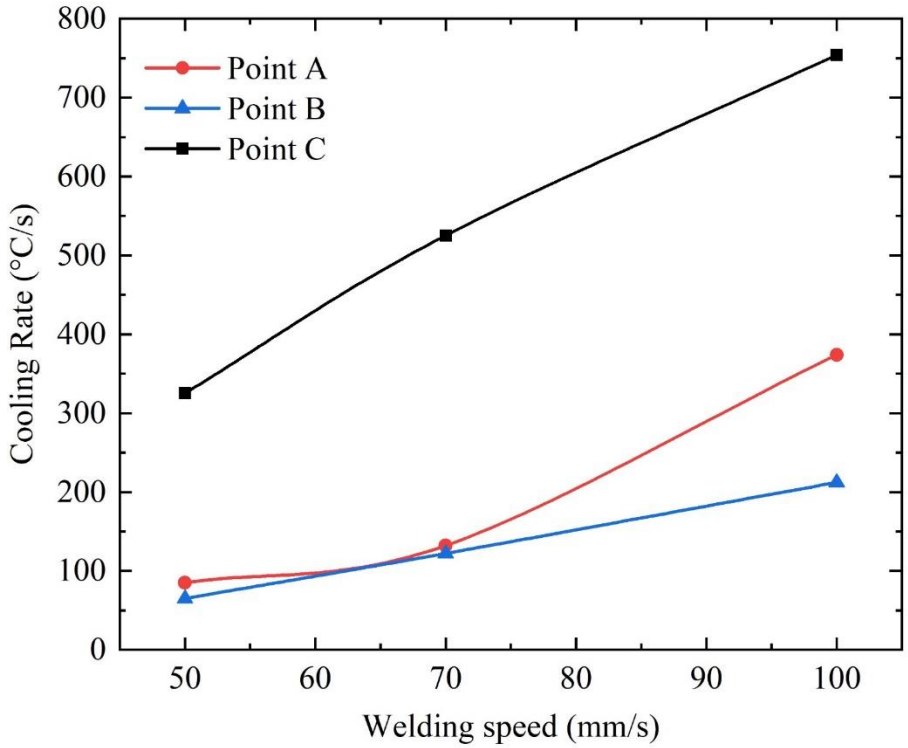

Figure 4.8 Predicted cooling rates as a function of welding speed at Points A, B, and C

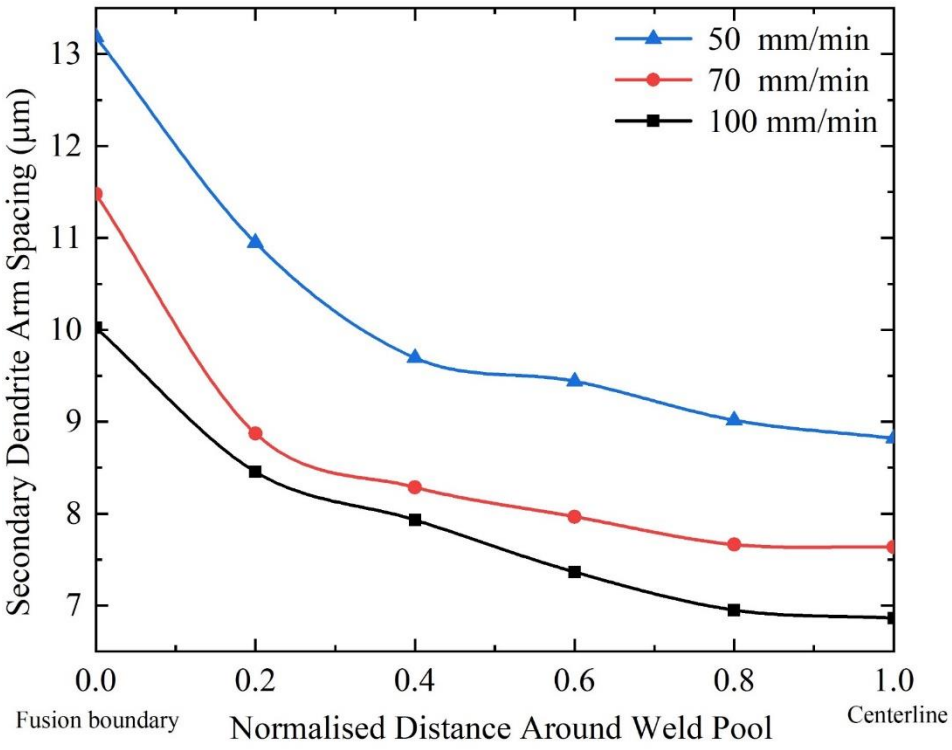

Figure 4.9 Predicted SDAS as a function of normalized distance around the weld pool at various welding speeds

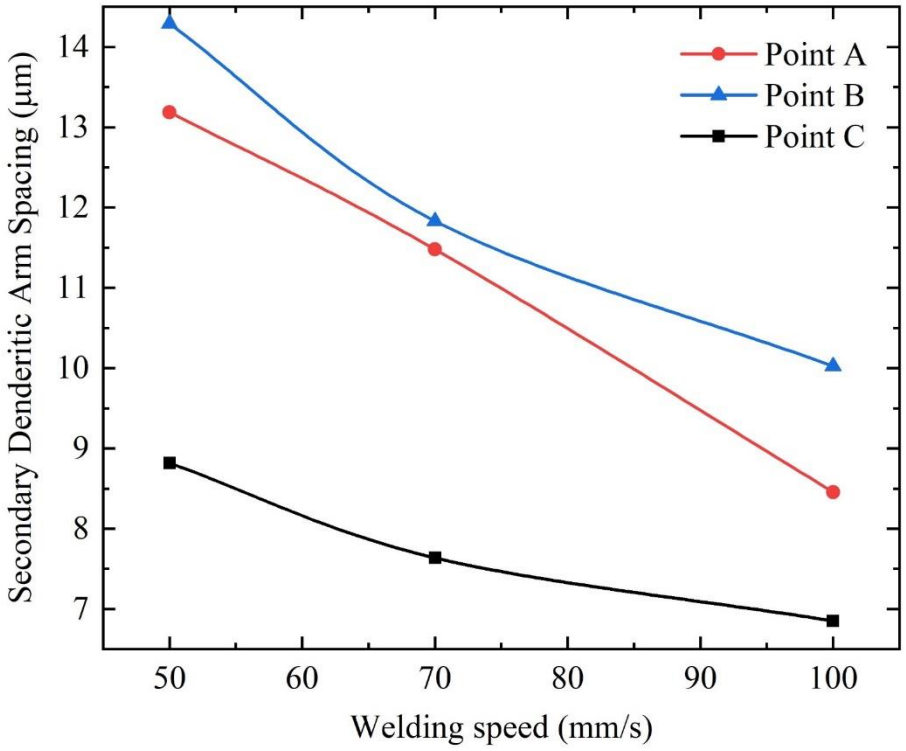

Figure 4.10 Predicted SDAS as a function of welding speed at Points A, B, and C

Figure 4.11 shows the deviation of G and R around the molten pool for various welding speeds. It is obvious that the R changes from the minimum value at the fusion boundary to the welding speed at the centerline of the weld surface for all welding speeds, see Figure 4.11a. Furthermore, increasing the welding speed increases the R around the weld pool. This increase is significant at the centerline. Wei et al. [128] studied the thermal modeling of the GTAW of aluminum alloys and reported that R increases from the fusion boundary to the centerline. Furthermore, the authors concluded that R increases with increasing welding speed [128]. Figure 4.11b shows that G gradually increases from the centerline to the fusion boundary and this increase is more considerable at the fusion boundary. Furthermore, increasing the welding speed increases the G around the weld pool. Similarly, Geng et al. [15] examined the solidification behavior of aluminum alloy to show that G is dramatically reduced from the fusion boundary to the centerline.

Kou [60] reported that the FZ solidification mode can be determined by evaluating the G/R ratio. The G/R ratio was therefore plotted for different points around the molten pool at various welding speeds, which is shown in Figure 4.11c. It can be observed from the figure that the G/R ratio is small at the centerline and shows no significant changes for all of the welding speeds from the centerline to the edge of the fusion boundary. At the edge of the fusion boundary, the G/R ratio is considerably increased for all welding speeds, and this increase is more profound for the lowest welding speed of 50 mm/min. Furthermore, at the edge of the fusion boundary, increasing the welding speed results in decreasing the G/R ratio. Wei et al. [128] and Ahn et al. [129] reported similar findings.

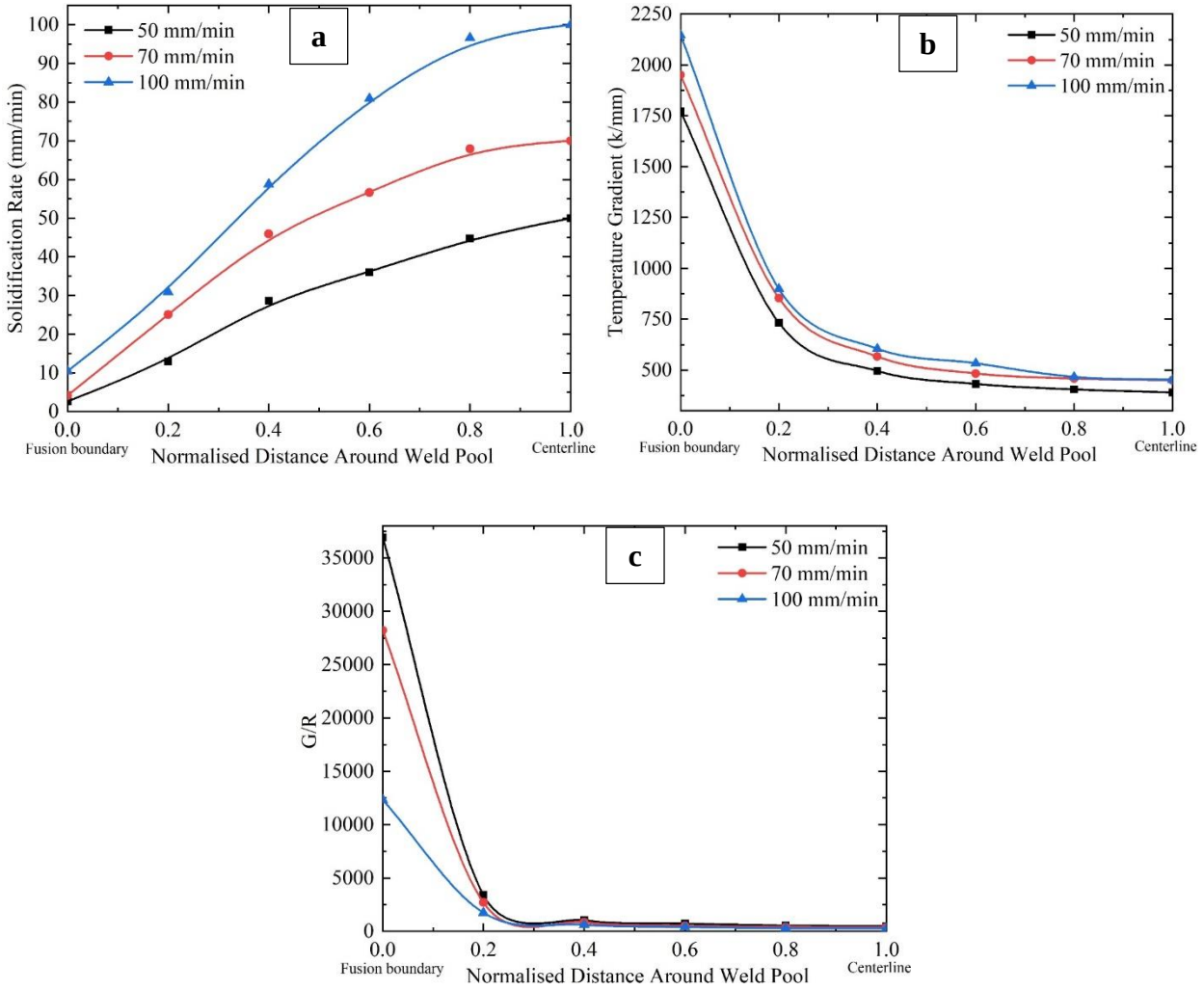

Figure 4.11 Variations of the solidification parameters around the weld pool for various welding cases: a. Solidification rate R, b. Temperature gradient G, and c. G/R ratio.

Gäumann et al. [115] developed a numerical model to describe the solidification morphology of CMSX-4 superalloy as a function of G and R. Their modeling showed that a higher G and lower R lead to the formation of a columnar structure. The impact of the welding speed on the dendritic structure in this study is shown in Figure 4.12. The microstructure is predicted to change from a mixed columnar-equiaxed structure at the centerline to a fully columnar structure at the fusion boundary for three welding speeds, as observed in Figure 4.12. Gäumann et al. [115] reported that near the weld centerline (low G), equiaxed dendrites nucleate and grow, which inhibit the growth of the columnar dendrites. Furthermore, with an increase in the welding speed, the volume fraction of the fully columnar structure is reduced, and vice versa. This reduction is the most considerable at the highest welding speed (100 mm/min). The predicted changes to the dendritic structure along the molten pool were experimentally validated at a welding speed of 50 mm/min.

The optical microstructure of the FZ is shown in Figure 4.13, and the magnified areas of the SDAS (1-4 in Figure 4.13) are shown in Figure 4.14. It can be observed that the dendritic structure at the centerline is mixed columnar-equiaxed and fully columnar close to the fusion boundary, which are in agreement with the numerically modeled result shown in Figure 4.12. The SDAS as a function of the normalized distance around the weld pool for both the experimental and modeling results is shown in Figure 4.15. It can be seen that both results exhibit a decrease in the SDAS from the fusion boundary to the weld centreline. Although there is a deviation between the experimental measurement and the numerical model prediction, their trends are in good agreement. Kou [60] reported that a coarse columnar structure is highly susceptible to cracking. Therefore, a higher welding speed, which results in a less columnar structure, can be used to reduce the susceptibility of the FZ to cracking.

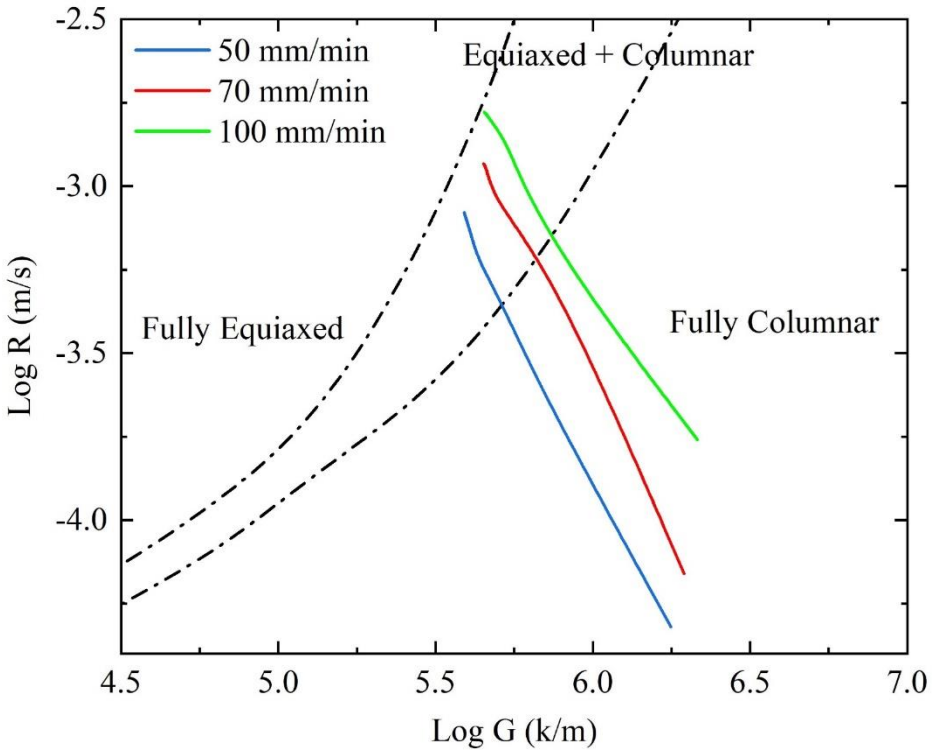

Figure 4.12 Differences in dendritic structure as a function of solidification variables at different welding speeds

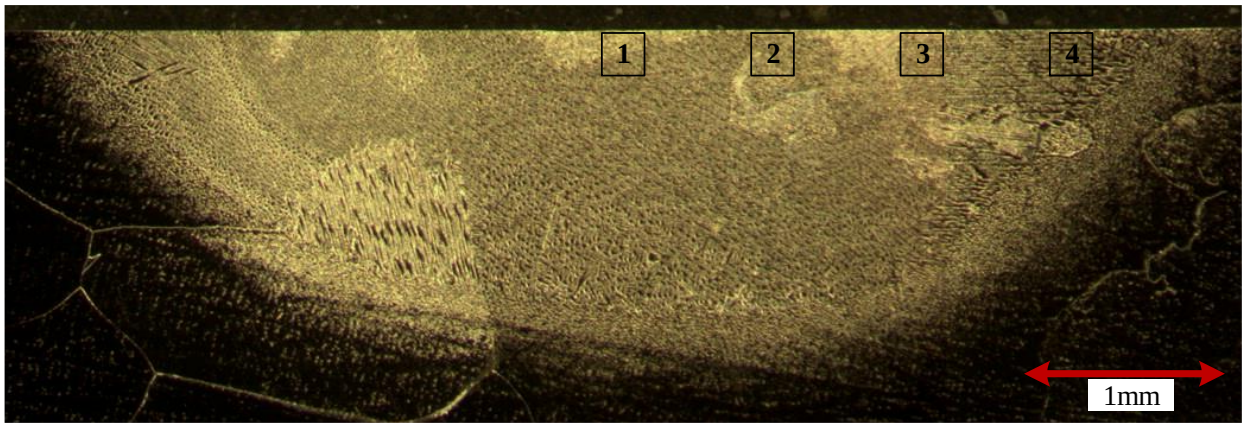

Figure 4.13 Optical microscopy image of dendritic microstructure of the FZ at welding speed of 50 mm/min

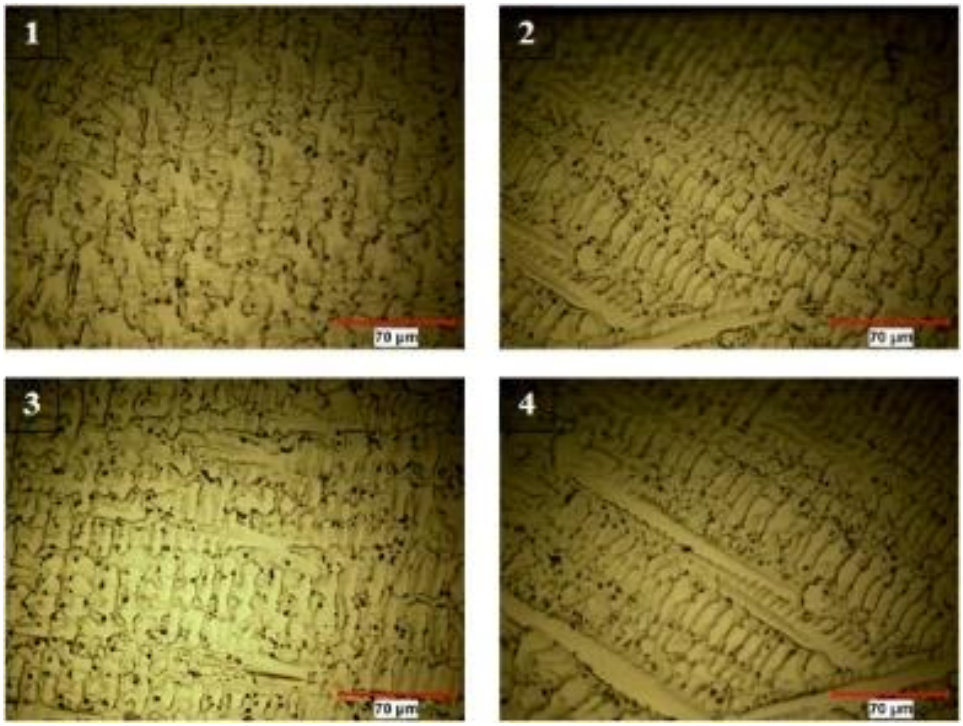

Figure 4.14 Optical microstructures with variations (1-4) in SDAS and dendritic structure within FZ at welding speed of 50 mm/min

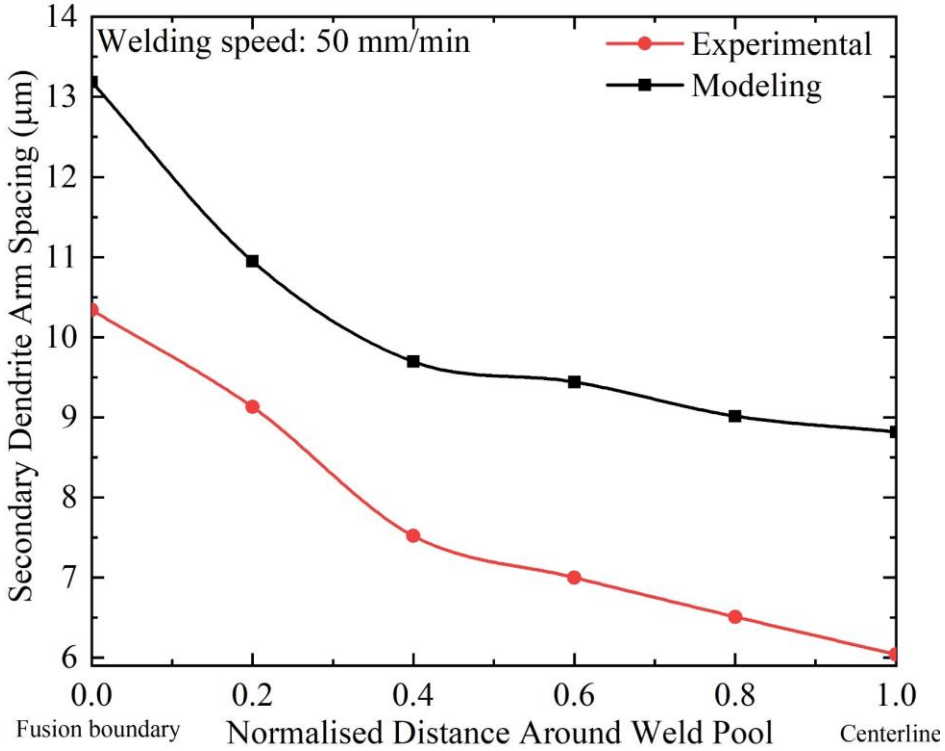

Figure 4.15 Comparison of experimental and modeled results for SDAS at welding speed of 50 mm/min

Figure 4.16, which is plotted based on Figure 4.11 and the CET criteria in Kurz et al. [67], shows the variations in the calculated CET parameter, $G^{3.4}/R$, around the weld pool at various welding speeds. It can be observed that $G^{3.4}/R$ is considerably reduced from a magnitude order of 10^{26} at the fusion boundary to 10^{22} at the centerline. This reduction suggests that there has been a columnar to equiaxed grain structure transition. The critical value ($G^{3.4}/R$) for a fully equiaxed grain structure is shown in Figure 4.16. According to the CET criteria in Kurz et al. [67], the area where $G^{3.4}/R$ is smaller than the critical value is predicted to be a fully equiaxed region. Therefore, from the centerline to the edge of the fusion boundary, a fully equiaxed grain structure is predicted for all three welding speeds. Similarly, Villaret et al. [130] reported that the largest volume fraction of equiaxed grains is found at the centerline, which is reduced towards the fusion boundary. Furthermore, Figure 4.16 also shows that as the welding speed increases, the fully equiaxed region is slightly increased. This is supported by the findings of Wei et al. [128] who found that increasing the welding speed promotes the formation of equiaxed grains within the FZ. These thus suggest that an increase in the welding speed could be beneficial to produce an equiaxed grain microstructure that may resist FZ cracking.

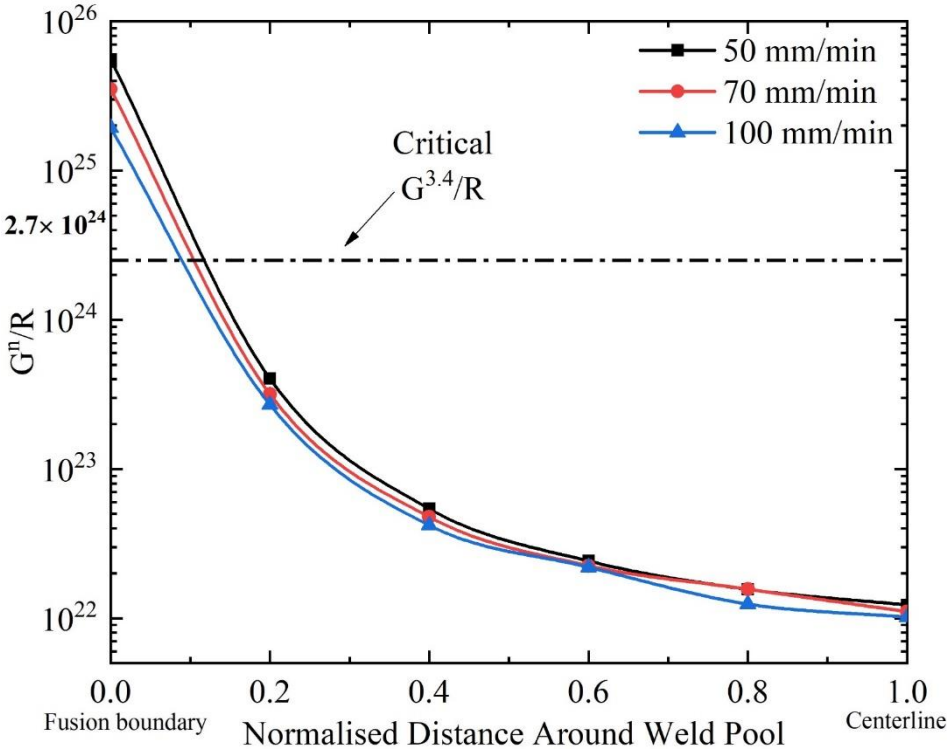

Figure 4.16 Variations of $G^{3.4}/R$ as a function of normalized distance around the weld pool at different welding speeds

4.3 Microstructure of As-Received CoWAlloy1

The optical and SEM micrographs of the as-received material are shown in Figure 4.17. Using the intercept method, the average grain size is measured to be approximately 1600 μm; see Figure 4.17a. Furthermore, CoWAlloy1 in the as-received condition exhibits an average hardness of 442 H_v. The SEM analysis shown in Figure 4.17b reveals the monomodal γ′ particle size distribution (PSD) with a particle size that ranges from 0.15 to 0.30 μm and an area fraction of 51%. In addition, the microstructure shows some blocky particles distributed randomly and along the grain boundaries that range from 2 to 6 μm in size. From the SEM-EDS analysis, these blocky particles were found to be rich in Ta, Hf, and Ti, which are MC-type carbide-forming elements. To positively identify the phases present in CoWAlloy1 in the as-received condition, a TEM analysis was conducted. Figure 4.18a shows a TEM bright-field image of CoWAlloy1 in the as-received condition with cuboidal γ′ precipitates. An analysis of the SADP taken from the [100] zone axis (Figure 4.18b) reveals superlattice reflections of the γ′ phase which confirms the presence of γ′ precipitates in the as-received condition.

Figure 4.19a shows a TEM bright-field image of the blocky phase in CoWAlloy1 in the as-received condition. A TEM-EDS analysis on this blocky particle shown in Figure 4.19b indicates that this particle is rich in Ta, Ti, and Hf. An analysis of the SADPs acquired from various zone axes (Figure 4.20) confirms that the phase is based on MC-type carbides with an FCC crystal structure and a lattice parameter of 4.32 Å. The presence of MC-type carbides has not been previously confirmed in CoWAlloy1.

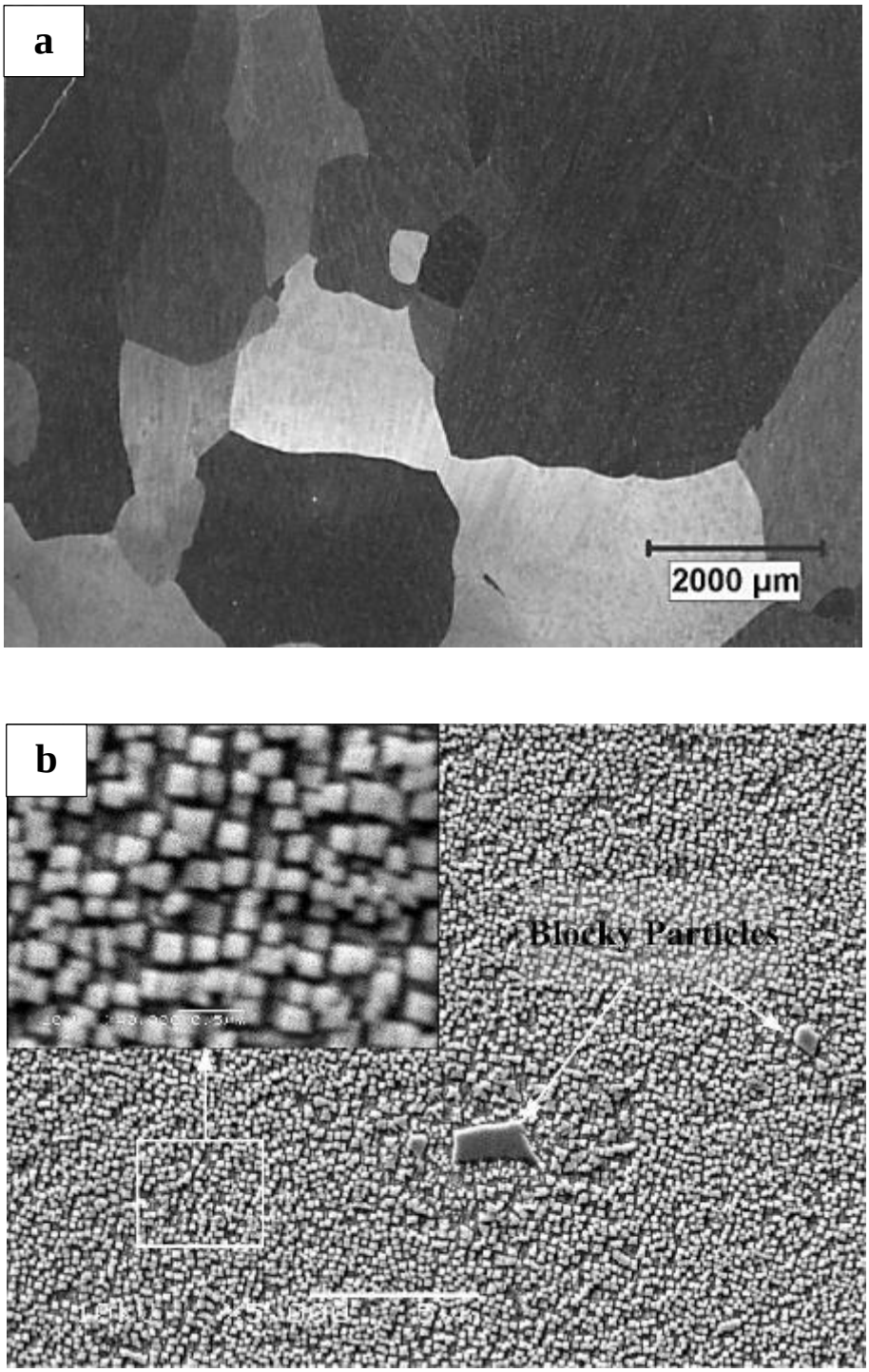

Figure 4.17 Microstructure of CoWAlloy1 in as received condition: a. Optical micrograph of grain structure, and b. SEM micrograph of monomodal γ′ PSD and presence of blocky particles.

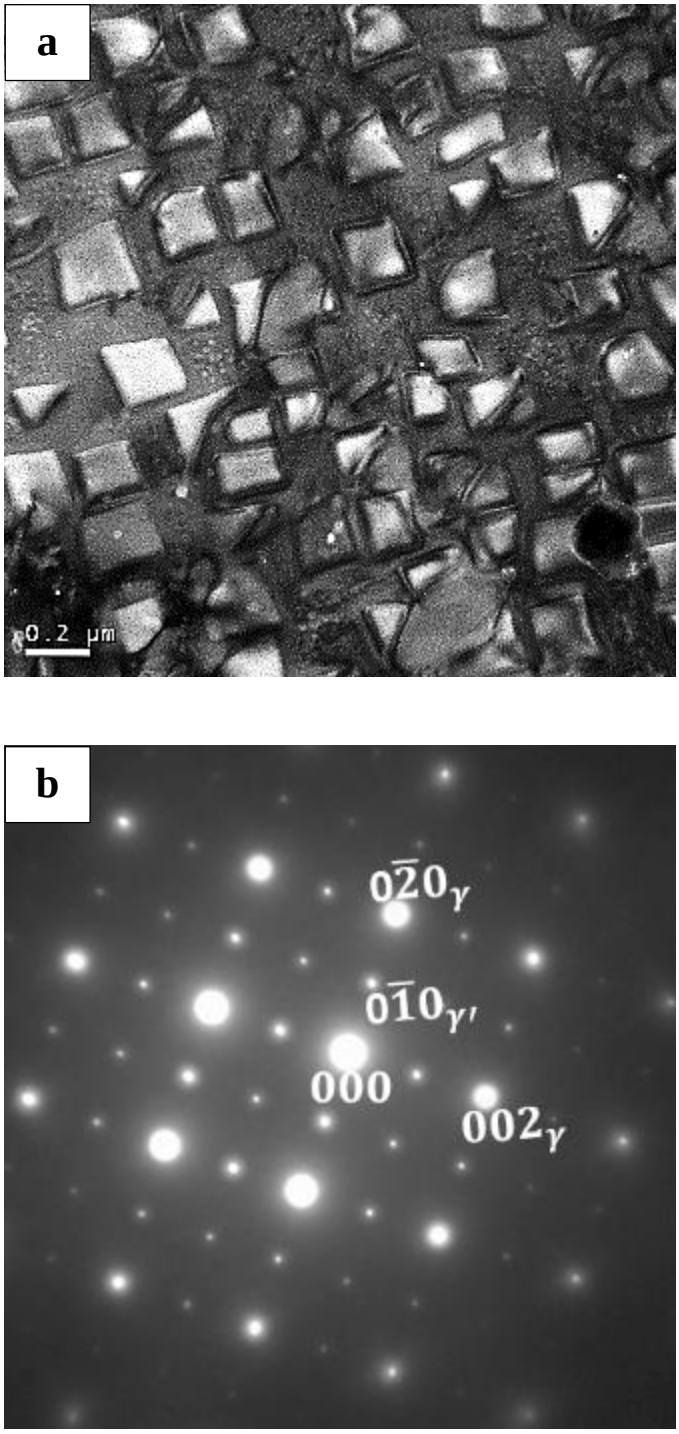

Figure 4.18 TEM analysis on CoWAlloy1 in as-received condition: a. Bright-field TEM image that shows cuboidal γ′ precipitates, and b. SADP taken from [100] zone axis that shows the superlattice reflections of γ′ phase in CoWAlloy1

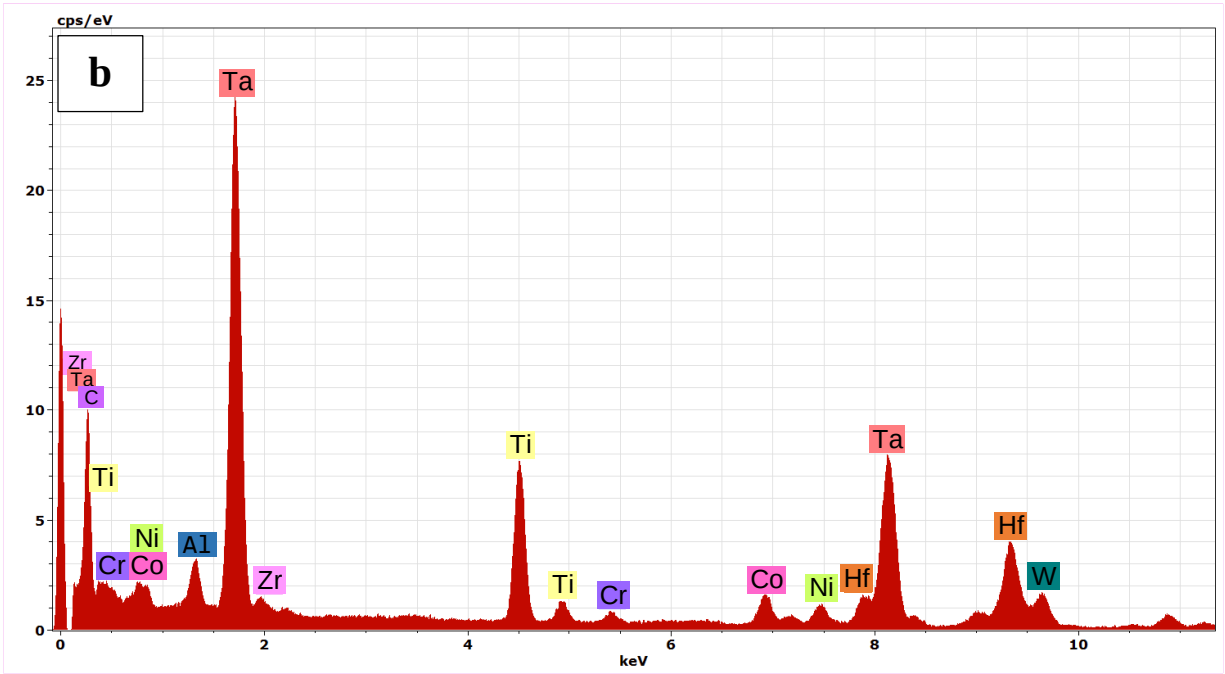

Figure 4.19 TEM examination of blocky particle in CoWAlloy1 in as-received condition: a. TEM bright-field image, and b. TEM-EDS analysis on blocky particle

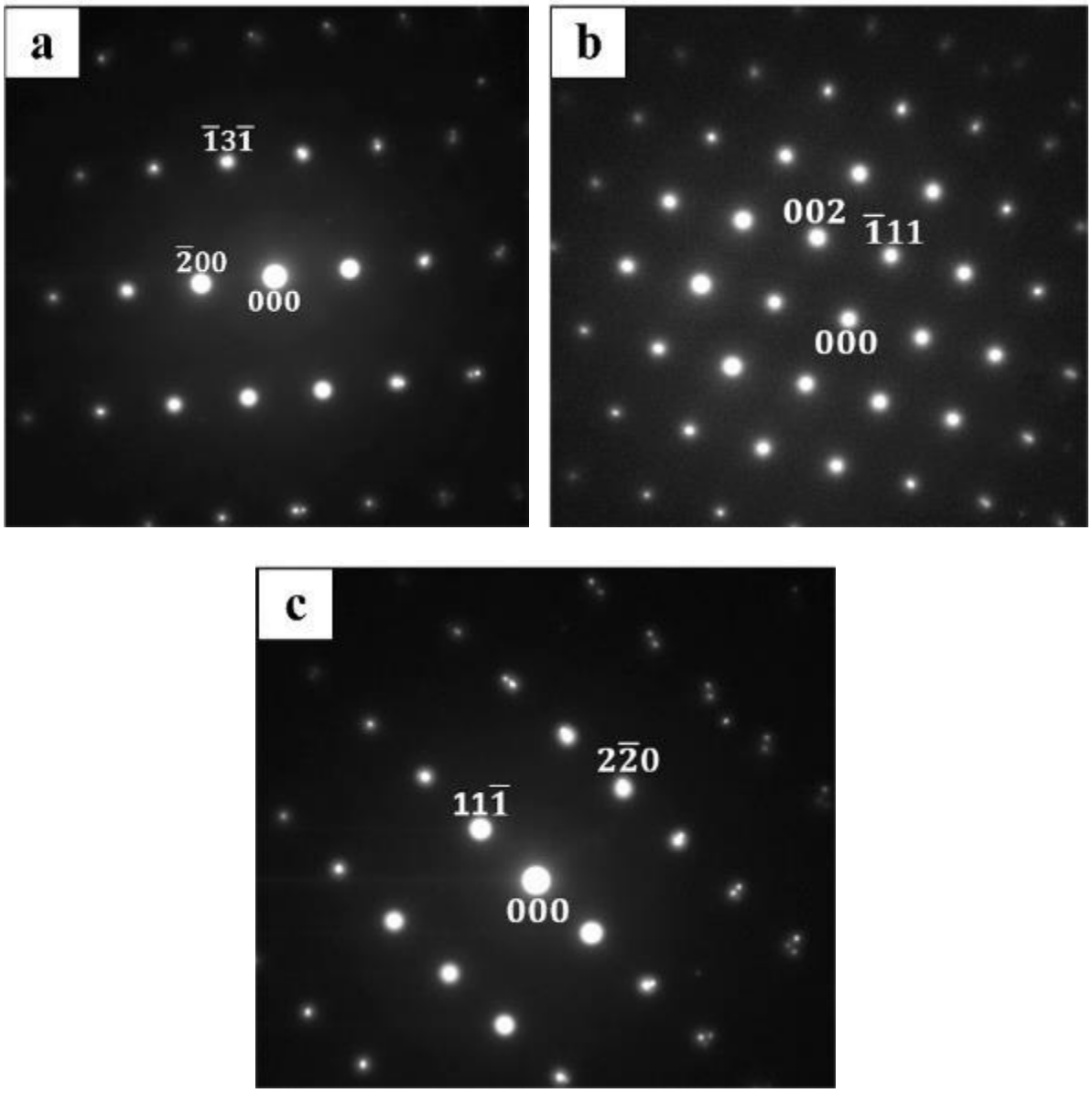

Figure 4.20 TEM analysis of CoWAlloy1 in as-received condition, SADPs that show reflections of MC-type carbide phase taken from a. [013], b. [110], and c. [112] zone axes.

4.4 Microstructure of CoWAlloy1 in Standard Heat-Treated Condition

Figure 4.21 shows the microstructure of the CoWAlloy1 subjected to the recommended STH for the alloy. As can be seen in Figure 4.21a, the SHT does not considerably affect the grain structure and size. However, the SHT results in an increase in the alloy hardness from 442 H_v to 509 H_v. Figure 4.21b shows the detailed microstructure of the STHed CoWAlloy1 which consists of a bimodal γ′ PSD with primary γ′ precipitates that range from 0.2 to 0.4 μm in size and secondary γ′ precipitates that range from 50 to 90 nm in size. In addition, Figure 4.21b reveals the presence of some blocky and irregularly shaped particles in the SHTed CoWAlloy1. An SEM-EDS analysis of these particles suggests that they are rich in Ta, Hf, and Ti, which are MC-type carbide-forming elements. To positively identify the phases present in the SHTed condition, a TEM analysis was subsequently performed. Figure 4.22 shows a TEM bright-field image of the SHTed CoWAlloy1 which confirms the presence of γ′ precipitates identified by the SADP taken from [111] zone axis.

The TEM bright-field image of the blocky phase in the SHTed CoWAlloy1 is shown in Figure 4.23a. A TEM-EDS analysis of this blocky particle shown in Figure 4.23b indicates that this particle is rich in Ta, Hf, and Ti. An analysis of the SADPs acquired from various zone axes (Figure 4.24) confirms that the phase is based on MC-type carbides with an FCC crystal structure and a lattice parameter of 4.32 Å.

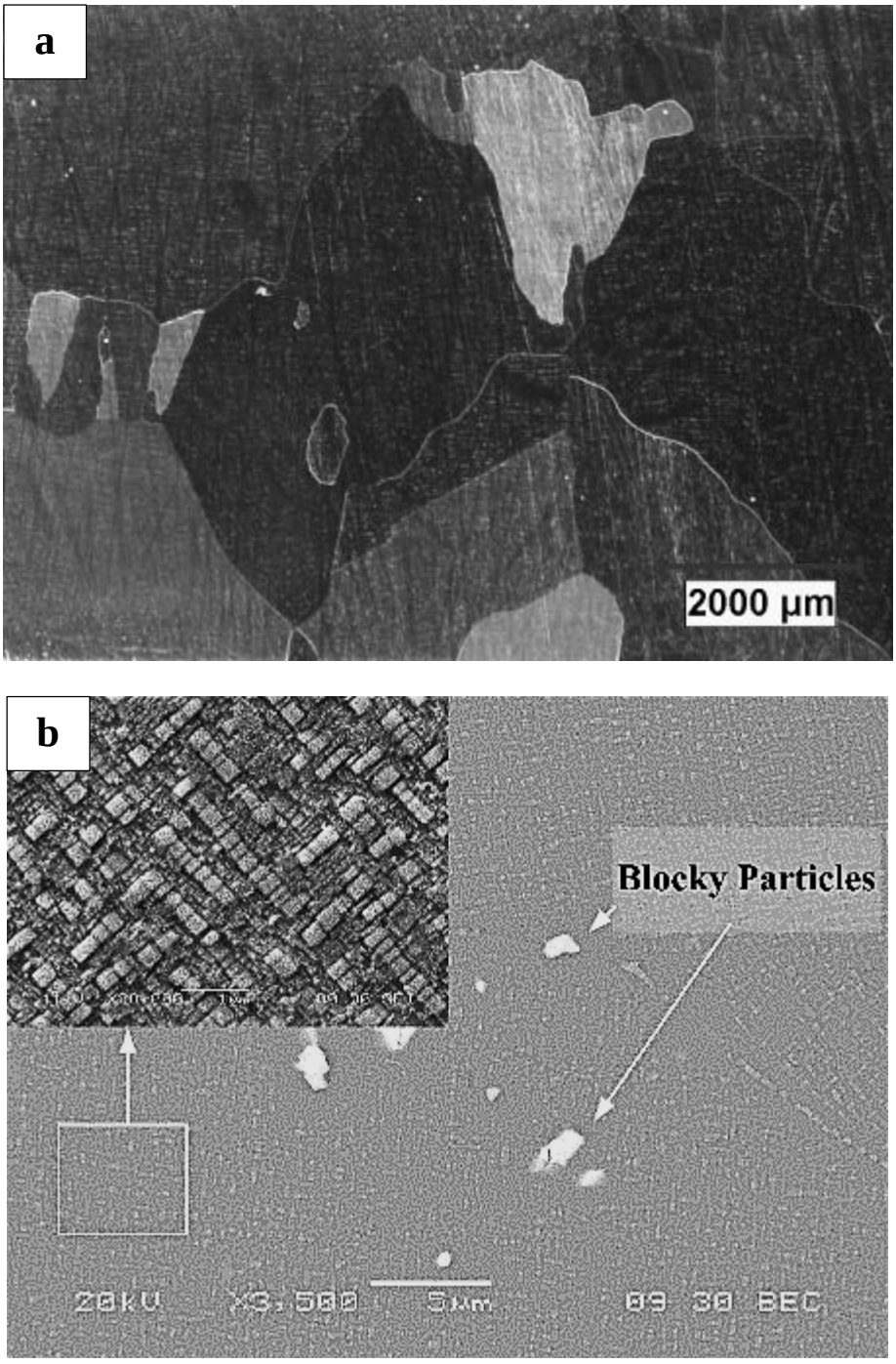

Figure 4.21 Microstructure of SHTed CoWAlloy1: a. Optical micrograph of grain structure, and b. SEM micrograph of bimodal γ′ PSD and presence of blocky particles.

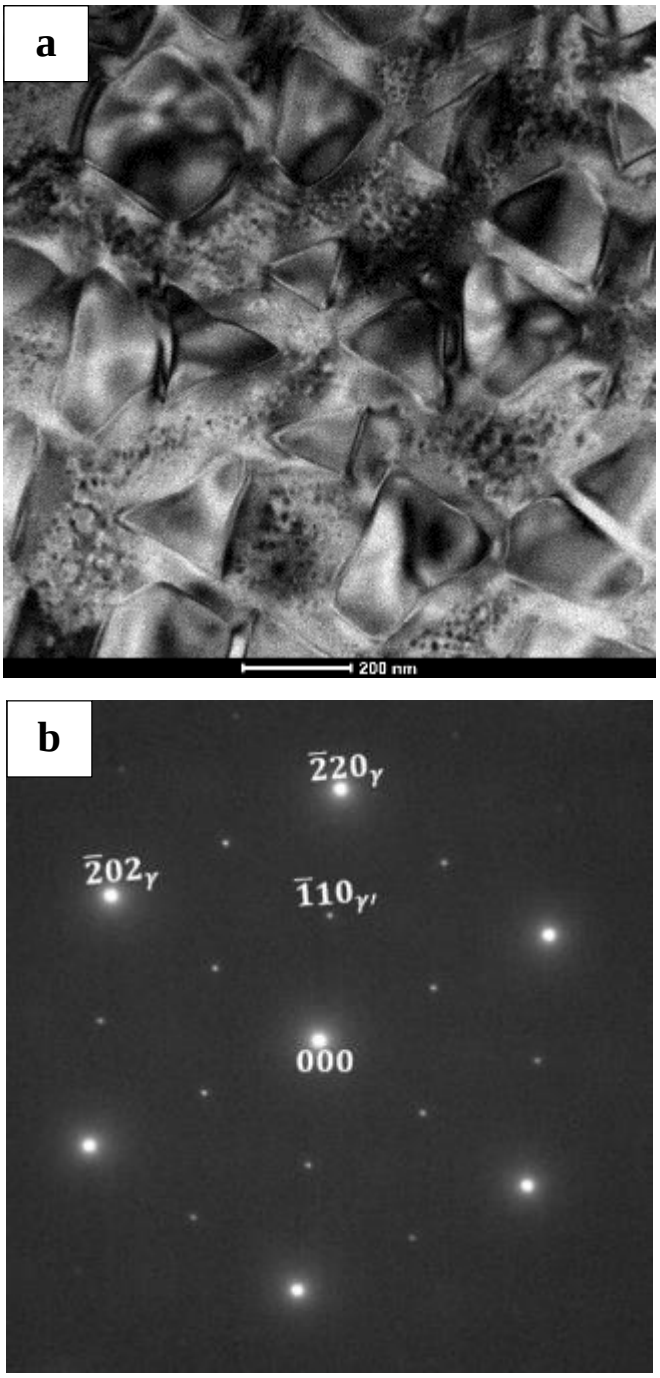

Figure 4.22 TEM analysis of SHTed CoWAlloy1: a. Bright-field TEM image of cuboidal and triangular γ′ precipitates, and b. SADP taken from [111] zone axis that shows presence of superlattice reflections of γ′ phase in SHTed CoWAlloy1.

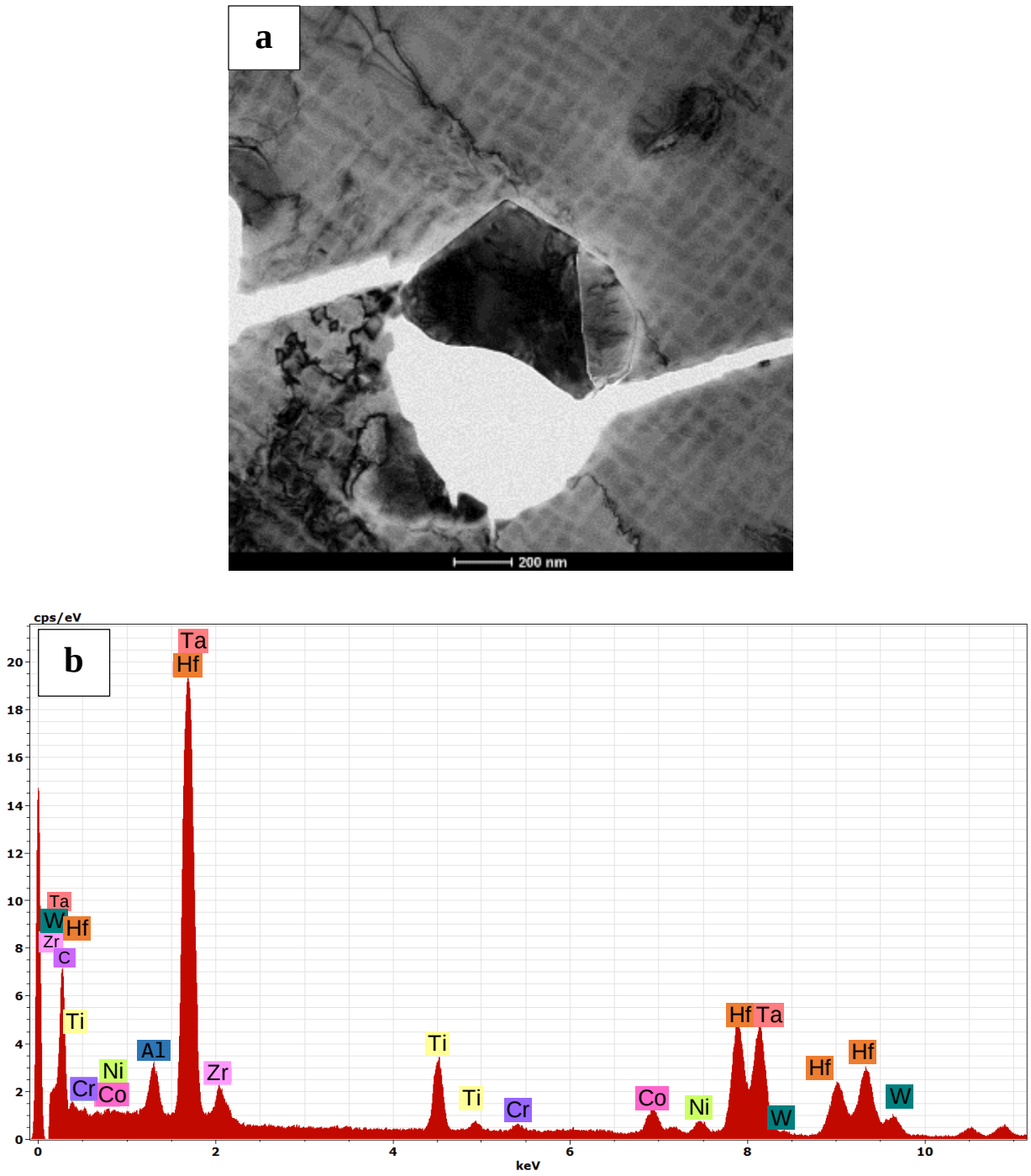

Figure 4.23 TEM examination of blocky particle in SHTed CoWAlloy1: a. TEM bright-field image, and b. TEM-EDS analysis of blocky particle

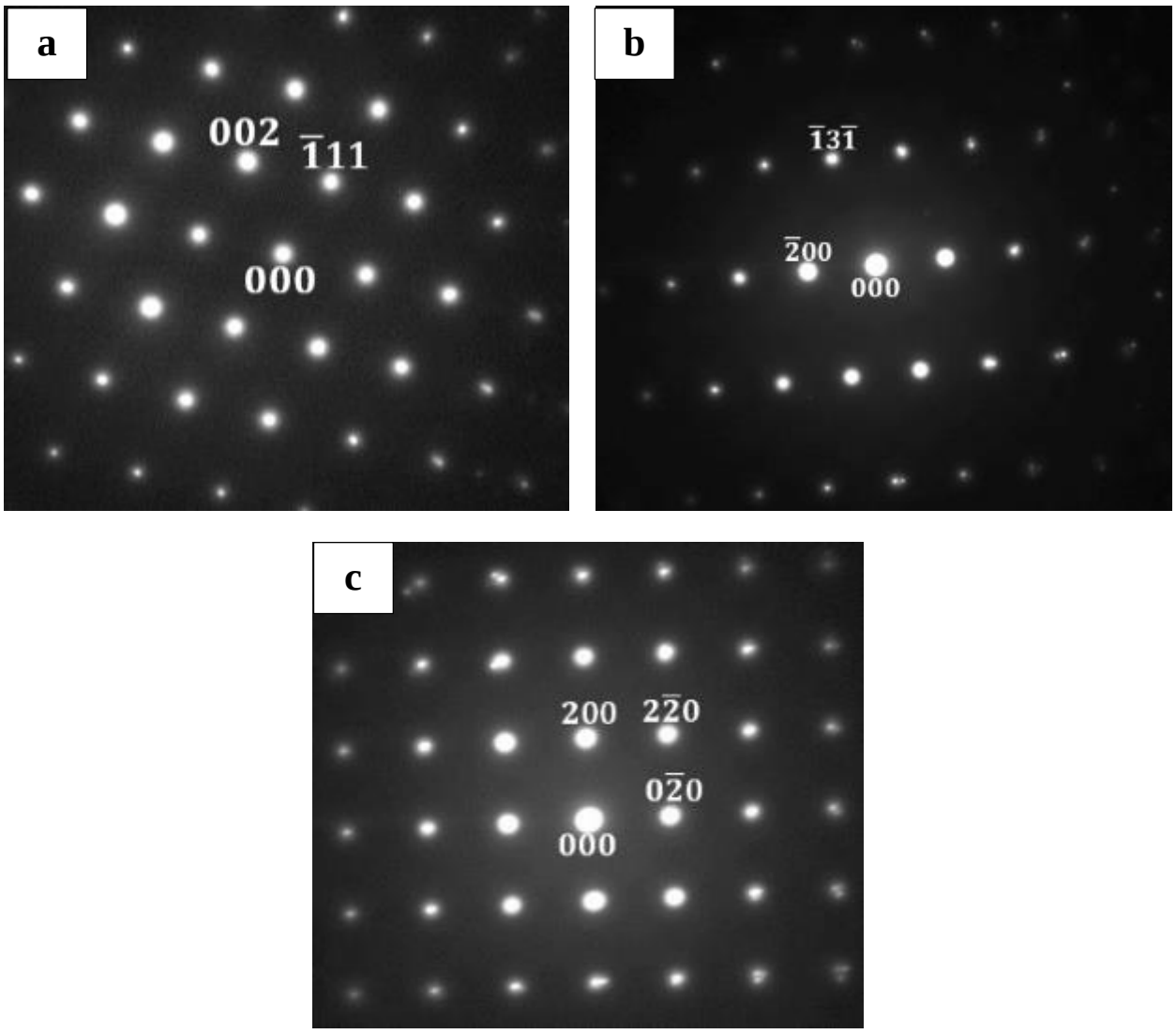

Figure 4.24 TEM analysis of SHTed CoWAlloy1, SADPs that show reflections of MC-type carbide phase taken from a. [110], b. [013], and c. [001] zone axes.

4.5 General Microstructure of the Arc Weld Region

Figure 4.25 shows the general microstructure of the autogenous BOP arc welded region in CoWAlloy1 in as-received condition by using the welding parameters listed in Table 3-3. It is worth mentioning that based on the developed model (Figure 4.16), all three sets of welding parameters result in an equiaxed grain structure in most of the FZ. Therefore, the lowest welding speed of 50 mm/min was considered for further investigation on the weldability of CoWAlloy1 due to the highest depth of penetration compared to the other sets of welding parameters. Although the formation of cracks can be detected in the HAZ in Figure 4.25, cracks are not observed in the FZ of all the examined welded samples, regardless of the pre-weld heat treatment condition. Detailed analyses of the FZ and HAZ are presented and discussed in the following sections.

4.5.1 Fusion Zone Microstructure

4.5.1.1 Optical Micrograph and EPMA Analysis of FZ

Figure 4.26 shows the optical micrograph of FZ of the sample welded in the as-received condition with a cellular-dendritic microstructure. The SDAS ranges from 6 to 10.4 µm, and the average value is calculated to be 8.2 µm. Equation 3-9 is used to evaluate the cooling rate from the calculated SDAS. Osoba et al. [86] reported that the degree of solid-state diffusion throughout the solidification process is mainly governed by the cooling rate. The cooling rate in the FZ is calculated to be around 414°C/s. The average chemical composition of 20 points in the center of the dendrite cores near the FZ boundaries was evaluated by using an EPMA and the values are summarized in Table 4-1. From the data, the partition coefficient of the solute elements, which represents the degree and direction of microsegregation throughout the solidification process, was calculated by simplifying the solute redistribution model developed by Bower et al. [131].

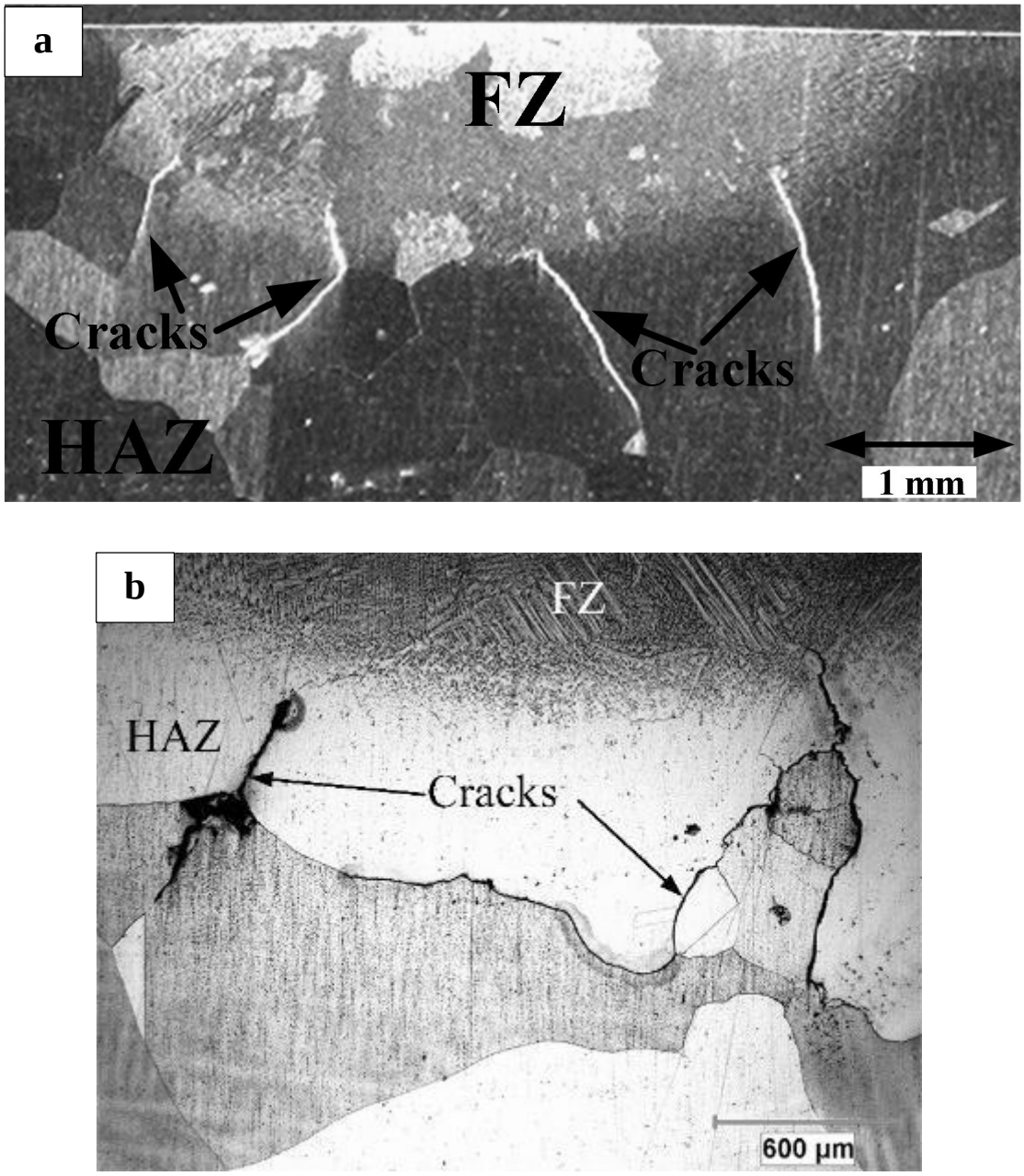

Figure 4.25 Optical micrograph of weld FZ and HAZ that show crack occurrence in HAZ: a. Low magnification, and b. High magnification

In this study, a rapid cooling rate is assumed to significantly limit the degree of solute back-diffusion. Another implicit assumption is that throughout the solidification process, the solute elements are not significantly diffused throughout the solid. Therefore, by neglecting undercooling at the dendrite edges, the solute redistribution at the beginning of solidification can be described reasonably well by using:

$$k = \frac{C_s}{C_0} \tag{4-1}$$

where C_s and C_0 are the element compositions in the dendrite core and nominal composition, respectively, and k denotes the equilibrium partition coefficient. Table 4-1 provides the initial partition coefficients of the alloying elements at the beginning of the solidification process. The result shows that Co and Ni have K values near unity, thus indicating that these elements segregate fairly uniformly between the dendrite core and interdendritic regions. In contrast, W and Cr have a K > 1, which shows that they segregate to the dendrite regions, while Al, Ta, Ti, Hf, Si, and Zr have a K < 1, which shows that they partition to the interdendritic region. The observed microsegregation behavior of the elements is in good agreement with the findings of previous research work on Co-based superalloys [132][133][134][135][136][8]. The partition coefficients of B and C could not be evaluated due to difficulties in obtaining accurate quantifications for these two light elements, and the impact of their back-diffusion can be substantial throughout the solidification process. Liu et al. [21] showed that the partition coefficient of C in Co-Al-W based superalloys is less than unity and segregates into the interdendritic liquid during solidification. Similarly, Sun et al. [137] showed that the partition coefficient of B in a Co-based superalloy, DZ40M, is less than unity, and partitions to the interdendritic regions. Therefore, in the current work, it is reasonable to infer that during the weld solidification of CoWAlloy1, both B and C

mainly segregate to the interdendritic regions. Ojo et al. [80] also reported that even though the partition coefficients are not necessarily constant throughout the solidification process, they can be well adapted to explain the formation of interdendritic micro-constituents.

4.5.1.2 Secondary Solidification Microconstituents in the FZ

Figure 4.27 shows an SEM image of a typical FZ microstructure. It can be seen that the interdendritic areas contain isolated second-phase particles that have blocky and rod-like morphologies (Particles A) and micro-constituents with a crown-like morphology (Micro-constituents B). An initial EDS analysis of Particles A by using SEM indicated that the particles are rich in MC-type carbide-forming elements such as Ta, Hf, and Ti. The SEM did not reveal the presence of γ′ precipitates in the FZ. In order to positively identify the interdendritic particles, Particles A and Micro-constituents B, TEM analyses were performed. Figure 4.28 shows the bright-field TEM image of a Particle A. The TEM-EDS microanalysis results on Particle A listed in Table 4-2 reveal that this particle is rich in the MC-type carbide forming elements of Ta, Ti, and Hf. An analysis of the SADP obtained from various zone axes (Figures 4.28b, 4.28c, and 4.28d) indicates that the phase is an MC-type carbide with an FCC crystal structure and lattice parameter of 4.32 Å. In addition to the MC-type carbides, the TEM analysis shows that Micro-constituents B are γ–γ′ eutectics, as confirmed through the SADP obtained from the [112] zone axis (insert of Figure 4.29). Furthermore, aside from the γ–γ′ eutectics, γ′ precipitates are also observed through dark field TEM imaging (Figure 4.29) to have formed within the FZ. However, the size of the γ′ precipitates varies with location, such that regions close to the γ-γ′ eutectics are observed to have coarser γ′ precipitates compared to regions further away from the eutectics (Figure 4.29).

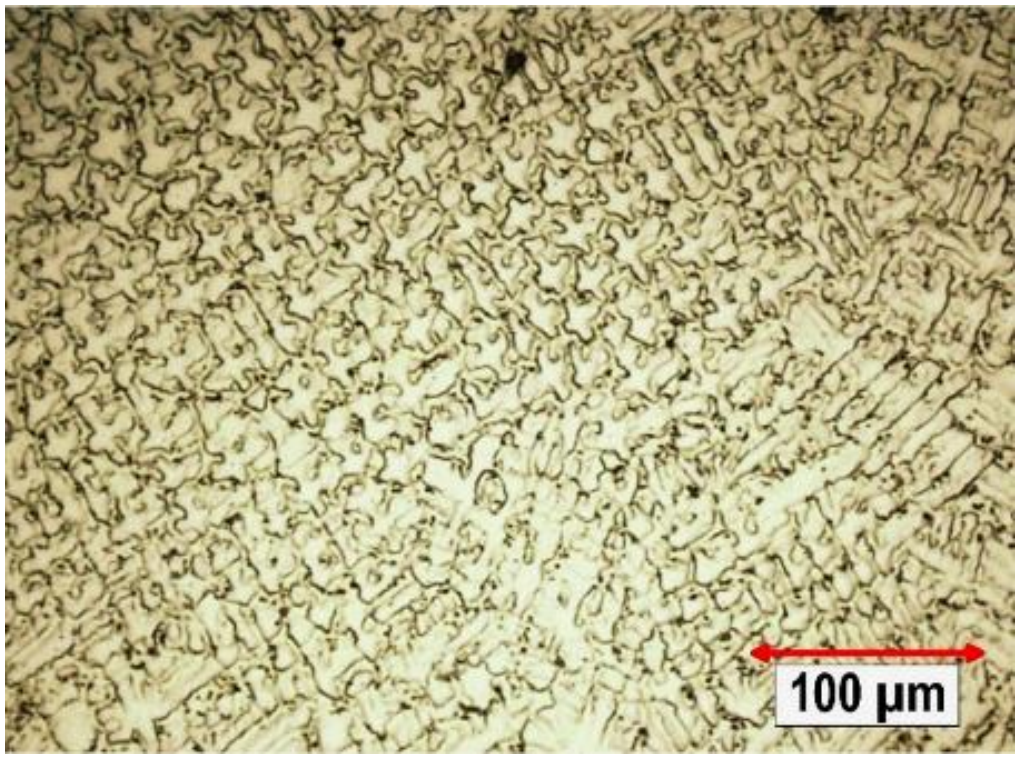

Figure 4.26 Optical micrograph of FZ

Table 4-1 Chemical composition (Wt. %) of dendrite core and calculated partition coefficient (K)

Element	Co	Ni	Cr	Al	W	Ti	Ta	Si	Hf	Zr
Dendritic Core (Wt. %)	41.72	29.56	11.18	2.34	9.71	1.44	3.43	0.012	0.057	0.006
$K=C_s/C_o$	1.02	0.97	1.09	0.88	1.08	0.74	0.77	0.68	0.19	0.42

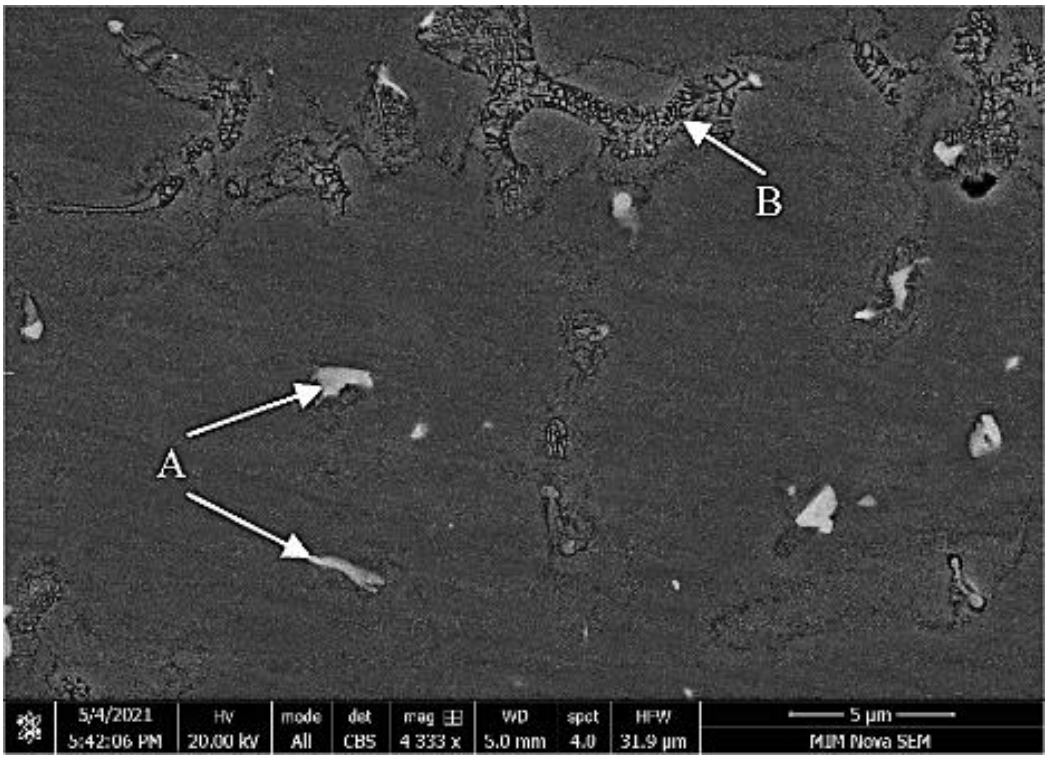

Figure 4.27 SEM micrograph of FZ

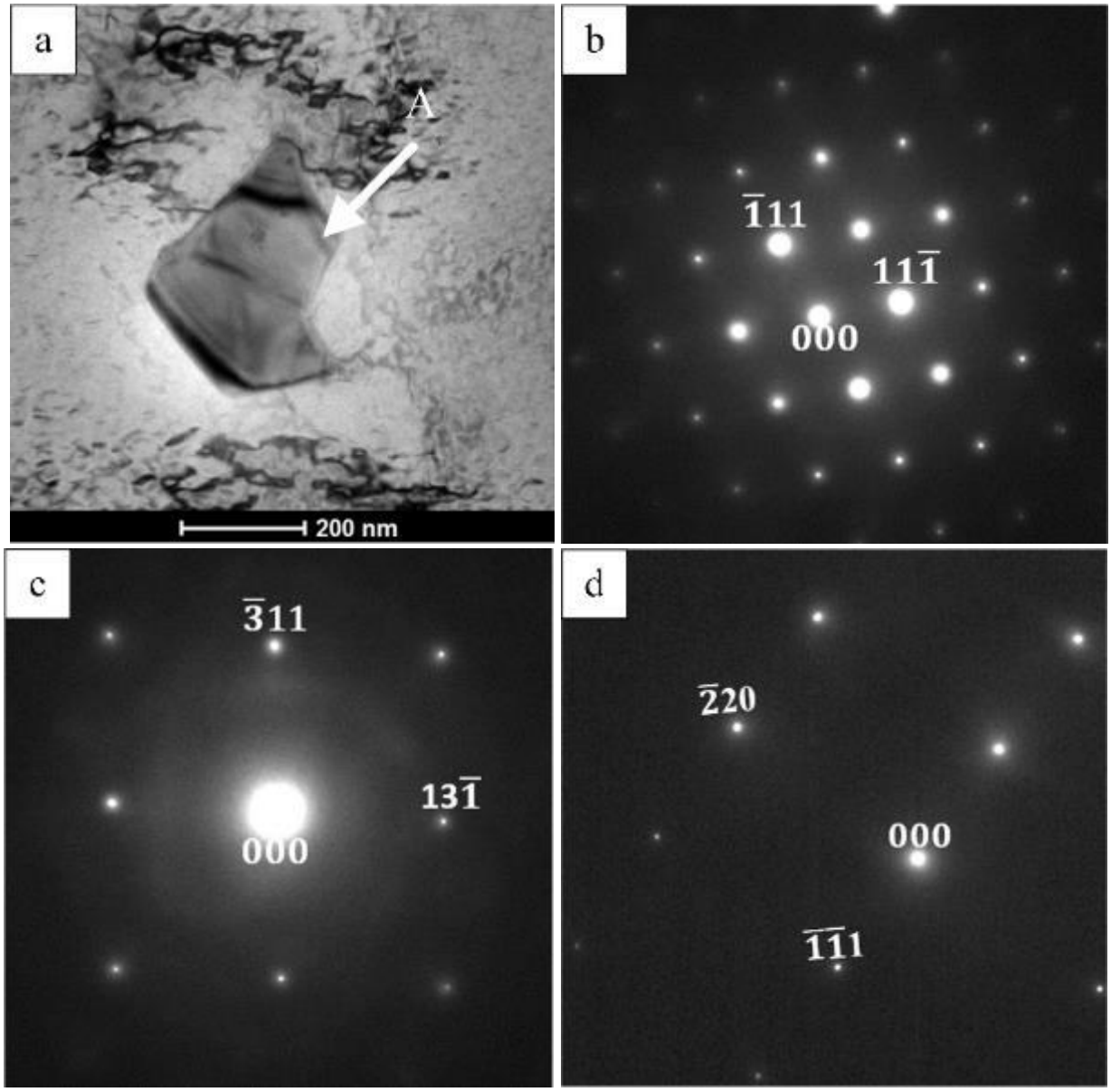

Figure 4.28. TEM examination of Particle A: a. Bright-field TEM image of blocky-shaped particle and SADP of Particle A from zone axes of b. [101], c. [215], and d. [112]

Table 4-2 Semi-quantitative TEM/EDS microanalyses of Particle A

Element	**Co**	**Ni**	**Cr**	**W**	**Ti**	**Ta**	**Hf**	**Zr**
(Wt. %)	2.10	1.51	1.14	4.93	20.77	53.05	14.97	1.47

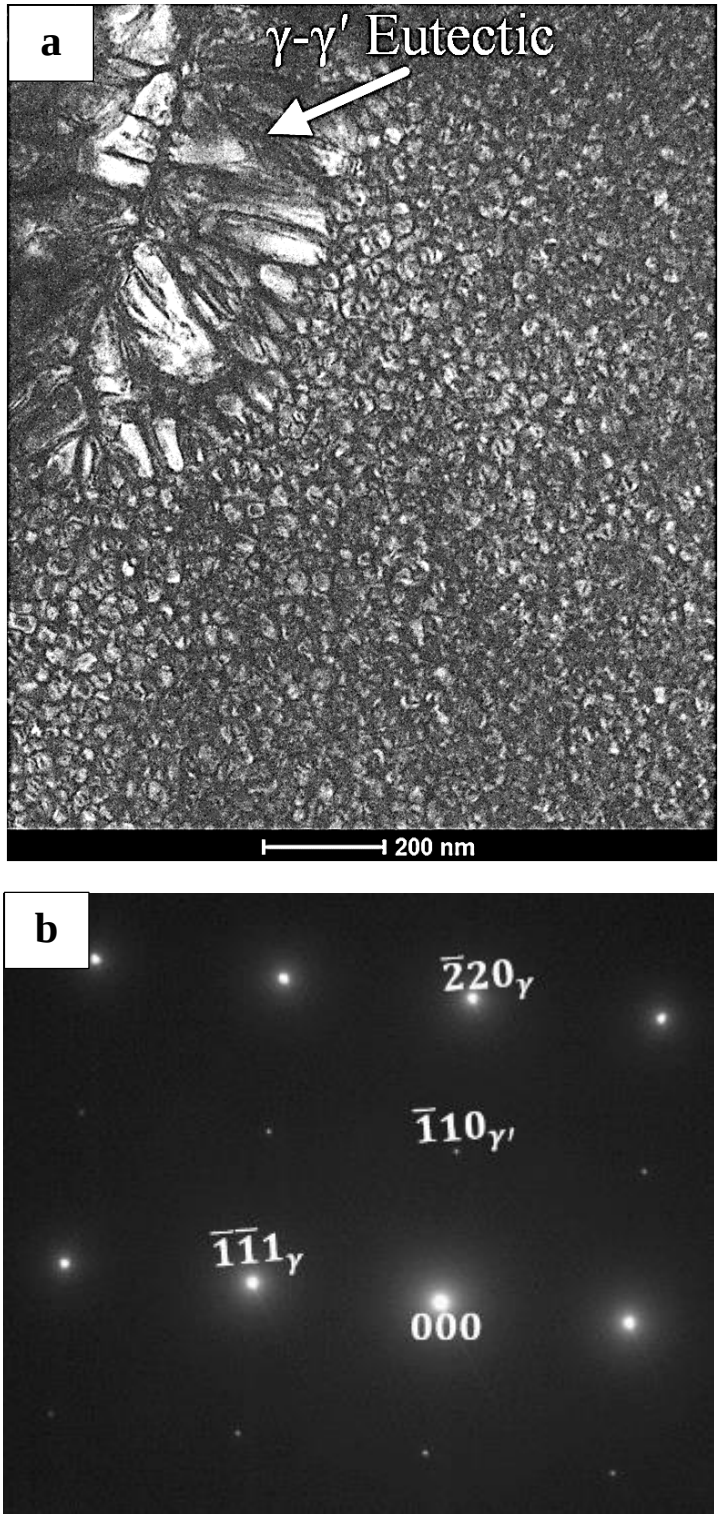

Figure 4.29 TEM analysis of FZ of welded CoWAlloy1: a. Dark-field TEM image that shows presence of γ–γ′ eutectics and γ′ precipitates with non-uniform distribution in the interdendritic region, and b. SADP obtained from the [112] zone axis

4.5.1.3 Discussion on Microstructural Development in the Weld FZ

The microstructural changes in the FZ are generally governed by two solidification processes: dendrite formation and solute distribution. JMatPro (7.0.0 version), a thermodynamics-based software, was used to study the solidification behavior in CoWAlloy1. The solidification reaction products were determined based on the Scheil-Gulliver solidification model. This model assumes no diffusion in the solid phase and infinite diffusion in the liquid phase (complete mixing in the liquid) during solidification [138][141]. Several studies have reported that the Scheil-Gulliver solidification model can accurately predict the solidification behavior of superalloys [138][139][140][141]. Figure 4.30 shows the schematic of the solidification reaction product sequence in CoWAlloy1. The solidification process is initiated with the formation of γ dendrites as the primary solid to form from liquid through the $L_1 \rightarrow \gamma + L_2$ reaction (Figure 4.30b). As the γ dendrites gradually form and grow, elements with a partition coefficient less than unity are increased in the interdendritic liquid. As the solute rejection of the interdendritic liquid continues during cooling, the solubility limit of the γ dendrites will be exceeded. Thus, secondary solidification constituents form in the interdendritic region. In CoWAlloy1, the carbide-forming elements such as Ti, Ta, Hf, and C, show considerable segregation to the interdendritic region. Also, these elements show limited solubility in Co, which results in the formation of MC-type carbides within the interdendritic region through a $L_2 \rightarrow \gamma + MC + L_3$ reaction over a range of temperatures (Figure 4.30c). As cooling continues, the supersaturation of the residual interdendritic liquid with γ′ forming elements such as Al, Ti, and Ta would occur and eventually lead to the formation of γ–γ′ eutectics through a $L_3 \rightarrow \gamma + \gamma'$ eutectic-type reaction over a range of temperatures (Figure 4.30). Zhou et al. [134] examined the solidification path of novel γ/γ′ in Co-based superalloys and reported that γ-γ′ eutectics form at the terminal stage of solidification.

Further cooling to a temperature that is adequately lower than the γ′ solvus temperature of 1070ºC [10] would cause the formation of γ′ precipitates to commence. The segregation of γ′ forming elements during solidification can lead to the formation of γ′ precipitates in the interdendritic regions at higher temperatures. More Al and Ti in the interdendritic region are known to increase the γ′ solvus temperature [142][143]. Therefore, as more time is available for the γ′ precipitates to grow in the interdendritic region, this can lead to the formation of coarser γ′ precipitates in the interdendritic regions, as observed in the present work. The non-uniform distribution of γ′ particles can, however, deteriorate the high-temperature properties and is one of the main reasons that necessitate the use of PWHT of superalloy weldments.

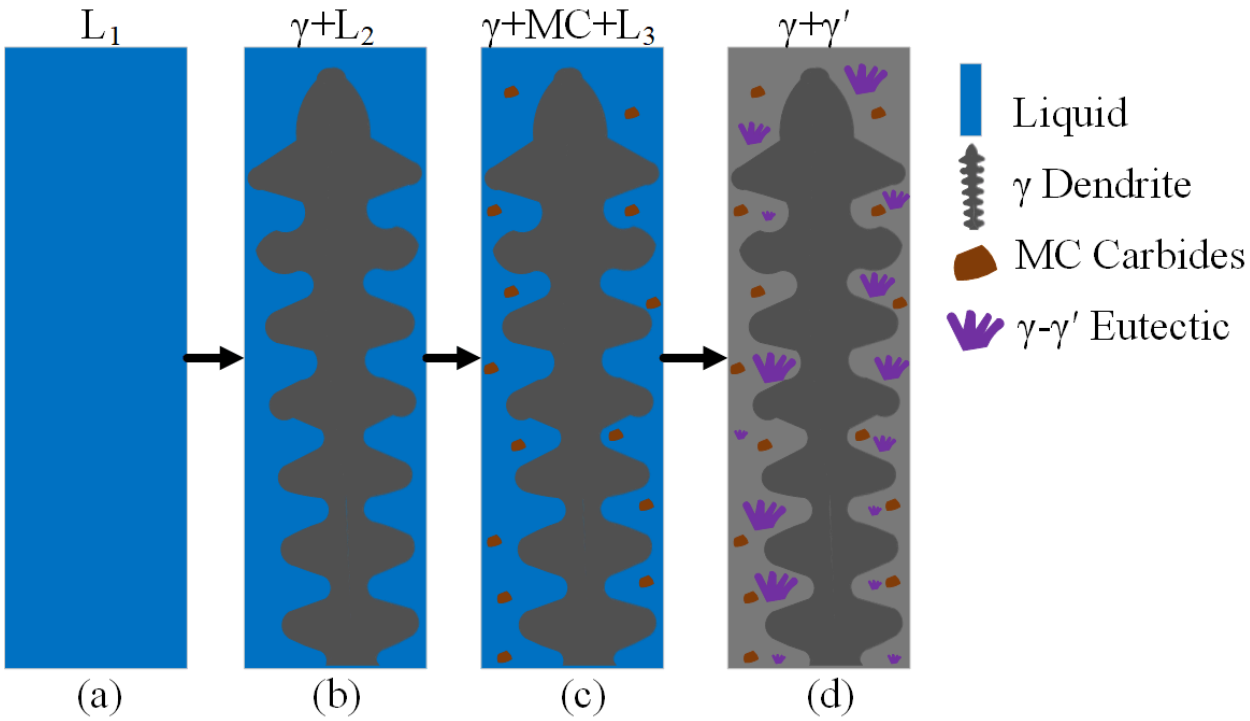

Figure 4.30 Schematic of the solidification reaction product sequence in CoWAlloy1 that shows formation of: a. Liquid (L_1), b. γ dendrite through $L_1 \rightarrow \gamma + L_2$ reaction, c. MC-type carbide through $L_2 \rightarrow \gamma + MC + L_3$ reaction, and d. γ–γ′ Eutectic through $L_3 \rightarrow \gamma + \gamma'$ eutectic-type reaction.

4.5.2 HAZ Microstructure of Welded CoWAlloy1 in As-Received Condition

Although cracks were not observed in the FZ of all of the examined welded samples, microcracks were still observed in their HAZ regardless of the pre-weld heat treatment. It can be seen from Figure 4.25 that the HAZ cracks are intergranular with an irregular morphology which has been identified as the typical morphology of liquation cracks in superalloys [12]. An SEM examination of the crack region at higher magnification (Figure 4.31) reveals the presence of intergranular resolidified eutectic-like constituents along the crack paths. This observation suggests that the HAZ cracking occurred due to both the liquid film formation along the grain boundaries and the effect of the tensile stress produced during weld cooling. Generally, the liquid film in HAZ can form through either a non-equilibrium phase transformation below the alloy solidus temperature (subsolidus) or melting above the solidus temperature (supersolidus). The latter is anticipated to occur in all weldments due to heating above the equilibrium solidus temperature of an alloy [87]. The formation of subsolidus liquation is more damaging in terms of HAZ cracking because it increases the melting range of an alloy and affects the characteristics of supersolidus melting by forming a non-equilibrium liquid film at lower temperatures [88]. The most widely accepted mechanism to explain for the subsolidus grain boundary liquation is grain boundary penetration, in which the liquation of particles such as carbides, sulfide, boride, etc., forms a liquid film that penetrates and spreads along the grain boundaries [144].

4.5.2.1 Liquation of MC Carbides

The SEM-EDS line scan analysis results of the liquated film shown in Figure 4.31a are presented in Figure 4.31b. The liquated film is rich in Ta, Hf, and Ti which are MC-type carbide-forming elements. Furthermore, the SEM-EDS point scan of the bright particles adjacent to the crack path

shown in Figure 4.32 suggests that these particles are rich in MC-type carbide forming elements. An SEM investigation at a higher magnification (insert of Figure 4.32) reveals that the cracks are prone to propagate along the interfaces between the MC-type carbide and the matrix. Therefore, subsolidus liquation of intergranular MC-type carbides found in the pre-weld CoWalloy1 could have contributed to the intergranular liquation cracking in the HAZ. The contribution of MC-type carbide liquation to HAZ cracking in superalloys has been reported in several Ni-based superalloys such as IN738 [89], IN738LC [145], IN718plus [127], Rene80 [18], and Waspaloy [146]. However, there have been few studies on the causes of HAZ cracking in γ′-strengthened Co-based superalloys. The only study is Liu et al. [21] who examined the weldability of γ′-strengthened Co-based superalloys to show that the liquation of M_6C-type carbides that precipitate at the grain boundaries contributes to the liquation cracking of the HAZ.

4.5.2.2 Constitutional Liquation of γ′ Precipitates

In addition to the liquation of MC-type carbides in the HAZ, evidence of liquating γ′ precipitates along the HAZ cracks is observed in this alloy (Figure 4.33a). The SEM analysis (Figure 4.33b) reveals the formation of resolidification products mostly on one side of the crack with a eutectic morphology (γ–γ′). Ojo et al. [87] reported that a rapid welding thermal cycle can cause the dissolution behavior of γ′ precipitates to deviate from equilibrium. Consequently, the existence of γ′ precipitates above the equilibrium solvus temperature of γ′ and until the temperature at which γ-γ′ eutectic reaction occurs, could lead to the constitutional liquation of γ′ precipitates and subsequent penetration of the liquid along the grain boundaries [87]. Based on the DSC analysis provided in Section 4.2.2 (Figure 4.2), it can be concluded that the transformation temperature of the γ-γ′ eutectics in CoWAlloy1 could occur at around 1203°C, which is considerably higher than

the solvus temperature of γ′ (1072°C) and lower than the solidus temperature (1306°C). These suggest the possible contribution of the sub-solidus liquation of γ′ to HAZ cracking in the CoWAlloy1 which was first introduced in Ojo et al. [87], and subsequently reported in several Ni-based superalloys [18][88][147][148].

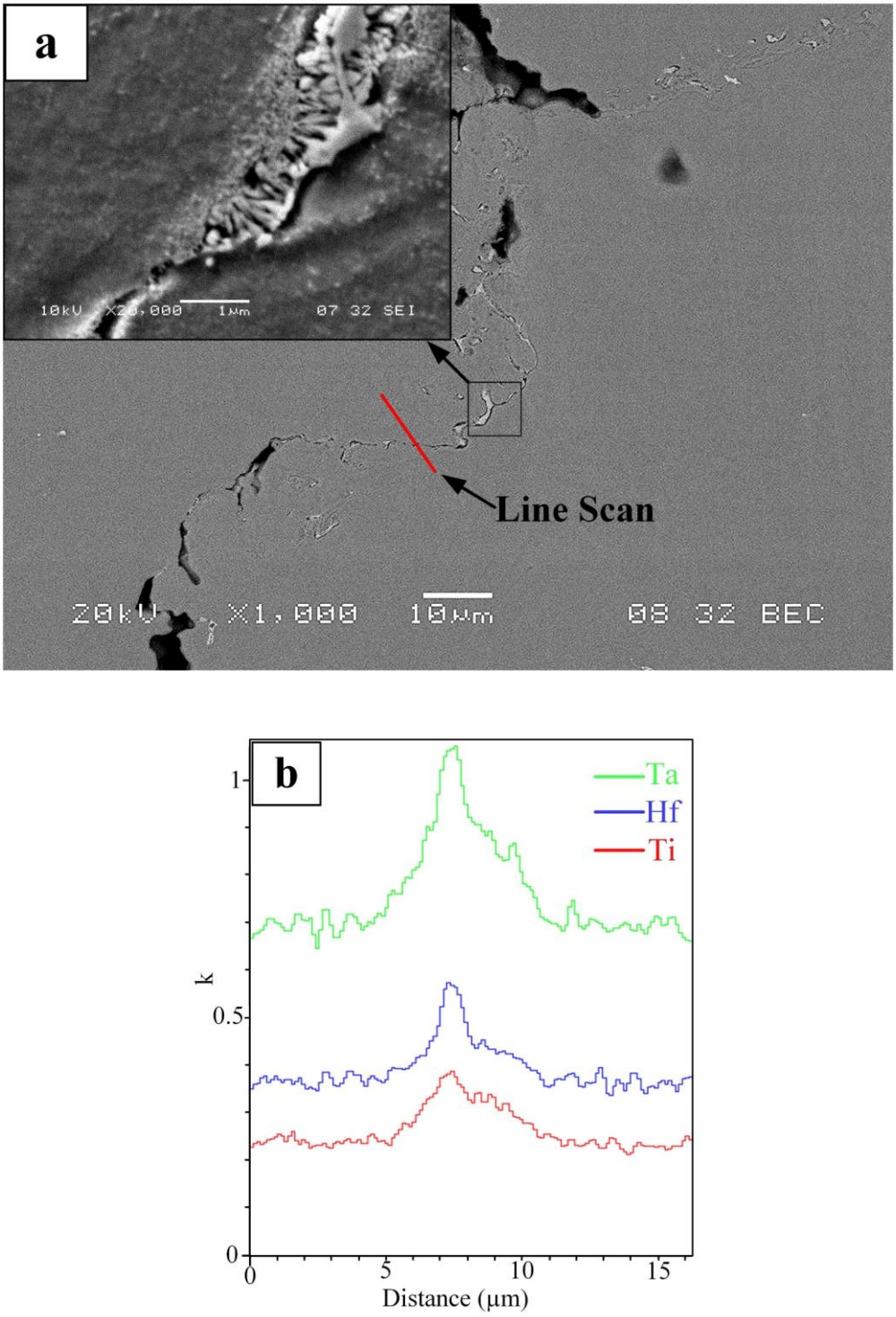

Figure 4.31 SEM analysis of crack region: a. Resolidified products along the crack path, and b. SEM-EDS analysis of liquated film in HAZ

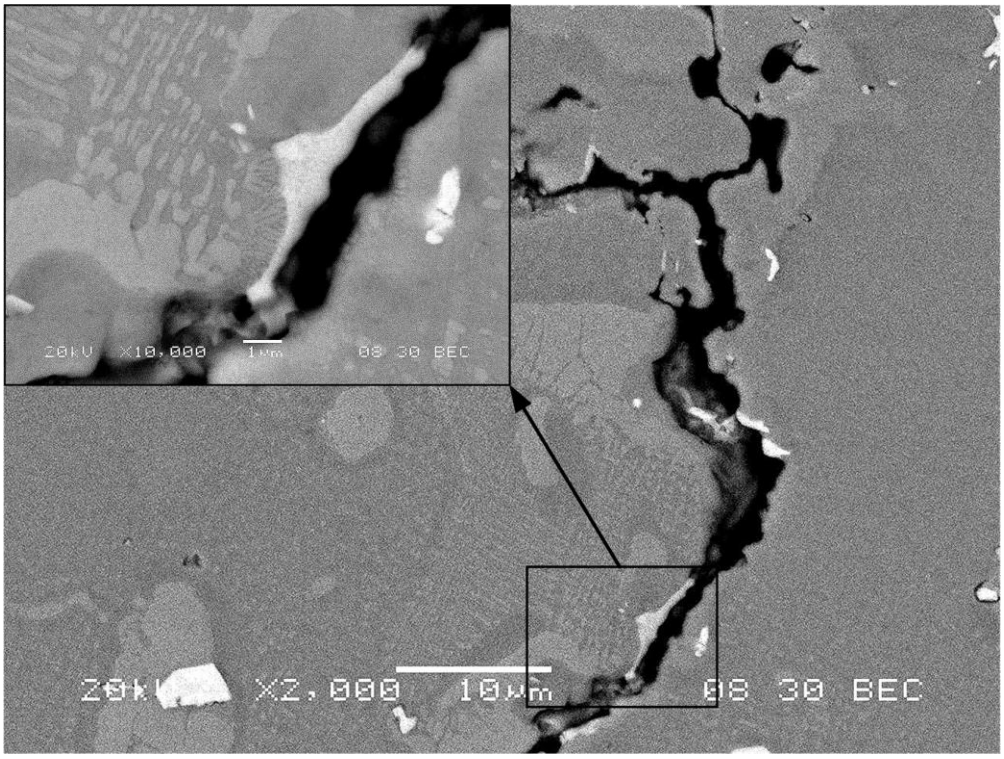

Figure 4.32 SEM micrograph that shows presence of MC-type carbides along crack path

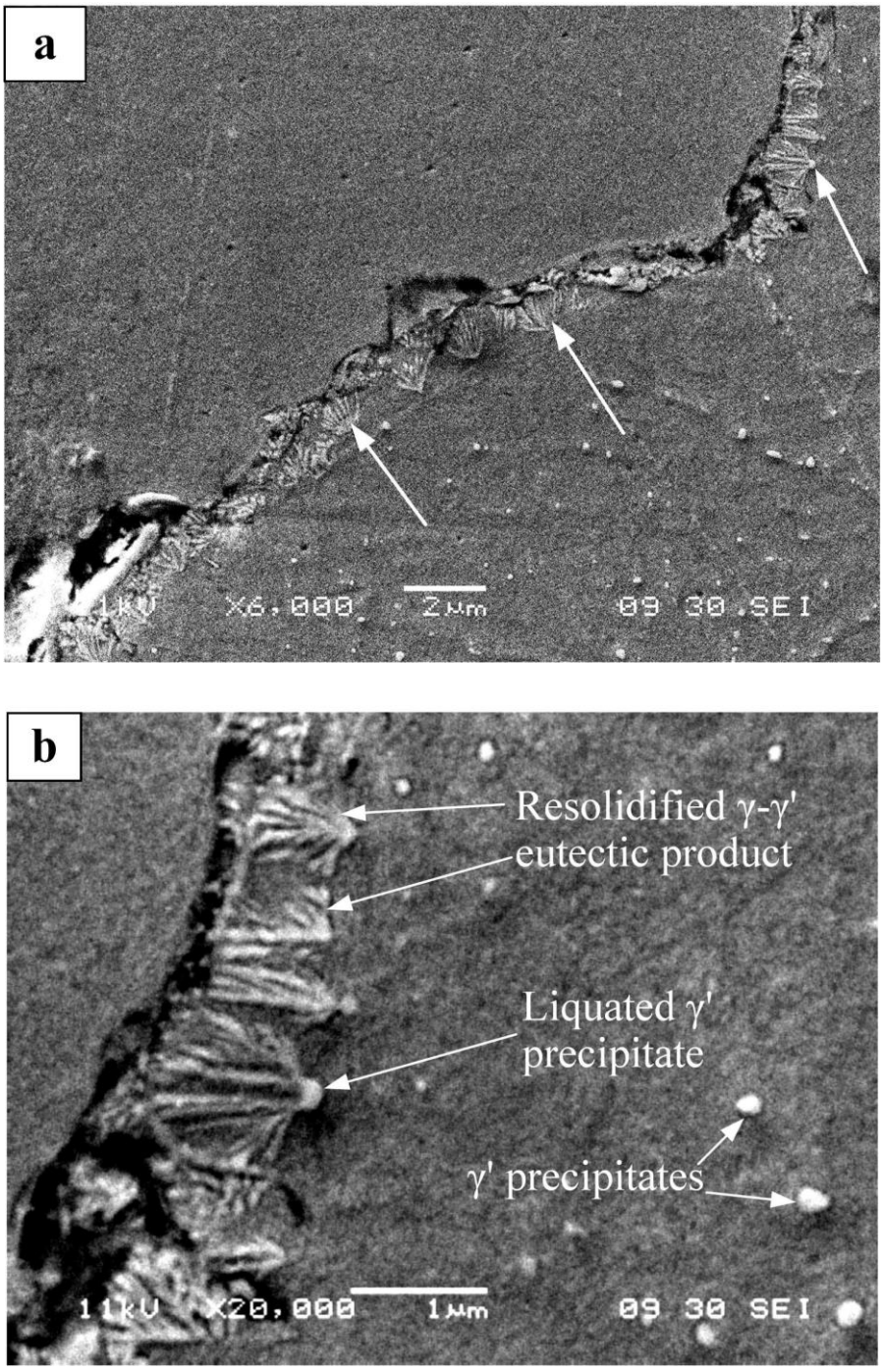

Figure 4.33 SEM micrograph of HAZ cracks that show: a. Liquated γ′ particles along the crack path, and b. Presence of resolidified γ-γ′ eutectic constituent along the crack

4.6 Enhanced Resistance to HAZ Cracking in CoWAlloy1 - Pre-Weld Thermal Process

Chaturvedi et al. [149] reported that HAZ cracking in superalloys can be minimized or eliminated through microstructural modifications with a pre-weld heat treatment. As explained in Section 4.5.2.2, γ′ liquation could contribute to HAZ cracking in CoWAlloy1. Furthermore, γ′ is the primary strengthening phase with a high volume fraction (51%) in the as-received condition. Cao et al. [150] reported that to reduce the HAZ cracking during welding, generally, γ′ precipitation-hardened superalloys need to use a pre-weld heat treatment that produces the dissolution of γ′ precipitates. Therefore, in this work, the pre-weld heat treatment temperatures that produce partial or full dissolution of γ′ precipitates are selected. Pre-weld heat treatment at 1170°C produces the complete dissolution of primary γ′ and at temperatures of 970, 1010, and 1070°C results in partial dissolution of the primary γ′. Figure 4.34 shows a comparison between the average TCL in the HAZ of the pre-weld heat-treated samples at various temperatures and cooling conditions. It should be noted that after these heat treatments, the average grain size of the samples remains unchanged (1600 μm). The average TCL values in the AC samples are found to be higher than those of water-quenched (WQ) at 4 different temperatures, i.e., 870, 970, 1070, and 1170ºC. However, heat treatment at 1010ºC shows a similar cracking susceptibility of the HAZ for both AC and WQ conditions. In addition, for both cooling conditions, increasing the heat treatment temperature from 870ºC to 1010ºC leads to a decrease in TCL. However, as the heat treatment temperature increases from 1010ºC to 1170ºC, the cracking susceptibility of the HAZ increases significantly. This behavior indicates that the TCL values of the HAZ follow a U-shape trend with an increase in heat-treatment temperature. It has been reported that HAZ cracking during welding superalloys is affected by both mechanical and microstructural characteristics [17]. In the

following sections, the effect of these factors on the cracking susceptibility of the HAZ of CoWAlloy1 is discussed.

4.6.1 Effect of Hardness on Cracking Susceptibility of HAZ

Pre-weld hardness is one of the factors that influence the cracking susceptibility of the HAZ during the welding of superalloys [151]. Generally, liquation cracking in the HAZ results from both the welding tensile stress as the mechanical driving force and embrittlement of grain boundaries caused by intergranular liquation as the metallurgical factor. The welding tensile stresses in γ′-strengthened superalloys arise due to thermo-mechanical stresses generated during cooling and shrinkage stresses as a result of rapid precipitation during cooling [144]. Osobo et al. [18] reported that the base alloy is capable of relaxing some of the stresses that are generated during welding. This behavior is related to the pre-weld material hardness that can considerably affect the welding stress magnitude in the HAZ. Therefore, a pre-weld condition with a lower degree of hardness can significantly reduce stress which is expected to enhance resistance to cracking in the HAZ.

Figure 4.35 illustrates the hardness variations of the pre-weld heat-treated samples with the same average grain size for both the WQ and AC conditions. As the pre-weld heat treatment temperature increases, the hardness value of the WQ samples gradually decreases which is due to the dissolution of the γ′ precipitates. On the other hand, the hardness values of the AC samples are almost the same when they are heat-treated at temperatures that range from 870°C to 1070°C, followed by a decrease as the temperature is increased to 1170°C. In addition, at temperatures that exceed 870°C, the WQ samples show considerably less hardness than the AC samples at the same heat treatment temperatures, which is due to the higher volume fraction of γ′ precipitates formed

during air cooling. In this work, an increase in the hardness is not accompanied by increased cracking susceptibility of the HAZ which contradicts common expectations. As an example, although the pre-weld heat treatment of 1170°C of the WQ sample produces the lowest hardness values among all the samples, it is second in the highest cracking susceptibility of the HAZ. Furthermore, there is a considerable difference between the hardness values for samples heat-treated at 1010ºC with the different cooling methods. However, the cracking susceptibility of the HAZ is comparable in these two samples. Therefore, in the CoWAloy1 samples which have the same pre-weld grain size, it is found that the hardness of the pre-weld alloy does not impact the cracking susceptibility of the HAZ during welding. This unusual behavior in CoWAlloy1 is discussed in Section 4.9.

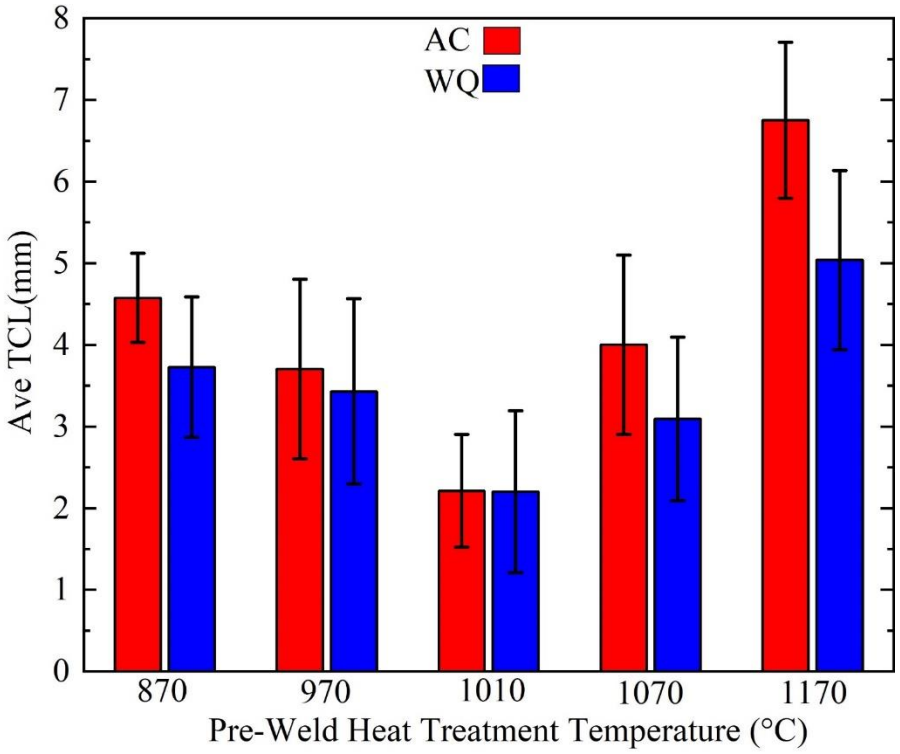

Figure 4.34 Cracking susceptibility of the HAZ of CoWAlloy1 at different pre-weld heat treatment temperatures

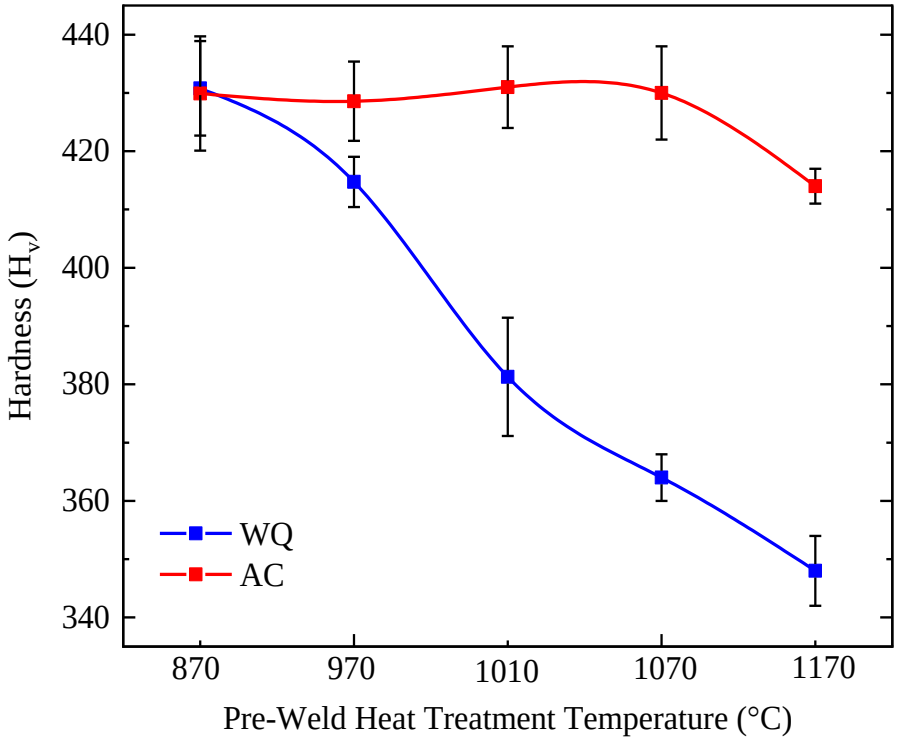

Figure 4.35 Variations in hardness of CoWAlloy1 with different pre-weld heat treatment temperatures and cooling conditions.

4.6.2 Effect of Grain Boundary Segregation on Cracking Susceptibility of HAZ

Another key factor that has been reported to affect the cracking susceptibility of the HAZ in superalloys, aside from hardness, is the grain boundary segregation of minor elements such as B [12], which can occur both before and during the welding process. The B total segregation as a function of temperature illustrated in Figure 2.16 shows a similar trend as the current work as shown in Figure 4.34 which is a U-shape relationship between the TCL in the HAZ and pre-weld heat treatment for both the AC and WQ conditions. This suggests that the grain boundary segregation of B controls the susceptibility of cracking in the HAZ of CoWAlloy1. Therefore, an increase in temperature from 870°C to 1010°C causes a shorter TCL in the HAZ possibly due to equilibrium grain boundary segregation. However, from 1010°C to 1170°C, the TCL increases which could be due to non-equilibrium grain boundary segregation. Furthermore, for the same temperatures as the cooling rate increases from AC to WQ, the TCL increases for all temperatures which is attributable to an increase in grain boundary elemental segregation. In addition, as the temperature increases, the contribution of non-equilibrium segregation is expected to increase, which can explain for the large difference in the TCL between the AC and WQ conditions at 1170°C. The results presented in Figure 4.34 show that the cracking susceptibility of the HAZ of CoWAlloy1 appears to be minimum at 1010°C which may be due to a balance between equilibrium and non-equilibrium grain boundary segregation.

To validate the dependency of the cracking susceptibility of the HAZ on the grain boundary segregation of B, a ToF-SIMS analysis was conducted on samples subjected to heat treatments at 1010°C and 1170°C and then subsequently AC. These two pre-weld heat treatments result in the shortest and longest TCL in the HAZ, respectively (Figure 4.34). The samples were marked with a nano-indenter to identify the grain boundary locations, and a ToF-SIMS line scan was performed

from one indentation mark to another. As shown in Figure 4.36, the B intensity at the grain boundaries in the 1170^{o}C AC sample is marginally higher than that in the 1010^{o}C AC sample. This indicates a larger degree of grain boundary segregation of B when the sample is heat treated at 1170^{o}C and then AC as opposed to 1010^{o}C and then AC. This result coupled with the analysis of the TCL in the HAZ (Figure 4.34) confirms that the grain boundary segregation of B controls the cracking susceptibility of the HAZ in CoWAlloy1.

Ojo [17] reported that elemental grain boundary segregation contributes to the susceptibility of superalloys to HAZ liquation cracking. This process consists of the segregation of minor elements such as B at the grain boundaries which results in a localized composition with a lower melting point at the grain boundaries. During the welding process, preferential melting occurs along these boundaries above a critical temperature, which renders them susceptible to the formation of HAZ liquation cracking. Grain boundary elemental segregation increases the solidification temperature range as a result of the low partitioning coefficient of B in superalloys, therefore, a larger volume of liquid persists to lower temperatures which may reduce resistance to HAZ cracking [20][152]. Furthermore, grain boundary segregation of minor elements such as B has been reported to increase the wettability of the liquid formed on the grain boundaries by reducing the solid-liquid interfacial energy. This increase in wettability facilitates the spread of the liquid film along the grain boundaries [87] which makes the grain boundaries prone to cracking.

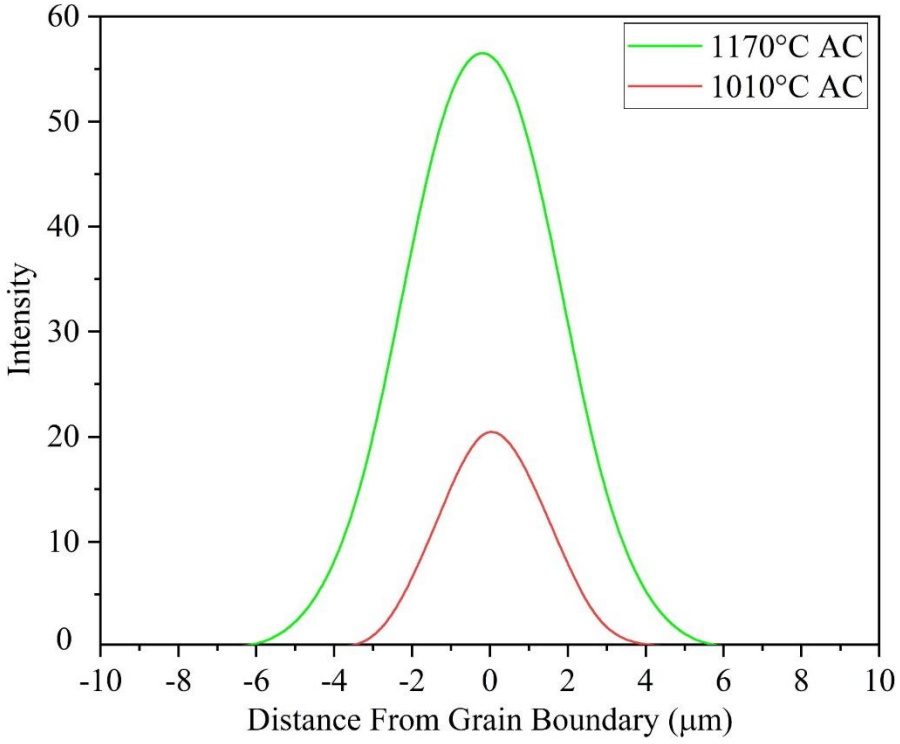

Figure 4.36 ToF-SIMS line scan profile of B intensity at grain boundaries of 1170°C AC and 1010°C AC samples

4.6.3 Effect of Grain Size on Cracking Susceptibility of HAZ

Another factor that affects the cracking susceptibility of the HAZ independent of second phases or composition, is the grain size [153]. To investigate the influence of grain size on the cracking resistance of the HAZ in CoWAlloy1, grain refinement was performed by using a cold rolling process and subsequent annealing heat treatment. Consequently, samples with an initial average grain size of 60 μm were obtained and subjected to three pre-weld heat treatments at temperatures of 870°C, 1010°C, and 1170°C and then AC, which produced a medium, the shortest, and longest TCL in the HAZ respectively, in the samples with a large grain size of 1600 μm (Figure 4.34). Figure 4.37 shows an optical micrograph of a weld region in the 1010°C AC sample with refined grains, which exhibits HAZ cracking. Figure 4.38 shows the TCL of the HAZ as a function of the three selected pre-weld heat treatments for two different grain sizes. The grain refinement from 1600 μm to 60 μm leads to a reduction in the TCL of the HAZ by 69%, 70%, and 55% for 870°C AC, 1010°C AC, and 1170°C AC respectively. Therefore, a smaller grain size considerably reduces the cracking susceptibility of the HAZ in CoWAlloy1. Osoba et al. [19] reported that the grain size controls the grain boundary surface area over which the intergranular liquid must spread. As the grain size is reduced, more grain boundary surface area would be available which allows the intergranular liquid film to spread more widely, thus resulting in a decrease in liquid film thickness. Miller and Chadwick [154] found the following correlation among the tensile stress (σ) needed to form the liquation crack, the surface tension at the solid-liquid interface (γ_{sl}), and the liquid film thickness (h),

$$\sigma = 2\gamma_{sl}/h \qquad (4\text{-}2)$$

According to Equation 4-2, it can be observed that the reduced liquid film thickness as a result of grain refinement can increase the amount of stress required to form liquation cracks, which leads to an increase in the cracking resistance of the HAZ. In addition, grain size refinement can reduce grain boundary elemental segregation, improve stress relaxation capability through grain boundary sliding, and increase the number of grain boundary triple points which increases the probability of inhibiting cracking [17][155][156].

According to the results of the weldability studies performed on arc-welded CoWAlloy1, HAZ cracking during welding can be minimized by subjecting the alloy to a pre-weld heat treatment that combines the low grain boundary segregation of B (1010°C AC) with a small grain size.

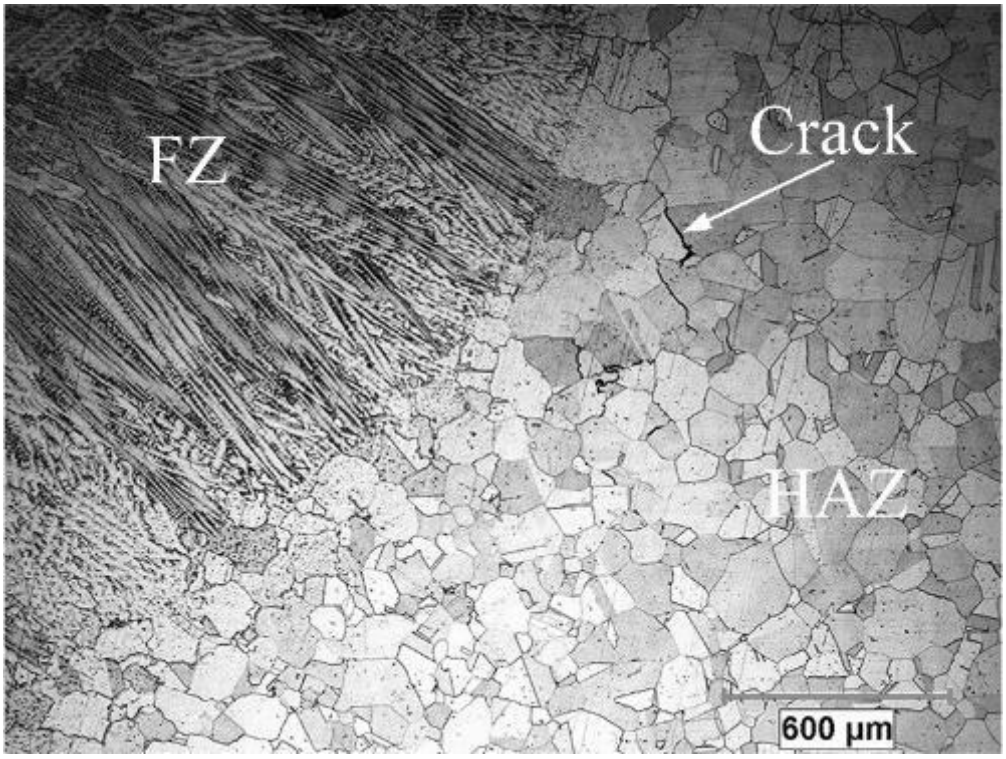

Figure 4.37 Optical micrograph of 1010°C AC sample with refined grains: HAZ cracking

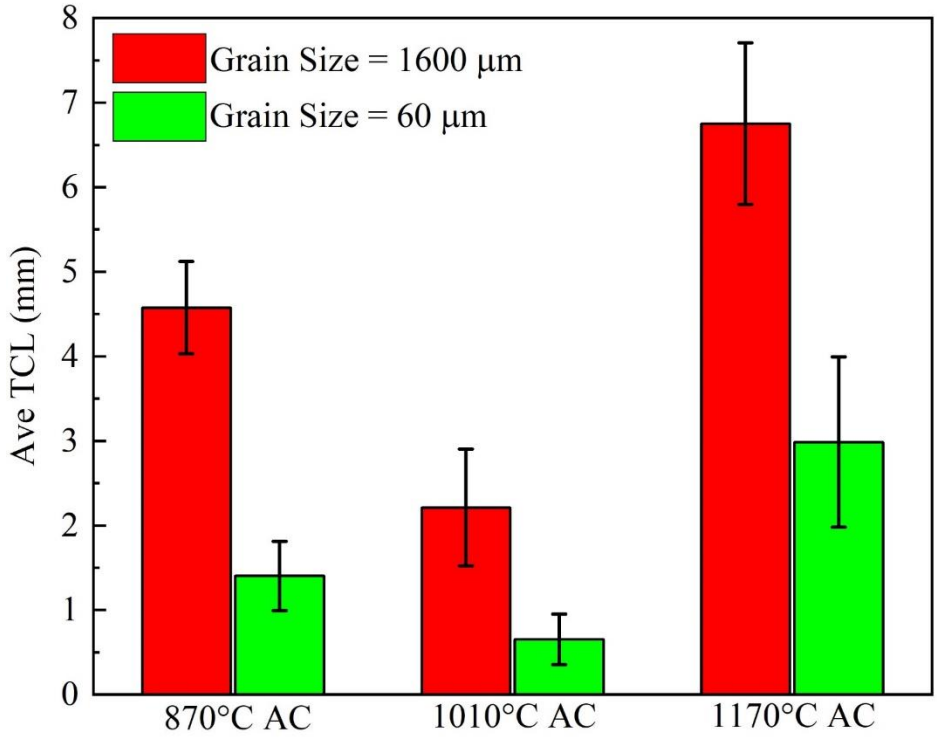

Figure 4.38 Cracking susceptibility of HAZ of CoWAlloy1 samples with different grain sizes subjected to various pre-weld heat treatments

4.7 Cracking Susceptibility of the HAZ during PWHT

Aside from cracking during welding, γ′-strengthened Co-based superalloys are also expected to be susceptible to HAZ cracking during PWHT. Similar to cracking during welding, a major factor that is anticipated to influence PWHT cracking in superalloys is the hardness of the alloy prior to PWHT [97]. In this work, two pre-weld heat treatment conditions are selected to investigate the effect of PWHT on the cracking susceptibility of the HAZ in CoWAlloy1. The first condition is using the 1010^{o}C AC sample with refined grains (henceforth 1010S) which produces the least amount of HAZ cracking during welding. The second condition is using the 1170^{o}C WQ sample with a large grain size (henceforth 1170L) which produces the least amount of hardness. The welded samples were subjected to a SHT as the PWHT. Figure 4.39 shows an SEM micrograph of the HAZ crack region of the PWHTed 1010S. It can be observed that there is a bimodal γ′ PSD and considerable γ′ re-precipitation in the HAZ.

Hardness measurements before and after the PWHT were conducted (Figure 4.40) and the hardness values of 1010S and 1170L were found to be 406 H_v and 348 H_v respectively. However, after the PWHT, both 1010S and 1170L exhibit the same hardness of 480 H_v. The measured TCL of the HAZ provided in Figure 4.41 shows that the PWHT increases the TCL by 215% and 111% for 1010S and 1170L, respectively. This shows that PWHT cracking of 1170L is less severe compared to 1010S. However, after PWHT, 1010S still has significantly less cracking at the HAZ overall compared to 1170L. This indicates that even though reducing the pre-weld hardness does not contribute to reducing the cracking susceptibility of the HAZ of CoWAlloy1 during welding, nevertheless, this minimizes HAZ cracking during the PWHT. Furthermore, minimizing HAZ cracking during welding appears to be more beneficial as the overall extent of cracking after the PWHT is governed by the extent of cracking of the HAZ which occurred during welding.

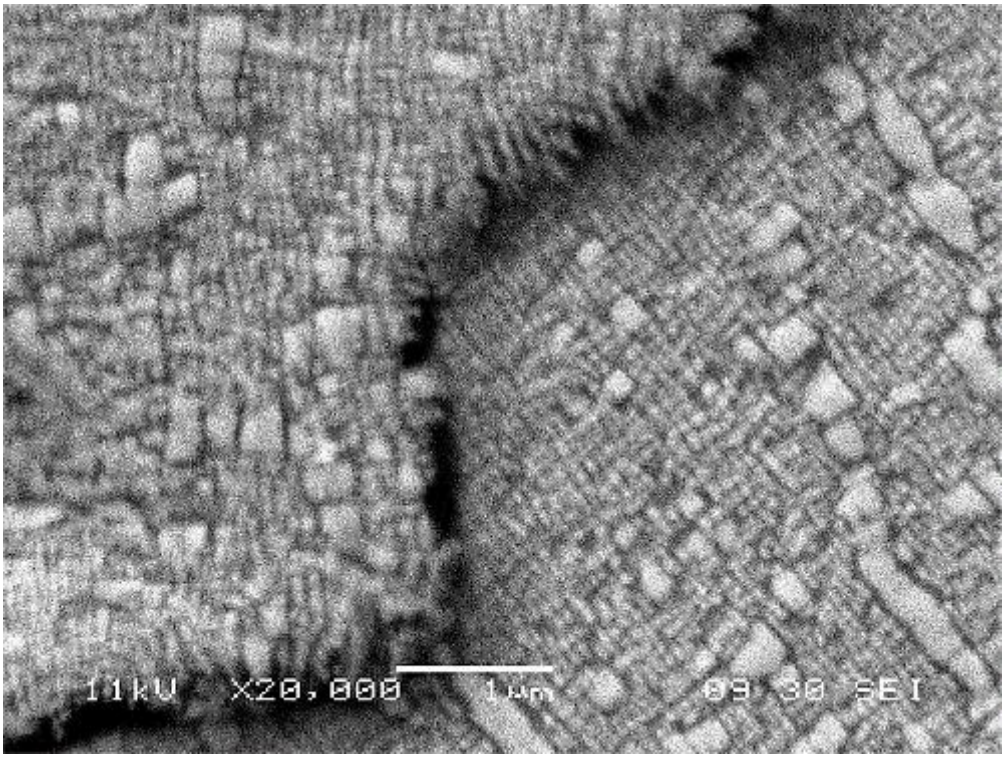

Figure 4.39 SEM micrograph of HAZ of PWHTed 1010S: re-precipitation of γ′ along a crack

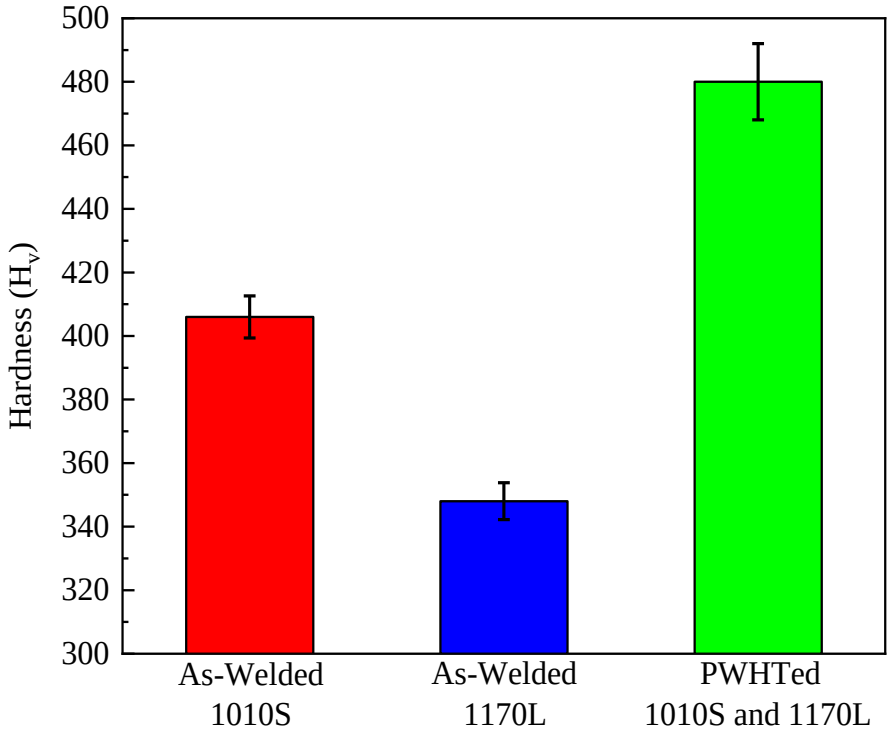

Figure 4.40 Comparison of hardness of as-welded vs PWHTed 1010S and 1170L

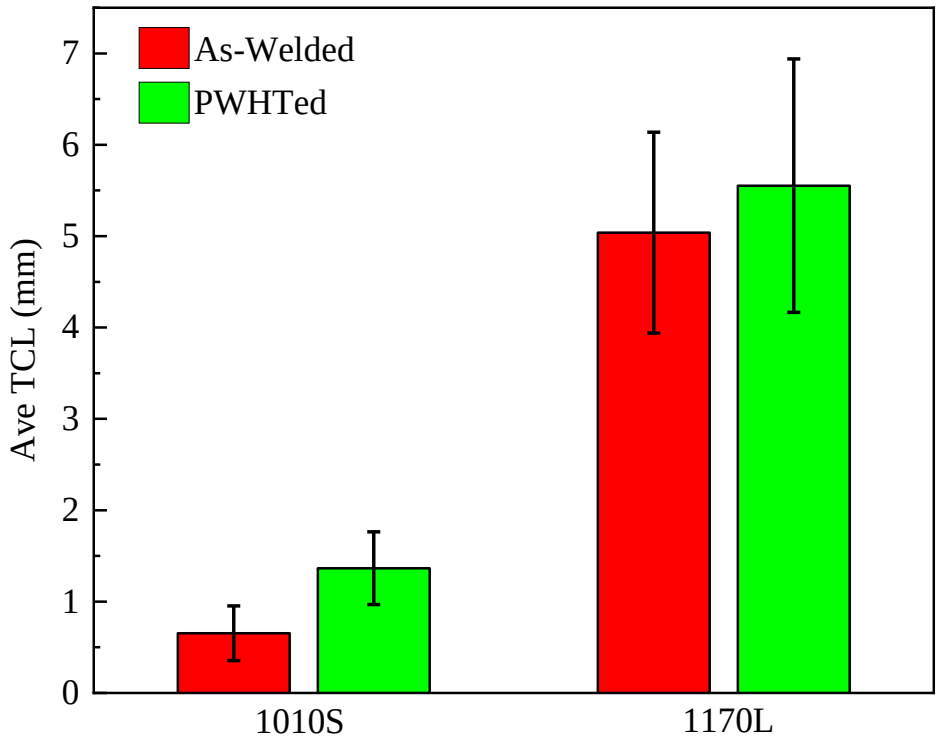

Figure 4.41 Cracking susceptibility of HAZ of PWHTed 1010S and 1170L

4.8 γ′ Re-Precipitation Behavior

The mechanical factor that causes the cracking of the HAZ in γ′-strengthened superalloys is attributed to the thermo-mechanical stress created during the cooling stage of the welding process and shrinkage stress due to rapid γ′ re-precipitation [144]. CoWAlloy1 has a high volume fraction of γ′ before welding which leads to poor weldability as a result of rapid γ′ re-precipitation and creating large shrinkage stresses during weld cooling [157]. Therefore, as γ′ re-precipitation significantly influences the cracking susceptibility of the HAZ in CoWAlloy1, in this section, γ′ re-precipitation behavior is discussed through a DSC investigation.

4.8.1 Analyses of DSC Curves for Cooling Rate

DSC signals for continuous cooling rates are shown in Figure 4.42. It is clear that one endothermic peak occurs for each cooling rate. The endothermic peak in the DSC signal is attributed to the γ′ precipitation [47]. Figure 4.42 shows that an increase in the cooling rate shifts the endothermic peak temperature to a lower temperature. For instance, at a cooling rate of 2.5°C/min, the peak temperature is 1047°C, but reduces to 1033°C at a cooling rate of 40°C/min. A similar trend has also been observed in some of the earlier studies [47][158].

Figure 4.43 is constructed by using the results of Figure 4.42 and Equation 3-11, which shows the extent of γ′ precipitates formed (F) as a function of temperature (T) for the four cooling rates. It is observed that precipitation initiates at ~1070°C for all conditions. However, the complete transformation temperature varies with the cooling rate. For example, the completion of γ′ precipitation occurs at 1028°C at a cooling rate of 2.5°C/min, while at this temperature, only 35% volume fraction of the γ′ precipitates is observed at a cooling rate of 40°C/min. This indicates that increasing the cooling rate can inhibit precipitation and complete precipitation occurs at a lower

temperature, which means the process requires a longer time. In other words, as the cooling rate increases, insufficient time is available for the solutes to diffuse and thus form precipitates. As a result, more energy is required for γ′ precipitation. According to Masoumi et al. [47], phase transformation processes in superalloys are diffusion-controlled. Furthermore, Azzam et al. [159] concluded that γ′ precipitate coarsening kinetics are controlled by the diffusion of W (in Co-Al-W ternary alloys).

The precipitation rate (*dF/dt*) as a function of temperature is shown in Figure 4.44. The plot is constructed by substituting data in Figure 4.43 into Equations 3-11 and 3-12. It is clear in Figure 4.44 that an increase in the cooling rate leads to a more rapid precipitation rate. However, the peak temperature at which the maximum transformation rate occurs shifts to lower temperatures. For instance, the maximum precipitation rate occurs at 1052°C at a cooling rate of 2.5°C/min, followed by 1047, 1044, and 1038°C at cooling rates of 10, 15, and 40°C/min, respectively.

4.8.2 Activation Energy

Figure 4.45 plots $ln(T_F^2/\beta)$ as a function of the inverse of temperature ($\frac{1000}{RT_F}$). The slope of the linear fit of these values gives the activation energy required for the γ′ precipitation. This is calculated to be 1775 kJ/mol for CoWAlloy1. The activation energy determined in the present study is higher than that of several other Ni-based superalloys [47][55][160][161][162]. Roy et al. [161] reported an activation energy of 337 kJ/mol for γ′ precipitates coarsening at the isothermal temperature in IN738LC. Masoumi et al. [47] provided a precipitation activation energy of 396 kJ/mol for the γ′ precipitates in AD730^{TM}. Meher et al. [56] reported that the growth rate of γ′ precipitates in Co-based superalloys is slower than that of Ni-based superalloys due to the very low diffusivity of the γ′-forming elements.

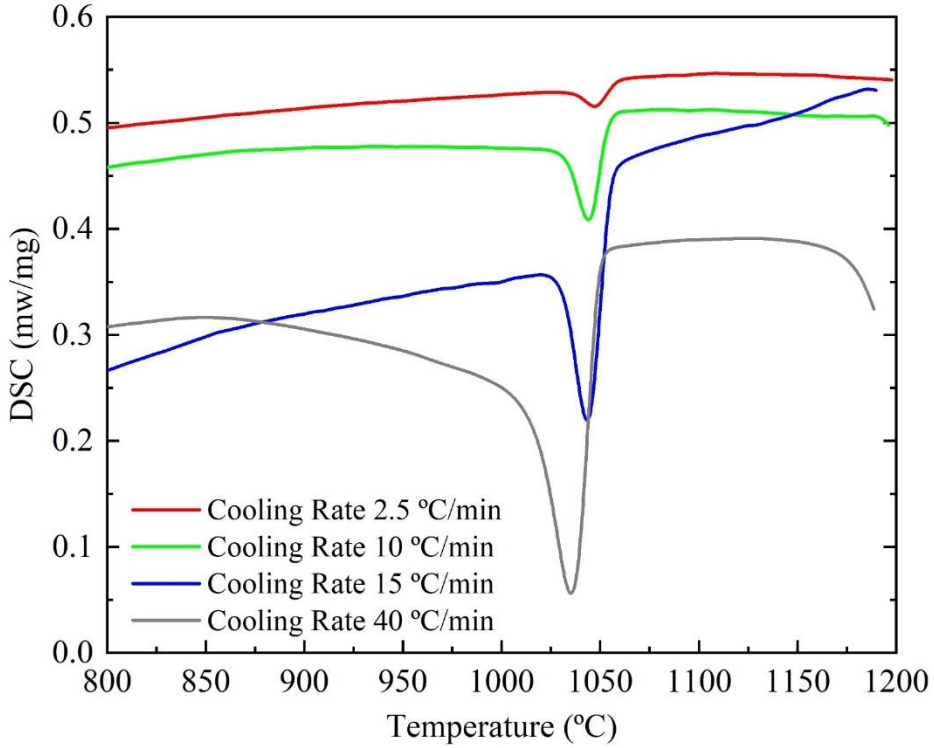

Figure 4.42 DSC curves that show γ′ precipitation peaks during cooling

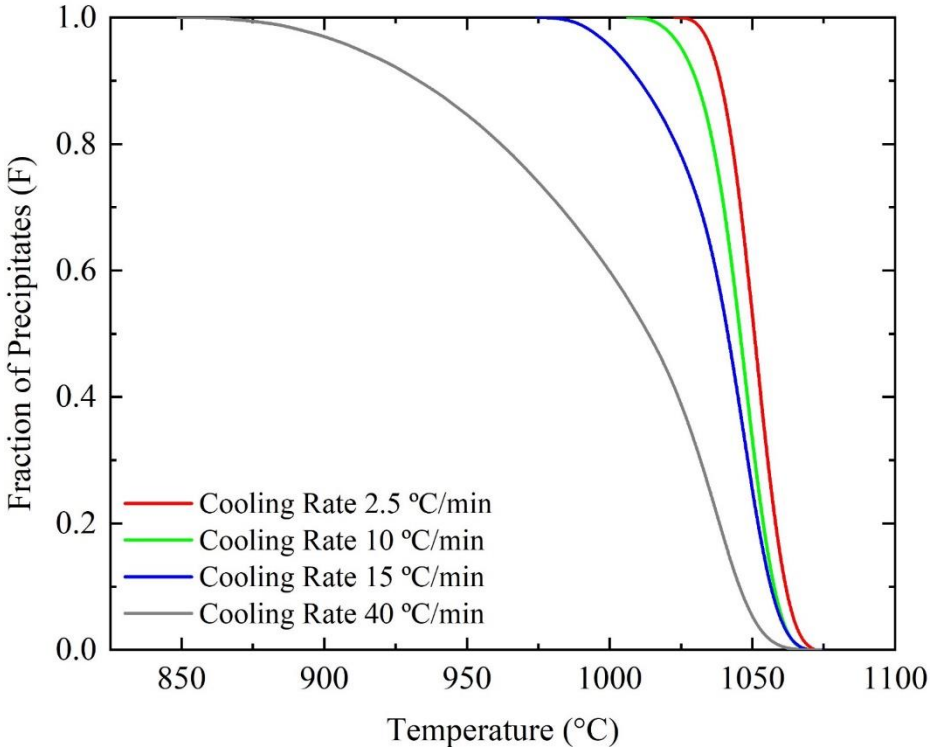

Figure 4.43 Amount of γ′ precipitates (*F*) as a function of temperature

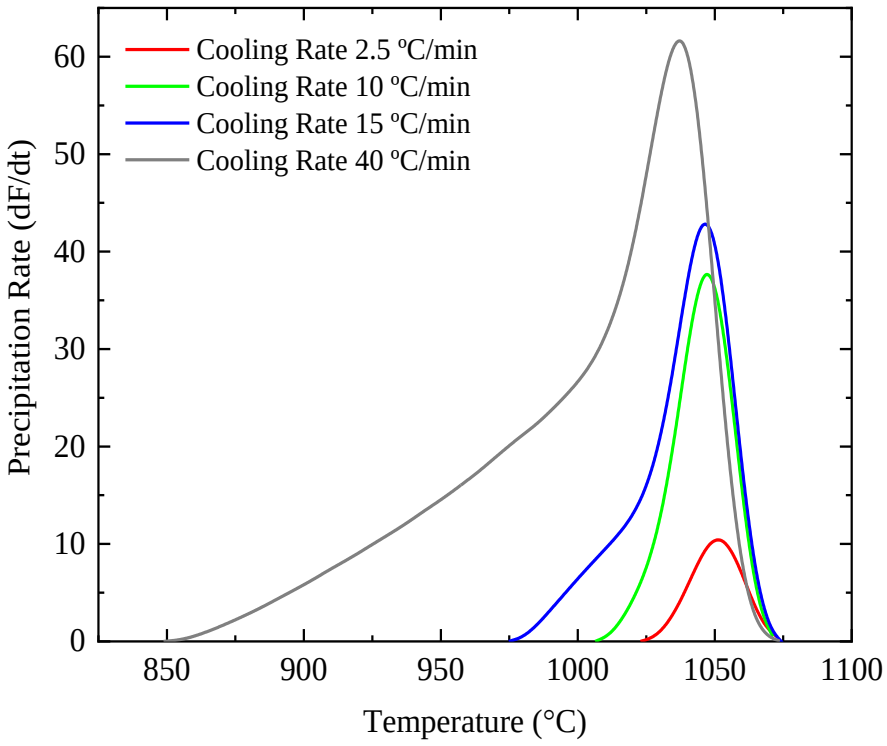

Figure 4.44 γ′ precipitation rate (*dF/dt*) as a function of temperature

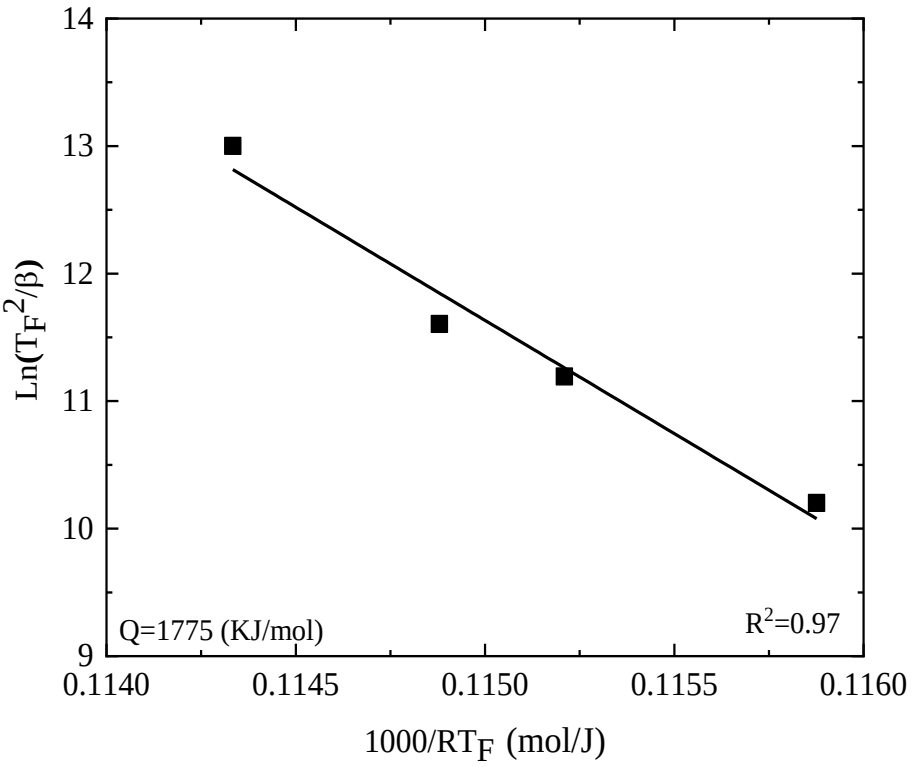

Figure 4.45 Relationship between $ln(T_F^2/\beta)$ and 1000/RT_F

4.8.3 Influence of Cooling Rate on γ′ Characteristics

Figure 4.46 illustrates the effect of different cooling rates on the morphology of the γ′ precipitates. It is clear that at all the cooling rates, the specimens show a monomodal γ′ PSD. In addition, the nucleation density increases with an increase in the cooling rate. The SEM microstructures of the specimens cooled at different cooling rates reveal that the γ′ morphology changes from cuboidal to near-spherical with increases in the cooling rate. An increase in the cooling rate reduces the time required for the growth of γ′ precipitates and allows them to retain their initial morphology i.e., spherical shape, to minimize the interfacial energy between γ/γ′. Elastic energy is another factor that determines the equilibrium shape of the precipitates [162]. This energy, which is related to the volume fraction of the precipitates and the extent of interaction between precipitates, enhances the growth of precipitates along the {001} plane during slow cooling rates. Therefore, the global internal energy increases as the γ/γ′ interfacial area increases [17]. To reduce the global internal energy, the morphology of the precipitates changes from spherical to cuboidal and then butterfly-shaped.

Figure 4.47 shows the relation between the γ′ precipitate size and the cooling rate. The figure shows that increasing the cooling rate reduces the size of the γ′ precipitates from 280 nm at 2.5ºC/min to 60 nm at 40ºC/min. A similar trend has also been reported in Mallikarjuna et al. [45], where the size of the γ′ precipitates in IN738LC alloy decreases with increases in the cooling rate, which is attributed to the reduced transport of γ′-forming elements [45].

Figure 4.48 illustrates the micro-hardness of the specimens as a function of cooling rate. It is worth mentioning that the micro-hardness of superalloys can be controlled by both the volume fraction and size of the γ′ precipitates. The statistical analysis performed by using ImageJ software on the SEM images of the specimens cooled at different rates reveals that the volume fraction of γ′ at all

cooling rates is nearly the same (51%). Therefore, a change in hardness values is considered to be a function of the precipitate size. Based on the data presented in Figure 4.48, it can be observed that an increase in the cooling rate leads to an increase in hardness as a result of the smaller γ' precipitates.

As the precipitate size increases, the inter-precipitate distance also increases; see Figure 4.46. This microstructure is in good agreement with the work of Kakehi et al. [163] who concluded that an increase in inter-precipitate distance can facilitate dislocation movement through the matrix channel. Therefore, the strength of the material is considerably reduced. However, a smaller precipitate size can reduce the inter-precipitate distance and inhibit dislocation movement, consequently increasing the strength.

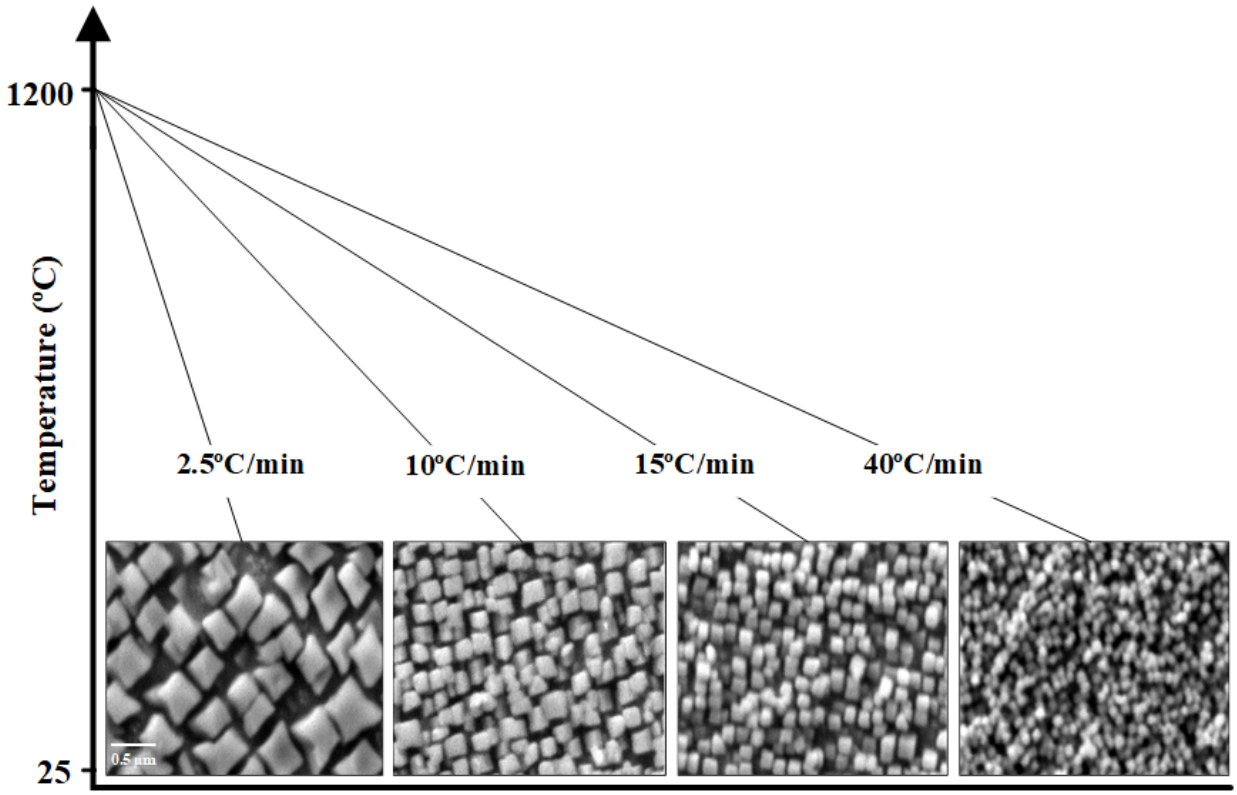

Figure 4.46 γ′ particle shapes: cuboidal at 2.5°C/min to near-spherical at 40°C/min

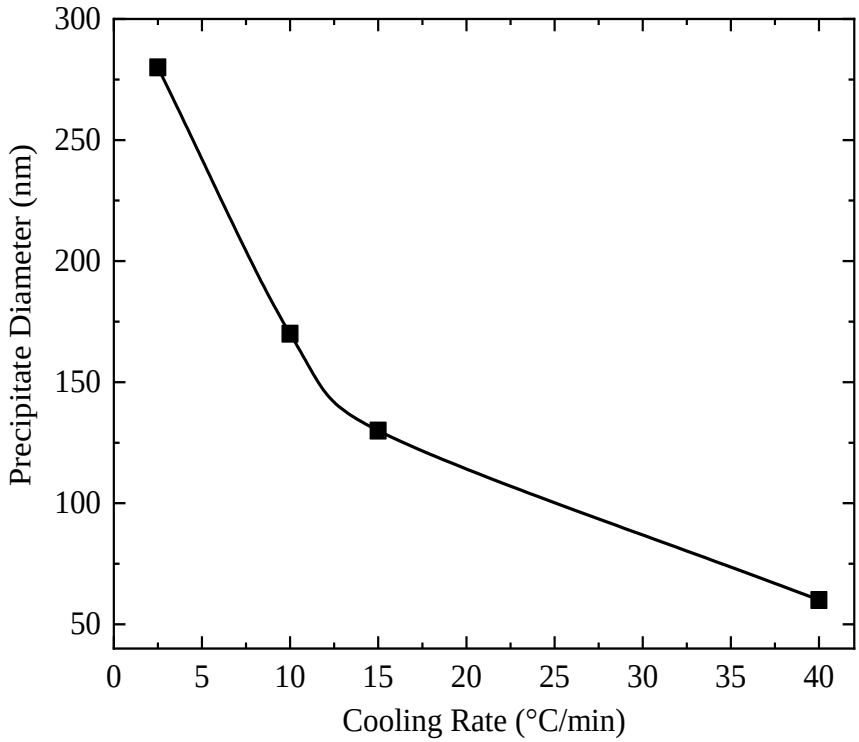

Figure 4.47 Average size of γ′ precipitates as a function of cooling rate

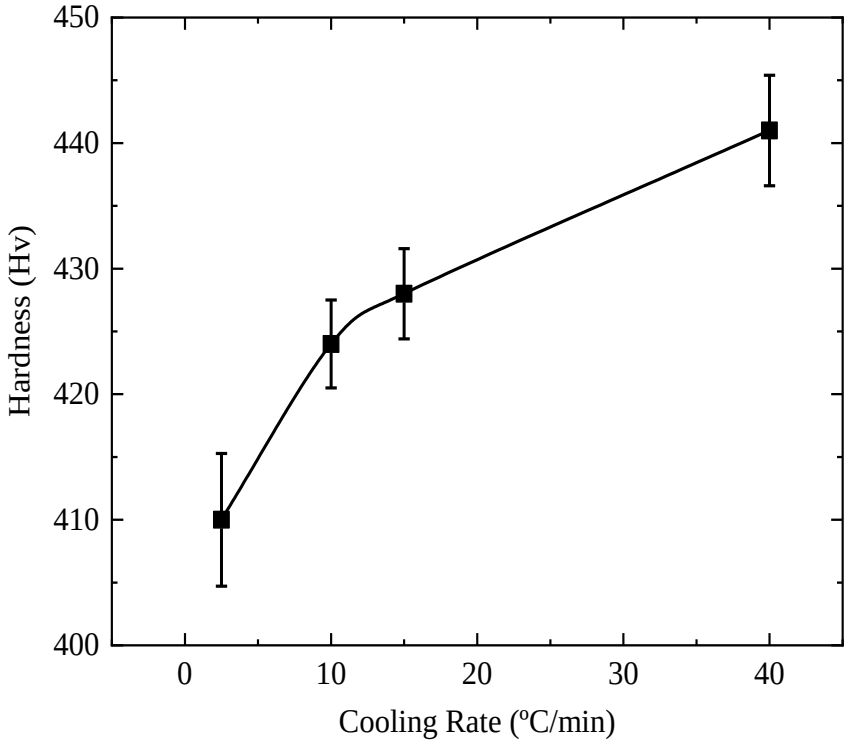

Figure 4.48 Relation between cooling rate and Vickers hardness

4.9 CoWAlloy1 Unusual Behavior

As discussed in Section 4.6.1, contrary to common superalloy behavior where increases in pre-weld hardness is accompanied by an increase in the cracking susceptibility of the HAZ during welding, increasing the pre-weld hardness does not affect the cracking susceptibility of the HAZ in CoWAlloy1.

The DSC studies (Section 4.8) showed that the γ′ precipitation activation energy is significantly higher than those of several other Ni-based superalloys. This means that γ′ precipitation in CoWAlloy1 has slower kinetics compared to the Ni-based superalloys. To validate this observation, the hardness values of CoWAlloy1 and commercially available cast Ni-based superalloy IN738LC were compared in the as-received condition and after being subjected to a temperature of 1170°C and then WQ (i.e., 1170°C WQ). The latter condition was selected to ensure the complete dissolution of the γ′ precipitates - Co_3(Al, W) and Ni_3(Al, Ti), at solvus temperatures of 1072°C and 1120°C [148], in CoWAlloy1 and IN738LC respectively.

Figure 4.49 shows that there is a drastic reduction in the hardness of CoWAlloy1 after being subjected to a heat treatment at 1170^{o}C and then WQ compared to the as-received condition. In contrast, the hardness value of IN738LC which is also subjected to a heat treatment at 1170^{o}C and then WQ shows a significant increase compared to that of the as-received condition.

Furthermore, an SEM analysis of IN738LC after being subjected to a heat treatment at 1170^{o}C and then WQ shows the formation of secondary γ′ precipitates with an average size of 65 nm which formed during cooling after the complete dissolution of the primary γ′ precipitates in the alloy at 1170^{o}C. On the other hand, primary and secondary γ′ precipitates are not observed in CoWAlloy1 after being subjected to a heat treatment at 1170^{o}C and then WQ. As γ′ is the main strengthening

phase in both superalloys, the change in hardness values is attributed to the kinetics of the γ′ formation during cooling from 1170°C. This can be observed in Figure 4.50, where IN738LC shows the rapid formation of γ′ precipitates during cooling compared to CoWAlloy1. This confirms that the γ′ precipitation kinetics in CoWAlloy1 is much slower than that in IN738LC. As the γ′ precipitation kinetics in CoWAlloy1 are slow, shrinkage stresses generated during cooling from the welding temperature would be low and as a result, may not have a significant influence on cracking during the welding process. This may explain why the hardness of CoWAlloy1 before welding does not govern the cracking susceptibility of the HAZ. In contrast, several studies on the weldability of IN738LC have shown that its pre-weld hardness influences the cracking susceptibility of the HAZ [164][165].

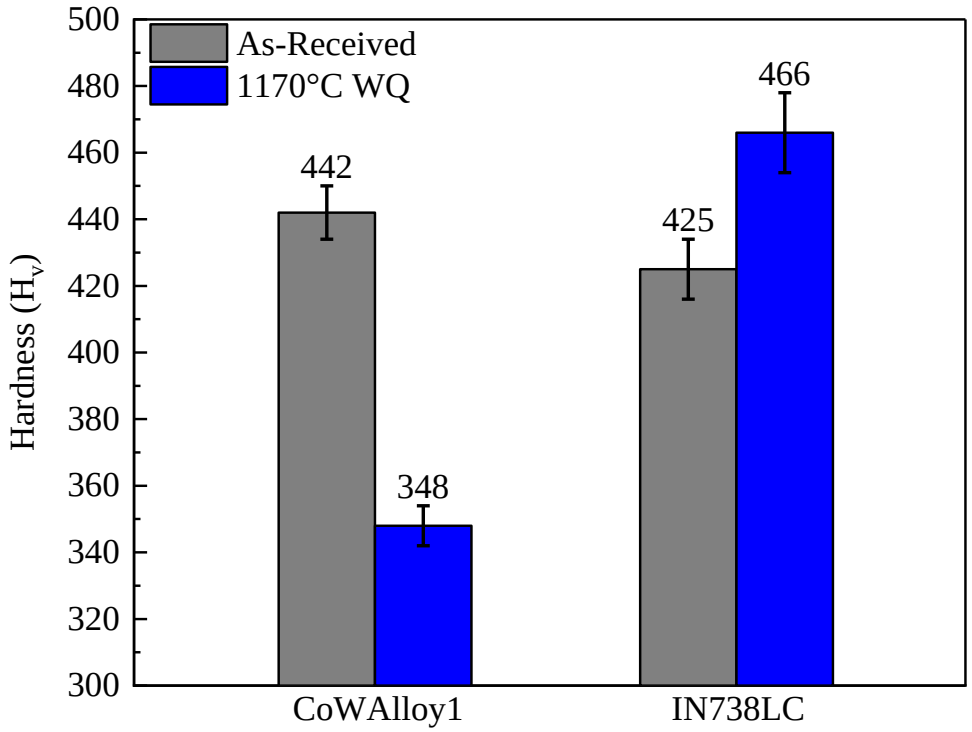

Figure 4.49 Variation of hardness in as-received conditions and solutionizing followed by water quenching: CoWAlloy1 vs. IN738LC

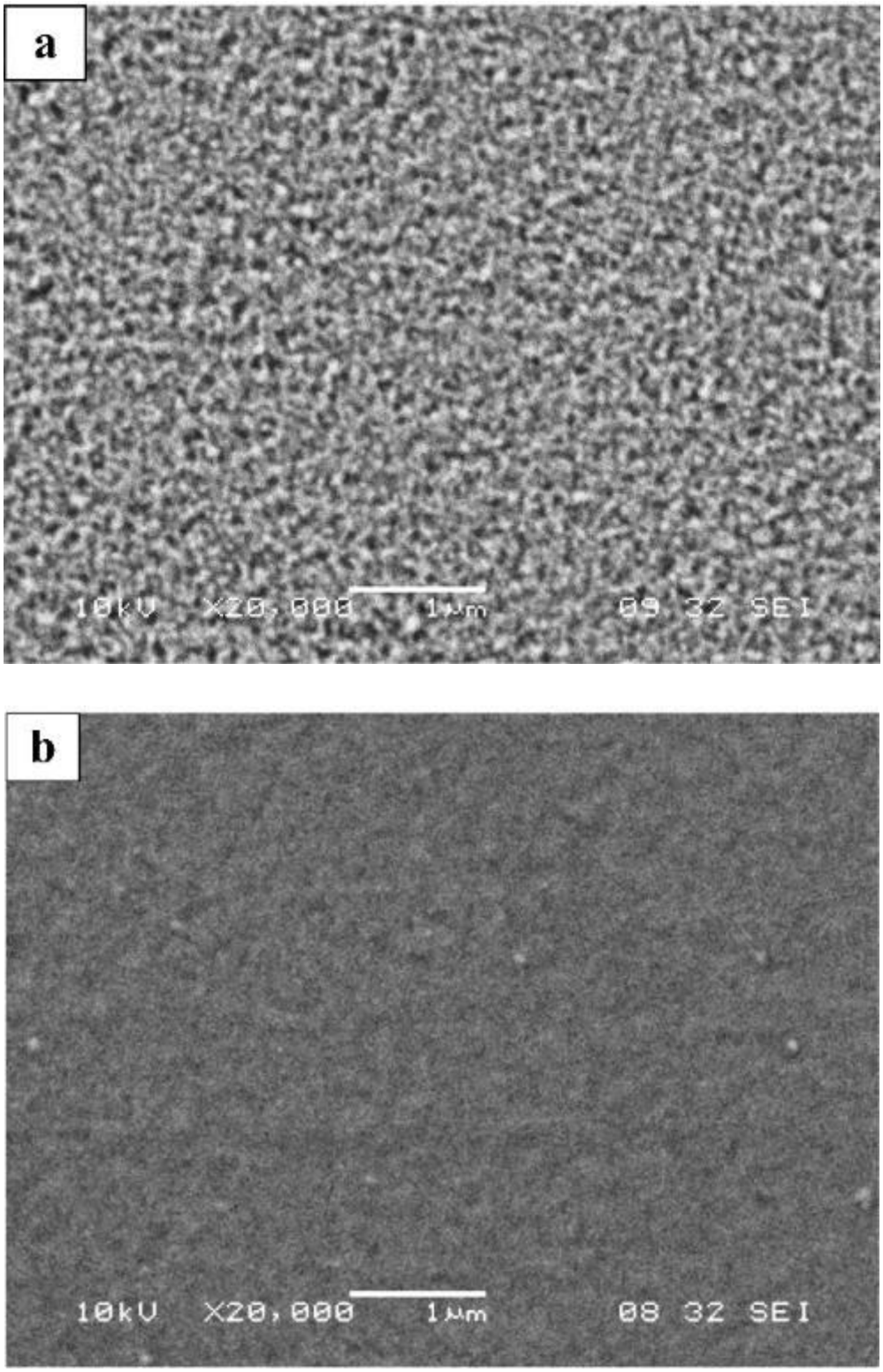

Figure 4.50 SEM micrographs of samples subjected to heat treatment of 1170°C and then WQ:

a. IN738LC (shows formation of γ′), and b. CoWAlloy1

4.10 Effect of Pre-Weld Heat Treatment and GTAW on Mechanical Properties and Hot Corrosion Behavior of CoWAlloy1

4.10.1 Mechanical Properties Study

To study the effect of pre-weld microstructural modifications on the tensile properties of the welded samples, a tensile test was conducted on the PWHTed samples (1010S and 1170L) and the alloy without welding but subjected to its full SHT. Figure 4.51 presents the stress-strain curves and ultimate tensile stress (UTS) for the various samples. It can be observed from Figures 4.51a and 4.51b that the PWHTed 1170L which exhibits the highest extent of cracking, shows very poor UTS and ductility. Even though both PWHTed 1170L and SHTed samples have a similar average grain size (1600 μm) and were subjected to the same PWHT, the strength and ductility of PWHTed 1170L are significantly lower than those of the SHTed without welding, which is attributable to the detrimental effect of HAZ cracking. In contrast, no loss in strength and just slightly lower ductility are observed in PWHTed 1010S compared to the SHTed sample without welding. The slight loss of ductility could be due to the low extent of HAZ cracking and the small grain size in this condition.

Tensile fracture locations of the two PWHTed samples are shown in Figure 4.52. In both samples, fracturing occurs at either the HAZ or FZ boundaries, which could be attributed to the formation of HAZ cracks in the welded samples. Overall, this work shows that by subjecting CoWAlloy1 to a pre-weld heat treatment that combines minimal grain boundary segregation of B with a small grain size, the HAZ cracking can be significantly inhibited both after welding and PWHT without major damage to its tensile properties.

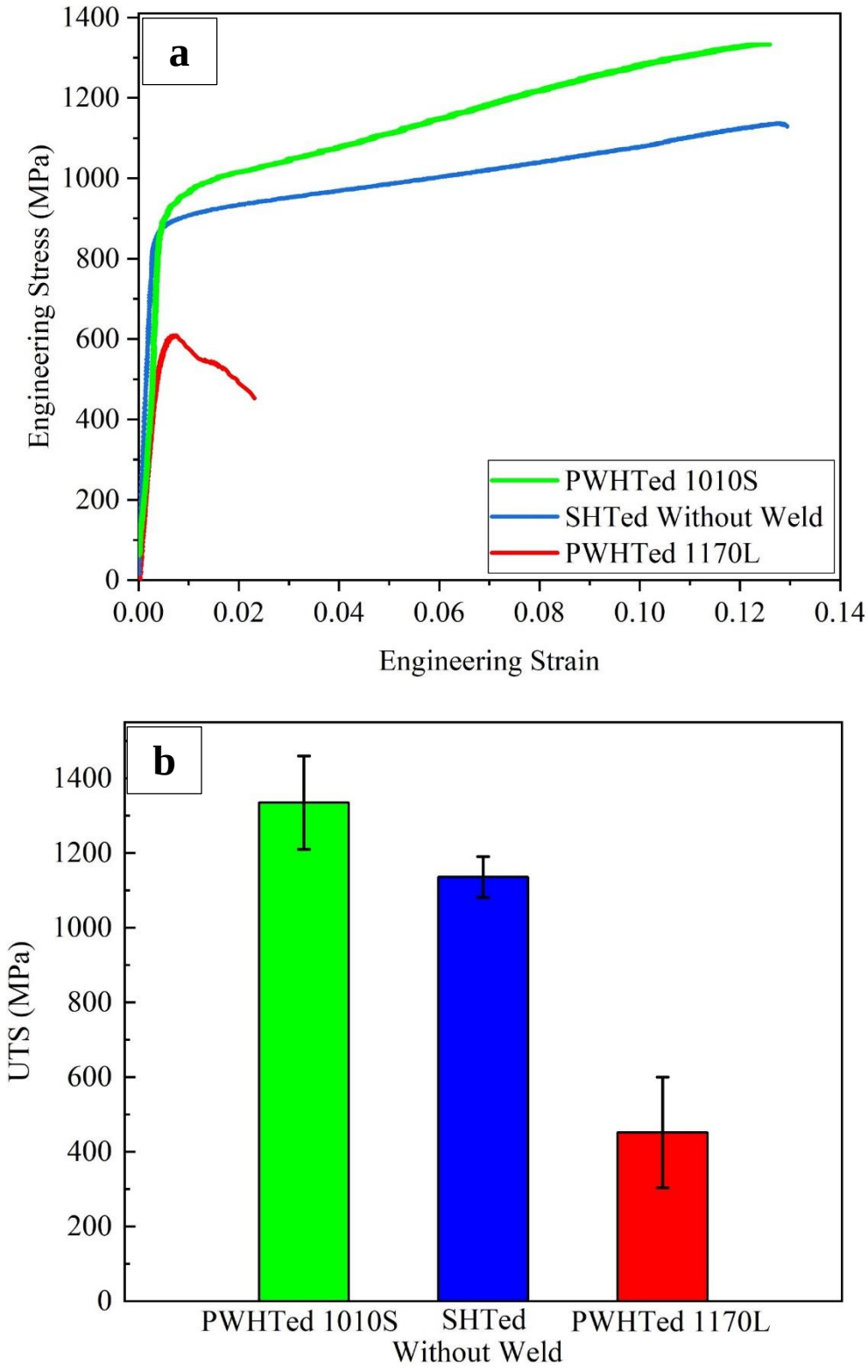

Figure 4.51 Tensile test results for various samples a. Engineering stress-strain, and b. A comparison between ultimate tensile stresses

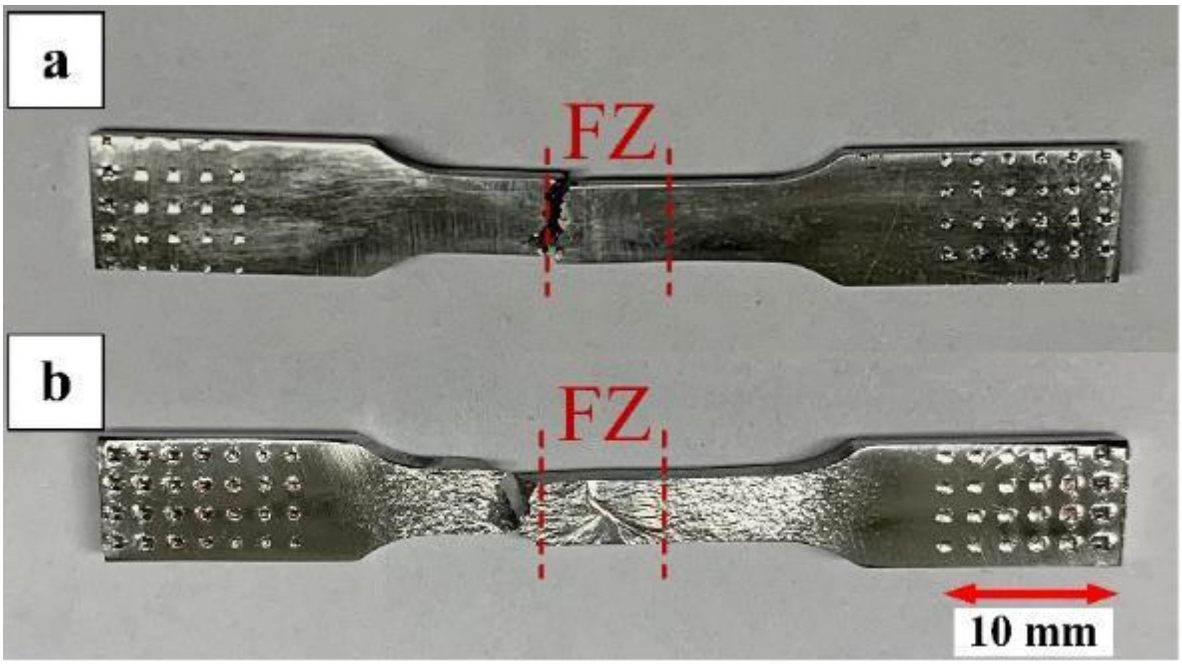

Figure 4.52 Location of the fracture in tensile samples: a. PWHTed 1170L, and b. PWHTed 1010S

4.10.2 Hot Corrosion

To study the effect of pre-weld microstructural modifications and welding process on the hot corrosion resistance of CoWAlloy1, a hot corrosion experiment was conducted on PWHTed 1010S and a sample that did not undergo welding but was still subjected to an SHT.

4.10.2.1 Weight Gain of Corroded Specimens

Figure 4.53 shows the weight gain per unit area of the welded and unwelded CoWAlloy1 specimens after 100 hrs of exposure to a corrosive environment at 750ºC. The welded specimen shows a slightly higher weight gain per unit area compared to the unwelded specimen which indicates that the former has a slightly lower resistance to hot corrosion compared to the unwelded specimen. However, the welded specimen still has higher resistance to hot corrosion compared to a conventional Ni-based superalloy, IN718 [121].

4.10.2.2 External Surfaces of Corroded Specimens

SEM micrographs of the exposed surface for both conditions are presented in Figure 4.54. Both specimens exhibit a comparable corroded surface morphology after 100 hrs of exposure to a corrosive environment. Furthermore, a semi-quantitative SEM/EDS analysis on the surface of the corroded specimens reveals that the compositions of the oxide layers and corrosive products in both specimens are similar and rich in Co, Cr, Ni, Al, Ta, Ti, W, Si, O, and S.

Asala et al. [23] reported that chemical inhomogeneity can lead to preferential corrosion in the FZ. To evaluate the occurrence of preferential corrosion in the welded specimen, the corroded surface of the FZ was studied at the early stages of the hot corrosion experiment (i.e., after 15 min of exposure).

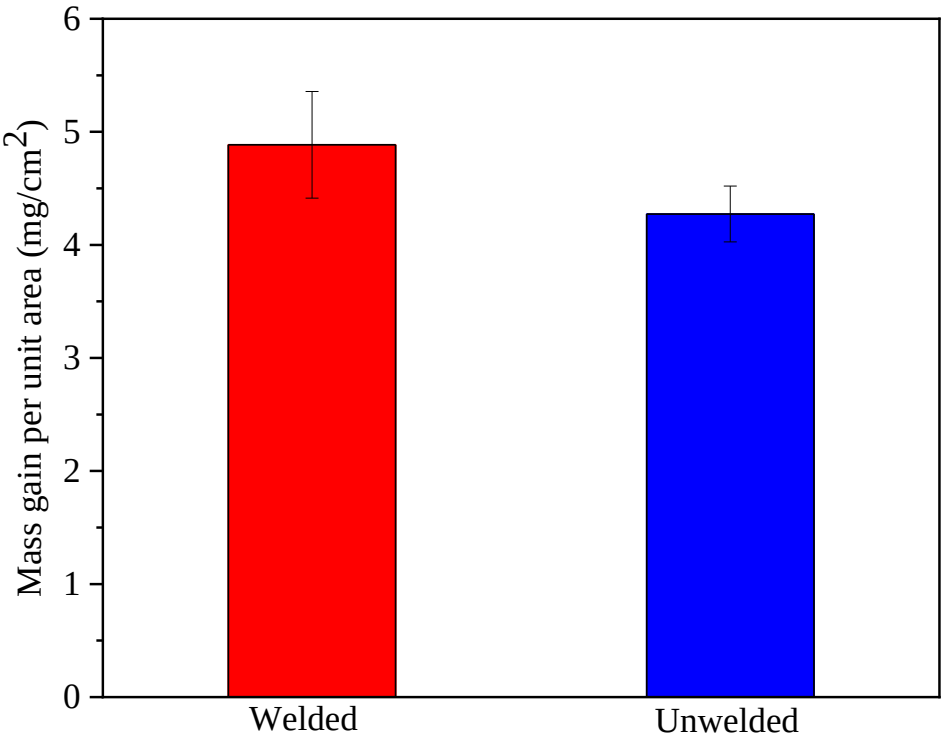

Figure 4.53 Weight gain per unit area after 100 hrs of exposure at 750ºC: welded vs. unwelded specimens.

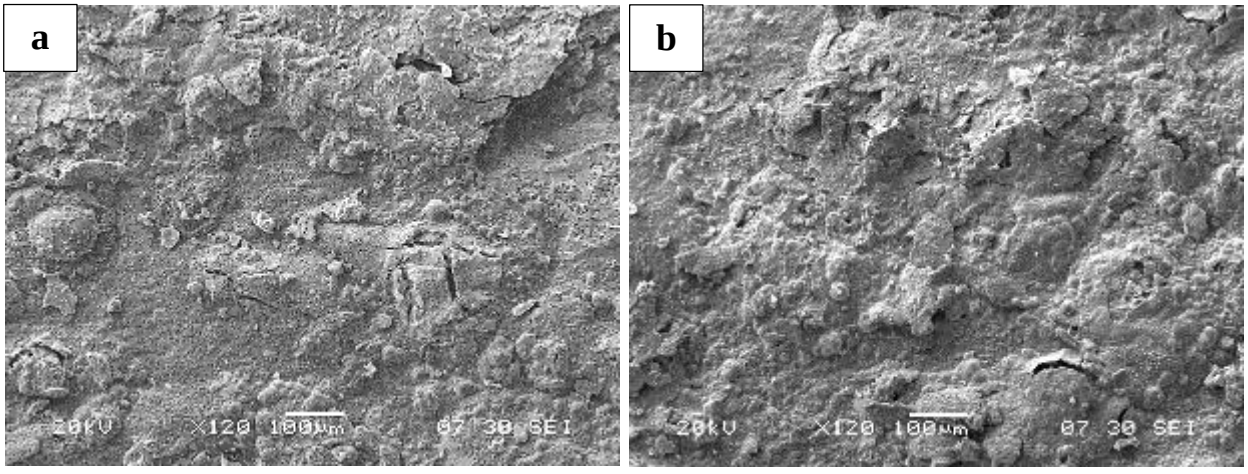

Figure 4.54 SEM micrograph of exposed surface after 100 hrs at 750ºC: a. Unwelded specimen, and b. Welded specimen

An SEM analysis on the corroded surface of the welded specimen (Figure 4.55a) reveals periodical valleys and ridges which suggest the occurrence of preferential corrosion in the FZ. Figures 4.55c-4.55i shows the results of the SEM/EDS line scan performed on the preferentially corroded region. This analysis reveals that the hill-like region is corroded more as this region is rich in O and S.

Furthermore, the SEM/EDS analysis shows that the hill-like region is rich in Al, B, C, Zr, and Si which mostly segregate in the interdendritic region. This indicates that the corroded hill-like region is attributed to the interdendritic region and the corroded valley-like region which corrodes less is attributed to the dendritic core (Figure 4.55b). It has been reported that Cr is the main element that controls the hot corrosion resistance of Co-based superalloys [107][108]. In CoWAlloy1, Cr segregates mostly at the dendritic core which leads to higher corrosion resistance in this region compared to the interdendritic regions.

Figure 4.56 shows the XRD results conducted on both the welded and unwelded specimens. The XRD results combined with the SEM/EDS analysis on the corroded surfaces reveal that the possible oxide layers formed on both specimens are Cr_2O_3, Al_2O_3, NiO, CoO, Co_3O_4, $CoAl_2O_4$, $NiAl_2O_4$, WO_3, SiO_2, TiO_2, and TaO_2. Furthermore, the possible corrosion products formed on the surface are Ni_3S_2 and Co_9S_8. These show that both the welded and unwelded conditions have similar oxide layers and corrosion products.

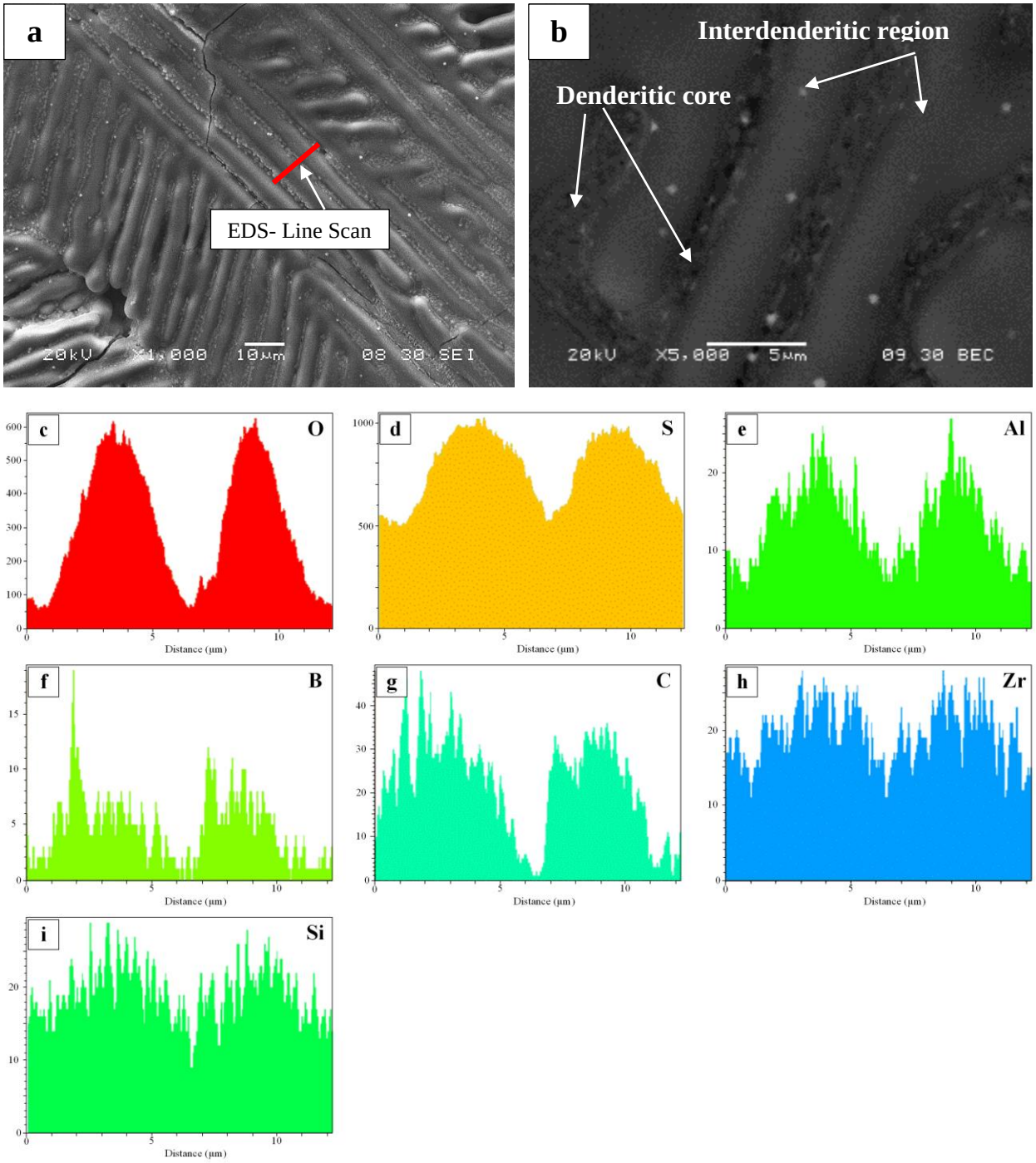

Figure 4.55 Microstructure of corroded FZ (a and b) and SEM/EDS line scan performed on the preferentially corroded region (c-i)

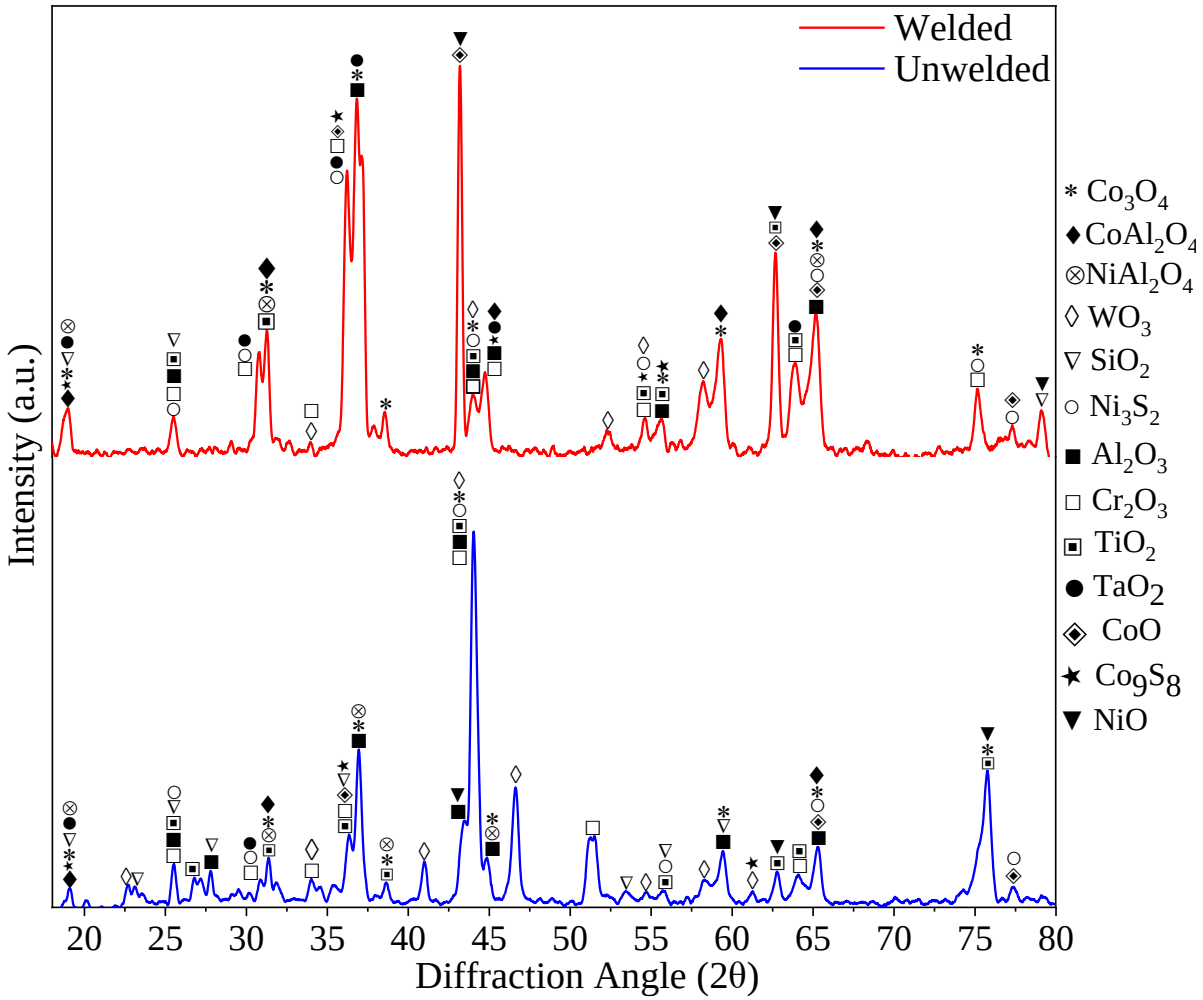

Figure 4.56 XRD results of the corroded surface of the welded and unwelded specimens after 100 hrs of exposure at 750°C.

4.10.2.3 Cross-Section of Corroded Specimens

The SEM micrographs of the cross-section of the welded and unwelded specimens after 100 hrs of exposure at 750°C, along with the corresponding SEM/EDS elemental mapping and line scans across the affected region, are shown in Figures 4.57 to 4.60. The cross-section morphology in both specimens is similar and includes three main sections of oxide scale, delamination, and internal sulphidation/oxidation. As can be observed from Figures 4.57a and 4.59a, the thickness of the oxide scale in the welded specimen is slightly higher than that of the unwelded specimen. It has been reported that the thickness of the oxide scale can significantly affect the degree of delamination [166][167]. Generally, delamination occurs during cooling to room temperature due to thermomechanical stresses [168]. The two figures show that more delamination can be observed in the welded specimen compared to the unwelded specimen. This higher delamination can be attributed to the larger oxide scale in the welded specimen which results in higher thermal stress.

The oxide scales in both the welded and unwelded specimens include two distinct oxide layers; the outer and the inner oxide layers (Figures 4.57a and 4.59a). SEM/EDS mapping and line scans across the affected region of the corroded specimens (Figures 4.57 to 4.60) reveal that the outer layer in both specimens mainly contains Co and O with a minor content of Ni. The SEM/EDS results coupled with the XRD analysis suggest the outer oxide layer to be mostly composed of Co-based oxides of CoO and Co_3O_4, with a minor amount of NiO. The formation of CoO, Co_3O_4, and NiO oxides is in agreement with the findings of previous studies on the oxidation of Co-based superalloys [169][170][171]. Gao et al. [169] reported that during the hot corrosion of Co-based superalloys, the oxide layers initially form on the alloy surface beneath the deposited molten mixed salt, followed by the occurrence of hot corrosion. As there is a higher concentration of Co and Ni than the other elements, at first, Co and Ni-rich oxides form, although Co and Ni have a weaker

affinity with O than Al and Cr [172]. The fluxing mechanism is the most widely used to explain for the initiation stage of hot corrosion in superalloys [173]. An essential condition required for the fluxing mechanism is the dissolution of the oxide scales at the interface of the molten salt and oxide scales. It has been reported that the reaction between molten salt and Co-rich oxides during the hot corrosion of Co-based superalloys leads to the dissolution of these oxides and the formation of a porous and non-protective outer oxide layer [108][174]. The formation of this non-protective oxide layer with many defects later increases the hot corrosion rate by facilitating the inward diffusion of S into the oxide scales [173]. It can be observed in Figures 4.57a and 4.59a that the outer layer in both specimens shows many defects, such as pores and microcracks. In addition, the outer layer of the welded specimen shows marginally more defects than that of the unwelded specimen which can be attributed to the slightly higher corrosion of the welded specimen.

Further investigation of the cross-section of the corroded specimens (Figures 4.57 to 4.60) reveals that the inner oxide layer of both the welded and unwelded specimens is enriched in O, Cr, Al, Ti, Ta, Si, and W. An SEM/EDS analysis coupled with the XRD results suggest that the inner oxide layer in both specimens mainly consist of Cr_2O_3 and Al_2O_3 oxides with a minor amount of $NiAl_2O_4$, $CoAl_2O_4$, TiO_2, TaO_2, WO_3, and SiO_2 oxides.

During the hot corrosion of CoWAlloy1, the formation of Co-based oxides as a result of the outward diffusion of Co leads to a reduction in Co concentration at the interface between the alloy and oxide scale. Hence, there is the accumulation of reactive elements - Cr, Al, Ti, Ta, Si, and W under the outer layer which react with O. As the oxidation rate of Al is faster than that of the other elements [172], Al_2O_3 first emerges in the inner oxide layer of both the welded and unwelded specimens. Subsequently, the reaction between Al_2O_3 with CoO and NiO leads to the formation of poorly protective oxides of spinel $NiAl_2O_4$ and $CoAl_2O_4$. The formation of these two spinels in

CoWAlloy1 is in agreement with the findings in previous studies on the oxidation of Co-based superalloys [175][176][177]. Zhu et al. [172] reported that Al_2O_3 cannot inhibit the outward atomic diffusion of the reactive elements and the inward diffusion of O. Therefore, the chemical gradient drives Cr, Ta, Ti, Si, and W to diffuse outward and react with O to form oxides in the inner oxide layer. Since the Cr content is higher than the other elements, Cr_2O_3 forms after the formation of Al-riched oxides. As the hot corrosion process continues, the remaining oxide layers form in the inner oxide layer. Based on the standard Gibbs free energy required for the formation of oxides, the oxides in the inner layer form in the order of TiO_2, SiO_2, TaO2, and WO_3 [178][179][180]. Xu et al. [181] reported that SiO_2, TaO_2, and WO_3 oxides preferentially form on the surface of the alloy. As can be observed in Figures 4.57 to 4.60, the adherent part of the oxide scales of both specimens mostly contains TaO_2, WO_3, and SiO_2, oxides.

A comparison between the inner oxide layer of both specimens with an SEM/EDS analysis (Figures 4.57 to 4.60) reveals that the Cr and Al-rich oxide layers show less porosity with higher contents of Cr and Al in the unwelded specimen. Therefore, a slightly higher resistance to hot corrosion of the unwelded specimen compared to the welded specimen can be attributed to the formation of denser Cr-oxide and Al-oxide layers in the unwelded specimen. In addition, the amount of Ti, Ta, W, and Si in the inner oxide layer of the welded specimen is slightly more than that of the unwelded specimen, which can be attributed to the chemical inhomogeneity in the FZ of the welded specimen.

Further analysis of the cross-section of the corroded specimens shows internal sulphidation/oxidation in both the welded and unwelded specimens. SEM/EDS mapping and line scan analysis (Figures 4.57 to 4.60) reveal that the matrix beneath the oxide scales is mainly depleted in Cr, Al, Co, and Ti. However, near the interface between the oxide scales and the alloy,

the matrix is rich in O, W, Ta, and Si, which indicates the occurrence of internal oxidation in both the welded and unwelded specimens. Furthermore, the internal sulphidation/oxidation region is enriched in Ni and S. From the SEM/EDS analysis, overlapping of the Ni and Co with S is evident and according to the XRD analysis, can be inferred as Ni_3S_2 and Co_9S_8 sulphides. Fu et al. [174] reported that the dissolution of the Co-oxide layer at the beginning of the hot corrosion leads to an increase in the corrosion rate and further dissolution of the protective layers of Al_2O_3 and Cr_2O_3. As the remaining oxide layers are not adequately protective, inward diffusion of S and O occurs. He et al. [182] reported that the oxidation of reactive elements results in their depletion at the matrix and subsequently enrichment of Ni at the alloy/scale interface. Furthermore, a reduction in the O activity due to the formation of reactive element oxides leads to an increase in the S activity. Therefore, the inward diffusion of S into the matrix is enhanced which leads to sulphuration with Ni and Co and continuously damages the matrix to form the affected zone [169][182]. As can be observed from Figures 4.57a to 4.59a, the internal sulphidation/oxidation thickness in the welded specimen is slightly larger than that found in the unwelded specimen which indicates a slightly lower resistance to hot corrosion as compared to the unwelded specimen. This result is in good agreement with the results acquired from the mass gain analysis shown in Figure 4.53.

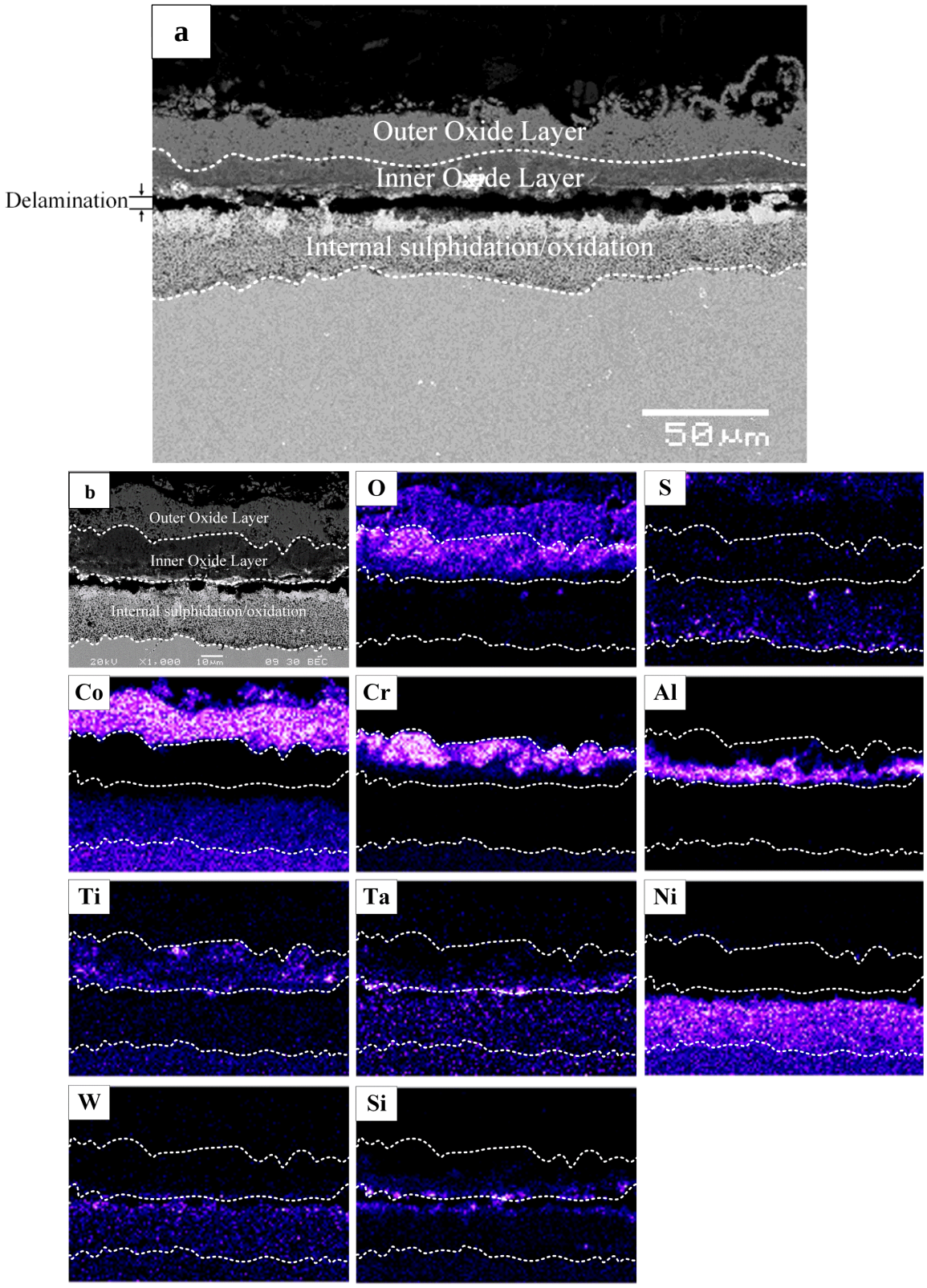

Figure 4.57 a. SEM images of cross-section of unwelded specimen after 100 hrs of exposure at 750ºC, and b. SEM/EDS compositional mapping of cross-section of unwelded specimen

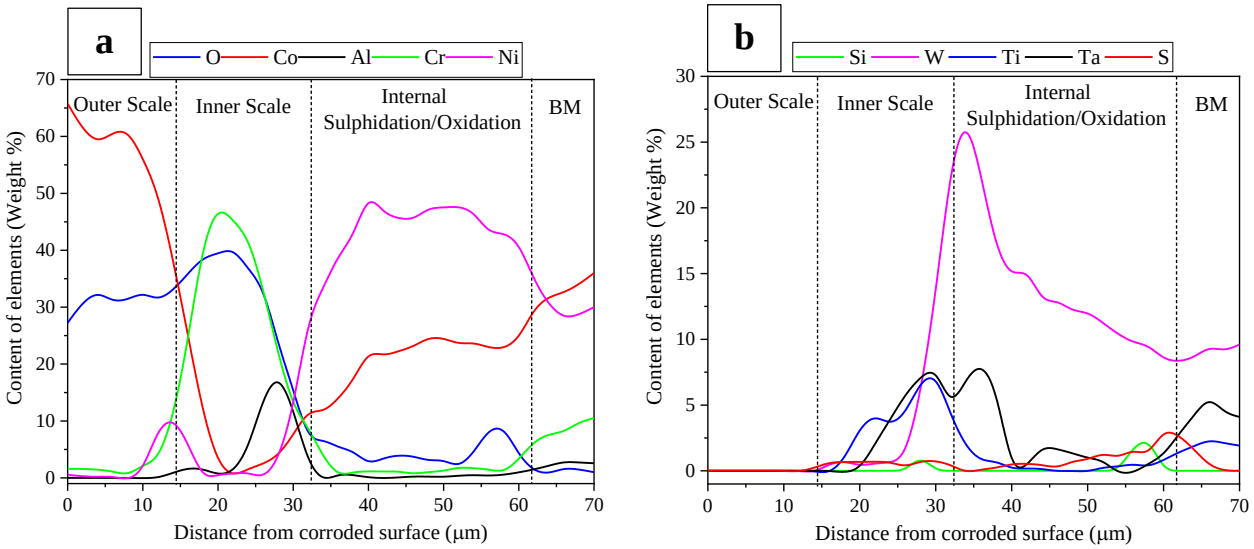

Figure 4.58 SEM/EDS composition plots of cross-section of unwelded specimen: a. O, Co, Al, Cr, and Ni, and b. Si, W, Ti, Ta, and S, versus distance after 100 hrs of exposure at 750°C. Scan starts from surface of corroded specimen (zero) moving into substrate with removal of delamination region.

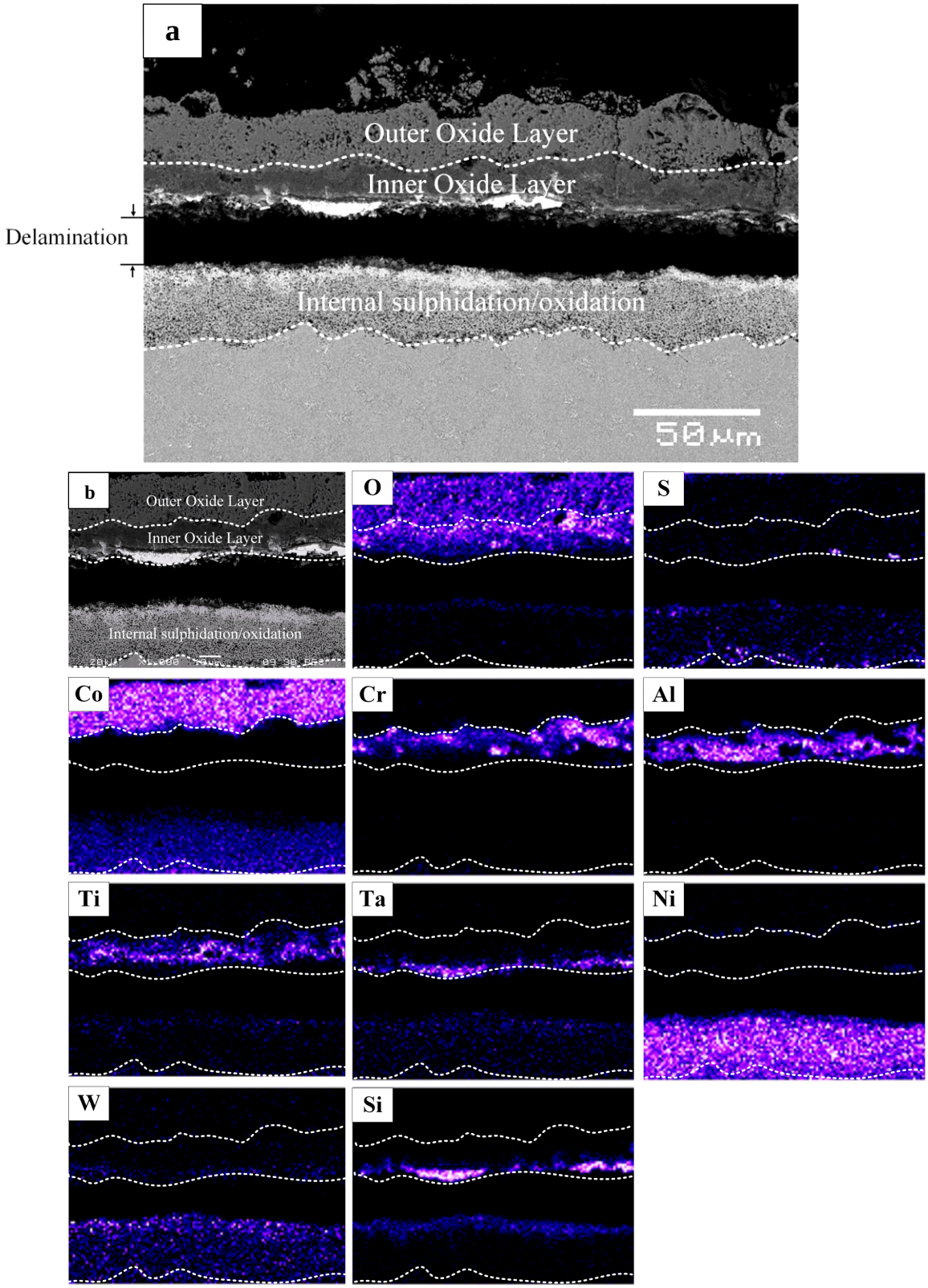

Figure 4.59 a. SEM images of cross-section of welded specimen after 100 hrs of exposure at 750ºC, and b. SEM/EDS compositional mapping of cross-section of welded specimen

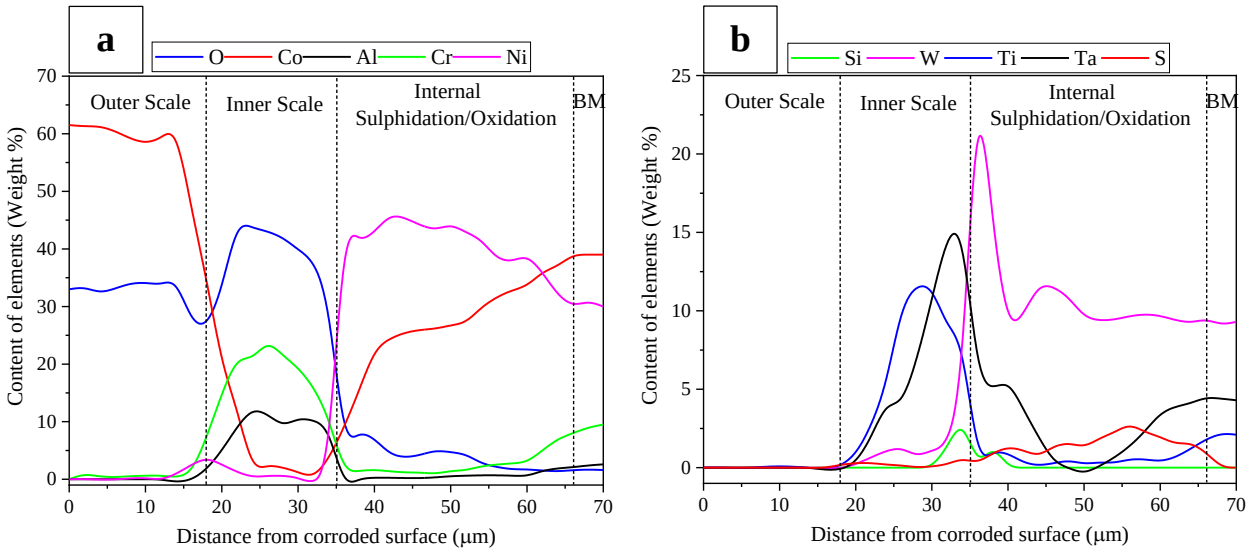

Figure 4.60 SEM/EDS composition plots of cross-section of welded specimen: a. O, Co, Al, Cr, and Ni, and b. Si, W, Ti, Ta, and S, versus distance after 100 hrs of exposure at 750°C. Scan starts from surface of corroded specimen (zero) moving into substrate with removal of delamination region.

4.11 Effect of Overaging On Cracking Susceptibility of HAZ in CoWAlloy1

Welding precipitation-hardened superalloys in an overaged condition has shown a significant improvement in the cracking resistance of the HAZ as compared to welding in solution heat treatment conditions [17][84][104]. Overaging treatment leads to the formation of coarse γ′ precipitates and decreases the pre-weld material hardness, which consequently enhances the alloy's capability to relax some of the stresses that are generated during welding [104]. In this section, the effect of overaging on the cracking susceptibility of the HAZ during welding and PWHT are discussed.

4.11.1 Effect of Overaging On Cracking Susceptibility of HAZ During Welding

To investigate the influence of overaging on the cracking susceptibility of the HAZ during welding two pre-weld heat treatment conditions are selected. The first condition is using the 1010S sample which produces the least amount of HAZ cracking during welding. The second condition is an overaged condition which is using a sample with refined grains subjected to a pre-weld heat treatment at 1010°C for 50 hrs, followed by air cooling. Figure 4.61 illustrates the hardness comparison between the two selected pre-weld heat-treated samples which have the same average grain size (60 μm), and were subjected to the same pre-weld heat treatment temperature and same cooling condition (air-cooling), but for various heat treatment times. This analysis showed that as heat treatment time increases from 4 hrs to 50 hrs, the pre-weld hardness reduces from 431 H_v to 374 H_v for the 1010S and overaged samples, respectively. This drastic reduction in hardness is attributed to the formation of a coarse γ′ precipitates in the overaged sample. The measured TCL of the HAZ provided in Figure 4.62 shows that although the overaged sample has a similar gain size, was subjected to the same pre-weld heat treatment temperature and cooling method, and

shows considerably lower hardness compared to the 1010S sample (Figure 4.61), both samples have comparable susceptibility to HAZ cracking. Therefore, as opposed to the common expectation that pre-weld overaging heat treatment reduces HAZ cracking in precipitation-hardened superalloys [84] during welding, overaging does not seem to affect susceptibility to HAZ cracking in CoWAlloy1 during welding. This result is consistent with the result from section 4.6 which showed that the cracking susceptibility of the HAZ during welding is not controlled by pre-weld hardness but by elemental grain boundary elemental segregation.

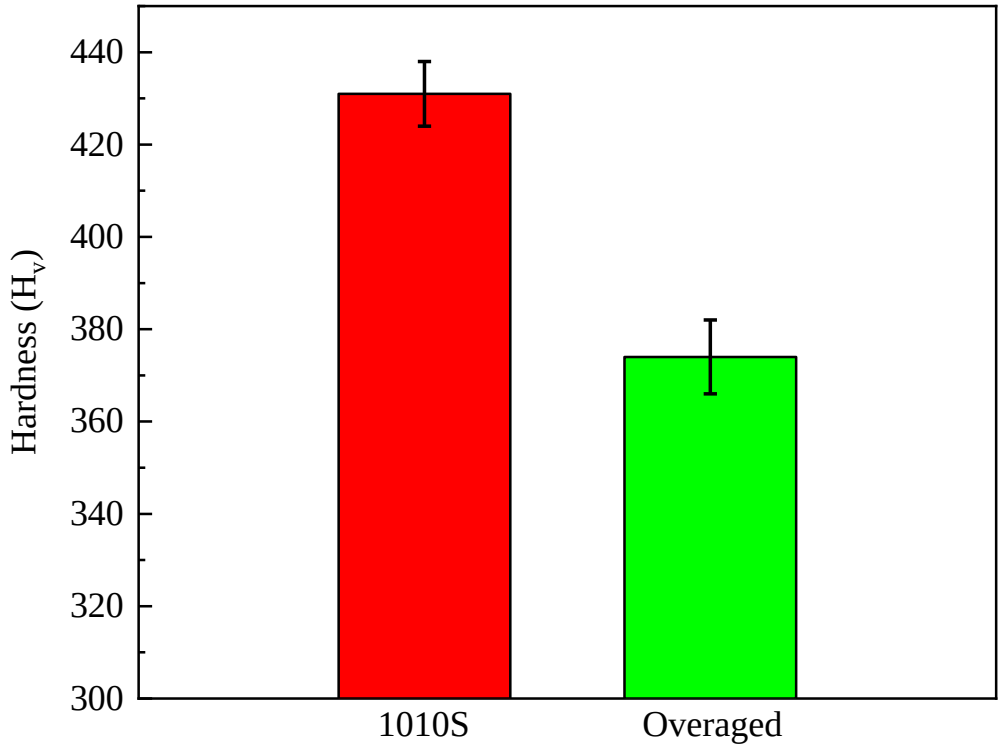

Figure 4.61 Comparison of the hardness of 1010S and overaged samples

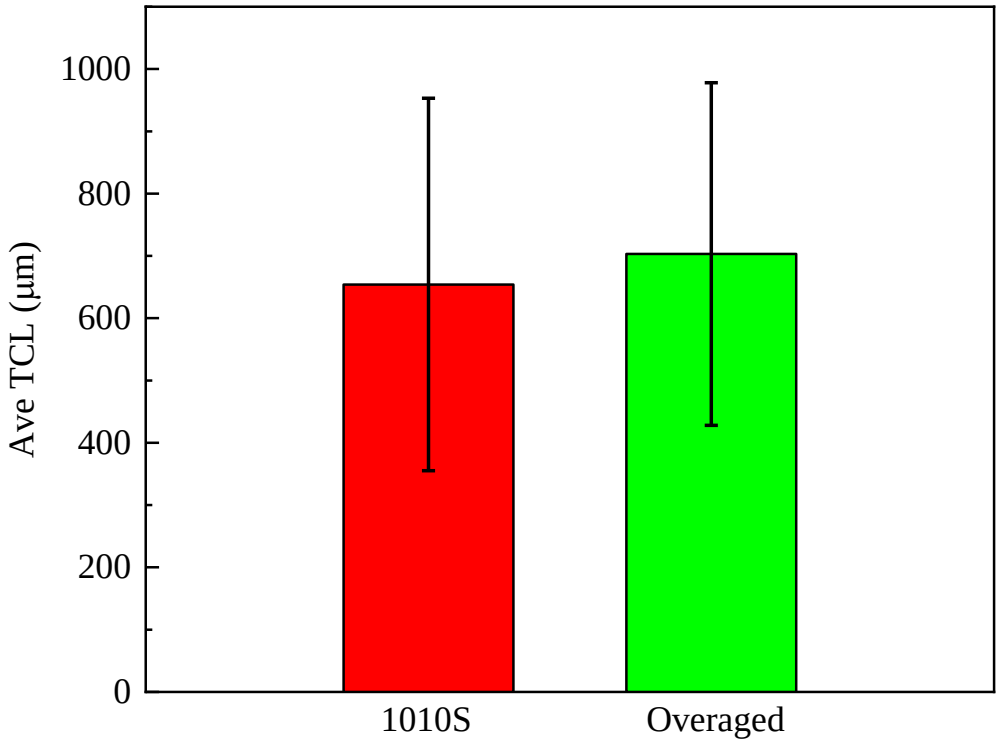

Figure 4.62 Comparison between TCL of the HAZ in 1010S and overaged samples

4.11.2 Effect of Overaging On Cracking Susceptibility of HAZ During PWHT

Overaging treatment has also been reported to reduce the cracking susceptibility of the HAZ in precipitation-strengthened superalloys during PWHT [99]. To investigate the influence of overaging on the cracking susceptibility of the HAZ during PWHT, two pre-weld heat treatment conditions are selected, the 1010S and overaged samples. The welded samples were subjected to a SHT as the PWHT. Hardness measurements before and after the PWHT were conducted (Figure 4.63) and the hardness values of the 1010S and overaged samples were found to be 431 Hv and 374 Hv, respectively. However, after the PWHT, both the 1010S and overaged samples exhibit the same hardness of 480 Hv. The measured TCL of the HAZ provided in Figure 4.64 shows that the PWHT increases the TCL of the HAZ by 215% for the 1010S sample. However, PWHT does not significantly affect the TCL of the HAZ in the overaged sample. This indicates that even though overaging does not contribute to reducing the cracking susceptibility of the HAZ of CoWAlloy1 during welding, nevertheless, this minimizes HAZ cracking during the PWHT. This result is consistent with the result from section 4.7 which showed that pre-weld hardness can significantly affect the PWHT cracking in the HAZ of CoWAlloy1.

According to this analysis, HAZ cracking in CoWAlloy1 during PWHT is minimized if the alloy is welded in the overaged condition. By subjecting the alloy to the overaged condition, PWHT cracking reduces by 46% compared to PWHTed 1010S.

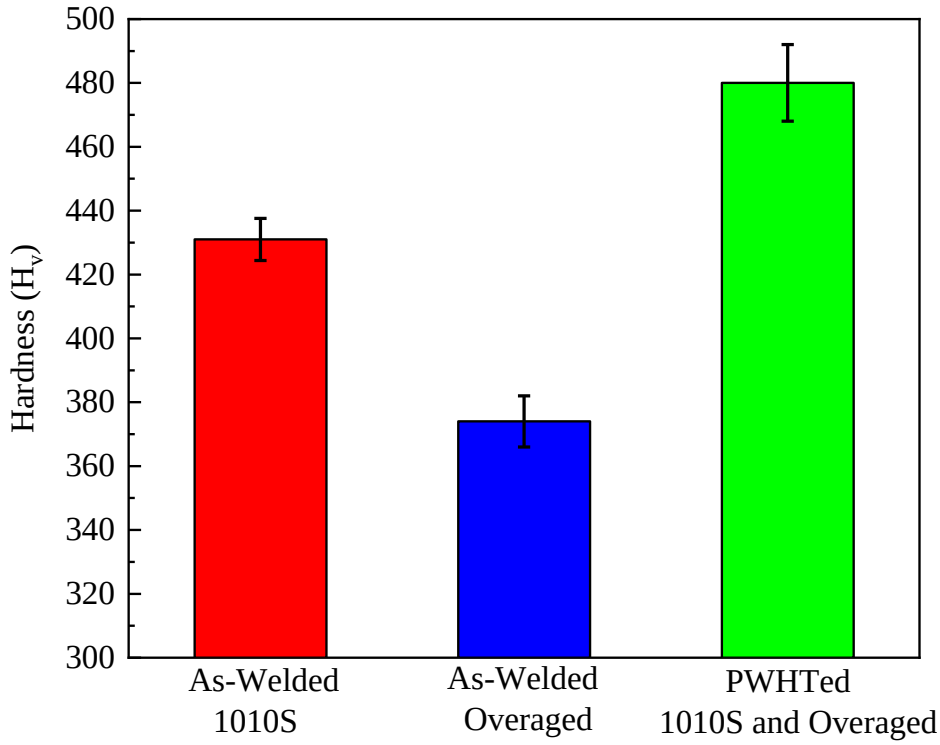

Figure 4.63 Comparison of hardness of as-welded vs PWHTed 1010S and overaged

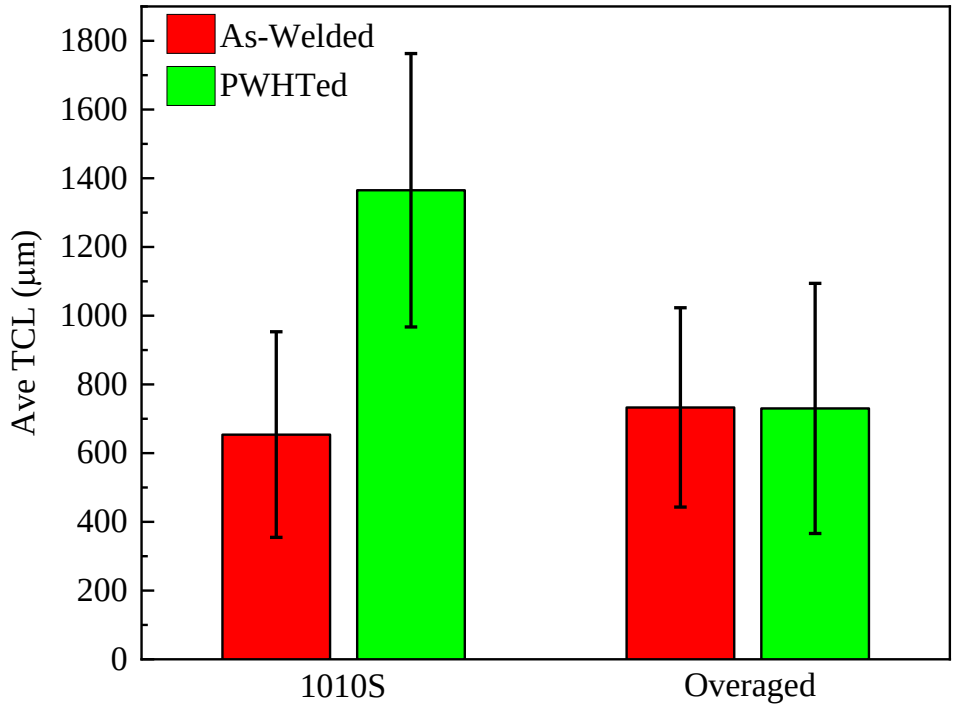

Figure 4.64 Cracking susceptibility of HAZ of PWHTed 1010S and overaged

CHAPTER 5

Summary and Conclusions

5.1 Summary

The outcomes of this research work are summarised into the following findings.

5.1.1 Numerical Modeling of GTAW of CoWAlloy1

A numerical model of the GTAW of CoWAlloy1 is developed to evaluate the influence of GTAW variables on the FZ microstructure and to obtain a window of optimum welding parameters that prevent cracking in the FZ. The major findings of the numerical modeling are as follows.

1. With constant input parameters for the welding process, the cooling rate is increased from the fusion boundary to the weld centreline. Furthermore, increasing the welding speed leads to an increase in the cooling rate within the FZ. This increase is higher at the centerline compared to the fusion boundary.

2. Increasing the welding speed results in the formation of a fine dendritic microstructure in the FZ due to an increase in the cooling rate.

3. The dendritic microstructure of the FZ is predicted to be mixed columnar-equiaxed at the weld centreline and fully columnar at the fusion boundary for all of the studied welding speeds. However, as the welding speed increases, the volume fraction of the fully columnar dendritic structure is slightly reduced.

4. The thermally modeled grain structure of the FZ is predicted to be fully equiaxed from the centerline to the edge of the fusion boundary for all three welding speeds. In addition, increasing the welding speed leads to a slight increase in the volume fraction of the region with the fully equiaxed grain structure.

5. The model developed in this study shows a good level of accuracy for predicting the solidification behavior of the FZ in the newly developed CoWAlloy1.

5.1.2 CoWAlloy1 Microstructure in As-Received vs. SHTed Conditions

The microstructure of CoWAlloy1 in the as-received and SHTed conditions are characterized by using various advanced microstructural characterization techniques, including SEM, TEM, and DSC. The key results of these microstructural analyses are as follows.

1. The microstructure of cast CoWAlloy1 in the as-received condition consists of a coarse grain structure that has a monomodal γ′ PSD with a particle size that ranges from 0.15 to 0.30 μm. On the other hand, the SHTed CoWAlloy1 shows a coarse grain structure that has a bimodal γ′ PSD with primary γ′ precipitates that range from 0.2 to 0.4 μm in size and secondary γ′ precipitates that range from 50 to 90 nm in size.

2. The presence of MC-type carbides (with M mostly Ti, Ta, and Hf) in the as-received and SHTed conditions is confirmed with a TEM analysis and reported for the first time in this material in this study.

3. The DSC analysis shows that the liquidus, solidus, γ′ solvus, and γ-γ′ eutectic temperatures in CoWAlloy1 are T_L=1384°C, T_S=1306°C, $T_{\gamma'}$=1072°C, and $T_{(\gamma\text{-}\gamma')_e}$=1203°C respectively.

5.1.3 FZ and HAZ Microstructural Characterization

Detailed study of the FZ and HAZ microstructures and the investigation of the primary causes of HAZ cracking are conducted by using various advanced characterization techniques, including SEM, TEM, and EPMA. The major findings are as follows.

1. Although the formation of cracks can be detected in the HAZ during the welding of the alloy, cracks are not observed in the FZ of all the examined welded samples, regardless of the pre-weld heat treatment condition.

2. The microsegregation behavior observed throughout the solidification of the FZ indicates that Co and Ni segregate fairly uniformly between the dendrites and interdendritic regions. On the other hand, W and Cr somewhat segregate to the dendrites, while Al, Ta, Ti, Hf, Si, and Zr tend to partition to the interdendritic liquid.

3. The TEM analysis of the FZ confirms the formation of secondary solidification products which consist of MC-type carbides and γ-γ′ eutectics within the interdendritic regions. Furthermore, the TEM analysis confirms the inhomogeneous distribution of the γ′ precipitates within the FZ.

4. A study of the microstructure of the HAZ shows that a primary cause of cracking is intergranular liquation due to the subsolidus liquation reaction of MC-type carbide particles and γ′ precipitates, which are found prior to welding.

5.1.4 Enhanced Resistance to HAZ Cracking during Welding and PWHT

The arc weldability of CoWAlloy1 is extensively studied and the effect of the factors that contribute to the cracking susceptibility of the HAZ is examined after applying pre-weld and post-weld heat treatments by using advanced microstructural characterization techniques including SEM and SIMS. The major findings of detailed weldability studies and the development of an effective thermal treatment procedure for the alloy to minimize HAZ cracking during welding and PWHT are as follows.

1. Weldability studies on CoWAlloy1 reveal that the TCL of the HAZ follows a U-shape trend with an increase in heat-treatment temperature in which the shortest TCL of the HAZ is found at 1010ºC. In addition, Although the average TCLs of the AC samples are longer than those of the WQ samples at 4 different temperatures, i.e., 870, 970, 1070, and 1170ºC, the pre-weld heat treatment at 1010ºC shows a similar cracking susceptibility of the HAZ for both the AC and WQ samples.

2. An analysis of the TCL of the HAZ and hardness measurements conducted on pre-weld heat-treated samples including overaged sample reveal that pre-weld hardness does not influence the cracking susceptibility of the HAZ during welding. According to the DSC measurements, this could be due to the slow γ' precipitation kinetics in CoWAlloy1 which results in low shrinkage stresses generated during cooling after welding.

3. The ToF-SIMS analysis confirms the dependency of the cracking susceptibility of the HAZ on the grain boundary segregation of B. The cracking susceptibility of the HAZ appears to be minimum at 1010°C as a result of a balance between equilibrium and non-equilibrium grain boundary segregation.

4. An investigation of the influence of grain size on the resistance of the HAZ to cracking reveals that grain refinement considerably reduces the cracking susceptibility. Grain refinement from 1600 μm to 60 μm leads to a reduction in the TCL of the HAZ by 70% with a pre-weld heat treatment at 1010°C and then air cooling.

5. The findings on PWHT cracking reveal that even though reducing the pre-weld hardness does not help to reduce the cracking susceptibility of the HAZ during welding, nevertheless, this minimizes HAZ cracking during the PWHT. Furthermore, minimizing HAZ cracking during welding appears to be more beneficial as the overall extent of cracking after the PWHT is governed by the extent of cracking of the HAZ which occurred during welding. According to this analysis, overaging heat treatment significantly reduces the HAZ cracking in CoWAlloy1 during PWHT.

6. A ToF-SIMS investigation combined with an analysis of the TCL of the HAZ shows that cracking susceptibility of the HAZ during welding and PWHT is minimized by subjecting the alloy to an overaging heat treatment (1010°C, 50 hrs, air cooling) that combines low grain boundary segregation of B, a small grain size, and low pre-weld hardness.

5.1.5 γ′ Re-precipitation Behavior

The γ′ re-precipitation behavior is examined through DSC and SEM. The key findings are as follows.

1. Increasing the cooling rate results in an increase in precipitation rates at different temperatures. As the cooling rate increases, the temperature at which the maximum precipitation rate occurs decreases. Furthermore, increasing the cooling rate leads to a delay in the completion of γ′

precipitation; for example, as the cooling rate increases from 2.5ºC/min to 40ºC/min, the temperature at which complete precipitation occurs declines from 1028ºC to 854ºC.

2. The activation energy for γ′ precipitation is calculated to be 1775 kJ/mol in CoWAlloy1, which is considerably higher than that of some of the other Ni-based superalloys which might be due to the lower rates of atomic diffusion in this Co-based superalloy.

3. The cooling rate affects the morphology and size of the γ′ precipitates. With increasing the cooling rate from 2.5ºC/min to 40ºC/min, the shape of the γ′ precipitates changes from cuboidal with an average size of 280 nm to near-spherical with an average size of 60 nm. These transformations in size and morphology result in an increase in hardness from 410 Hv to 441 Hv.

5.1.6 Mechanical Properties and Hot Corrosion Behavior of CoWAlloy1

The effect of the pre-weld microstructural modifications on both the mechanical properties and hot corrosion resistance of CoWAlloy1 are evaluated. The key findings are as follows.

1. An investigation of the mechanical properties of welded CoWAlloy1 shows significant degradation in the tensile properties due to the occurrence of HAZ cracking during welding which can be avoided if the material is subjected to the pre-weld heat treatment identified in this work.

2. Welding leads to the formation of a dendritic solidification structure with significant elemental micro-segregation in the FZ. The depletion of Cr in the interdendritic region reduces the local resistance of the interdendritic region to hot corrosion and leads to preferential corrosion in the FZ.

3. An analysis of the corroded specimens with electron microscopy and spectroscopy techniques reveals that both the welded and unwelded specimens have the same types of oxide layers and corrosion products.

4. The probable hot corrosion mechanism that occurs in CoWAlloy1 is initially the oxidation of alloying elements beneath the deposited molten mixed salt, followed by fluxing of the oxide layers by the molten salt and inward diffusion of S and O which leads to internal oxidation/sulphidation.

5. Hot corrosion studies reveal that by using the new pre-weld heat treatment, welding does not produce a substantial reduction in hot corrosion resistance of CoWAlloy1. The slight reduction in hot corrosion resistance can be due to preferential corrosion in the welded specimen as a result of elemental segregation.

5.2 Conclusions

The major conclusions from this research work are as follows.

1. The numerical model developed to simulate the GTAW of CoWAlloy1 shows an adequate level of accuracy for predicting FZ solidification behavior and selecting the window of welding parameters that prevent FZ cracking.

2. A microstructural study of arc welded CoWAlloy1 shows that this alloy cracks during welding and the cracks are mainly confined to the HAZ while the FZ is crack-free, regardless of the used pre-weld heat treatment condition.

3. A TEM analysis of the FZ confirms the formation of γ′, MC-type carbides, and γ-γ′ eutectics but no formation of deleterious phases.

4. A detailed microstructural study shows that the primary cause of HAZ cracking during welding is intergranular liquation due to the subsolidus liquation reaction of MC-type carbide particles and γ′ precipitates, which are found prior to welding.

5. The proposed pre-weld heat treatment in this work based on minimizing the grain boundary segregation of B and grain size refinement results in a significant reduction in HAZ cracking during welding and PWHT. In addition, the new pre-weld heat treatment results in minimal deterioration of the mechanical properties and does not produce a substantial reduction in hot corrosion resistance of CoWAlloy1.

CHAPTER 6

Recommendations for Future Work

The following are some recommendations for related future work.

1. The proposed pre-weld thermal treatment procedure developed in this study is found to be effective in drastically reducing intergranular liquation cracking in the HAZ during GTAW. Since the mechanism of this liquation cracking is the same in the alloy irrespective of the type of fusion welding technique used, it is recommended that the proposed pre-weld heat treatment be applied to other fusion welding techniques such as laser-arc hybrid welding. Chaturvedi [12] reported that laser-arc hybrid welding has great potential for joining superalloys for aerospace applications.

2. This study focuses on the arc weldability of cast polycrystalline CoWAlloy1. However, CoWAlloy1 has not been manufactured in the directionally solidified (DS) and single crystal (SX) forms yet. It is recommended that this study be extended to develop single crystal CoWAlloy1 and investigate the effect of the grain structure on the microstructure and weldability of the alloy during GTAW.

3. Thamburaj et al. [183] reported that the condition of an alloy before welding (governed by the pre-weld heat treatment) and the PWHT schedule significantly influence the susceptibility of an alloy to cracking during the PWHT. Therefore, several combinations of pre-weld and post-weld heat treatments are required to be investigated to acquire the optimum combination that results in the least amount of cracking or no cracking in CoWAlloy1 after PWHT. In this study, the newly developed pre-weld heat treatment shows considerable potential in reducing HAZ cracking during welding. However, the PWHT plan which is the same as the recommended SHT results in PWHT

cracking. Therefore, a new PWHT schedule is recommended that minimizes/eliminates HAZ cracking after PWHT.

4. In this study, the effect of the preclusion of weld cracking by the new pre-weld heat treatment procedure is investigated on the tensile properties at room temperature and hot corrosion behavior of CoWAlloy1. It is recommended that a comprehensive study of the mechanical behavior of PWHTed specimens, including elevated-temperature tensile testing, high cycle, and low cycle fatigue studies, and thermo-mechanical fatigue and creep test be conducted.

Research Contributions from This Work

Peer-Reviewed Journal Publications:

1. H.R. Abedi, O.A. Ojo, Enhanced Resistance to Gas Tungsten Arc Weld Heat-Affected Zone Cracking in a Newly Developed Co-Based Superalloy, **Materials Science and Engineering: A**, 851, **(2022)**, 143618.

2. H.R. Abedi, O.A. Ojo, Microstructural Analysis of Fusion Zone in Gas Tungsten Arc-Welded Newly Developed Co-Based Superalloy. **Metall Mater Trans A** 53, 377–381 (**2022**).

3. H.R. Abedi, O.A. Ojo, Numerical Modeling of Gas Tungsten Arc Welding of a Newly Developed Cobalt-Based Superalloy. **Metall Mater Trans A** 52, 5043–5054 (**2021**).

4. H.R. Abedi, O.A. Ojo, and Cao, X. Effect of Cooling Rate on Precipitation Behavior of Gamma Prime in a Newly Developed Co-Based Superalloy. **JOM** 72, 4054–4059 (**2020**).

Conference Presentation:

H.R. Abedi, O.A. Ojo, On the Welding Speed Dependency of Fusion Zone Microstructure in a Newly Developed Co-Based Superalloy, **Canadian Materials Science Conference** (**2021**), Kingston, Canada.

REFERENCES

[1] C.T. Sims, N.S. Stoloff, and W.C. Hagel, *Superalloys II: High-Temperature Materials for Aerospace and Industrial Power*. Wiley-Interscience, 1987.

[2] S. Zhang, and D. Zhao, *Aerospace materials handbook*. CRC Press, 2016. doi: 10.1201/b13044.

[3] J. Sato, T. Omori, K. Oikawa, I. Ohnuma, R. Kainuma, and K. Ishida, "Cobalt-Base High-Temperature Alloys," *Science*, vol. 312, no. 5770, pp. 90–91, 2006, doi: 10.1126/science.1121738.

[4] A. Bauer, S. Neumeier, F. Pyczak, and M. Göken, "Microstructure and creep strength of different γ/γ′- strengthened Co-base superalloy variants," *Scr. Mater.*, vol. 63, no. 12, pp. 1197–1200, 2010, doi: 10.1016/j.scriptamat.2010.08.036.

[5] M.S. Titus, A. Suzuki, and T.M. Pollock, "Creep and directional coarsening in single crystals of new γ-γ′ Cobalt-base alloys," *Scr. Mater.*, vol. 66, pp. 574–577, 2012, doi: 10.1016/j.scriptamat.2012.01.008.

[6] A. Bauer, S. Neumeier, F. Pyczak, R.F. Singer, and M. Göken, "Creep properties of different γ′-strengthened Co-base superalloys," *Mater. Sci. Eng. A*, vol. 550, pp. 333–341, 2012, doi: 10.1016/j.msea.2012.04.083.

[7] S.V. L. Klein, A. Bauer, S. Neumeier, M. Göken, "High temperature oxidation of γ/γ′-strengthened Co-base superalloys," *Corros. Sci.*, vol. 53, pp. 2027–2034, 2011.

[8] M. Tsunekane, A. Suzuki, and T.M. Pollock, "Single-crystal solidification of new Co-Al-W-base alloys," *Intermetallics*, vol. 19, no. 5, pp. 636–643, 2011, doi: 10.1016/j.intermet.2010.12.018.

[9] A. Suzuki, and T.M. Pollock, "High-temperature strength and deformation of γ/γ′ two-phase Co-Al-W-base alloys," *Acta Mater.*, vol. 56, no. 6, pp. 1288–1297, 2008, doi: 10.1016/j.actamat.2007.11.014.

[10] S. Neumeier, L.P. Freund, and M. Göken, “Novel wrought γ/γ′ cobalt base superalloys with high strength and improved oxidation resistance,” *Scr. Mater.*, vol. 109, pp. 104–107, 2015, doi: 10.1016/j.scriptamat.2015.07.030.

[11] L.P. Freund, S. Giese, D. Schwimmer, H.W. Höppel, S. Neumeier, and M. Göken, “High temperature properties and fatigue strength of novel wrought γ/γ′ Co-base superalloys,” *J. Mater. Res.*, vol. 32, no. 24, pp. 4475–4482, 2017, doi: 10.1557/jmr.2017.315.

[12] M. C. Chaturvedi, *Welding and joining of aerospace materials*, 2ed ed. Woodhead Publishing, 2020. doi: https://doi.org/10.1016/C2018-0-03659-2.

[13] J. Chen, E. Salvati, F. Uzun, C. Papadaki, Z. Wang, J. Everaerts, and A.M. Korsunsky, “An experimental and numerical analysis of residual stresses in a TIG weldment of a single crystal nickel-base superalloy,” *J. Manuf. Process.*, vol. 53, no. February, pp. 190–200, 2020, doi: 10.1016/j.jmapro.2020.02.007.

[14] S. Lampman, *Weld Integrity and Performance*. ASM International, 1997. doi: https://doi.org/10.31399/asm.tb.wip.9781627083591.

[15] S. Geng, P. Jiang, X. Shao, L. Guo, and X. Gao, “Heat transfer and fluid flow and their effects on the solidification microstructure in full-penetration laser welding of aluminum sheet,” *J. Mater. Sci. Technol.*, vol. 46, pp. 50–63, 2020, doi: 10.1016/j.jmst.2019.10.027.

[16] R. Ghanavati, and H. Naffakh-Moosavy, “Additive manufacturing of functionally graded metallic materials: A review of experimental and numerical studies,” *J. Mater. Res. Technol.*, vol. 13, pp. 1628–1664, 2021, doi: 10.1016/j.jmrt.2021.05.022.

[17] O. A. Ojo, “On liquation cracking of cast Inconel 738LC superalloy welds,” Ph.D. Thesis, University of Manitoba, 2004. [Online]. Available: http://hdl.handle.net/1993/20151

[18] L.O. Osoba, R.K. Sidhu, and O.A. Ojo, “On preventing HAZ cracking in laser welded DS Rene 80 superalloy,” *Mater. Sci. Technol.*, vol. 27, no. 5, pp. 897–902, 2011, doi: 10.1179/026708309X12560332736593.

[19] L.O. Osoba, R.G. Ding, and O.A. Ojo, “Improved Resistance to Laser Weld Heat-Affected

Zone Microfissuring in a Newly Developed Superalloy HAYNES 282," *Metall. Mater. Trans. A*, vol. 43, pp. 4281–4295, 2012, doi: 10.1007/s11661-012-1212-7.

[20] O.A. Idowu, O.A. Ojo, and M.C. Chaturvedi, "Crack-free electron beam welding of allvac 718plus®superalloy," *Weld. J.*, vol. 88, no. 9, pp. 179–187, 2009, doi: https://app.aws.org/wj/supplement/wj0909-179.pdf.

[21] C. Liu, Y. Sun, M. Wen, T. He, and J. Yu, "Effect of Cr addition on microstructure and welding solidification cracking susceptibility of Co-Al-W based superalloys," *J. Manuf. Process.*, vol. 56, no. Part A, pp. 820–829, 2020, doi: 10.1016/j.jmapro.2020.03.049.

[22] S.H. Cho, J.S. Cha, S.H. Kim, E.Y. Choi, J.H. Lee, and J.M. Hur, "Hot corrosion behaviour of Inconel 625 weldments in molten lithium salt," *Corros. Eng. Sci. Technol.*, vol. 50, no. 8, pp. 606–617, 2015, doi: 10.1179/1743278215Y.0000000015.

[23] G. Asala, J. Andersson, and O.A. Ojo, "Hot corrosion behaviour of wire-arc additive manufactured Ni-based superalloy ATI 718Plus®," *Corros. Sci.*, vol. 158, no. February, p. 108086, 2019, doi: 10.1016/j.corsci.2019.07.010.

[24] F.R. Morral, "Cobalt-base Alloys in aerospace," *Sp. Congr. Proc.*, vol. 1970, pp. 53–64, 1970.

[25] D.L. Klarstrom, "Wrought cobalt- base superalloys," *J. Mater. Eng. Perform.*, vol. 2, no. 4, pp. 523–530, 1993, doi: 10.1007/BF02661736.

[26] K. Shinagawa, T. Omori, J. Sato, K. Oikawa, I. Ohnuma, R. Kainuma, and K. Ishida, "Phase Equilibria and Microstructure on γ′ Phase in Co-Ni-Al-W System," *Mater. Trans.*, vol. 49, no. 6, pp. 1474–1479, 2008, doi: 10.2320/matertrans.MER2008073.

[27] S. Meher, and R. Banerjee, "Partitioning and site occupancy of Ta and Mo in Co-base γ/γ′ alloys studied by atom probe tomography," *Intermetallics*, vol. 49, pp. 138–142, 2014, doi: 10.1016/j.intermet.2014.01.020.

[28] Q.F. F. Xue, H.J.Zhou, X.F.Ding, M.L.Wang, "Improved hightemperature γ′ stability of Co–Al–W-base alloys containing Ti and Ta," *Mater. Lett.*, vol. 112, pp. 215–218, 2013.

[29] S. Kobayashi, Y. Tsukamoto, and T. Takasugi, “The effects of alloying elements (Ta, Hf) on the thermodynamic stability of γ′-Co3 (Al, W) phase,” *Intermetallics*, vol. 31, pp. 94–98, 2012, doi: 10.1016/j.intermet.2012.06.006.

[30] K. Shinagawa, T. Omori, and K. Oikawa, “Ductility enhancement by boron addition in Co–Al–W high-temperature alloys,” *Scr. Mater.*, vol. 61, no. 6, pp. 612–615, 2009, doi: 10.1016/j.scriptamat.2009.05.037.

[31] L.P. Freund, A. Stark, F. Pyczak, N. Schell, M. Göken, and S. Neumeier, “The grain boundary pinning effect of the μ phase in an advanced polycrystalline γ/γ′ Co-base superalloy,” *J. Alloys Compd.*, vol. 753, pp. 333–342, 2018, doi: 10.1016/j.jallcom.2018.04.204.

[32] F. Xue, H.J. Zhou, X.F. Ding, M.L. Wang, and Q. Feng, “Improved high temperature γ′ stability of Co-Al-W-base alloys containing Ti and Ta,” *Mater. Lett.*, vol. 112, pp. 215–218, 2013, doi: 10.1016/j.matlet.2013.09.023.

[33] A.C.L. Kimmel, T.F. Malkowski, S. Griffiths, B. Hertweck, T.G. Steigerwald, L.P. Freund, S. Neumeier, M. Göken, J.S. Speck, and E. Schluecker, “High-temperature corrosion of Inconel®Alloy 718, Haynes®282®Alloy and CoWAlloy1&2 in supercritical ammonia/ammonium chloride solution,” *J. Cryst. Growth*, vol. 498, no. June, pp. 289–300, 2018, doi: 10.1016/j.jcrysgro.2018.06.018.

[34] R.C. Reed, *The Superalloys Fundamentals and Applications*. Cambridge University Press, 2006. doi: https://doi.org/10.1017/CBO9780511541285.

[35] C.H. Zenk, S. Neumeier, H.J. Stone, and M. Göken, “Mechanical properties and lattice misfit of γ/γ′-strengthened Co-base superalloys in the Co-W-Al-Ti quaternary system,” *Intermetallics*, vol. 55, pp. 28–39, 2014, doi: 10.1016/j.intermet.2014.07.006.

[36] M.J. Donachie, and S.J. Donachie, *Superalloys: A Technical Guide*, 2ed ed. ASM international, 1988. [Online]. Available: https://www.asminternational.org/documents/10192/1849770/ACFAACF.pdf

[37] A. Mottura, A. Janotti, and T.M. Pollock, “Alloying effects in the gamma prime phase of

Co-based superalloys," *Superalloys 2012*, pp. 685–693, 2012, [Online]. Available: https://www.tms.org/Superalloys/10.7449/2012/Superalloys_2012_685_693.pdf

[38] A.J. Ardell, "Precipitation hardening," *Metall. Trans. A*, vol. 16, pp. 2131–2165, 1985, doi: https://doi.org/10.1007/BF02670416.

[39] J.-S. Zhang, *High Temperature Deformation and Fracture of Materials*. Elsevier, 2010.

[40] W. Gui, H. Zhang, M. Yang, T. Jin, X. Sun, and Q. Zheng, "The investigation of carbides evolution in a cobalt-base superalloy at elevated temperature," *J. Alloys Compd.*, vol. 695, pp. 1271–1278, 2017, doi: 10.1016/j.jallcom.2016.10.256.

[41] W.H. Jiang, X.D. Yao, H.R. Guan, Z.Q. Hu, and W.H. Jiang, "Secondary carbide precipitation in a directionally solified cobalt-base superalloy," *Metall. Mater. Trans. A*, vol. 30, no. 3, pp. 513–520, 1999, doi: 10.1007/s11661-999-0043-7.

[42] M. Kolb, L.P. Freund, F. Fischer, … M. Göken, "On the grain boundary strengthening effect of boron in γ/γ′ Cobalt-base superalloys," *Acta Mater.*, vol. 145, pp. 247–254, 2018, doi: 10.1016/j.actamat.2017.12.020.

[43] J.C. Bennett, Jennifer L., Orion L. Kafka, Haiguang Liao, Sarah J. Wolff, Cheng Yu, Puikei Cheng, Gregory Hyatt, Kornel Ehmann, "Cooling rate effect on tensile strength of laser deposited Inconel 718," *Procedia Manuf.*, vol. 26, pp. 912–919, 2018, doi: 10.1016/j.promfg.2018.07.118.

[44] S.A. Sajjadi, H.R. Elahifar, and H. Farhangi, "Effects of cooling rate on the microstructure and mechanical properties of the Ni-base superalloy UDIMET 500," *J. Alloys Compd.*, vol. 455, no. 1–2, pp. 215–220, 2008, doi: 10.1016/j.jallcom.2007.01.091.

[45] H.T. Mallikarjuna, W.F. Caley, and N.L. Richards, "The effect of cooling rate on the γ′composition, morphology and corrosion behaviour of IN738LC," *Corros. Sci.*, vol. 149, pp. 37–44, 2019, doi: 10.1016/j.corsci.2018.12.036.

[46] Y. Mei, Y. Liu, C. Liu, C. Li, L. Yu, Q. Guo, and H. Li, "Effects of cold rolling on the precipitation kinetics and the morphology evolution of intermediate phases in Inconel 718

alloy," *J. Alloys Compd.*, vol. 649, pp. 949–960, 2015, doi: 10.1016/j.jallcom.2015.07.149.

[47] F. Masoumi, D. Shahriari, M. Jahazi, J. Cormier, and A. Devaux, "Kinetics and Mechanisms of γ′ Reprecipitation in a Ni-based Superalloy," *Sci. Rep.*, vol. 6, pp. 1–16, 2016, doi: 10.1038/srep28650.

[48] A. Yang, Y. Xiong, and L. Liu, "Effect of cooling rate on the morphology of γ′ precipitates in a nickel-base superalloy under directional solidification," *Sci. Technol. Adv. Mater.*, vol. 2, no. 1, pp. 105–107, 2001, doi: 10.1016/S1468-6996(01)00034-1.

[49] S. Behrouzghaemi, and R.J. Mitchell, "Morphological changes of γ′ precipitates in superalloy IN738LC at various cooling rates," *Materials Science and Engineering A*, vol. 498, no. 1–2. pp. 266–271, 2008. doi: 10.1016/j.msea.2008.07.069.

[50] H. Bian, X. Xu, Y. Li, Y. Koizumi, Z. Wang, and M. Chen, "Regulating the coarsening of the γ′ phase in superalloys," *NPG Asia Materials*, vol. 7, no. 8. pp. e212–e212, 2015. doi: 10.1038/am.2015.96.

[51] H. Monajati, M. Jahazi, R. Bahrami, and S. Yue, "The influence of heat treatment conditions on γ′ characteristics in Udimet® 720," *Mater. Sci. Eng. A*, vol. 373, no. 1–2, pp. 286–293, 2004, doi: 10.1016/j.msea.2004.01.027.

[52] A.K. Dwarapureddy, E. Balikci, S. Ibekwe, and A. Raman, "Activation energy for growth in single size distribution and the dissolution features of γ′ precipitates in the superalloy IN738LC," *J. Mater. Sci.*, vol. 43, no. 6, pp. 1802–1810, 2008, doi: 10.1007/s10853-007-2342-y.

[53] Y. Li, K. Chen, and N. Tamura, "Mechanism of heat affected zone cracking in Ni-based superalloy DZ125L fabricated by laser 3D printing technique," *Mater. Des.*, vol. 150, pp. 171–181, 2018, doi: 10.1016/j.matdes.2018.04.032.

[54] F. Hanning, A.K. Khan, J. Steffenburg-Nordenström, O. Ojo, and J. Andersson, "Investigation of the effect of short exposure in the temperature range of 750–950°C on the ductility of haynes® 282® by advanced microstructural characterization," *Metals (Basel).*, vol. 9, no. 12, 2019, doi: 10.3390/met9121357.

[55] J. Tiley, G.B. Viswanathan, R. Srinivasan, R. Banerjee, D.M. Dimiduk, and H.L. Fraser, "Coarsening kinetics of γ′ precipitates in the commercial nickel base Superalloy René 88 DT," *Acta Mater.*, vol. 57, no. 8, pp. 2538–2549, 2009, doi: 10.1016/j.actamat.2009.02.010.

[56] S. Meher, S. Nag, J. Tiley, A. Goel, and R. Banerjee, "Coarsening kinetics of γ′ precipitates in cobalt-base alloys," *Acta Mater.*, vol. 61, no. 11, pp. 4266–4276, 2013, doi: 10.1016/j.actamat.2013.03.052.

[57] V.A. Vorontsov, J.S. Barnard, K.M. Rahman, H.Y. Yan, P.A. Midgley, and D. Dye, "Coarsening behaviour and interfacial structure of γ′ precipitates in Co-Al-W based superalloys," *Acta Mater.*, vol. 120, pp. 14–23, 2016, doi: 10.1016/j.actamat.2016.08.023.

[58] D.F. Heaney, *Handbook of Metal Injection Molding*. Woodhead Publishing, 2012. doi: 10.1533/9780857096234.

[59] A. Mashhuriazar, H. Omidvar, Z. Sajuri, C.H. Gur, and A.H. Baghdadi, "Effects of pre-weld heat treatment and heat input on metallurgical and mechanical behaviour in HAZ of multi-pass welded in-939 superalloy," *Metals (Basel).*, vol. 10, no. 11, pp. 1–17, 2020, doi: 10.3390/met10111453.

[60] Sindo Kou, *Welding Metallurgy*, 2ed ed. New Jersey: John Wiley & Sons, Inc., 2002. doi: 10.1016/S0016-7878(62)80017-0.

[61] R.W. Messler, *Principles of Welding: Processes, Physics, Chemistry, and Metallurgy*. John Wiley & Sons, 1999. doi: 10.1002/9783527617487.

[62] David H. Phillips, *Welding Engineering: An Introduction*. John Wiley & Sons, 2016.

[63] S.A. David, S.S. Babu, and J.. Vitek, "Welding: Solidification and Microstructure," *Jom*, vol. 55, pp. 14–20, 2003, doi: https://doi.org/10.1007/s11837-003-0134-7.

[64] T. Trivedi, R., David, S.A., Eshelman, M.A., Vitek, J.M., Babu, S.S., Hong, T. and DebRoy, "In situ observations of weld pool solidification using transparent metal-analog systems," *J. Appl. Phys.*, vol. 93, no. 8, pp. 4885–4895, 2003, doi: 10.1063/1.1559934.

[65] J. F. Lancaster, *Metallurgy of Welding*. Elsevier, 1999.

[66] G. Li, X. Lu, X. Zhu, J. Huang, L. Liu, and Y. Wu, "The defects and microstructure in the fusion zone of multipass laser welded joints with Inconel 52M filler wire for nuclear power plants," *Opt. Laser Technol.*, vol. 94, pp. 97–105, 2017, doi: 10.1016/j.optlastec.2017.02.005.

[67] W. Kurz, C. Bezençon, and M. Gäumann, "Columnar to equiaxed transition in solidification processing," *Sci. Technol. Adv. Mater.*, vol. 2, no. 1, pp. 185–191, 2001, doi: 10.1016/S1468-6996(01)00047-X.

[68] E.A. Bonifaz, and N.L. Richards, "Modeling cast IN-738 superalloy gas tungsten arc welds," *Acta Mater.*, vol. 57, no. 6, pp. 1785–1794, 2009, doi: 10.1016/j.actamat.2008.12.022.

[69] M.J. Bermingham, D.H. StJohn, J. Krynen, S. Tedman-Jones, and M.S. Dargusch, "Promoting the columnar to equiaxed transition and grain refinement of titanium alloys during additive manufacturing," *Acta Mater.*, vol. 168, pp. 261–274, 2019, doi: 10.1016/j.actamat.2019.02.020.

[70] P. Schempp, and M. Rethmeier, "Understanding grain refinement in aluminium welding," *Weld. World*, vol. 59, no. 6, pp. 767–784, 2015, doi: 10.1007/s40194-015-0251-2.

[71] J.W. Park, S.S. Babu, J.M. Vitek, E.A. Kenik, and S.A. David, "Stray grain formation in single crystal Ni-base superalloy welds," *J. Appl. Phys.*, vol. 94, no. 6, pp. 4203–4209, 2003, doi: 10.1063/1.1602950.

[72] E. Vandersluis, and C. Ravindran, "Comparison of Measurement Methods for Secondary Dendrite Arm Spacing," *Metallogr. Microstruct. Anal.*, vol. 6, no. 1, pp. 89–94, 2017, doi: 10.1007/s13632-016-0331-8.

[73] X. Xue, and L. Xu, "Numerical simulation and prediction of solidification structure and mechanical property of a superalloy turbine blade," *Mater. Sci. Eng. A*, vol. 499, no. 1–2, pp. 69–73, 2009, doi: 10.1016/j.msea.2007.12.052.

[74] M.M. Franke, R.M. Hilbinger, C.H. Konrad, U. Glatzel, and R.F. Singer, “Numerical determination of secondary dendrite arm spacing for IN738LC investment castings,” *Metall. Mater. Trans. A Phys. Metall. Mater. Sci.*, vol. 42, no. 7, pp. 1847–1853, 2011, doi: 10.1007/s11661-010-0585-8.

[75] H.L. Yunpeng Mei, Yongchang Liu, Chenxi Liu, Chong Li, Liming Yu, Qianying Guo, “Effect of base metal and welding speed on fusion zone microstructure and HAZ hot-cracking of electron-beam welded Inconel 718,” *Mater. Des.*, vol. 89, pp. 964–977, 2016, doi: 10.1016/j.matdes.2015.10.082.

[76] K.S. Bal, J. Dutta Majumdar, and A. Roy Choudhury, “Effect of electron beam accelerating voltage on the melt zone area, secondary-dendrite arm spacing and fusion line microstructure of bead-on-plate welded Hastelloy C-276 sheet,” *Optik (Stuttg).*, vol. 183, no. January, pp. 355–366, 2019, doi: 10.1016/j.ijleo.2019.02.084.

[77] D.M. Stefanescu, and R. Ruxanda, “Fundamentals of Solidification,” *Mater. Park. OH ASM Int.*, pp. 71–92, 2004, doi: 10.31399/asm.hb.v09.a0003724.

[78] R.G. Ding, O.A. Ojo, and M.C. Chaturvedi, “Fusion zone microstructure of laser beam welded directionally solidified Ni3Al-base alloy IC6,” *Scr. Mater.*, vol. 54, no. 5, pp. 859–864, 2006, doi: 10.1016/j.scriptamat.2005.11.010.

[79] J.A. Brooks, and R.W. Krenzer, “Progress Toward a More Weldable a-286 - 1.,” *Weld. J. (Miami, Fla)*, vol. 53, no. 6, pp. 4–7, 1974.

[80] O.A. Ojo, N.L. Richards, and M.C. Chaturvedi, “Microstructural study of weld fusion zone of TIG welded IN 738LC nickel-based superalloy,” *Scr. Mater.*, vol. 51, no. 7, pp. 683–688, 2004, doi: 10.1016/j.scriptamat.2004.06.013.

[81] M.J. Strum, L.T. Summers, and J.W. Morris, “The Aging Response of a Welded Iron-Based Superalloy An alloy with improved hot cracking resistance exhibits pronounced differences in aging response and resulting strength level between base and weld metal regions”.

[82] S. Chen, H. Hu, M. Zhao, and L. Rong, “Effect of post-weld aging treatment on the precipitation and mechanical behavior of Fe-Ni based alloy weldment,” *Mater. Sci. Eng. A*,

vol. 718, no. December 2017, pp. 363–370, 2018, doi: 10.1016/j.msea.2018.01.127.

[83] L. Jeffus, *Welding: Principles and Applications*, 8th ed. Delmar Publishers Inc, 2017.

[84] E. Jenney, Cynthia L., and Annette O'Brien, *Welding Handbook* 10th ed., vol. 1. American Welding Society, 2019.

[85] R. G. Baker, "Weldability and Its Implications for Materials Requirements," *Philos. Trans. R. Soc. London. Ser. A, Math. Phys. Sci.*, vol. 282, no. 1307, pp. 207–223, 1976.

[86] L.O. Osoba, R.G. Ding, and O.A. Ojo, "Microstructural analysis of laser weld fusion zone in Haynes 282 superalloy," *Mater. Charact.*, vol. 65, pp. 93–99, 2012, doi: 10.1016/j.matchar.2011.12.009.

[87] O.A. Ojo, N.L. Richards, and M.C. Chaturvedi, "Contribution of constitutional liquation of gamma prime precipitate to weld HAZ cracking of cast Inconel 738 superalloy," *Scr. Mater.*, vol. 50, no. 5, pp. 641–646, 2004, doi: 10.1016/j.scriptamat.2003.11.025.

[88] O.T. Ola, O.A. Ojo, and M.C. Chaturvedi, "On the development of a new pre-weld thermal treatment procedure for preventing heat-affected zone (HAZ) liquation cracking in nickel-base in 738 superalloy," *Philos. Mag.*, vol. 94, no. 29, pp. 3295–3316, 2014, doi: 10.1080/14786435.2014.956838.

[89] K.C. Chen, T.C. Chen, R.K. Shiue, and L.W. Tsay, "Liquation cracking in the heat-affected zone of IN738 superalloy weld," *Metals (Basel).*, vol. 8, no. 6, pp. 12–14, 2018, doi: 10.3390/met8060387.

[90] J.J. Pepe, and W.F. Savage, "The Weld Heat-Affected Zone of the 18Ni Maraging Steels," *Weld. J.*, vol. 49, no. 12, pp. 545–553, 1970.

[91] S.D.K. Lippold, John C., and J.N. DuPont, *Welding metallurgy and weldability of nickel-base alloys*. John Wiley & Sons, 2011. [Online]. Available: http://library1.nida.ac.th/termpaper6/sd/2554/19755.pdf

[92] W. Chen, M.C. Chaturvedi, N.L. Richards, and G. McMahon, "Grain boundary segregation

of boron in INCONEL 718," *Metall. Mater. Trans. A Phys. Metall. Mater. Sci.*, vol. 29, no. 7, pp. 1947–1954, 1998, doi: 10.1007/s11661-998-0020-6.

[93] X. Huang, M.C. Chaturvedi, N.L. Richards, and J. Jackman, "The effect of grain boundary segregation of boron in cast alloy 718 on HAZ microfissuring - A SIMS analysis," *Acta Mater.*, vol. 45, no. 8, pp. 3095–3107, 1997, doi: 10.1016/S1359-6454(97)00017-7.

[94] K.R. Vishwakarma, and M.C. Chaturvedi, "Effect of boron and phosphorus on HAZ microfissuring of Allvac 718 Plus superalloy," *Mater. Sci. Technol.*, vol. 25, no. 3, pp. 351–360, 2009, doi: 10.1179/174328407X243032.

[95] G. Asala, and O.A. Ojo, "On post-weld heat treatment cracking in tig welded superalloy ATI 718Plus," *Results Phys.*, vol. 6, pp. 196–198, 2016, doi: 10.1016/j.rinp.2016.03.011.

[96] M.T. Rush, P.A. Colegrove, Z. Zhang, and D. Broad, "Liquation and post-weld heat treatment cracking in Rene 80 laser repair welds," *J. Mater. Process. Technol.*, vol. 212, no. 1, pp. 188–197, 2012, doi: 10.1016/j.jmatprotec.2011.09.001.

[97] R.K. Sidhu, N.L. Richards, and M.C. Chaturvedi, "Post-weld heat treatment cracking in autogenous GTA welded cast Inconel 738LC superalloy," *Mater. Sci. Technol.*, vol. 23, no. 2, pp. 203–213, 2007, doi: 10.1179/174328406X131055.

[98] A.B. Kilgore, M.L. Koehler, J.W. Metzler, and S.R. Sturges, *Welding, Brazing, and Soldering Handbook*, vol. 6. ASM International, 1993.

[99] O.A. Ojo, and M.C. Chaturvedi, "Liquation microfissuring in the weld heat-affected zone of an overaged precipitation-hardened nickel-base superalloy," *Metall. Mater. Trans. A Phys. Metall. Mater. Sci.*, vol. 38, no. 2, pp. 356–369, 2007, doi: 10.1007/s11661-006-9025-1.

[100] J. Caron, C. Heinze, C. Schwenk, M. Rethmeier, S.S. Babu, and J. Lippold, "Effect of continuous cooling transformation variations on numerical calculation of welding-induced residual stresses," *Weld. J.*, vol. 89, no. 7, pp. 151–160, 2010.

[101] D.A. Metzler, "A gleeble®-based method for ranking the strain-age cracking susceptibility

of Ni-based superalloys," *Weld. J.*, vol. 87, no. 10, pp. 249–256, 2008.

[102] O.T. Ola, O.A. Ojo, and M.C. Chaturvedi, "Laser arc hybrid weld microstructure in nickel based IN738 superalloy," *Mater. Sci. Technol. (United Kingdom)*, vol. 29, no. 4, pp. 426–438, 2013, doi: 10.1179/1743284712Y.0000000129.

[103] G.N. Vigilante, S. Bartolucci, J. Izzo, M. Witherell, and S.B. Smith, "Gleeble testing to assess solid/liquid metal embrittlement of gun steels by copper," *Mater. Manuf. Process.*, vol. 27, no. 8, pp. 835–839, 2012, doi: 10.1080/10426914.2011.648693.

[104] L.O. Osoba, "A study on laser weldability improvement of newly developed Haynes 282 superalloy, PhD Thesis," University of Manitoba, 2012. [Online]. Available: https://mspace.lib.umanitoba.ca/bitstream/handle/1993/8156/Osoba_Lawrence.pdf?sequence=1

[105] F. S. Pettit and G. H. Meier, "Oxidation and hot corrosion of superalloys," *Superalloys*, vol. 85, no. 1, pp. 651–687, Aug. 1984.

[106] R.M. Eliaz, N., Shemesh, G., & Latanision, "Hot Corrosion in Gas Turbines.," *Eng. Fail. Anal.*, vol. 9, no. 1, pp. 31–43, 2002, doi: https://doi.org/10.1016/S1350-6307(00)00035-2.

[107] J. Stringer, "High-Temperature Corrosion of Superalloys.," *Mater. Sci. Technol.*, vol. 3, no. 7, pp. 482–493, 1986, doi: 10.1080/02670836.1987.11782259.

[108] D. Coutsouradis, A. Davin, and M. Lamberigts, "Cobalt-based superalloys for applications in gas turbines," *Mater. Sci. Eng.*, vol. 88, no. C, pp. 11–19, 1987, doi: 10.1016/0025-5416(87)90061-9.

[109] Z.G. Sun, G. F., Wang, Z. D., Lu, Y., Zhou, R., Ni, Z. H., Gu, X., & Wang, "Numerical and experimental investigation of thermal field and residual stress in laser-MIG hybrid welded NV E690 steel plates," *J. Manuf. Process.*, vol. 34, pp. 106–120, 2018, doi: 10.1016/j.jmapro.2018.05.023.

[110] X. Shan, C.M. Davies, T. Wangsdan, N.P. O'Dowd, and K.M. Nikbin, "Thermo-mechanical modelling of a single-bead-on-plate weld using the finite element method," *Int.*

J. Press. Vessel. Pip., vol. 86, no. 1, pp. 110–121, 2009, doi: 10.1016/j.ijpvp.2008.11.005.

[111] J. Ahn, E. He, L. Chen, R.C. Wimpory, J.P. Dear, and C.M. Davies, "Prediction and measurement of residual stresses and distortions in fibre laser welded Ti-6Al-4V considering phase transformation," *Mater. Des.*, vol. 115, pp. 441–457, 2017, doi: 10.1016/j.matdes.2016.11.078.

[112] M. Zain-ul-abdein, D. Nélias, J.F. Jullien, F. Boitout, L. Dischert, and X. Noe, "Finite element analysis of metallurgical phase transformations in AA 6056-T4 and their effects upon the residual stress and distortion states of a laser welded T-joint," *Int. J. Press. Vessel. Pip.*, vol. 88, no. 1, pp. 45–56, 2011, doi: 10.1016/j.ijpvp.2010.10.008.

[113] A. Ghosh, A. Yadav, and A. Kumar, "Modelling and experimental validation of moving tilted volumetric heat source in gas metal arc welding process," *J. Mater. Process. Technol.*, vol. 239, pp. 52–65, 2017, doi: 10.1016/j.jmatprotec.2016.08.010.

[114] R. Han, S. Lu, W. Dong, D. Li, and Y. Li, "Multi-scale simulation for the columnar to equiaxed transition in the weld pool," *ISIJ Int.*, vol. 56, no. 6, pp. 1003–1012, 2016, doi: 10.2355/isijinternational.ISIJINT-2015-738.

[115] M. Gäumann, C. Bezençon, P. Canalis, and W. Kurz, "Single-crystal laser deposition of superalloys: Processing-microstructure maps," *Acta Mater.*, vol. 49, no. 6, pp. 1051–1062, 2001, doi: 10.1016/S1359-6454(00)00367-0.

[116] M. Suta, "SIMS – Secondary Ion Mass Spectrometry," *Solid State Chem.*, pp. 6–7, 2011.

[117] M. Anderson, A.L. Thielin, F. Bridier, P. Bocher, and J. Savoie, "δ Phase precipitation in Inconel 718 and associated mechanical properties," *Mater. Sci. Eng. A*, vol. 679, no. August 2016, pp. 48–55, 2017, doi: 10.1016/j.msea.2016.09.114.

[118] M. Chen, K. Feng, M. Li, and C. Zhou, "Hot corrosion behaviour of Al-Si-Dy coating on new γ′-strengthened cobalt-based alloy," *Corrosion Science*, vol. 166. 2020. doi: 10.1016/j.corsci.2020.108431.

[119] X. Qi, Q. Hou, M. Chen, S. Zhu, M. Li, and C. Zhou, "Microstructure and hot corrosion

behavior of Al-Si-Hf coating on new γ′-strengthened cobalt-based superalloy," *Surf. Coatings Technol.*, vol. 405, no. July 2020, 2021, doi: 10.1016/j.surfcoat.2020.126519.

[120] Y.T. Xu, T.D. Xia, and J.Q. Yan, "Effect of alloying element tungsten on hot corrosion behavior of novel Co-Al-W superalloys," *Zhongguo Youse Jinshu Xuebao/Chinese J. Nonferrous Met.*, vol. 21, no. 1, pp. 110–117, 2011.

[121] G.S. Mahobia, N. Paulose, and V. Singh, "Hot corrosion behavior of superalloy IN718 at 550 and 650 C," *J. Mater. Eng. Perform.*, vol. 22, no. 8, pp. 2418–2435, 2013, doi: 10.1007/s11665-013-0532-0.

[122] Y.K. Liu, and Y.M. Zhang, "Control of 3D weld pool surface," *Control Eng. Pract.*, vol. 21, no. 11, pp. 1469–1480, 2013, doi: 10.1016/j.conengprac.2013.06.019.

[123] R. Sudhakaran, V. Vel-Murugan, and P.S. Sivasakthivel, "Effect of process parameters on depth of penetration in gas tungsten arc welded (GTAW) 202 grade stainless steel plates using response surface methodology," *J. Eng. Res.*, vol. 9, no. 1, pp. 64–79, 2012.

[124] H.N. Moosavy, M.R. Aboutalebi, and S.H. Seyedein, "An analytical algorithm to predict weldability of precipitation- strengthened nickel-base superalloys," *J. Mater. Process. Technol.*, vol. 212, no. 11, pp. 2210–2218, 2012, doi: 10.1016/j.jmatprotec.2012.06.010.

[125] N. Coniglio, and C.E. Cross, "Effect of weld travel speed on solidification cracking behavior. Part 1: weld metal characteristics," *Int. J. Adv. Manuf. Technol.*, vol. 107, no. 11–12, pp. 5011–5023, 2020, doi: 10.1007/s00170-020-05231-y.

[126] Z. Li, G. Yu, X. He, S. Li, and Y. Zhao, "Numerical and experimental investigations of solidification parameters and mechanical property during laser dissimilar welding," *Metals (Basel).*, vol. 8, no. 10, 2018, doi: 10.3390/met8100799.

[127] K.R. Vishwakarma, N.L. Richards, and M.C. Chaturvedi, "Microstructural analysis of fusion and heat affected zones in electron beam welded ALLVAC® 718PLUS™ superalloy," *Mater. Sci. Eng. A*, vol. 480, no. 1–2, pp. 517–528, 2008, doi: 10.1016/j.msea.2007.08.002.

[128] H.L. Wei, J.W. Elmer, and T. Debroy, “Origin of grain orientation during solidification of an aluminum alloy,” *Acta Mater.*, vol. 115, pp. 123–131, 2016, doi: 10.1016/j.actamat.2016.05.057.

[129] J. Ahn, E. He, L. Chen, J. Dear, Z. Shao, and C. Davies, “In-situ micro-tensile testing of AA2024-T3 fibre laser welds with digital image correlation as a function of welding speed,” *Int. J. Light. Mater. Manuf.*, vol. 1, no. 3, pp. 179–188, 2018, doi: 10.1016/j.ijlmm.2018.07.003.

[130] V. Villaret, F. Deschaux-Beaume, and C. Bordreuil, “A solidification model for the columnar to equiaxed transition in welding of a Cr-Mo ferritic stainless steel with Ti as inoculant,” *J. Mater. Process. Technol.*, vol. 233, pp. 115–124, 2016, doi: 10.1016/j.jmatprotec.2016.02.017.

[131] T.F. Bower, H.D. Brody, and M.C. Flemings, “Measurements of Solute Redistribution in Dendritic Solidification,” *Trans. Metall. Soc. AIME*, vol. 236, pp. 624–633, 1966.

[132] T.H. Koßmann, Jörg, Christopher H. Zenk, Inmaculada Lopez-Galilea, Steffen Neumeier, Aleksander Kostka, Stephan Huth, Werner Theisen, Mathias Göken, Ralf Drautz, “Microsegregation and precipitates of an as-cast Co-based superalloy—microstructural characterization and phase stability modelling,” *J. Mater. Sci.*, vol. 50, no. 19, pp. 6329–6338, 2015, doi: 10.1007/s10853-015-9177-8.

[133] S.A.F. Murray, Sean P., Kira M. Pusch, Andrew T. Polonsky, Chris J. Torbet, Gareth GE Seward, Ning Zhou, “A defect-resistant Co–Ni superalloy for 3D printing,” *Nat. Commun.*, vol. 11, no. 1, pp. 1–11, 2020, doi: 10.1038/s41467-020-18775-0.

[134] X. Zhou, H. Fu, Y. Zhang, H. Xu, and J. Xie, “Effect of Al and W Contents on the Solidification and Solution Microstructure of Novel γ/γ′ Cobalt-Base Superalloys,” *Adv. Eng. Mater.*, vol. 21, no. 12, pp. 1–10, 2019, doi: 10.1002/adem.201900641.

[135] C.A. Stewart, S.P. Murray, A. Suzuki, T.M. Pollock, and C.G. Levi, “Accelerated discovery of oxidation resistant CoNi-base γ/γ′ alloys with high L12 solvus and low density,” *Mater. Des.*, vol. 189, p. 108445, 2020, doi: 10.1016/j.matdes.2019.108445.

[136] X. Zhou, H. Fu, Y. Zhang, H. Xu, and J. Xie, “Effect of Ta and Ti on the solidification characteristics of novel γ′-strengthened Co-base superalloys,” *J. Alloys Compd.*, vol. 768, pp. 464–475, 2018, doi: 10.1016/j.jallcom.2018.07.218.

[137] Z. Sun, X. Chen, L. Zhang, S. Zhang, and J. Feng, “Experimental and numerical study of transient liquid phase diffusion bonded dz40m superalloys,” *Crystals*, vol. 11, no. 5, 2021, doi: 10.3390/cryst11050479.

[138] N. Saunders, A.P. Miodownik, and J.P. Schillé, “Modelling of the thermo-physical and physical properties for solidification of Ni-based superalloys,” *J. Mater. Sci.*, vol. 39, no. 24, pp. 7237–7243, 2004, doi: 10.1023/B:JMSC.0000048737.32055.7a.

[139] J. Kangazian, M. Shamanian, A. Kermanpur, E. Foroozmehr, and M. Badrossamay, “Investigation of microstructure-tensile behavior relationship in Hastelloy X Ni-based superalloy processed by laser powder-bed fusion: Insights into the elevated temperature ductility loss,” *Mater. Sci. Eng. A*, vol. 823, no. May, p. 141742, 2021, doi: 10.1016/j.msea.2021.141742.

[140] A. Ghasemi, A.M. Kolagar, and M. Pouranvari, “Microstructure-performance relationships in gas tungsten arc welded Hastelloy X nickel-based superalloy,” *Mater. Sci. Eng. A*, vol. 793, no. July, p. 139861, 2020, doi: 10.1016/j.msea.2020.139861.

[141] P. Tao, H. Li, B. Huang, Q. Hu, S. Gong, and Q. Xu, “The crystal growth, intercellular spacing and microsegregation of selective laser melted Inconel 718 superalloy,” *Vacuum*, vol. 159, no. September 2018, pp. 382–390, 2019, doi: 10.1016/j.vacuum.2018.10.074.

[142] M. Ooshima, K. Tanaka, N.L. Okamoto, K. Kishida, and H. Inui, “Effects of quaternary alloying elements on the γ′ solvus temperature of Co-Al-W based alloys with fcc/L12 two-phase microstructures,” *J. Alloys Compd.*, vol. 508, no. 1, pp. 71–78, 2010, doi: 10.1016/j.jallcom.2010.08.050.

[143] Y. Zhang, H. Fu, X. Zhou, Y. Zhang, and J. Xie, “Effects of aluminum and molybdenum content on the microstructure and properties of multi-component γ′-strengthened cobalt-base superalloys,” *Mater. Sci. Eng. A*, vol. 737, no. September, pp. 265–273, 2018, doi:

10.1016/j.msea.2018.09.058.

[144] O.A. Ojo, “Intergranular liquation cracking in heat affected zone of a welded nickel based superalloy in as cast condition,” *Mater. Sci. Technol.*, vol. 23, no. 10, pp. 1149–1155, 2007, doi: 10.1179/174328407X213323.

[145] R.K. Sidhu, N.L. Richards, and M.C. Chaturvedi, “Effect of aluminium concentration in filler alloys on HAZ cracking in TIG welded cast lnconel 738LC superalloy,” *Mater. Sci. Technol.*, vol. 21, no. 10, pp. 1119–1131, 2005, doi: 10.1179/174328405X62279.

[146] M. Qian, and J.C. Lippold, “The effect of multiple postweld heat treatment cycles on the weldability of Waspaloy®,” *Weld. J.*, vol. 81, no. 11, 2002.

[147] M.A. González, D.I. Martínez, A. Pérez, H. Guajardo, and A. Garza, “Microstructural response to heat affected zone cracking of prewelding heat-treated Inconel 939 superalloy,” *Mater. Charact.*, vol. 62, no. 12, pp. 1116–1123, 2011, doi: 10.1016/j.matchar.2011.09.006.

[148] O.A. Ojo, N.L. Richards, and M.C. Chaturvedi, “Study of the fusion zone and heat-affected zone microstructures in tungsten inert gas-welded INCONEL 738LC superalloy,” *Metall. Mater. Trans. A Phys. Metall. Mater. Sci.*, vol. 37, no. 2, pp. 421–433, 2006, doi: 10.1007/s11661-006-0013-2.

[149] M.C. Chaturvedi, W. Chen, A. Saranchuk, and N.L. Richards, “The Effect of B Segregation on Heat-Affected Zone Microfissuring in EB Welded Inconel 718,” no. January, pp. 743–751, 2012, doi: 10.7449/1997/superalloys_1997_743_751.

[150] X. Cao, B. Rivaux, M. Jahazi, J. Cuddy, and A. Birur, “Effect of pre- and post-weld heat treatment on metallurgical and tensile properties of Inconel 718 alloy butt joints welded using 4 kW Nd:YAG laser,” *J. Mater. Sci.*, vol. 44, no. 17, pp. 4557–4571, 2009, doi: 10.1007/s10853-009-3691-5.

[151] A.T. Egbewande, H.R. Zhang, R.K. Sidhu, and O.A. Ojo, “Improvement in laser weldability of INCONEL 738 superalloy through microstructural modification,” *Metall. Mater. Trans. A Phys. Metall. Mater. Sci.*, vol. 40, no. 11, pp. 2694–2704, 2009, doi: 10.1007/s11661-009-9962-6.

[152] K. Vishwakarma, and M. Chaturvedi, “A study of HAZ microfissuring in a newly developed Allvac® 718 PLUS™ superalloy,” *Proc. Int. Symp. Superalloys*, pp. 241–250, 2008, doi: 10.7449/2008/superalloys_2008_241_250.

[153] R.G. Thompson, “Microfissuring of Alloy 718 in the Weld Heat-Affected Zone,” *Jom*, vol. 40, no. 7, pp. 44–48, 1988, doi: https://doi.org/10.1007/BF03258151.

[154] W.A. Miller, and G.A. Chadwick, “On the magnitude of the solid/liquid interfacial energy of pure metals and its relation to grain boundary melting,” *Acta Metall.*, vol. 15, no. 4, pp. 607–614, 1967, doi: 10.1016/0001-6160(67)90104-6.

[155] C. Cheung, U. Erb, and G. Palumbo, “Application of grain boundary engineering concepts to alleviate intergranular cracking in Alloys 600 and 690,” *Mater. Sci. Eng. A*, vol. 185, no. 1–2, pp. 39–43, 1994, doi: 10.1016/0921-5093(94)90925-3.

[156] M.T. Rush, P.A. Colegrove, Z. Zhang, and B. Courtot, “An investigation into cracking in nickel-base superalloy repair welds,” *Adv. Mater. Res.*, vol. 89–91, pp. 467–472, 2010, doi: 10.4028/www.scientific.net/AMR.89-91.467.

[157] M.B. Henderson, D. Arrell, R. Larsson, M. Heobel, and G. Marchant, “Nickel based superalloy welding practices for industrial gas turbine applications,” *Sci. Technol. Weld. Join.*, vol. 9, no. 1, pp. 13–21, 2004, doi: 10.1179/136217104225017099.

[158] Y. Danis, C. Arvieu, E. Lacoste, T. Larrouy, and J.M. Quenisset, “An investigation on thermal, metallurgical and mechanical states in weld cracking of Inconel 738LC superalloy,” *Mater. Des.*, vol. 31, no. 1, pp. 402–416, 2010, doi: 10.1016/j.matdes.2009.05.041.

[159] A. Azzam, T. Philippe, A. Hauet, F. Danoix, D. Locq, P. Caron, and D. Blavette, “Kinetics pathway of precipitation in model Co-Al-W superalloy,” *Acta Mater.*, vol. 145, pp. 377–387, 2018, doi: 10.1016/j.actamat.2017.12.032.

[160] S. Zhao, X. Xie, G.D. Smith, and S.J. Patel, “Gamma prime coarsening and age-hardening behaviors in a new nickel base superalloy,” *Mater. Lett.*, vol. 58, no. 11, pp. 1784–1787, 2004, doi: 10.1016/j.matlet.2003.10.053.

[161] I. Roy, E. Balikci, S. Ibekwe, and A. Raman, “Precipitate growth activation energy requirements in the duplex size γ′ distribution in the superalloy IN738LC,” *J. Mater. Sci.*, vol. 40, no. 23, pp. 6207–6215, 2005, doi: 10.1007/s10853-005-3154-6.

[162] T. Grosdidier, A. Hazotte, and A. Simon, “Precipitation and dissolution processes in γ/γ ′ single crystal nickel-based superalloys,” *Mater. Sci. Eng. A*, vol. 256, no. 1–2, pp. 183–196, 1998, doi: 10.1016/s0921-5093(98)00795-3.

[163] K. Kakehi, “Effect of primary and secondary precipitates on creep strength of Ni-base superalloy single crystals,” *Mater. Sci. Eng. A*, vol. 278, no. 1–2, pp. 135–141, 2000, doi: 10.1016/S0921-5093(99)00579-1.

[164] K. Banerjee, N.L. Richards, and M.C. Chaturvedi, “Effect of filler alloys on heat-affected zone cracking in preweld heat-treated IN-738 LC gas-tungsten-arc welds,” *Metall. Mater. Trans. A Phys. Metall. Mater. Sci.*, vol. 36, no. 7, pp. 1881–1890, 2005, doi: 10.1007/s11661-005-0051-1.

[165] M. Montazeri, and F.M. Ghaini, “The liquation cracking behavior of IN738LC superalloy during low power Nd:YAG pulsed laser welding,” *Mater. Charact.*, vol. 67, pp. 65–73, 2012, doi: 10.1016/j.matchar.2012.02.019.

[166] K. Kawagishi, A. Sato, and H. Harada, “A concept for the EQ coating system for Nickel-based superalloys,” *Jom*, vol. 60, no. 7, pp. 31–35, 2008, doi: 10.1007/s11837-008-0086-z.

[167] A. Fossati, M. Di Ferdinando, A. Lavacchi, U. Bardi, C. Giolli, and A. Scrivani, “Improvement of the isothermal oxidation resistance of CoNiCrAlY coating sprayed by High Velocity Oxygen Fuel,” *Surf. Coatings Technol.*, vol. 204, no. 21–22, pp. 3723–3728, 2010, doi: 10.1016/j.surfcoat.2010.04.059.

[168] J.A. Haynes, M.K. Ferber, W.D. Porter, and E.D. Rigney, “Characterization of alumina scales formed during isothermal and cyclic oxidation of plasma-sprayed TBC systems at 1150°C,” *Oxid. Met.*, vol. 52, no. 1, pp. 31–76, 1999, doi: 10.1023/a:1018870923397.

[169] B. Gao, L. Wang, Y. Liu, X. Song, S.Y. Yang, and Z.Y. Yao, “Corrosion behavior of new type Co-based superalloys with different Ni contents,” *Corros. Rev.*, vol. 35, no. 6, pp. 455–

462, 2017, doi: 10.1515/corrrev-2017-0003.

[170] D. Mudgal, S. Singh, and S. Prakash, “High Temperature Cyclic Oxidation Behavior of Ni and Co Based Superalloys,” *J. Miner. Mater. Charact. Eng.*, vol. 11, no. 03, pp. 211–219, 2012, doi: 10.4236/jmmce.2012.113017.

[171] F. Zhong, F. Fan, S. Li, and J. Sha, “High-temperature oxidation behaviour of novel Co-Al-W-Ta-B-(Mo, Hf, Nb) alloys with a coherent γ/γ′–dominant microstructure,” *Prog. Nat. Sci. Mater. Int.*, vol. 26, no. 6, pp. 600–612, 2016, doi: 10.1016/j.pnsc.2016.11.005.

[172] H.Y. Zhu, Ying-xin, Chong Li, Yong-chang Liu, Zong-qing Ma, “Effect of Ti addition on high-temperature oxidation behavior of Co–Ni-based superalloy,” *J. Iron Steel Res. Int.*, vol. 27, no. 10, pp. 1179–1189, 2020, doi: 10.1007/s42243-020-00379-z.

[173] K.L. Luthra, “Low Temperature Hot Corrosion of Cobalt-Base Alloys" Part II. Reaction Mechanism K.L.,” vol. 13, no. October, pp. 1853–1864, 1982.

[174] G. Fu, X. Guo, Q. Liu, X. Zhao, and Y. Su, “Hot corrosion of co-based alloys with 25%NaCl+75%Na2SO 4 coating at 1173 K,” *High Temp. Mater. Process.*, vol. 32, no. 3, pp. 317–321, 2013, doi: 10.1515/htmp-2012-0134.

[175] F. Pedraza, B. Bouchaud, J. Balmain, G. Bonnet, V. Kolarik, and J. Menuey, “On the development of a protective oxide system in rare earth oxide coated nickel superalloy under isothermal oxidation conditions,” *Mater. Sci. Forum*, vol. 696, no. Cvd, pp. 284–289, 2011, doi: 10.4028/www.scientific.net/MSF.696.284.

[176] S. Seal, S.C. Kuiry, and L.A. Bracho, “Studies on the surface chemistry of oxide films formed on IN-738LC superalloy at elevated temperatures in dry air,” *Oxid. Met.*, vol. 56, no. 5–6, pp. 583–603, 2001, doi: 10.1023/a:1012569803467.

[177] G. Moskal, “Oxidation behavior of Co-Al-Mo-Nb and Co-Ni-Al-Mo-Nb new tungsten-free y-y’ cobalt-based superalloys,” *Ochr. Przed Korozją*, vol. 1, no. 9, pp. 28–32, 2017, doi: 10.15199/40.2017.9.5.

[178] J. Wang, M. Chen, S. Zhu, and F. Wang, “Ta effect on oxidation of a nickel-based single-

crystal superalloy and its sputtered nanocrystalline coating at 900-1100 °c," *Appl. Surf. Sci.*, vol. 345, pp. 194–203, 2015, doi: 10.1016/j.apsusc.2015.03.157.

[179] R.R. Srivastava, J. chun Lee, M. Bae, and V. Kumar, "Reclamation of tungsten from carbide scraps and spent materials," *J. Mater. Sci.*, vol. 54, no. 1, pp. 83–107, 2019, doi: 10.1007/s10853-018-2876-1.

[180] R.E. Ricker, "Corrosion of Intermetallics," *Corros. Mater.*, no. January 2005, pp. 490–512, 2018, doi: 10.31399/asm.hb.v13b.a0003837.

[181] S. Xu, T. Lu, K. Shen, J. Lan, B. Hu, H. Zhang, Y. Tang, H. Cao, and G. Zheng, "High temperature oxidation resistance of Ti-5553 alloy with electro-deposited SiO2 coating," *Mater. Chem. Phys.*, vol. 275, no. September 2021, p. 125306, 2022, doi: 10.1016/j.matchemphys.2021.125306.

[182] D.G. He, Y.C. Lin, Y. Tang, L. Li, J. Chen, M.S. Chen, and X.M. Chen, "Influences of solution cooling on microstructures, mechanical properties and hot corrosion resistance of a nickel-based superalloy," *Mater. Sci. Eng. A*, vol. 746, no. January, pp. 372–383, 2019, doi: 10.1016/j.msea.2019.01.015.

[183] R. Thamburaj, w. Wallace, and J.A. Goldak, "Post-weld heat-treatment cracking in superalloys," *Int. Met. Rev.*, vol. 28, no. 1, pp. 1–22, 1983, doi: 10.1179/imtr.1983.28.1.1.